

UNIVERSITY OF CALIFORNIA

Los Angeles

Numerical and Experimental Analysis of Diesel and JP-5
Transport in Unsaturated Soils

A dissertation submitted in partial satisfaction of the
requirements for the degree of Doctor of Philosophy
in Civil Engineering

by

Jun Zhou

1994

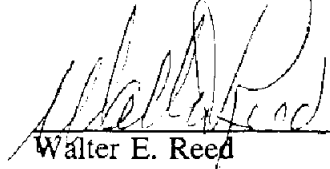
The dissertation of Jun Zhou is approved.



Menachem Elimelech



Thomas C. Harmon



Walter E. Reed



Michael K. Stenstrom, Committee Chair

University of California, Los Angeles

1994

TABLE OF CONTENTS

LIST OF FIGURES	vii
LIST OF TABLES	x
ACKNOWLEDGMENT	xi
ABSTRACT	xii
I. INTRODUCTION	1
II. LITERATURE REVIEW	5
III. EXPERIMENTAL	12
III.1 System and Apparatus	12
III.1a Test Chamber	12
III.1b Monitoring wells	12
III.1c Fuel delivery system	16
III.1d Hydrocarbon vapor monitoring system	16
III.2 Materials	17
III.3 Experimental Procedures	19
III.4 Sensor Calibration	21
IV. EXPERIMENTAL RESULTS	24
IV.1 Averaged Temporal Concentration Curves	24
IV.1a Test II (diesel in sand)	25
IV.1b Test III (diesel in soil)	35
IV.1c Test IV (JP-5 in sand)	36
IV.2 Time of Arrival (TOA)	37
IV.3 Concentration Contour Maps	42
IV.4 Concentration vs. Contour Radius	43

IV.5 Diesel Wetted Soil Pictures	51
V. MATHEMATICAL SIMULATION	58
V.1 Governing Equation	58
V.2 Initial and Boundary Conditions	63
V.2a Initial conditions	64
V.2b Boundary conditions	64
V.3 Parameters	72
V.3a Capillary pressure	72
V.3b Relative permeability	74
V.4 Finite Difference Equation	77
V.5 Alternating Direction Implicit (ADI) Method	80
V.6 Finite Difference Initial Conditions	81
V.7 Finite Difference Boundary Conditions	81
V.8 Picard Iteration Method	85
V.9 Mass Transfer in the Gas Phase	87
V.9a Gas Diffusion Equation in Porous Media	87
V.9b Initial and Boundary Conditions	91
V.9c Diffusion Coefficient in Porous Media	92
V.10 Numerical Algorithm	95
V.11 Parameter Estimation and The Complex Method of Box	96
VI. RESULTS AND DISCUSSION	99
VI.1 Model Verification	99
VI.2 Parameters Estimated With the Complex Method	107
VI.3 Objective function	110

VI.4 Parameter Estimation Using Hypothetical Data	118
VI.5 Experimental Parameter Estimation and Result Simulation	130
VI.5a Normalized hydrocarbon vapor concentration	130
VI.5b Parameter estimation for Test II and Test III	132
VI.5c Numerical simulation results for Test III	136
VI.5d Numerical simulation results for Test II	138
VI.5e Numerical simulation for Test IV	143
VII. CONCLUSIONS AND FUTURE WORK	148
VII.1 Summary and Conclusions	148
VII.2 Recommendations for Future Research	151
REFERENCES	152
APPENDIX A Numerical Model Derivation	163
APPENDIX B Vapor concentration contour maps	169
APPENDIX C Experimental Observed Vapor Concentration Data	191
APPENDIX D LAVS-1 Hydrocarbon Vapor Sensor Sensitivity	198
APPENDIX F Program Source Code	201

LIST OF FIGURES

Figure 1.	Schematic of the Experimental Set-up	13
Figure 2.	Pictures of the test chamber and data acquisition system	14
Figure 3.	Map of the hydrocarbon vapor monitoring wells	16
Figure 4.	Typical hydrocarbon vapor sensor calibration curve	23
Figure 5.	Temporal diesel vapor concentrations for Test II (a)	26
Figure 6.	Temporal diesel vapor concentrations for Test II (b)	27
Figure 7.	Temporal diesel vapor concentrations for Test III	28
Figure 8.	Temporal JP-5 vapor concentrations for Test IV (a)	29
Figure 9.	Temporal JP-5 vapor concentrations for Test IV (b)	30
Figure 10.	Temporal JP-5 vapor concentrations for Test IV (c)	31
Figure 11.	Temporal JP-5 vapor concentrations for Test IV (d)	32
Figure 12.	Temporal JP-5 vapor concentrations for Test IV (e)	33
Figure 13.	The TOA dependence on horizontal distance for Test II	38
Figure 14.	The TOA dependence on horizontal distance for Test IV	39
Figure 15.	The TOA dependence on vertical depth for Test II	40
Figure 16.	The TOA dependence on vertical depth for Test IV	41
Figure 17.	Diesel vapor concentration as function of contour radius for Test II at $z=2'$	44
Figure 18.	Diesel vapor concentration as function of contour radius for Test II at $z=5'$	45
Figure 19.	Diesel vapor concentration as function of contour radius for Test II at $z=8'$	46
Figure 20.	JP-5 vapor concentration as function of contour radius for Test IV at $z=2'$	47
Figure 21.	JP-5 vapor concentration as function of contour radius for	

Test IV at z=5'	48
Figure 22. JP-5 vapor concentration as function of contour radius for Test IV at z=8'	49
Figure 23. Soil surface picture taken at the end of Test III	53
Figure 24. Diesel wetted soil surface at the end of Test III	54
Figure 25. Vertical view of diesel wetted soil at the end of Test III (a)	55
Figure 26. Vertical view of diesel wetted soil at the end of Test III (b)	56
Figure 27. Vertical view of diesel wetted soil at the end of Test III (c)	57
Figure 28. Boundary schematic and saturated liquid entry zone	63
Figure 29. Egg-shaped liquid entry zone	67
Figure 30. Disk-like liquid entry zone	68
Figure 31. Column-like liquid entry zone	69
Figure 32. Hemispherical liquid entry zone	71
Figure 33. Conical discrete liquid entry zone	82
Figure 34. Water content distribution at t=0.17 hr.	102
Figure 35. Water content distribution at t=1.00 hr.	103
Figure 36. Water content distribution at t=2.75 hrs.	104
Figure 37. Water content distribution at t=6.00 hrs.	105
Figure 38. Comparison of predicted water wetting fronts to the experimental observations and the predictions by others.	106
Figure 39. The objective function constructed with unscreened vapor concentration observations changes with α factor	112
Figure 40. The objective function constructed with unscreened vapor concentration observations changes with n factor	113
Figure 41. The objective function constructed with unscreened vapor concentration observations changes with λ factor	114
Figure 42. The objective function constructed with screened vapor concentration observations changes with α factor	115

Figure 43.	The objective function constructed with screened vapor concentration observations changes with n factor	116
Figure 44.	The objective function constructed with unscreened vapor concentration observations changes with λ factor	117
Figure 45.	The convergence of the objective function	122
Figure 46.	Intrinsic permeability values searched by the parameter estimation technique	123
Figure 47.	van Genuchten's α values searched by the parameter estimation technique	124
Figure 48.	van Genuchten's n values searched by the parameter estimation technique	125
Figure 49.	λ factor values searched by the parameter estimation technique	126
Figure 50.	Vapor diffusivity values searched by the parameter estimation technique	127
Figure 51.	Estimated capillary pressure vs. saturation functional curve for diesel in soil	134
Figure 52.	Normalized diesel vapor concentration profile predicted by the model compared with the experimental observations	137
Figure 53.	Predicted diesel saturation distribution at the end of Test III ($t=720$ hrs)	139
Figure 54.	Predicted diesel wetting front (solid line) at the end of Test III and the observed location (dotted points)	140
Figure 55.	Normalized diesel vapor concentration profile of model predictions and experimental observations for Test II (diesel in soil)	142
Figure 56.	Predicted diesel saturation distribution at the end of Test II ($t=650$)	144
Figure 57.	Parameter search resulted in little improvement in the objective function when applied to the data of Test IV (JP-5 in sand)	145
Figure 58.	Normalized JP-5 vapor concentration profile of model predictions and experimental observations for Test IV	147
Figure B1-B21.	Vapor concentration contour maps	170-190
Figure D1-D2.	Sensitivity of LAVS-1 sensor to various hydrocarbons	199-200

LIST OF TABLES

Table 1.	Sand/Soil Particle Distribution Analysis Results	18
Table 2.	Properties of Diesel and JP-5 (Guthrie, 1967)	19
Table 3.	Summary of the Test Parameters	24
Table 4.	The measured location of diesel wetting front at the end of Test III	52
Table 5.	Simulation Parameters for Clothier and Scotter's Data	101
Table 6.	Estimated Values of α and n For Selected Soils	108
Table 7.	Typical Values of Hydraulic Conductivity and Permeability	110
Table 8.	Simulation parameters used to generate the hypothetical data	118
Table 9.	Hypothetical "observation" data	119
Table 10.	Input Values for the parameter estimation model simulating the hypothetical data	121
Table 11.	Parameter estimation results for the hypothetical data	129
Table 12.	Determined saturated hydrocarbon vapor concentration	132
Table 13.	Parameter estimation results for Test II and Test III	133
Table 14.	Simulation parameters for Test III	136
Table 15.	Simulation parameters for Test II	141
Table 16.	Simulation parameters for Test IV	146

ACKNOWLEDGMENT

I wish to express my sincere appreciation to my advisor, Professor Michael K. Stenstrom, for his support and guidance during this research. I also wish to thank the other members of my dissertation committee, professors Menachem Elimelech, Thomas C. Harmon, and Walter Reed for their encouragement and advice during this study.

A special gratitude is due to Dr. Wen S. Young, president of Universal Sensors and Devices, Inc., for his support and encouragement. I would also like to thank my other fellow employees at Universal Sensors and Devices, Inc., especially Dr. Michael T. Lin, for their assistance and corporation during the experimental study. I also like to acknowledge Mr. Tanwir Chaudrey and Mr. Nicholas J. Olah for their valuable suggestions and comments on this research.

The experimental part of this study was co-sponsored by Universal Sensors and Devices, Inc., and The U.S. Naval Civil Engineering Laboratory.

Finally, I am grateful to my parents, my family and my closest friends for the support and encouragement they have consistantly provided throughout the years of my education.

ABSTRACT OF THE DISSERTATION

Numerical and Experimental Analysis of Diesel and JP-5 Transport in Unsaturated Soils

by

Jun Zhou

Doctor of Philosophy in Civil Engineering

University of California, Los Angeles, 1994

Professor Michael K. Stenstrom, Chair

Long-term and large-scale experiments were conducted to evaluate the migration of diesel and JP-5 fuels in sand and soil media. The experiments were conducted in a 3.66×4.27×3.05 meter (12×14×10 feet) test chamber with 56 monitoring wells installed to continuously monitor the hydrocarbon vapor concentration in three dimensions. Slower transport of diesel than JP-5 in a sand medium was observed in both horizontal and vertical directions. Fuel transport in soil was more limited than in sand. Accordingly, the concentrations measured in the contaminated soil were much higher than that in sand. In contrast to the concentration contour maps showing strong heterogeneity of fuel migration in sand, the diesel-wetted soil pictures demonstrated a much more homogeneous movement. Also discussed are the Time of Arrival and concentration versus contour radius for the experiments with diesel and JP-5 in sands.

An axial-symmetric three dimensional numerical model simulating both the

liquid infiltration and the vapor diffusion in unsaturated soil was developed. The resulting partial differential governing equations were solved by the finite difference alternating direction implicit (ADI) method. The Picard iteration method was used to solve the nonlinear difference equations.

A new technique was developed to better describe the moving boundary at the liquid entry zone. The boundary condition near the liquid entry zone was treated as a discrete conical moving boundary, which was determined by a mass balance over the liquid entry zone that included the accumulation term. The liquid infiltration model was verified by applying it to the experimental data of Clothier and Scotter (1982) to simulate water infiltration in sand.

The complex method of Box was used to identify the model parameters. The parameter estimation technique was tested with a set of hypothetical data generated by the transport model with a given set of parameters. The five independent model parameters were successfully estimated within substantially wide limits.

Both the diesel vapor concentration profile and the liquid wetting front in the soil medium predicted by the model using the parameters estimated from the diesel vapor concentration data showed satisfactory match to the experimental observations (Test III). The numerical simulation of the transport of diesel fuel in sand (Test II) was also conducted and the results generally agreed with the experimental results. Numerical simulation of JP-5 transport experiment in sand (Test IV) was not successful. Possible reasons include the influences of chromatographic separation on the vapor diffusion, and the evaporation loss of the light components on the liquid migration.

I. INTRODUCTION

During the past decade, leaking underground storage tanks (USTs) have received tremendous attention from environmentalists. According to the US EPA's recent survey (U.S. E.P.A., 1986), there are 2.5 to 5 million underground storage tanks in the United States, and about 80% are used for storage of petroleum products and organic solvents. Even very conservative estimates have put the number of leaking tanks at up to 25% of the total. Leaking underground storage tanks (including underground pipelines), combined with hazardous waste landfill sites, and accidental spills during product transportation and filling, pose a great contamination threat to groundwater, which supplies about 50% of the nation's drinking water. Groundwater contamination is so prohibitively expensive to remediate that the prevention of pollutants from reaching the water table is of great importance.

In most places, USTs are installed far above the water table. After a leak or a spill occurs, contaminants must travel through the unsaturated zone (also called the vadose zone) of soil before reaching the groundwater. Often such movement may take a sufficiently long time for people to become aware of and take proper actions to prevent groundwater contamination. Vadose zone hydrocarbon vapor monitoring is one leak detection method recommended and accepted by almost all the environmental jurisdictions. Research to determine the migration mechanism of contaminants in unsaturated soils is essential to the proper mapping of the environment near monitoring wells around potential leak sources. Other immediate beneficiaries of this research are soil vapor extraction technology, contamination site assessment, and in-situ soil bioremediation techniques. Unfortunately few such studies have been conducted, and the phenomena related to the migration of volatile hydrocarbon contaminant in

unsaturated soils remains poorly understood.

The underlying physical processes that occur during the migration of volatile organic chemicals from a leaking UST are extremely complicated. Downward liquid flow in porous media is influenced by both capillary and gravitational forces. In a heterogeneous soil, hydrodynamic instability developed at soil textural interfaces can cause "fingering" to further complicate the problem of the liquid flow. As the liquid infiltrates into soil, its volatile components tend to escape from the liquid body and travel ahead of the liquid front via molecular diffusion. The diffusion process is retarded by the adsorption and desorption occurring at the soil surface. Chemical adsorption can also occur if the organic carbon content of the soil is high. In a shallow soil, or in a soil adjacent to underground structures, the thermal and pressure gradients may induce advective flow in the gas phase. Other processes such as biodegradation and chromatographic separation add more complexity to the problem. While the identification of the most dominating process(es) is difficult and varies from case to case, a general understanding is that the capillary and gravitational flow of liquid and the molecular diffusion of vapor in gas phase are the most important processes during the migration.

Existing researchers have developed many mathematical models of chemical transport in the groundwater itself, with a growing number of studies investigating the simultaneous flow of nonaqueous phase liquid (NAPL) and water in soil. Organic liquid and vapor transport after infiltrated into unsaturated soil from a point source have been unfairly neglected. There are few experimental studies and most were conducted either in one dimension or at rather small scale, which often results in observing only the early capillary suction-dominated transport mechanism.

Demonstration of gravitational flow requires large scale and long term observation. This study focuses on the experimental and numerical investigation of the liquid and vapor transport of petroleum fuels in unsaturated soil from a *point source*.

The experiments were conducted in a relatively large test chamber to study the fuel percolation in soils which overcame the shortcomings characteristic from many small scale laboratory tests. Hydrocarbon vapor monitoring devices were used in the experiments to record the three dimensional transient hydrocarbon concentration distribution in the test chamber. Diesel fuel and jet fuel (JP-5) were selected as the infiltration liquids to demonstrate the transport dependence on liquid properties. The characteristics of fuel transport in different soils were compared by using sand and natural soil as the porous media. The fuel discharge rates were selected slightly higher than the leaking criteria for a UST set by the US EPA.

Mathematical models simulating water infiltration in soil from a point source have been developed by many hydrologists in studying trickle irrigation. Analytical as well as numerical techniques have been proposed in solving the governing Richards' equation. Difficulties in solving the governing equation arise not only from its nonlinear nature but also from the moving boundary near the infiltration source. Conventional treatment of the saturated liquid entry zone as a growing disk (Brandt et al., 1971) may overestimate the infiltration rate by neglecting the storage in the liquid entry zone. The current study developed a finite difference model with a moving conical boundary around the infiltration source in cylindrical coordinates to simulate the fuel infiltration in soils.

A separate moving boundary finite difference model describing the vapor diffusion was also developed to simulate the fuel vapor transport ahead the liquid

front.

The solution to the problem of unsaturated liquid hydrocarbon flow coupled with vapor diffusion requires the parameters correlating the hydraulic and diffusive properties of the system to be known *a priori*; however, accurate description of all the related parameters for a specific case of interest often does not exist. Models often depend upon measurements in the literature on materials having similar composition. Since the variations of the parameters, such as the hydraulic conductivity, are generally enormous even for similar types of soils, such direct adoption of literature measurements may induce an error much larger than the model approximation.

Parameter estimation using an optimization technique was carried out in this study based on our own experimental observations. The complex method of Box (1964) was used to estimate the soil hydraulic conductivity, hydraulic pressure and saturation relationship, and fuel properties from the observation of transient hydrocarbon vapor concentration distribution. The data collected in the transport experiments of diesel in natural soil and of JP-5 in sand were used to the parameter estimation. The transport model was tested by the comparison of both the simulated diesel liquid front and vapor distribution to the experimental observations.

II. LITERATURE REVIEW

Despite a growing number of researchers investigating groundwater contamination by organic solvents and petroleum products, transport of volatile organic chemicals in unsaturated porous medium from a point source remains poorly understood. A literature search found very few investigations, both theoretically and experimentally. Related studies, such as water infiltration, vapor transport, multiphase flow, etc., have been performed with greater efforts, and are reviewed in this chapter.

Downward liquid migration through unsaturated soil is often called infiltration. Water infiltration has been studied by soil physicists for many years. Comprehensive reviews of the principles governing the water infiltration process can be found in the papers by Childs (1967) and by Philip (1969).

Research on water infiltration from a point source can be traced back to the early 1960s when trickle irrigation became popular. Both theoretical and experimental efforts have concentrated on the study of water content distribution and the solute migration following infiltration. Analytical solutions of the infiltration model assume either a linear relation between the moisture diffusivity and the saturation (Philip, 1968, 1969), or a negligible gravitational flow, such as the effective hemisphere absorption model by Clothier and Scotter (1982) and by Ben-Asher et al. (1986).

Warrick (1974) extended the linearization technique of steady infiltration to time dependent processes, and thus simplified the numerical simulation of unsteady infiltration. Healey and Warrick (1988) solved a dimensionless Richard's equation and obtained a set of empirical equations for estimating dimensionless location of the wetting front and water volume. Coefficients for the equations were obtained for a

variety of soil types and discharge rates. Despite the limitations caused by the arbitrary assumptions and approximations, such techniques minimized the physical parameter requirements and simplified the calculation procedures with fairly accurate results.

The first finite difference model for studying multi-dimensional transient infiltration from a trickle source was developed by Brandt et al. (1971). Kirchhoff transformations were applied to linearize the water-saturation-based nonlinear Richards' equation. The infiltration boundary at the soil surface was treated as a growing disk with zero storage. The approach was followed by several researchers (van der Ploeg and Benecke, 1974; Levin et al., 1979; Ababou, 1981; Mostaghimi and Mitchell, 1983; Fletcher Armstrong and Wilson, 1983; Ragab et al., 1984; Lafolie et al., 1989). Inaccurate treatment of the boundary condition at the soil surface was recognized as one of the major problems associated with the approach (Lafolie et al., 1989).

Many experimental studies of trickle infiltration of water have also been conducted. To verify their theoretical model, Brandt et al. (1971) and Bresler et al. (1971) conducted laboratory as well as field experiments. In their laboratory experiments, an air-dried loam soil from Gilat, Israel was used. The field experiment was done in a coarse sandy soil. Various discharge rates were employed in the experiments. The results agreed with the theoretical predictions of the effect of infiltration rate on the shape of the wetted front. Slower water discharge rates resulted in deeper and narrower penetration profiles. Such an effect was ascribed to the influence of the discharge rate on the size of water entry saturated zone. Increasing water discharge rate produced a swollen water entry zone.

Hachum et al.(1976) conducted a two dimensional experiment in a 48x48x2

inch chamber to study water movement and distribution in homogeneous soil media from a trickle source. Two different soils, loamy sand and silt loam, were used together with various water application rates. The experiment showed that the gravity force played a more important role in sand soil than in loam soil. In sand soil, horizontal advancement of the wetting front was much slower than the vertical penetration, while in loamy soil, water tended to propagate at the same rate in both directions due to the domination of capillary force. The effect of discharge rate on the movement of the wetting front was found to be similar to the effect found by Bresler et al. (1971).

In contrast to the findings by Bresler et al. (1971) and by Hachum et al. (1976) Bar-Yosef and Sheikholami (1976) concluded from their experiment, conducted in a sandy soil, that increasing the trickle discharge rate increased the vertical movement of the wetting front, but decreased horizontal movement. Studies of the effect of evaporation showed a decrease in water content throughout the entire wetted soil volume, with a maximal decrease occurring in the top 3-cm soil layer and in the margins of the wetted soil volume.

The wetting front profile obtained by Clothier and Scotter (1982) from experiments conducted in a fine sandy loam showed that the gravitational force was insignificant in the early infiltration. The hemispheric profile changed with a relatively faster vertical movement after the capillary force decayed.

Simultaneous multiphase flow of particularly oil, water, and air has been studied by petroleum engineers for more than half of a century. The extension of Darcy's law to multiphase flow with the concept of relative permeability was performed as early as the 1930s (Muskat and Meres, 1936; Muskat et al. 1937).

Reviews of early studies of multiphase flow in porous media can be found in a number of text books and technical papers (Dullien, 1979; Peaceman, 1977; Bear, 1972; deWiest, 1969; Wooding and Morel Seytoux, 1976; Philip, 1970; Philip, 1973).

It was not until the 1970s that the basic concepts used by petroleum engineers to simulate the behavior of oil reservoirs were adopted by environmental engineers to study the migration of organic contaminants in soil and in ground water. Qualitative descriptions of the migration of hydrocarbons through the unsaturated zone, their spreading, and penetration into groundwater have been provided by several researchers (Schwille, 1981, 1967; API, 1972; Schwille, 1984; Mackey et al., 1985). Numerous research papers have been published on the numerical simulation of the movement of spilled or leaking petroleum products in both unsaturated and saturated zones (Hochmuth and Sunada, 1985; Faust, 1985; Abriola and Pinder, 1985a, 1985b; Corapcioglu and Baehr, 1987; Baehr and Corapcioglu, 1987; Baehr, 1987; Kaluarachchi and Parker, 1989; Kuppusamy et al., 1987; Parker et al., 1987; Sleep and Sykes, 1989; Kaluarachchi and Parker, 1990, Kim and Stenstrom, 1994a,b). Transport models have focused on the distribution of dissolved chemicals in groundwater and the multiphase flow models have emphasized the simultaneous flow of NAPLs and water.

Compared with water infiltration, fewer experiments have been done to study the migration of organic contaminants in the subsurface soil system. Early experiments studying oil movement in porous media can be found in the works by Laughlin and Davies (1961) and by Nielson et al. (1962). Schwille and his group in Koplentz, West Germany have conducted extensive experimental investigations since 1975 on organic chemical transport in porous media, which are widely recognized as the pioneering work in developing qualitative and quantitative descriptions of the

contamination of the subsurface aquatic system by organic chemicals (Schwille, 1988).

Frankenberger and Troech (1982) observed that the saturated conductivities of water, methanol and n-propane in two soils initially decreased and steady states were reached after 1500 hours of continuous leaching. Schramm et al. (1986) measured the saturated conductivities for xylene, kerosene, isopropyl alcohol, ethylene glycol, and water in eight soils. They found that xylene had the highest conductivity and ethylene glycol ranked the lowest.

By measuring the advancing rate of the wetting front, Amoiozagar et al. (1986) evaluated the movement of organic liquids in dry soils. One dimensional experiments were conducted with six organic liquids penetrating through vertical and horizontal columns packed with five soils. Power functions were used to match the experimental relations between the distance and the arrival time of the wetting front. It was suggested that the advancing rate of the pure organic liquid into dry soils might be predicted by the advancing rate of water and the saturated conductivity values.

Barbee and Brown (1986) carried out a field experiment measuring the movement of xylene through unsaturated soils. A significant amount of xylene was detected by a pen sampler at 61 cm depth approximately 1 day, 1 hour and 0.5 hour after a volume equivalent to 5 cm-depth of xylene was spilled to loamy sand, silt sand and clay, respectively. The fast movement of xylene was also found when a lesser amount of xylene was applied in other simulated spills. A relatively uniform moving front of xylene was seen in the loamy sand but in silt loam and clay, xylene movement was strongly enhanced by the flow through interped micropores.

Abdul (1988) simulated the migration of organic liquids through the unsaturated zone down to the water table by running diesel fuel into a 44.7 inch long sand column

with a pre-established water table. It was concluded that significant lateral spreading of oil in the capillary fringe might exist after an oil spill or leak because higher oil pressure was needed to displace the pure water in the capillary fringe and under the water table. Such difficulty of displacement of pure water in the capillary fringe may prevent oil from reaching the water table, especially when the leak occurs in a sand system.

Acher et al. (1989) reported the laboratory study of movement of a synthetic kerosene and its vapor in soil columns. A vapor front was clearly observed to move faster than the liquid front when kerosene penetrated into dry soils. The vapor movement ceased when the moisture content of the soil increased above 4%. The upward liquid movement was also inhibited when the water content reached 12%. A redistribution experiment showed that the vapor movement after the liquid front stopped advancing depended strongly on the volatility. The penetration results for oven-dried and air-dried sands showed an enhanced penetration rate by moisture, which was explained by the absorption/desorption processes.

In his experiments, Young (1986) also reported the inhibited movement of gasoline when the soil moisture was higher than 10%. When soil moisture was low (between 5 and 10%), however, all the organic chemicals moved faster than in a completely dry soil. During his uplift column experiments, he also found that the upward advance of liquid acetone was faster than gasoline, but the gasoline vapor arrived at the end of the 2 feet long column earlier than the acetone vapor.

Summarizing the overall state of the subject, more thorough research needs to be done both theoretically and experimentally for the following reasons:

1. Laboratory experiments conducted to study water infiltration by previous

researchers have concluded that the capillary absorption is important and mostly dominant in the early stage of liquid infiltration.

2. Previous experimental studies on VOC transport in unsaturated soil have reported a vapor front traveling in advance of the liquid front soon after the liquid was introduced into the soil.
3. The previous experiments, however, provided few quantitative observations on both VOC liquid and vapor distributions in soil, and most of them were conducted in either one dimensional soil columns, or at rather small scale.
3. Both analytical and numerical models have been developed by previous researchers for water infiltration from a point source, even though the models' assumptions, as well as other technical aspects, such as the linearization techniques of the moisture diffusivity function and the moving boundary treatment, are still being actively investigated.
4. There is no available mathematical model capable of simulating the simultaneous VOC liquid and vapor transport when infiltrating into unsaturated soils from a point source.
5. Mathematical models available for simulating the multiphase flow of NAPL and water may not be suitable for liquid infiltration because of either their extraordinary complexity or their inability to handle the capillary force dominated flow problem.
6. The numerical infiltration models need to be improved to better handle the moving boundary at the interface of the saturated and unsaturated zone near the infiltration source.

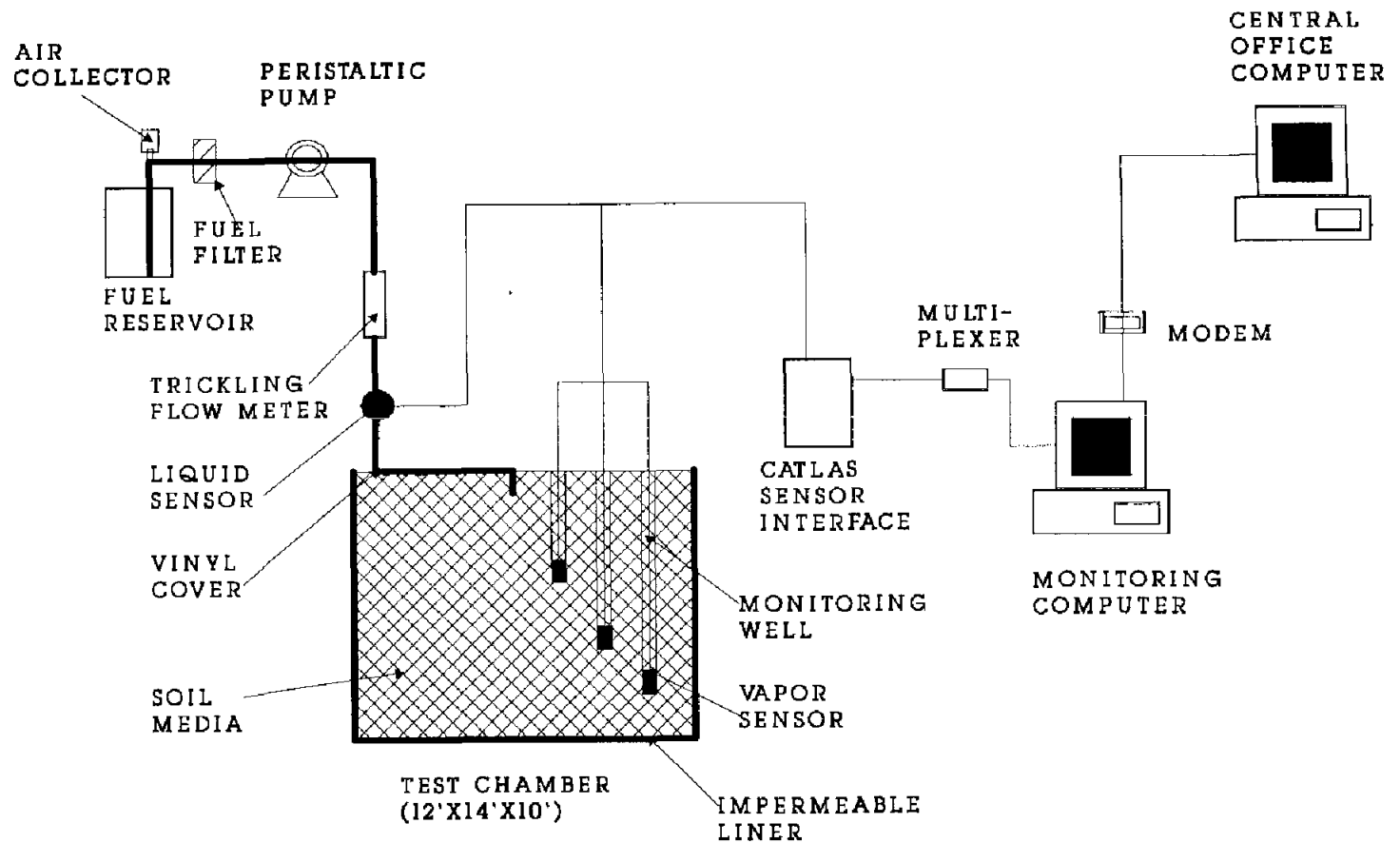
III. EXPERIMENTAL

III.1 System and Apparatus

All the experiments of this study were performed at the research laboratory site of Universal Sensors and Devices, Inc. (USD, Chatsworth, California). The test site is located in a remote high desert area 20 miles south of Tehachapi township, California. The elevation of the test area is about 4500 feet. This area normally receives very little rainfall, and no rain fell during the course of all three tests; however there was a light snowfall (less than 1.0 inch) during Test II. The experimental set-up includes a test chamber, a fuel delivery system and a hydrocarbon monitoring system as shown in Figure 1.

III.1a Test Chamber

The open top concrete test chamber was built along a hillside at the laboratory site. About 50% of the outside north, south and east walls were buried by backfills. The inner dimensions of the chamber was 14×12×10 (W×H×D) feet. A 3 foot wide open space was constructed on the west side wall to unload the soils. A wooden door was used to block the opening before loading the soils. Metallic liners were used to cover the inside walls and floor to prevent possible fuel leaks through the concrete walls. During the tests the chamber top was covered with a double layer vinyl plastic sheet to prevent evapotranspiration or rain water intrusion. A computer room was built next to the west of the chamber (Figure 2).



EXPERIMENTAL APPARATUS

Figure 1. Schematic of the Experimental Set-up

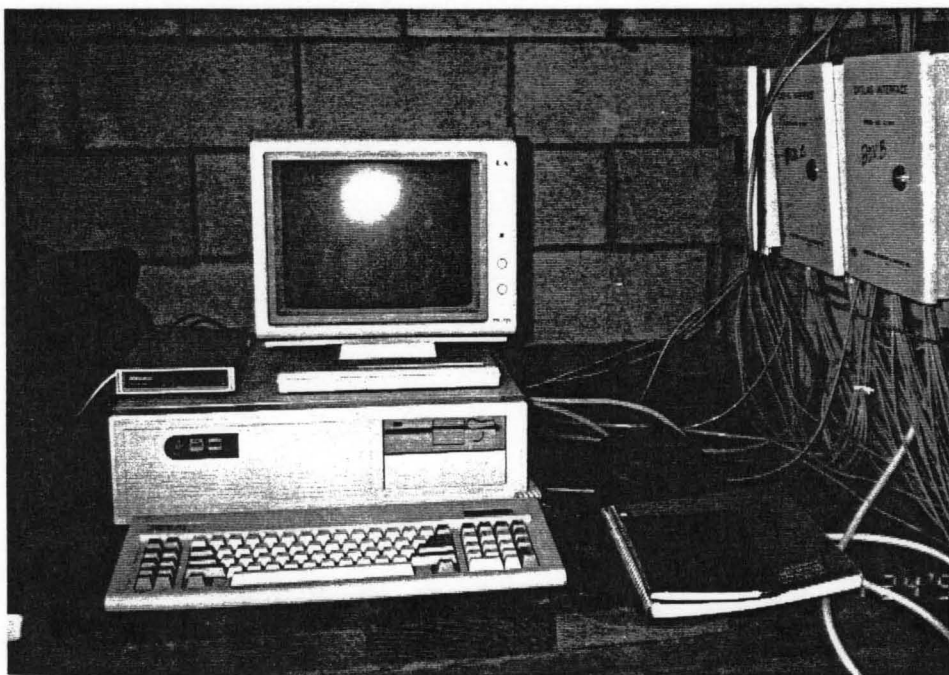
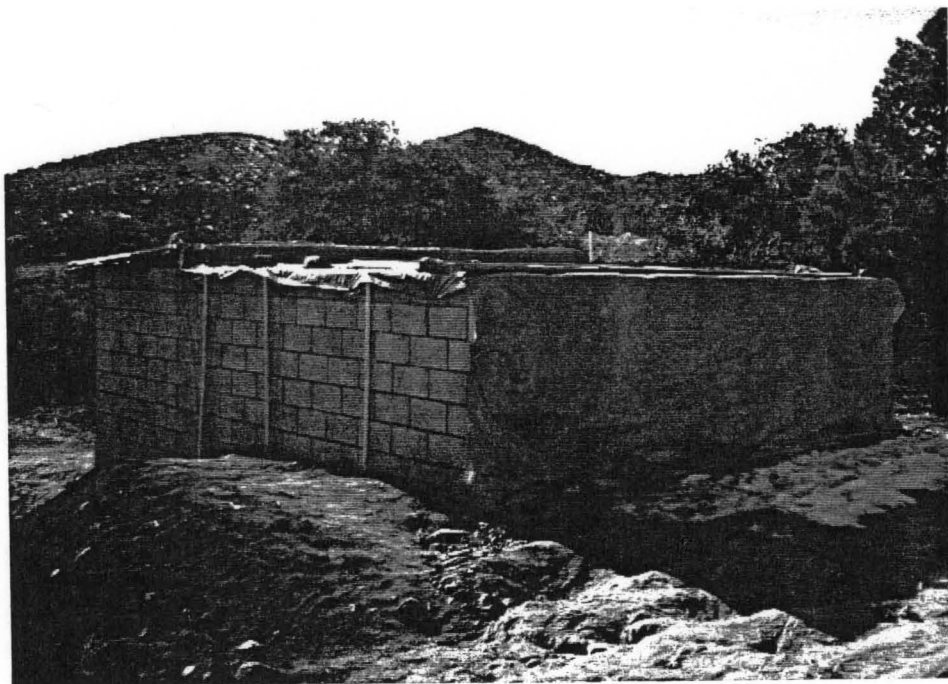


Figure 2. Pictures of the test chamber and data acquisition system

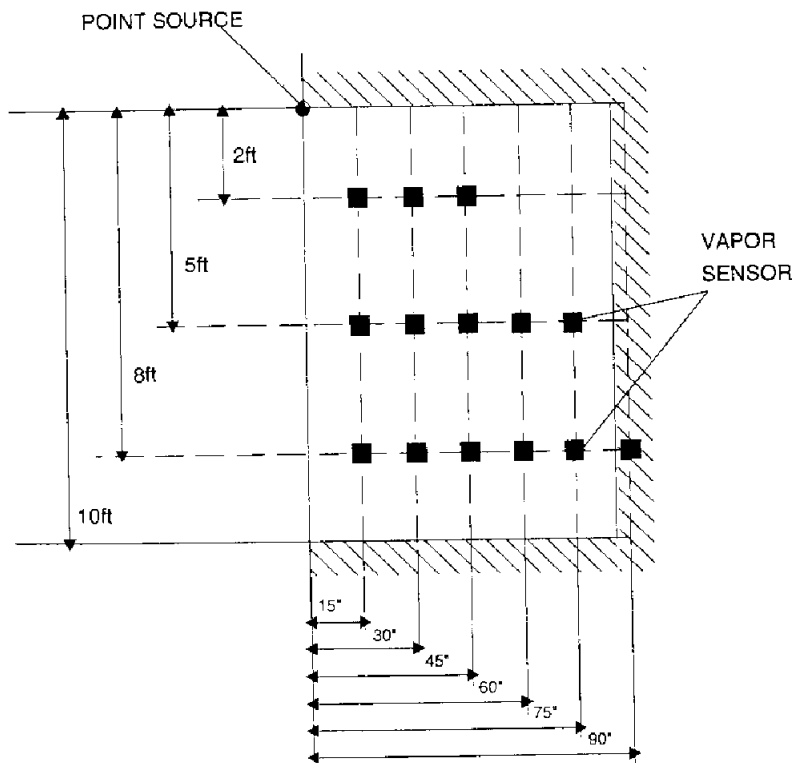
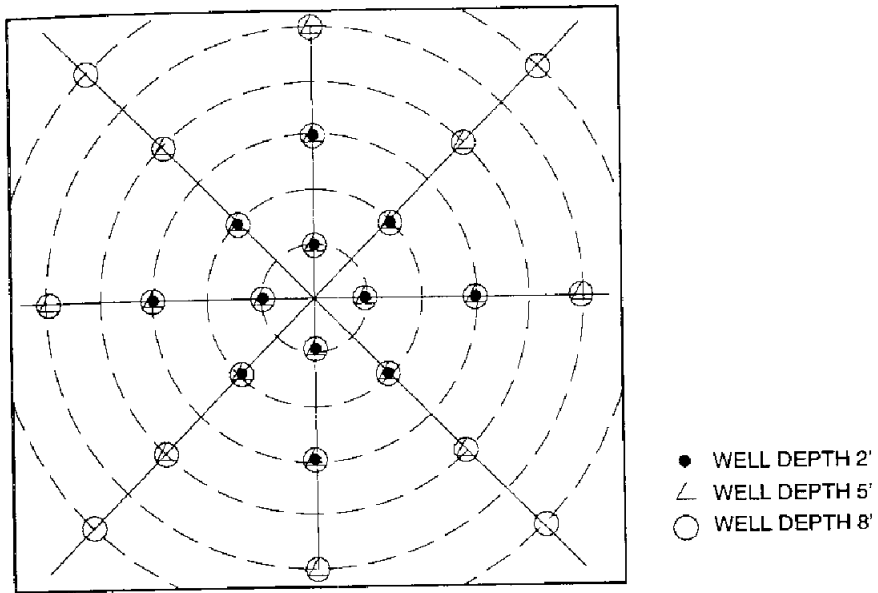


Figure 3. Map of the hydrocarbon monitoring wells

III.1d *Hydrocarbon vapor monitoring system*

A metal oxide semiconductor (MOS) sensor, first introduced by a Japanese engineer, N. Taguchi, in 1968, has a special property when exposed to reducing or combustible gases. Its electric conductivity increases due to the electron transfer in the adsorption process. MOS sensors with this property have found a wide variety of applications in gas leak detection. Vapor monitoring using the MOS sensor has also been long recognized by almost all regulation agencies as one of several most favorable leak detection methods for underground fuel storage tanks (Scheinfeld, et al., 1986; Nelson and Dablow, 1986). A MOS sensor, sensitive to many hydrocarbon vapor molecules, is capable of detecting vapor phase concentrations as low as tens of ppm (parts per million). The sensor's ability to quickly and fully recover from exposure to high concentration made it an ideal device for our experiment.

Fifty-six LAVS-1 hydrocarbon vapor sensors manufactured by USD along with four CATLAS interface units (USD) were used in the experiments. The sensors were installed at the bottom end of each monitoring well in contact with the soils.

Data acquisition and transmission were accomplished by an IBM-compatible personal computer. A 16-bit 4 channel analog/digital conversion card controlled four multiplexers to acquire signals from the vapor sensors. The converted digital signals were then stored as data files on the hard disk. Those files were uploaded daily through a modem to the central computer at the USD main office. During the experiments continuous fuel delivery was remotely monitored by a liquid sensor on the fueling line.

III.2 Materials

Two types of media, sand and top soil, were used in the experiments and purchased from commercial aggregate plants. The sand classified as "washed plaster sand" was obtained from Tehachapi Lumber Center and the topsoil obtained from Jim Honeycutt Trucking, Tehachapi, California. The sand had a dry bulk density of 1.85 g/cm³. The average moisture content of the sand used in the experiments was 3.9%. The top soil is a silt loam soil, and had a moisture content of 4.1% and a dry bulk density of 1.74 g/cm³. Soil particle size analysis was conducted according the ASTM D422-63 standard procedure and the results are listed in Table 1.

Table 1. Sand/Soil Particle Distribution Analysis Results

Sieve Size (Microns)	Sand			Top Soil	
	Sample I % Total	Sample II % Total	Average % Total	Grain Size (Microns)	Average % Total
1000	42.20	45.93	44.07	2000.0	0.0
850	46.38	50.62	48.50	850.0	20.3
600	60.08	64.13	62.11	425.0	38.3
355	78.14	80.75	79.45	250.0	50.4
250	88.01	89.36	88.69	150.0	59.7
212	91.81	92.58	92.20	75.0	68.7
180	94.76	95.33	95.05	33.9	77.2
150	96.70	96.82	96.76	21.7	79.9
125	98.42	98.41	98.42	12.6	81.0
106	99.83	99.32	99.58	8.9	82.1
90	100.36	99.76	100.06	6.4	84.8
75	100.67	100.07	100.37	4.5	86.3
63	100.87	100.21	100.54	3.2	87.8
<63	101.18	100.43	100.81	1.3	88.6

The total porosity of the media estimated from the density and specific gravity measurements was 40.1% for the sand and 47.6% for the top soil. The ASTM D2937 and D854 standard methods were used to measure the soil density and specific gravity. The saturated hydraulic conductivity of the sand and the top soil was measured to be 8.3×10^{-6} and 1.7×10^{-6} m/sec., respectively, following the ASTM D5084 standard test method.

Both diesel and JP-5 fuels used in the tests were acquired from a naval base in Southern California. The densities of the diesel and JP-5 used were 0.88 and 0.82 g/m³, respectively. Viscosity measurements for the fuels were conducted at three temperatures using Cannon 50-Z83 and 200-Z51 viscometers and the results are listed in Table 2.

Table 2. Properties of Diesel and JP-5 (Guthrie, 1967)

Property	Diesel (DFM)	JP-5
Density (g/cm ³)	0.88	0.82
Viscosity (cp)		
10°C	5.27	2.39
15°C	5.01	2.23
20°C	4.69	2.00
Distillation test (Guthrie, 1967):		
IBP, °F	397	338
10%, °F	448	369
20%, °F		382
50%, °F	509	410
90%, °F	582	464
EP, °F	622	500

III.3 Experimental Procedures

The sand/soil was first delivered to the test site by trucks and then loaded into the test compartment with the help of a small front end loader. During the backfill,

the soil or sand was periodically compacted using a shop-made compacting plate after five inches of sand/soil load was added.

The monitoring wells were installed after loading. Prior to insertion of each PVC pipe, a steel pipe of similar diameter, with a conical-shaped plug installed at the end, was hammered into the backfill at the specified locations to desired depths. The steel pipe was then pulled out and the PVC pipe inserted into the vacant hole. To prevent the short-pass for liquid fuel migration along the outside wall of the pipe, additional compaction around the pipe was performed after it was installed.

Each vapor sensor was lowered down to the bottom of the monitoring well. The outside diameter of the sensor was slightly smaller than the inner diameter of the PVC pipe. The loss of fuel vapor due to diffusion through the gap was insignificant. Nevertheless, paper tissue and duct tape were used to seal the well cap.

After sensor installation, the chamber was covered with a double layer vinyl plastic sheet (0.1mm) and the power to the monitoring system was activated. The system was left alone for 24 hours to stabilize. After a stable baseline was obtained, the test fuel was discharged at the center of the chamber surface.

Once activated, the computer scanned and recorded all sensor signals. Data points recorded for each sensor were in millivolt readings of the analog signals sent from the CATLAS interface units. Each data point represented an average over approximately 10 minutes. Data were stored in files designated by the date. The signal from the liquid sensor installed in the fuel discharging line was also recorded.

Data files stored during the tests were accessed through the modem from the central computer at USD's main office. File transfer was performed daily to monitor the operation and evaluate the test progress.

III.4 Sensor Calibration

As mentioned earlier, vapor sensor signals were recorded as millivolts during the experiments. Quantitative analysis would have been difficult for such signals without calibration because of the different sensitivities of the sensors to the fuel vapor and the nonlinearity between the sensor signal and the corresponding vapor concentration. Both diesel and JP-5 fuels are hydrocarbon mixtures and direct calibration is very difficult. Simpler, indirect calibration was performed using mixtures of normal butane ($\text{CH}_3\text{CH}_2\text{CH}_2\text{CH}_3$), isopentane ($((\text{CH}_3)_2\text{CHCH}_2\text{CH}_3)$) and air as calibration gases (a surrogate for actual test fuels). Three premixed calibration gases (Matheson Gas) had concentrations of 250 parts per million (ppm) n-butane + 250 ppm i-pentane, 500 ppm n-butane + 500 ppm i-pentane and 1500 ppm n-butane + 1500 ppm i-pentane, respectively.

During calibration all sensors were exposed to the calibration gas for at least 40 minutes until their signals became stable. Signals were then recorded for the calibration gas in use as one calibration point for the sensors. The three calibration points thus obtained plus the baseline point recorded when the sensor was in fresh air constructed the calibration curve.

Three on-site calibrations were conducted for each test. The first calibration was conducted at the beginning of the test before the sensors were inserted into the wells. During the second calibration which was conducted about 15 days after each test started, all the sensors were quickly removed from the monitoring wells, and after the sensor calibration, the sensors were quickly reinstalled into the wells. Except during the short time for the sensor removal and reinsertion, the well top ends remained sealed and the chamber surface covered. The last calibration for each test

was conducted after the test was terminated and before the soil was excavated. During the second calibration, the soil vapor monitoring program was interrupted but the computer, the CATLAS interface boxes, and the fuel discharge system remained on. A calibration program was run on the monitoring computer to record the calibration signals. Each calibration lasted for about 2 hours. The results obtained from all three calibrations were averaged to form the final calibration curves for the test. Figure 4 shows a typical sensor calibration curve.

It must be noted that the vapor concentration values reported in the following chapters are the relative concentration of the hydrocarbon vapor detected by the sensors expressed in ppm as the calibration gas instead of the actual vapor presented in the soil media. As mentioned earlier, both JP-5 and diesel fuels are complicated mixtures of hundreds organic chemicals. When organic mixtures migrate in unsaturated soils, their vapor composition alters because of the physical, chemical and biological processes, such as aging and chromatographic separation; therefore, the actual vapor concentration is impossible to continuously monitor without extremely expensive equipments. Measurement with the field-proven devices calibrated using surrogate chemical(s) is the only practical means to quantitatively describe the hydrocarbon vapor presence in a petroleum fuel contaminated soil.

The reader should also keep in mind that the sensitivity of the sensor differs for different chemicals. Figure D1 and Figure D2 show the sensitivity of the sensors used in the current study to various organic chemicals.

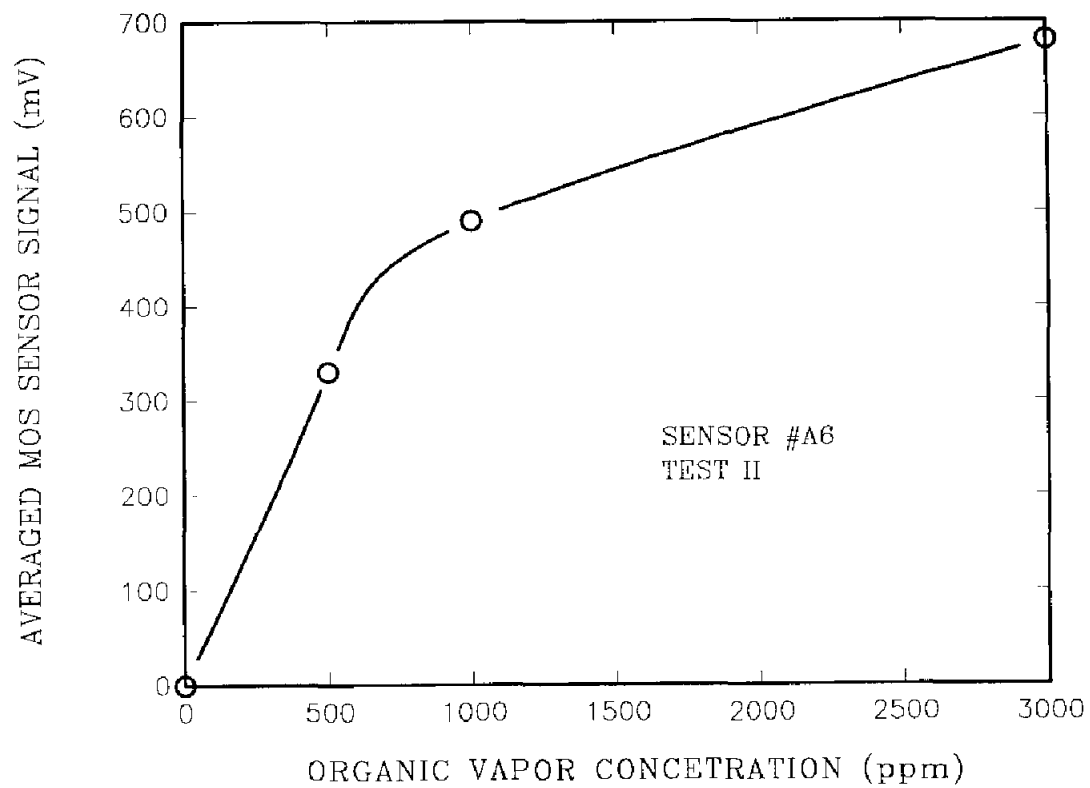


Figure 4. Typical calibration curve for the vapor sensors

IV. EXPERIMENTAL RESULTS

Four tests simulating diesel and JP-5 transport in sand and soil were conducted and the test parameters are shown in Table 3. The first test was a "shake down" test to perfect system operation, and the results are not reported.

Table 3. Summary of the Test Parameters

	Test II	Test III	Test IV
Media Material	Sand	Soil	Sand
Fuel	Diesel	Diesel	JP-5
Fuel Discharge Rate (gal/hr)	0.033	0.035	0.048
Total Fuel Discharged (gal)	23.7	25.3	29.5
Starting Time	4:00 pm 03-25-90	12:50pm 05-11-90	4:20pm 07-05-90
Test Lasting Time (hr)	718	723	621

IV.1 Averaged Temporal Concentration Curves

During the tests, vapor sensor signals were recorded and later converted into hydrocarbon vapor concentration expressed as volumetric parts per million (ppm) based on the averaged calibration results. It should be noted that the concentrations obtained were not expressed as ppm of the actual testing fuel, but as of the calibration gas mixture of n-butane and i-pentane.

In all three tests the vapor sensors were located so that only places at certain depths with designated radii were monitored. On each circle at one depth there were four sensors installed in four directions orthogonal to each other. If a perfectly

homogeneous packing of soils had been achieved, an axially symmetric fuel migration pattern would have been obtained and the concentration readings for all the four sensors would have been the same. The averaged concentrations of the four sensors at each depth on the circle of certain radius were plotted against the time and are shown in Figures 5 - 12.

In the following discussion, we designate the location for each sensor group by $RaLb$ where the a represents circle number and the b indicates the level number. Circle #0, 1, 2, 3,.... have radii of 0, 15, 30, 45 inches,..... and level #1, 2, and 3 are 2, 5 and 8 feet down from the top surface of the chamber, respectively. For example, location R2L1 is at circle #2 ($r=30$ in.) and level #1 (depth=2 ft.). Under the homogeneous assumption, the sensor's horizontal orientation is not included in the designation. This notation is also used later in describing the simulation results.

IV.1a *Test II (diesel in sand)*

When a volatile liquid is discharged into a porous medium, both vapor and liquid tends to penetrate through the void spaces of the media. For the vapor phase such penetration is normally dominated by ordinary molecular diffusion and Knudsen flow. The liquid migration, on the other hand, is driven by capillary and gravitational forces. At the beginning when the liquid phase first contacts porous media, the saturation gradient in front of the wetted area is so high that capillary force is the primary driving force to the liquid movement. Liquid tends to move fast in all directions and the wetting front is nearly spherical. As liquid migration proceeds, the capillary force declines because of the decrease in the saturation gradient. Further liquid movement is then controlled by gravitational force.

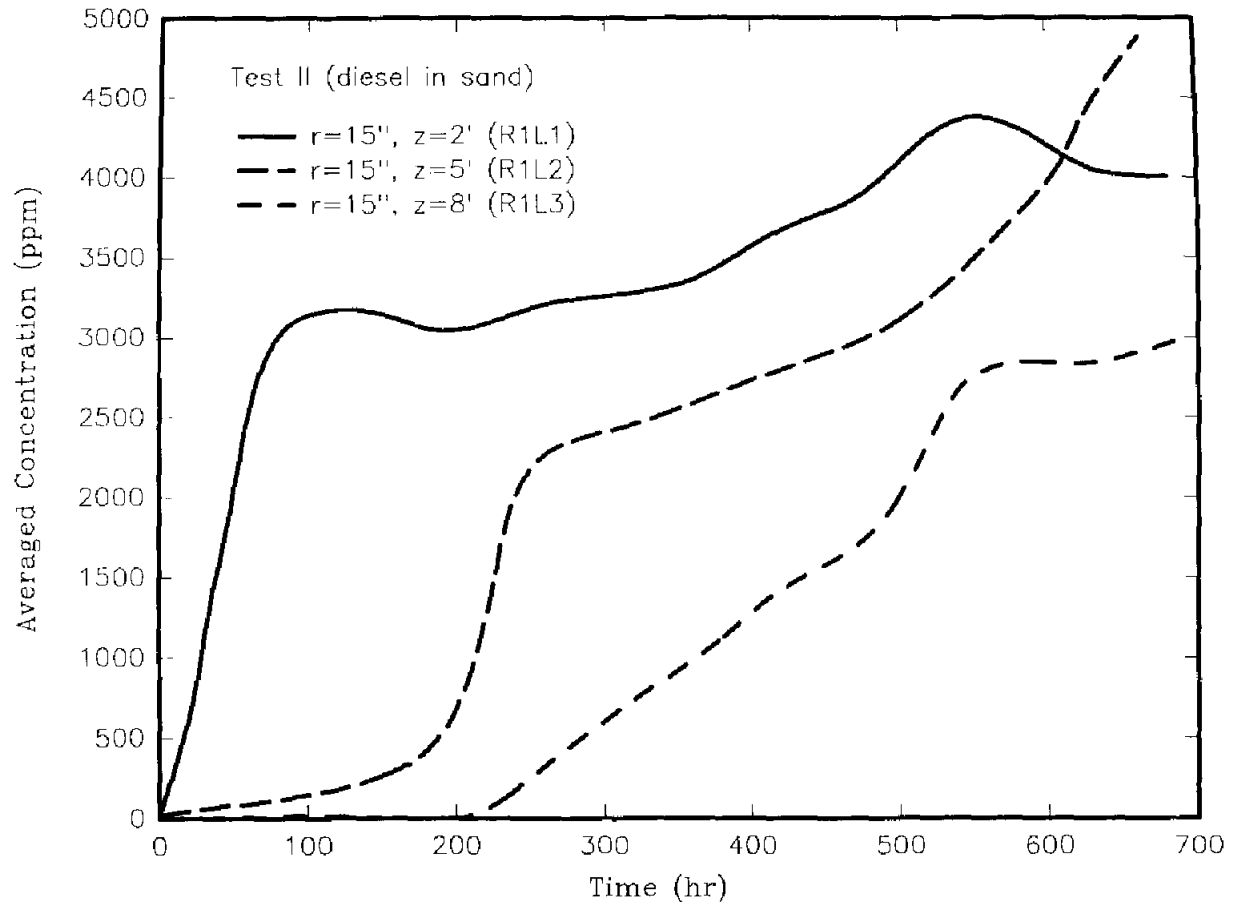


Figure 5. Temporal diesel vapor concentration for Test II (a)

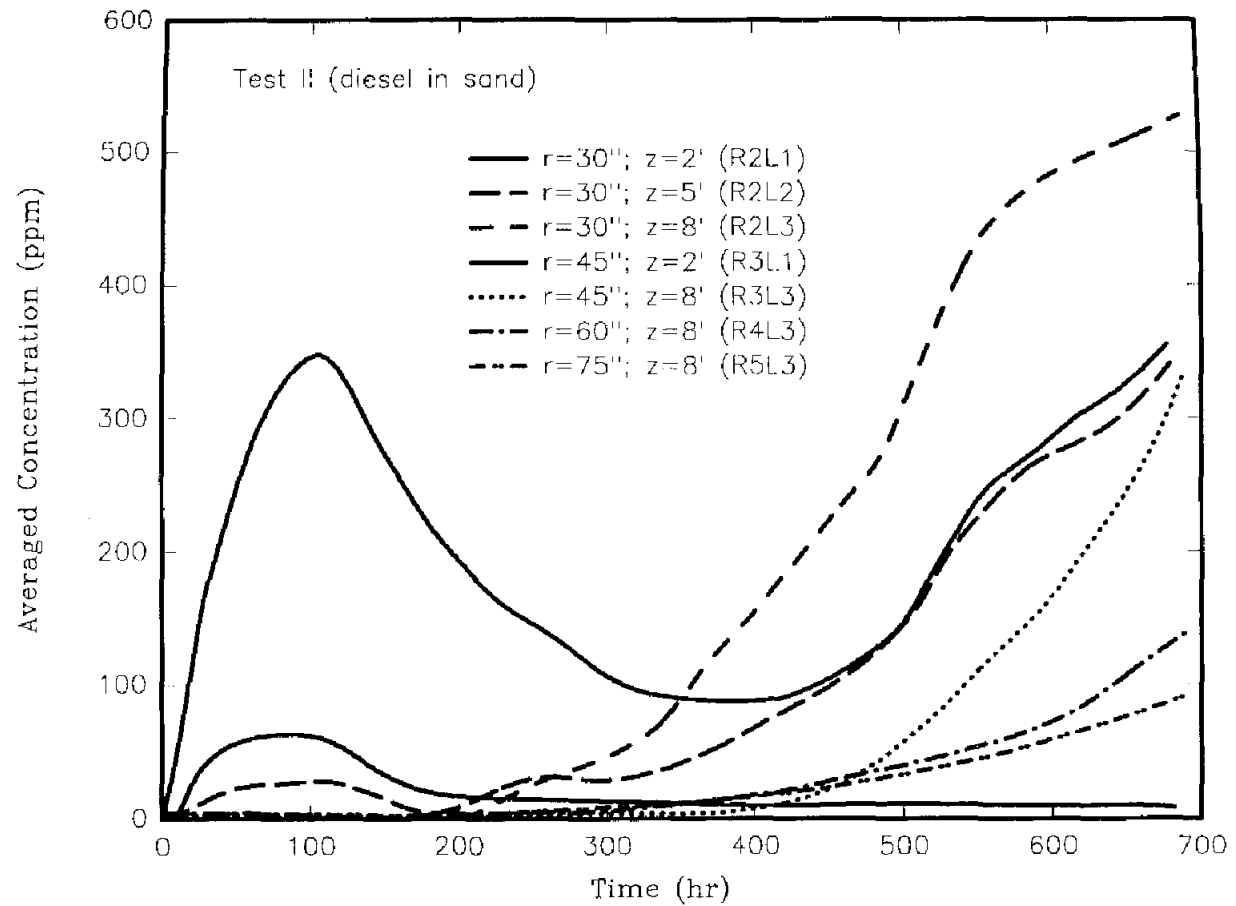


Figure 6. Temporal diesel vapor concentration for Test II (a)

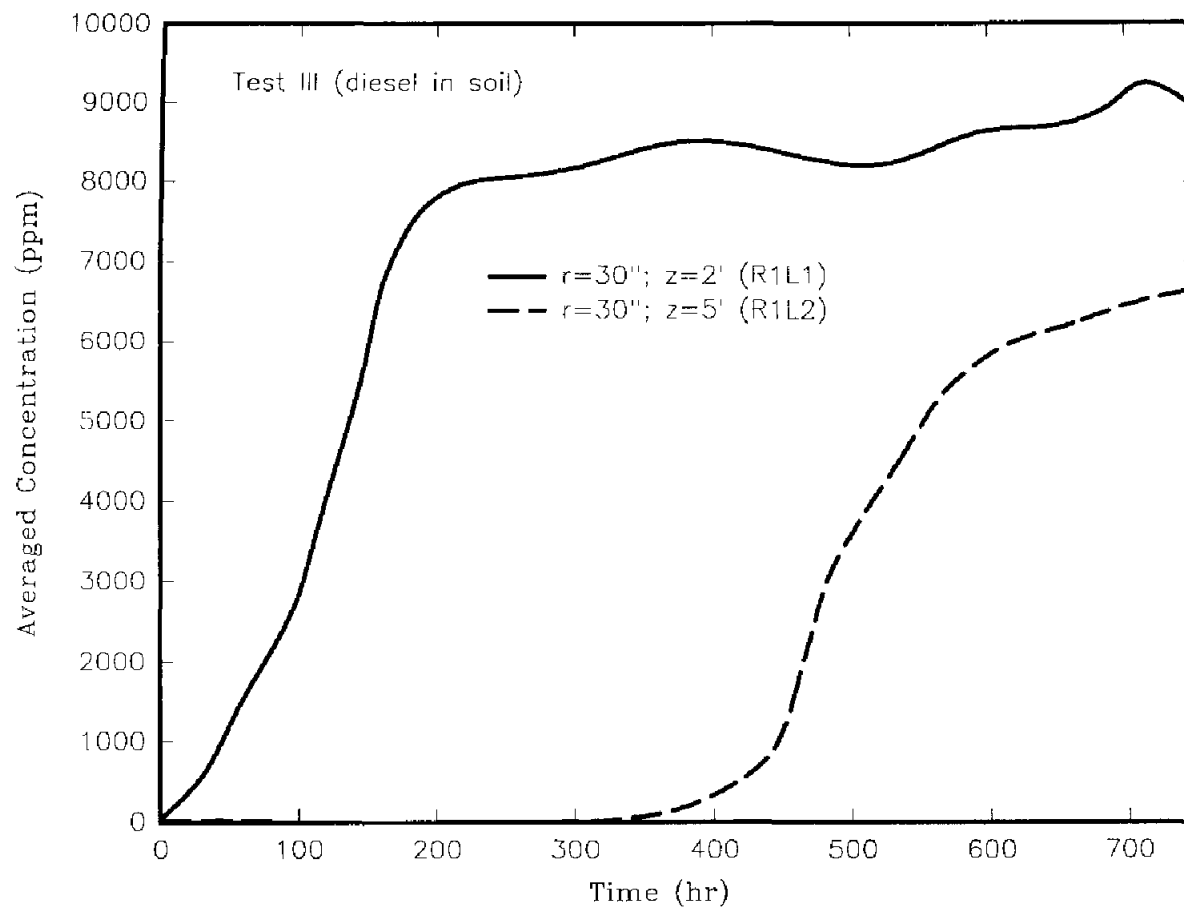


Figure 7. Temporal diesel vapor concentration for Test III

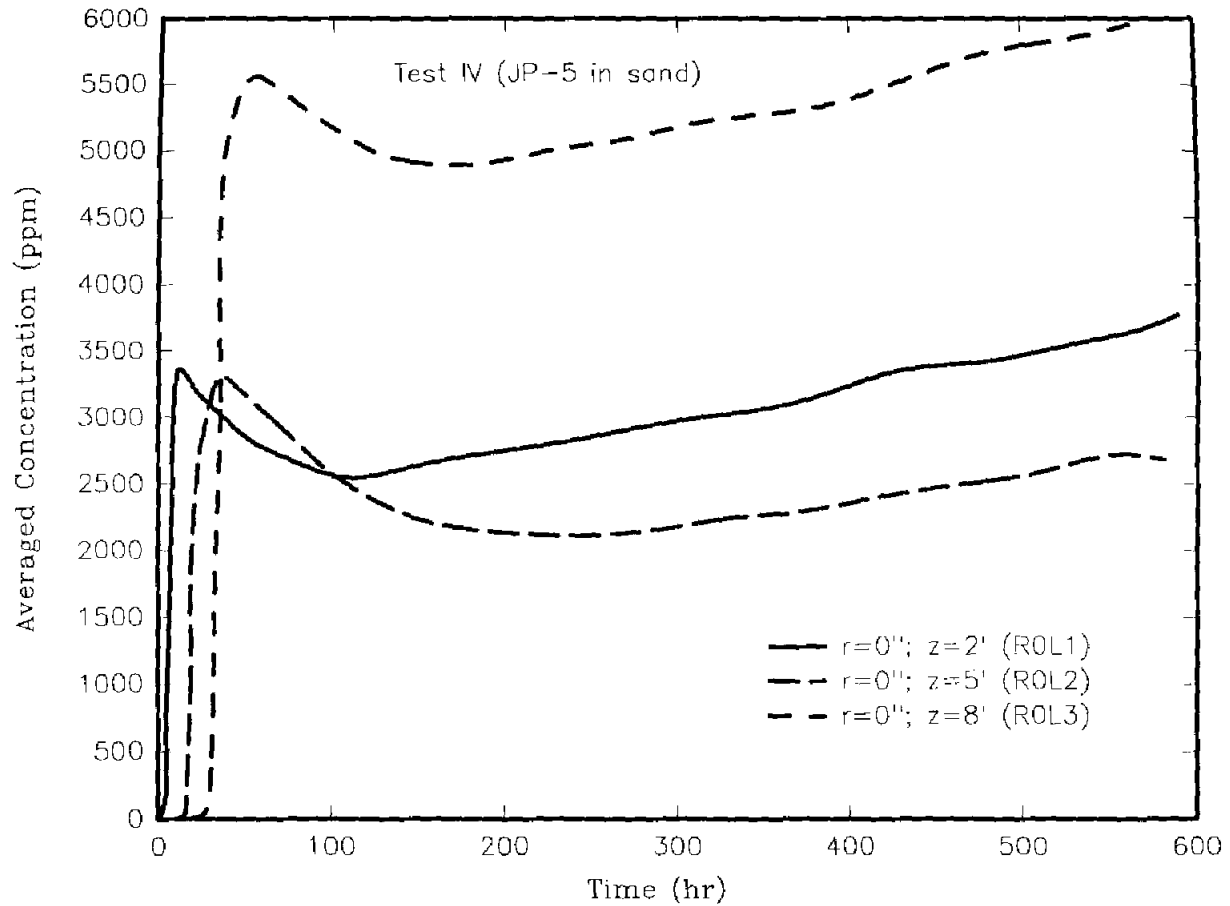


Figure 8. Temporal JP-5 vapor concentration for Test IV (a)

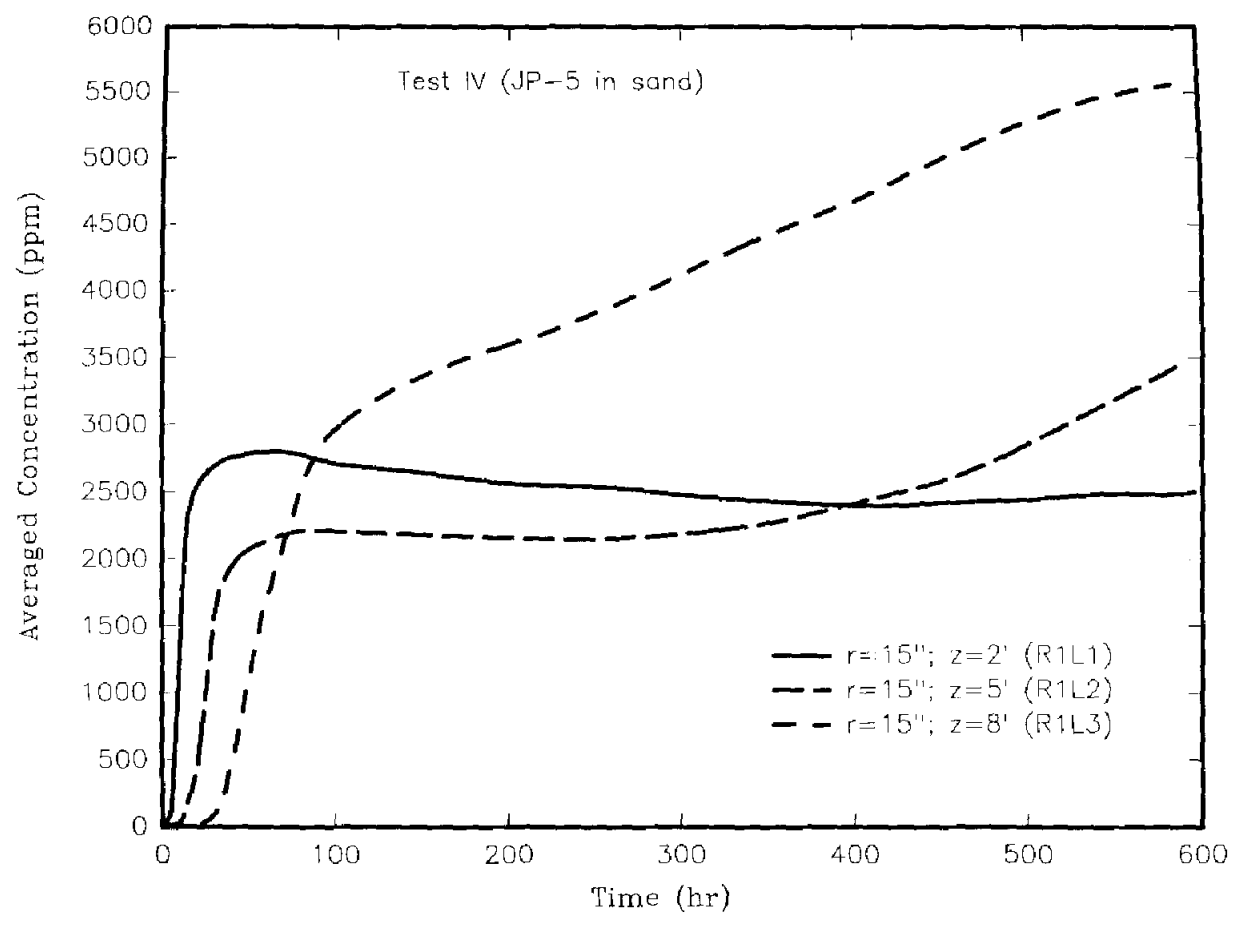


Figure 9. Temporal JP-5 vapor concentration for Test IV (b)

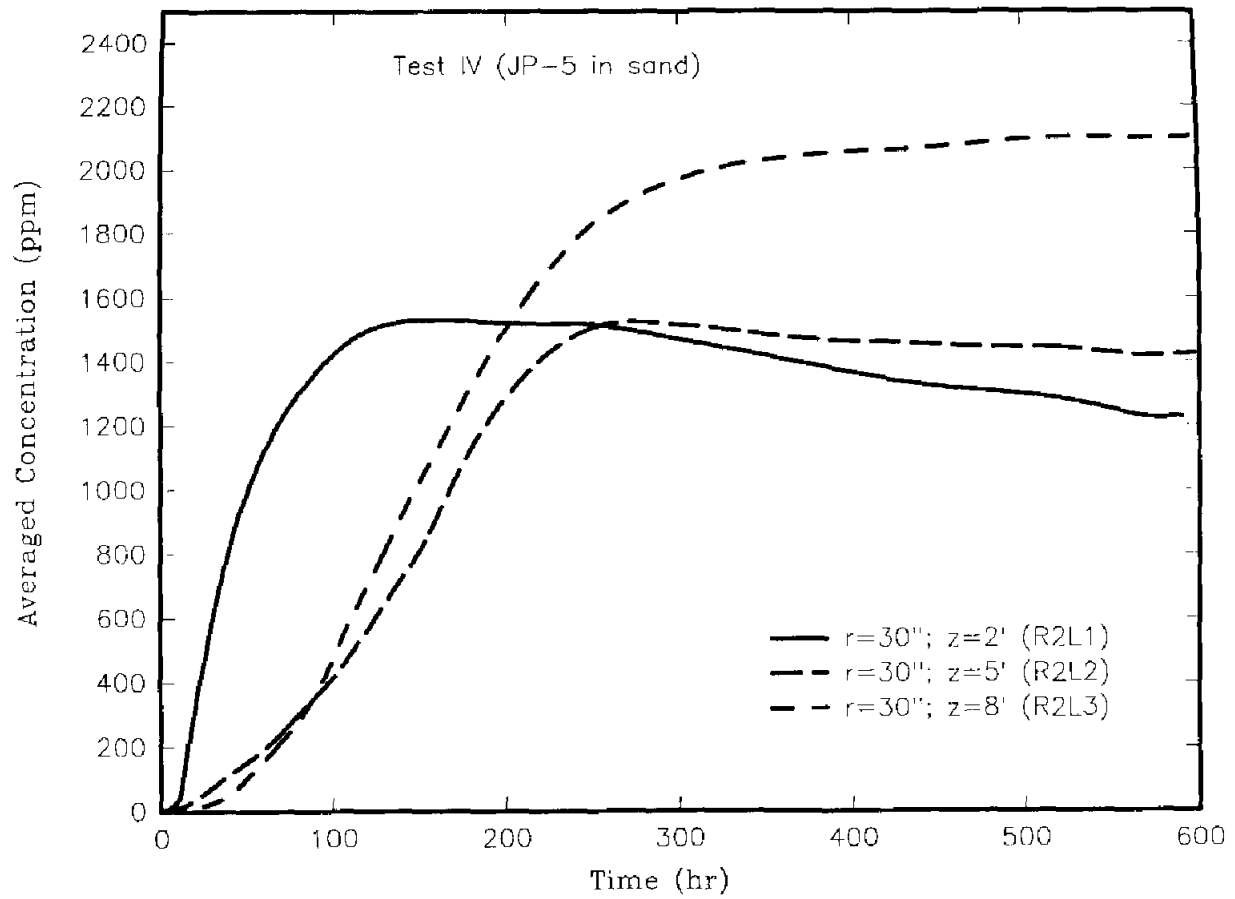


Figure 10. Temporal JP-5 vapor concentration for Test IV (c)

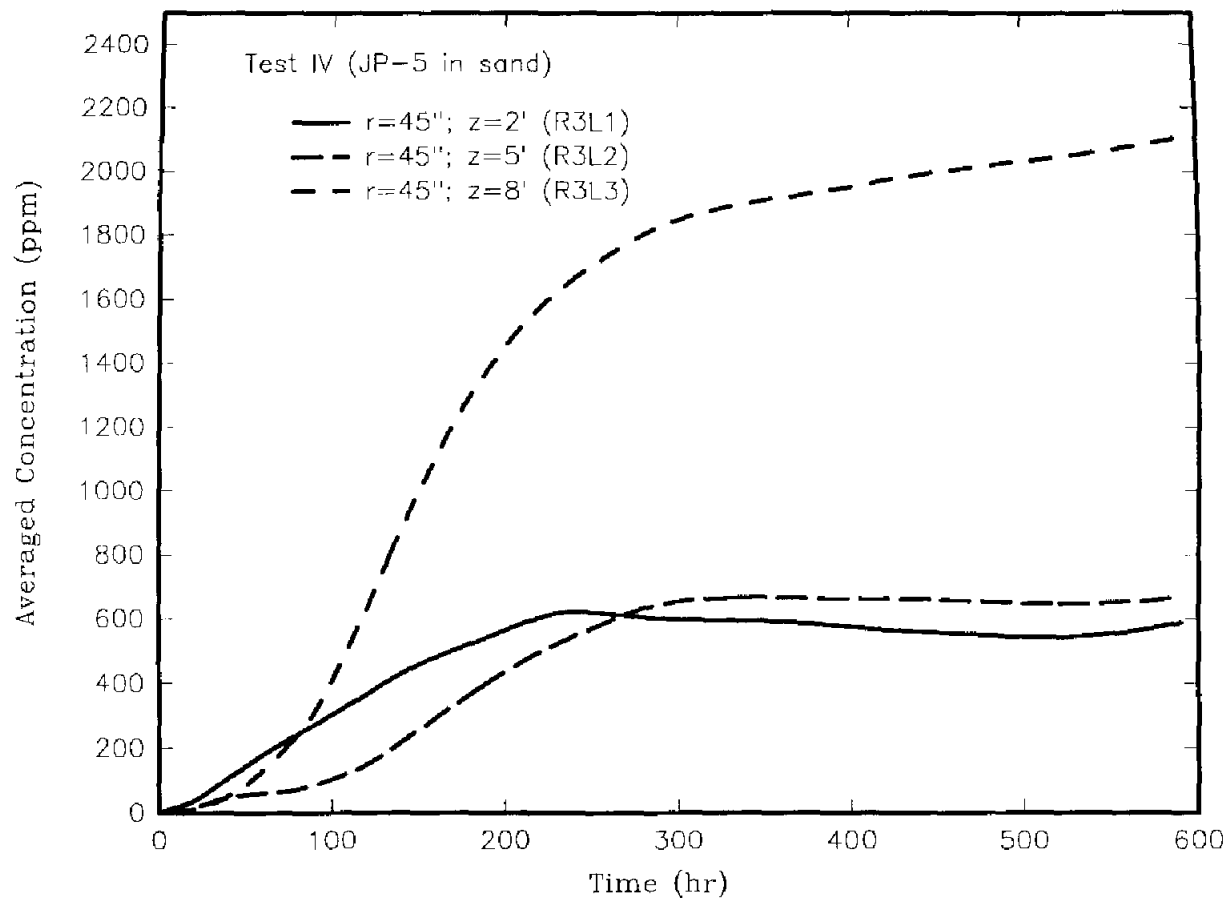


Figure 11. Temporal JP-5 vapor concentration for Test IV (d)

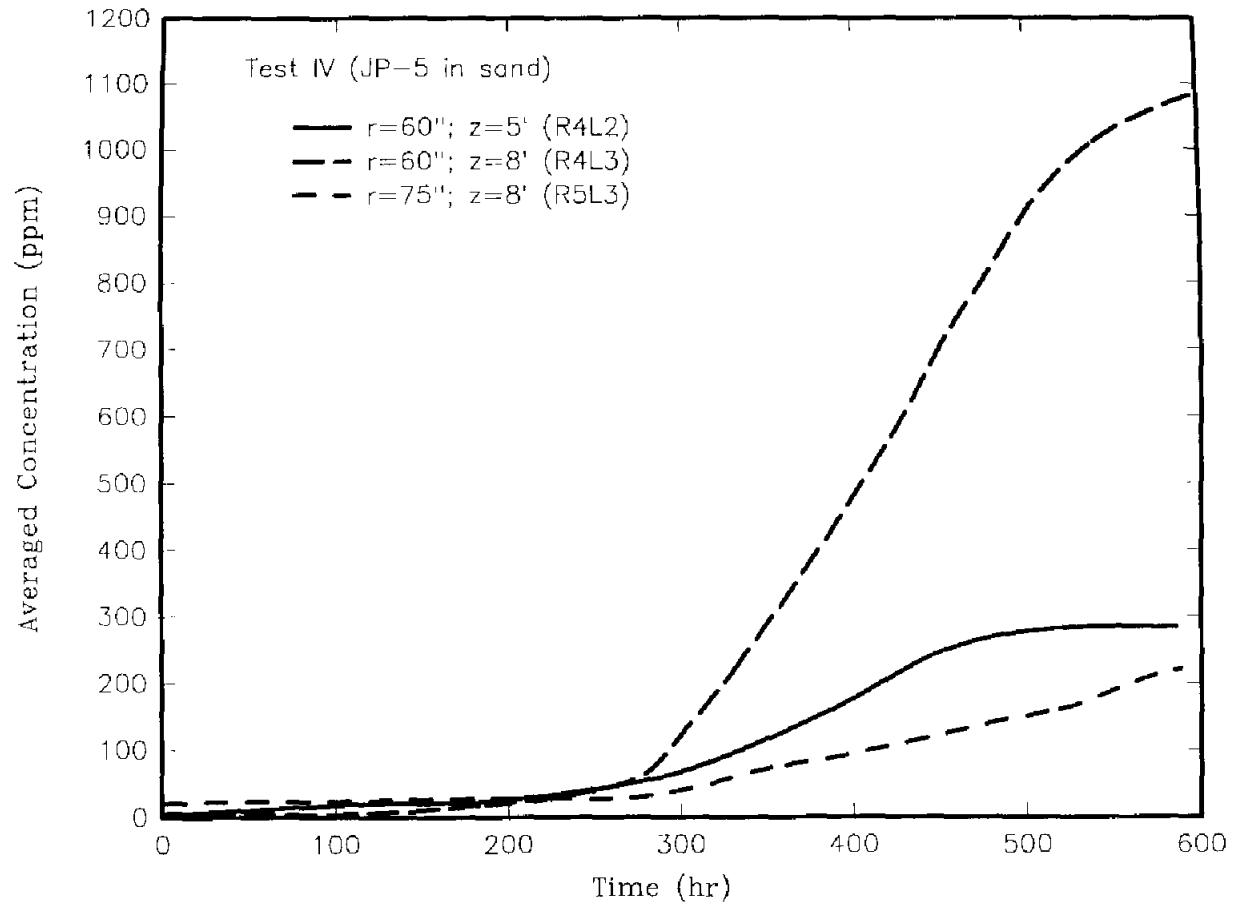


Figure 12. Temporal JP-5 vapor concentration for Test IV (e)

In Test II, the early appearance of diesel vapor on the sensors at location R1L1 indicated a fast initial fuel migration. Figure 5 shows the concentration vs. time for the first circle ($r=15$ in.) at all three monitored depths. It was expected that the sensors near the discharge source would detect the fuel earlier on circle #1. The shape of the concentration curves suggested that a dispersion type of diesel migration occurred during the test. At the beginning of the test the fuel was sucked by the high capillary force and experienced a fast movement with a sharp front when it passed location R1L1. The sharp front was relaxed when the fuel moved further. Low concentration fuel vapor dispersed to location R1L2 not long after it had been detected at location R1L1, and the concentration slowly increased until the major plume arrived many hours later. After the major plume arrived, a more stable concentration which we called pseudo-equilibrium concentration was established, and the concentration build-up rate started declining. The relaxed fuel front was seen more clearly from the curve at location R1L3. Pseudo-equilibrium concentration was also observed at that location.

Lateral spreading of diesel was insignificant compared with vertical penetration (Figure 6). None of the sensors located outside the first circle experienced a fully developed dispersion type of concentration profile. Concentrations at the end of the test were so low that the existence of liquid fuel at those locations was very unlikely. It was interesting that concentrations detected by the bottom level sensors were all higher than those found by the sensors installed at 2 ft. and 5 ft. levels on the same circle. This might have been caused by the impermeable bottom of the chamber. We were not able to explain the early concentration build-ups at locations R2L1, R2L2 and R3L1. Such build-ups reached their peaks at about 100 hrs and started dying out then.

IV.1b *Test III (diesel in soil)*

The migration of diesel in soil was much slower than in sand because of the lower permeability and higher adsorption. In experiment III, there were only eight sensors at locations near the discharge point (locations R1L1 and R1L2) that had detected diesel after 700 hours of testing (Figure 7). Concentration at location R1L1 began to build-up three and half hours after the test started and increased to a pseudo equilibrium concentration of about 8000 ppm after 200 hours. Compared with diesel movement in sand where concentration reached a pseudo-equilibrium value of 3000 ppm in only about 80 hours (Figure 5), an early conclusion of slower diesel movement in soil could be stated. Such a conclusion was immediately challenged by the fact that the time for diesel concentration to reach 3000 ppm at location R1L1 in soil was observed to be only about 100 hours (Figure 7). The initial diesel movements in soil and sand are, therefore, equivalent. Lower permeability of soil inhibited the diesel movement; however, smaller pore size and stronger surface tension between diesel and soil resulted in a stronger capillary force, which dominated the initial movement of diesel in porous media. The overall results might be similar initial migration rates of diesel in soil and sand.

After further migration, the gravitational force, independent of the media, became dominant and the effect of low permeability on the movement became clearer. The concentration at location R1L2 for Test III began to increase after about 300 hours, and reached pseudo-equilibrium concentration of about 6000 ppm by the end of the test; in Test II, however, the diesel appeared at the same location after only 10 hours and the pseudo-equilibrium concentration was reached by 250 hours.

In Test III, diesel never reached location R1L3. All the diesel added (about

25.3 gallons) was confined in a volume of less than 8 feet in depth and 30 inches in radius. The pseudo-equilibrium concentrations at both detectable locations for Test III were much higher than the ones at the same locations for Test II.

IV.1c *Test IV (JP-5 in sand)*

Test IV simulated the migration of JP-5 in sand. To directly monitor the downward movement of JP-5 in sand, three more sensors were added in the center of the chamber at the depths of 2, 5 and 8 feet, respectively. The locations of these sensors were designated as R0L1, R0L2 and R0L3. Compared to diesel fuel, JP-5, which has lower viscosity and higher volatility, moved more rapidly in both horizontal and vertical directions, as observed in the concentration vs. time plot (Figures 8-12). Again, fast initial migration due to the capillary suction was clearly seen when JP-5 traveled the first 2 feet to reach location R0L1 in just 2 hours, but took more than 12 hours to move to the next sensor location R0L2 which is only 3 feet below. The time needed for the fuel to migrate the following 3 feet from R0L2 to R0L3 was 18 hours. Figure 8 also shows that vapor concentrations at the central locations built up rather quickly. Unfortunately, there were no comparison data at the central locations for Test II and Test III. The concentration recorded by the bottom sensors ($z=8$ ft.) exhibited much higher pseudo-equilibrium values than those by top and middle sensors, which indicates that fuel accumulation occurred at the impermeable chamber bottom. The time needed for JP-5 to appear at location R1L1 was not much shorter than that for diesel fuel to reach the same location in Test II and Test III, implying an equally fast initial capillary-driven fuel movement; however, JP-5 vapor concentration reached a pseudo-equilibrium value much faster. Fuel accumulation on the chamber bottom,

although not physically observed, was indicated by the continuous concentration increase at locations R1L2 and R1L3 (Figure 9).

The significant level of JP-5 concentration found at locations other than R1L1, R1L2, and R1L3 indicated a much wider area of lateral spreading for JP-5 than for diesel. JP-5 was not only detected by the bottom sensors but also by those at the top and middle levels of circles 2 and 3 (Figures 10, 11). The JP-5 dispersed horizontally as far as 75 inches (Figure 12). It is believed that the impermeable bottom partially contributed to the wide spreading.

IV.2 Time of Arrival (TOA)

Time of Arrival (TOA) is defined as the time in hours required for the fuels to first appear on the sensors at certain locations. Figures 13-16 show the TOA as a function of the horizontal radius and the vertical depth for Tests II and IV. No data are plotted for Test III because the fuel was confined to a small volume during the test. Since the downward liquid movement in porous media is usually faster than the lateral spreading due to the gravity, the TOA value at a specific location is not directly related to the absolute distance from the leak source. It depends on both horizontal and vertical distances.

For a given depth, TOA is expected to increase with radius, which is interpreted as positive slopes for all curves in the plots of TOA vs. radius. Slower lateral diesel spreading in sand resulted in the greater slopes of the curves for $z=2$ ft. and $z=5$ ft. in Figure 13. As diesel migrated further, the horizontal cross sectional area of its front increased, which led to a flat portion in the early part of the curve for $z=8$ ft. The other flat portion of the same curve represented the contribution of the

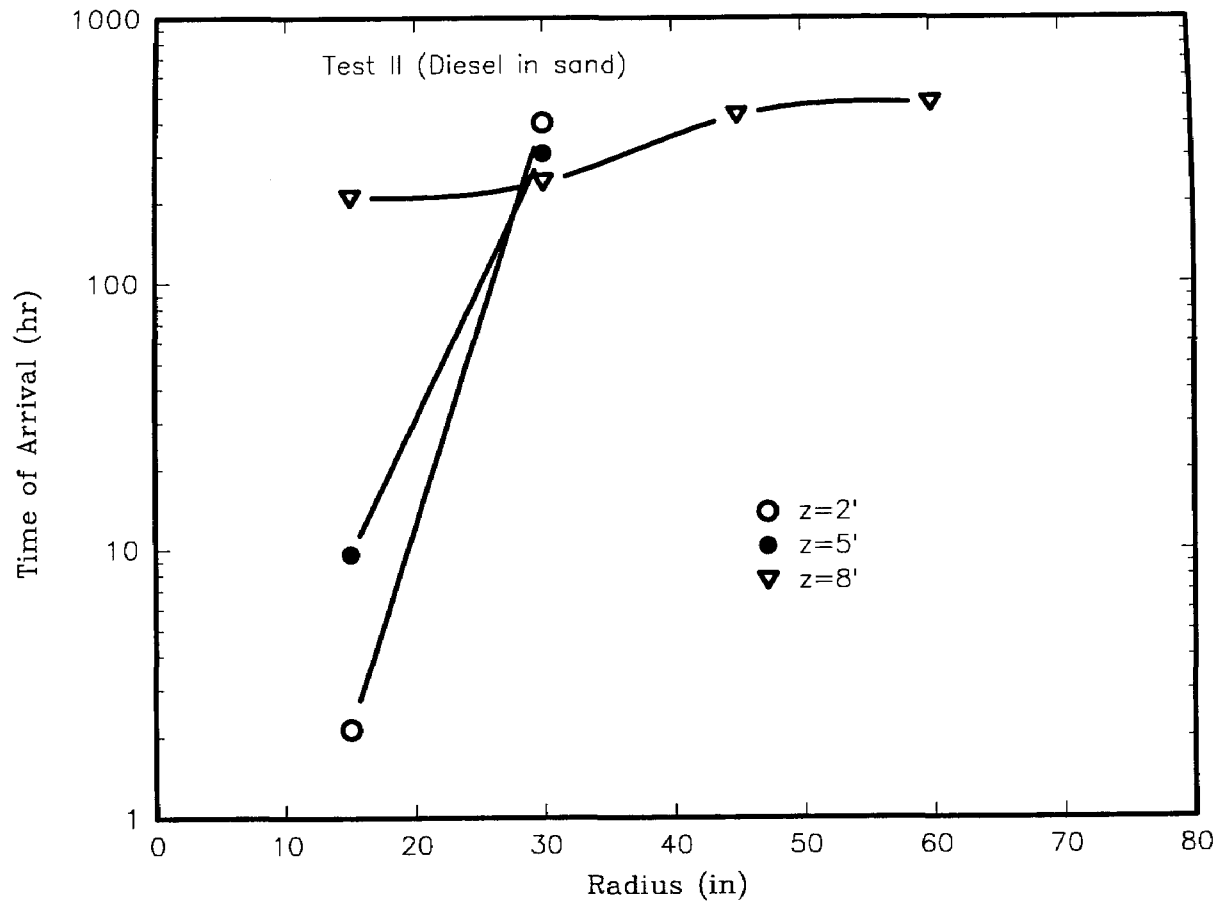


Figure 13. The TOA dependence on horizontal distance for Test II

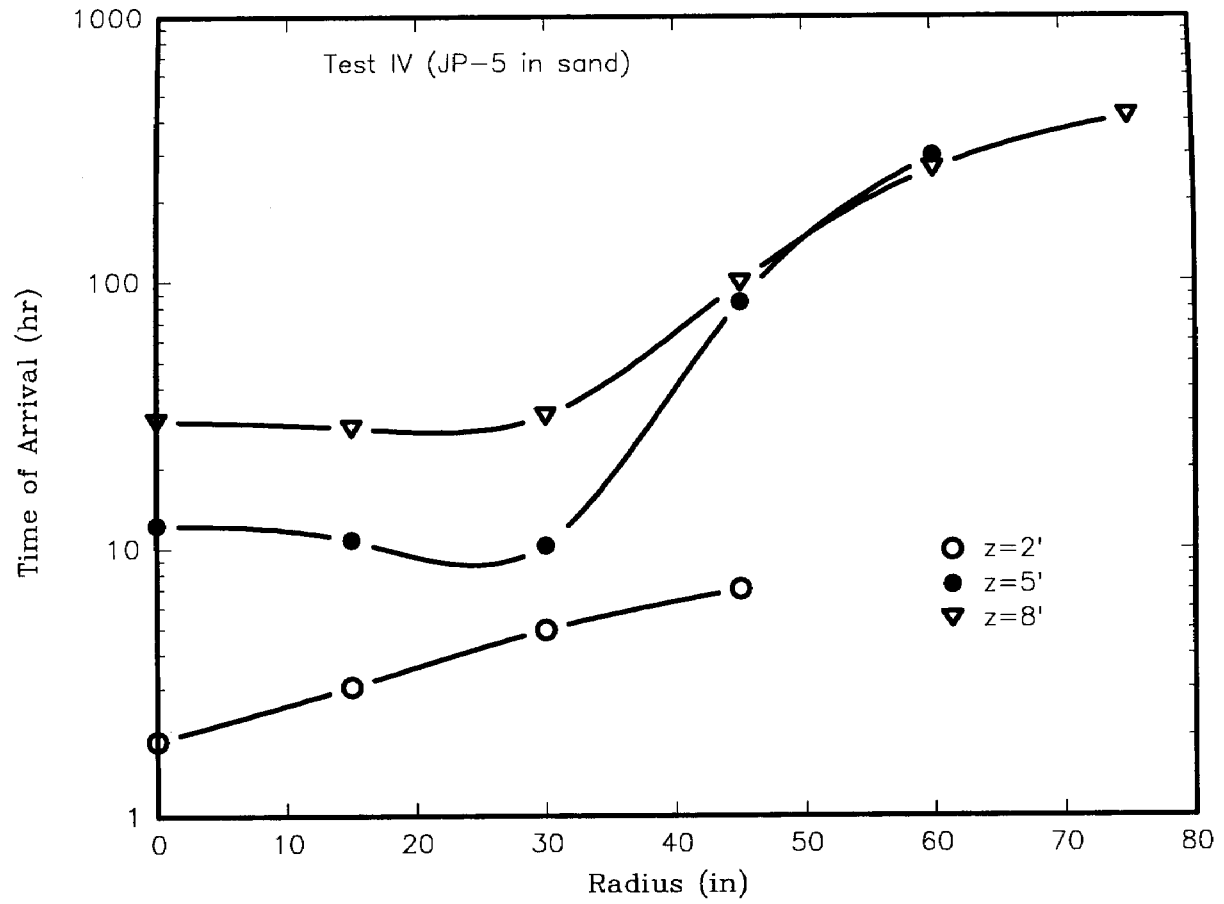


Figure 14. The TOA dependence on horizontal distance for Test IV

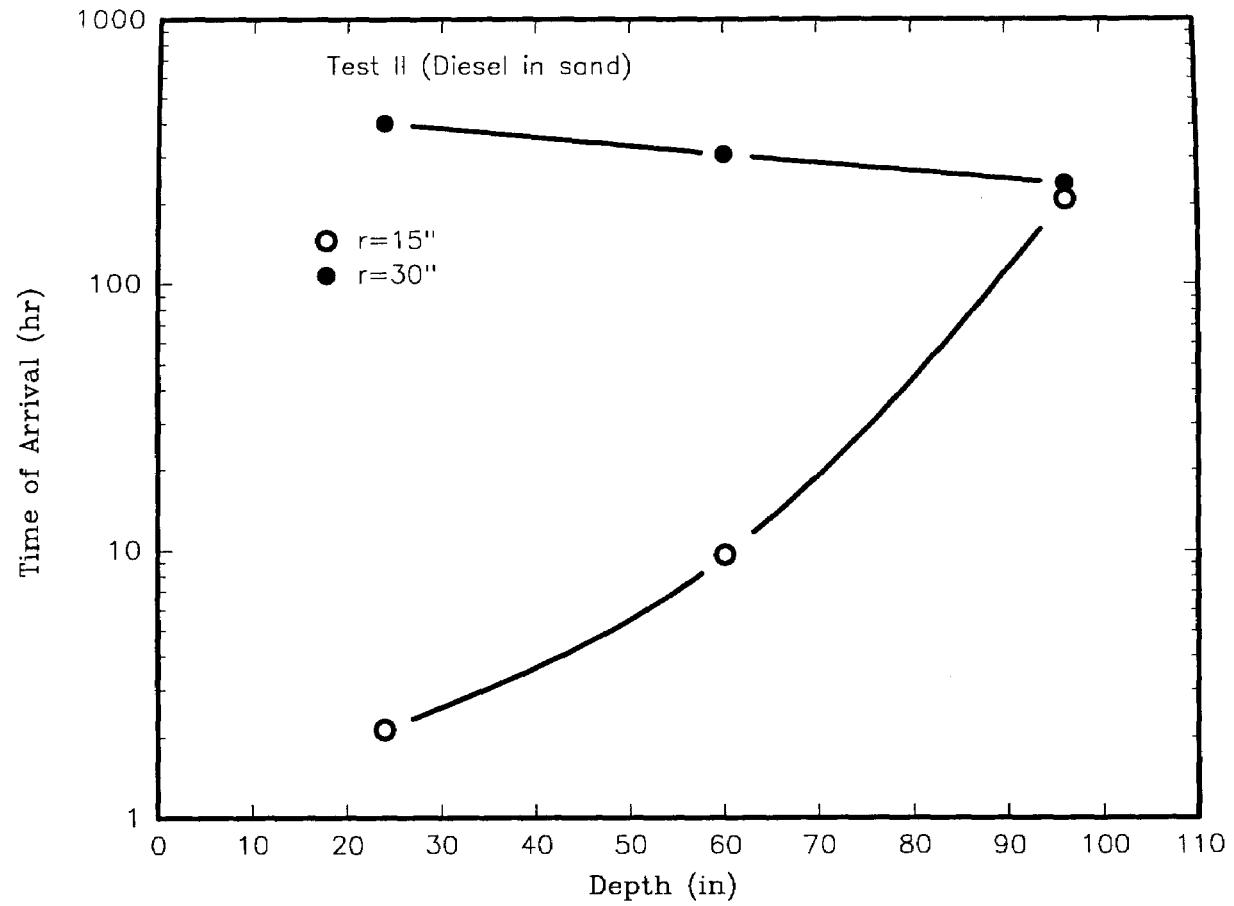


Figure 15. The TOA dependence on vertical depth for Test II

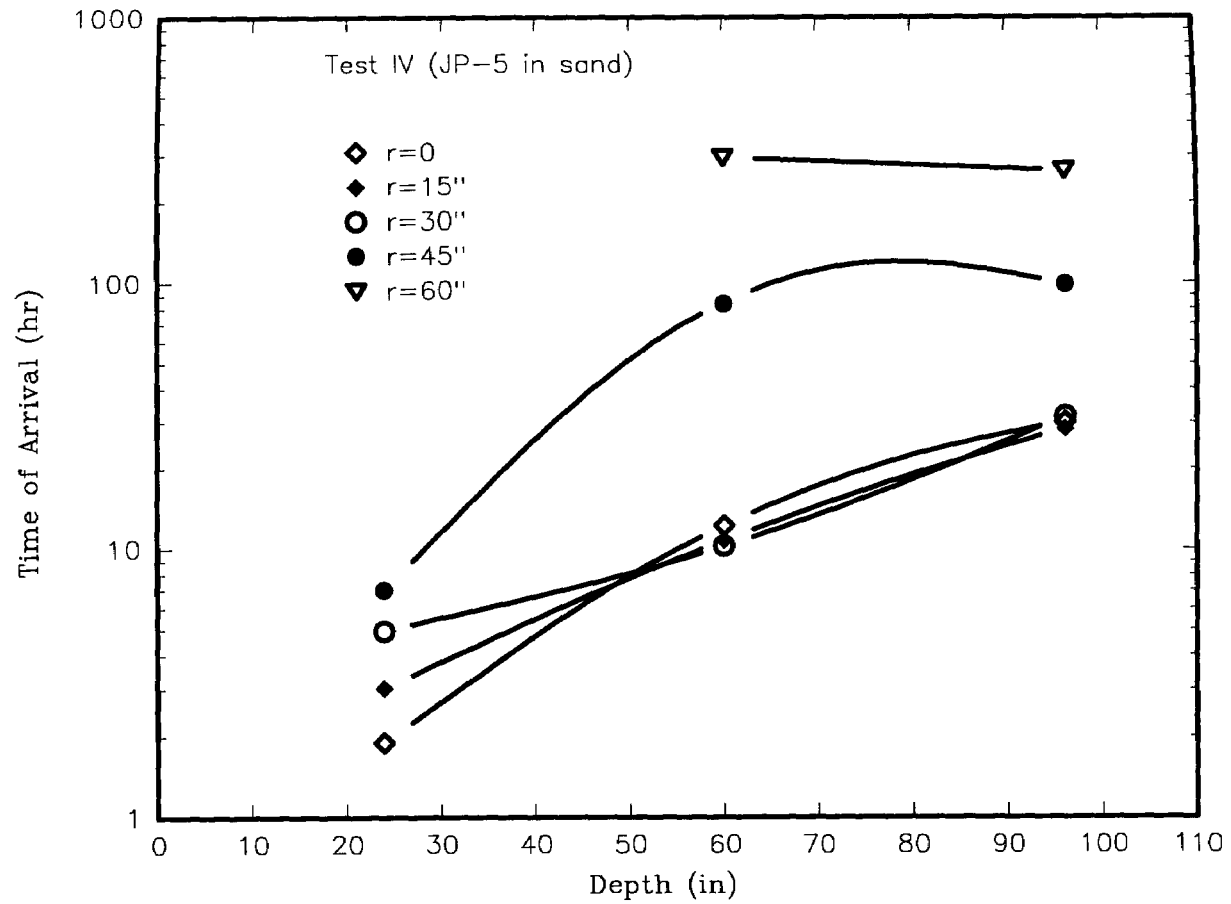


Figure 16. The TOA dependence on vertical depth for Test IV

impermeable bottom boundary to the lateral diesel spreading.

The smaller slope of the curve for $z=2$ ft. in Figure 14 than in Figure 13 indicated a faster spreading of JP-5 than diesel. The virtually equal TOAs of the first three points of line $z=5$ ft. implied that the cross sectional area of JP-5 front had already developed to 30 inches in radius when it arrived at the 5 feet level. The impermeable boundary also caused a decrease in slope in the late portion of the curves for $z=8$ ft.

The TOA vs. depth curves were not always monotonically increasing. Near the infiltration center line, the TOA was smaller for shallow sensors. As the radius, r , increased, however, the TOAs for the bottom sensors were smaller than that for the middle and even top sensors. After diesel was discharged into sand in Test II the top sensors on circle #1 ($z=2$ ft., $r=15$ in.) detected the first arrival and the bottom ones ($z=8$ ft.) the last arrival (Figure 15). Those on circle #2 ($r=30$ in.), however, showed an opposite trend. Diesel reached the 8 foot sensors first and the above sensors many hours later. The wider spread of JP-5 in sand resulted in more monotonically increasing curves of TOA with depth (Figure 16). TOA increased with depth even for sensors on circle #3 ($r=45$ in.). A sign change in the slope was also observed when the radius increased to 60 inches.

IV.3 Concentration Contour Maps

For a perfectly homogenous system the concentration contours at a certain level and certain time should be a group of concentric round circles. In actual practice, a carefully packed porous medium can be far from homogeneous. Heterogeneity always exists in a real system and concentration contours are all irregularly shaped.

Vapor concentration contour maps for Test II and Test IV were obtained through the interpolation among the data provided by all 56 sensors. The results are plotted in Figure B1-B21 in the Appendix B. Nonhomogeneous movements were observed at a very early stage of the tests. The contour shape became more irregular as the experiments continued. The most irregular contour lines in each contour map were the outermost ones: zero concentration contour lines. It is believed that both the inhomogeneous liquid propagation and gas diffusion attributed to the irregularity of the low concentration contour line.

IV.4 Concentration vs. Contour Radius

Although a certain degree of heterogeneity existed in the experiments, the concept of homogeneous movement may still be applicable in the analysis by assuming contour lines as a group of perfect circles. The area inside each contour circle of both Test II and Test IV was numerically integrated and then used to calculate the average radius, as if it were a round circle. The radius thus obtained is called a contour radius. The concentration was plotted against the contour radius for each test at a certain depth and certain time, as shown in Figures 17-22.

Figure 17 shows the concentration vs. contour radius for Test II at level 1 (2 ft. below the top surface). A dispersion type of horizontal migration of diesel in sand was observed from the shape of the curve. The horizontal propagation became very slow after 100 hours. The diesel front propagated 50 inches in the first 50 hours but moved only 7 inches in the next 550 hours. The concentration at 10 inches radius increased from zero to 2300 ppm in the first 50 hours and increased only 500 ppm in the following 550 hours.

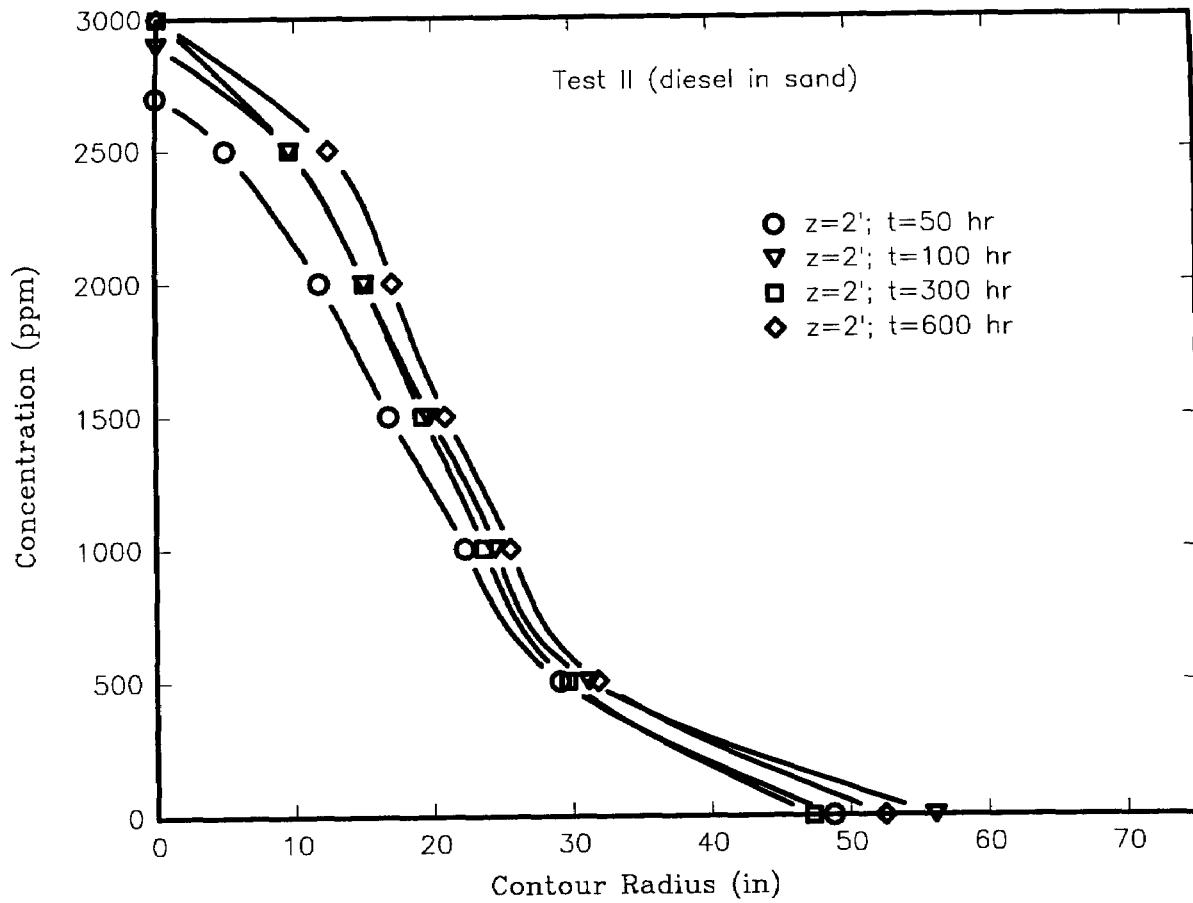


Figure 17. The diesel vapor concentration as a function of contour radius for Test II at $z=2$ ft.

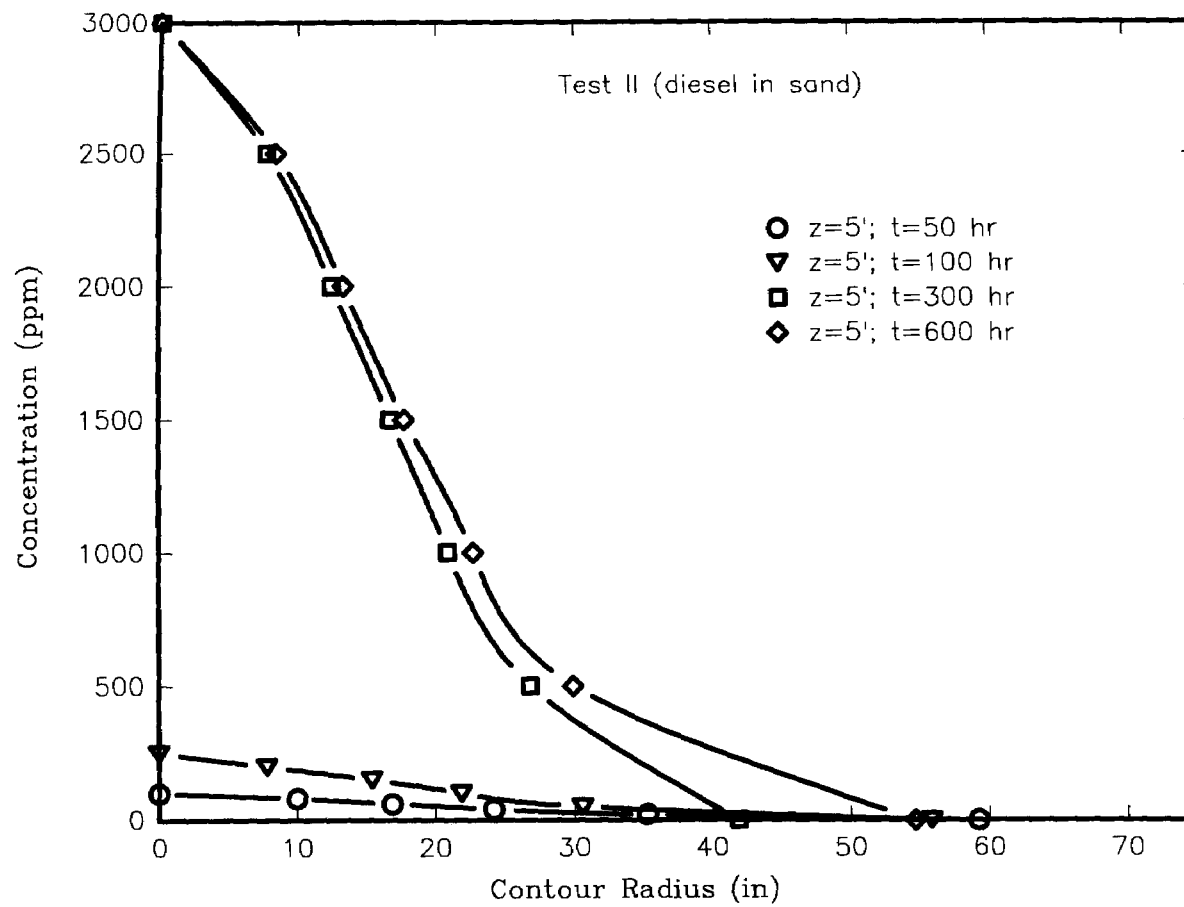


Figure 18. The diesel vapor concentration as a function of contour radius for Test II at $z=5$ ft.

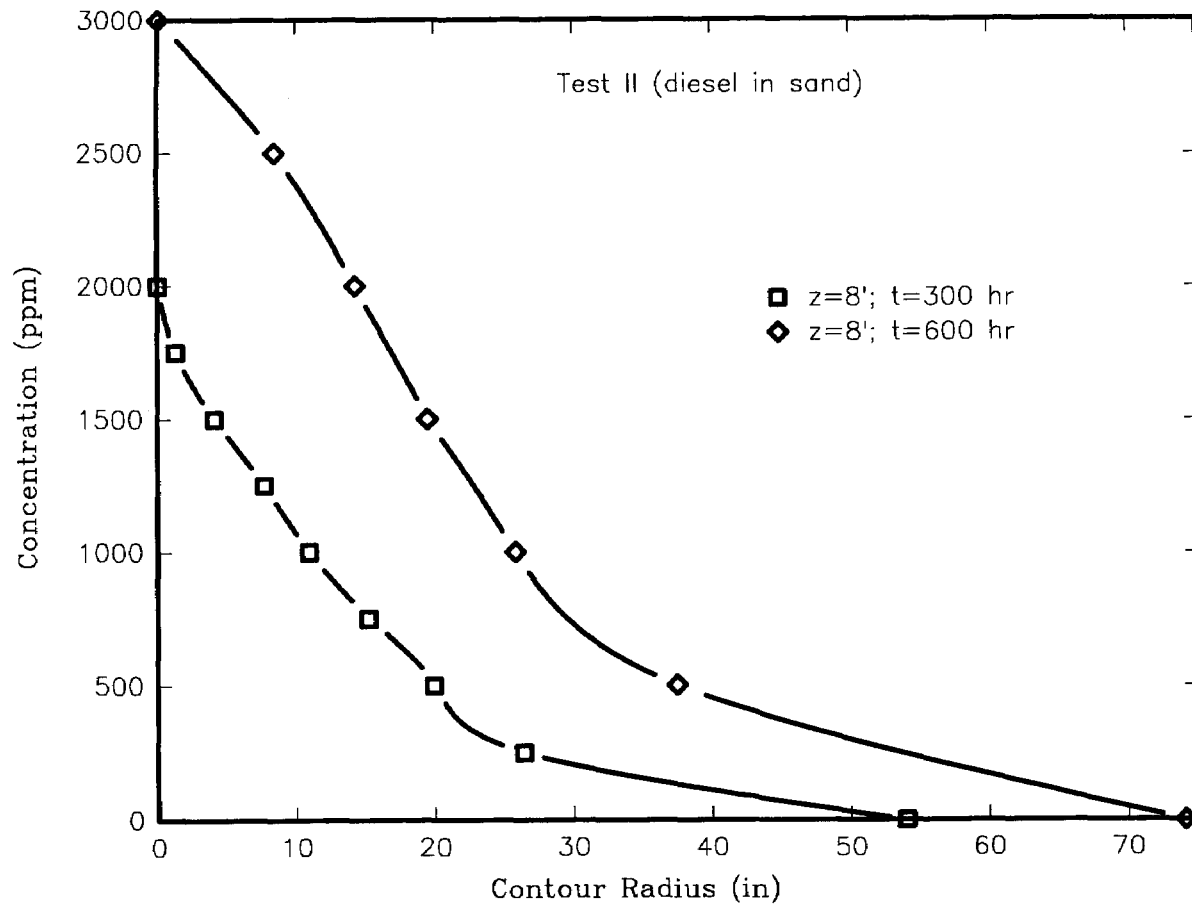


Figure 19. The diesel vapor concentration as a function of contour radius for Test II at $z=8$ ft.

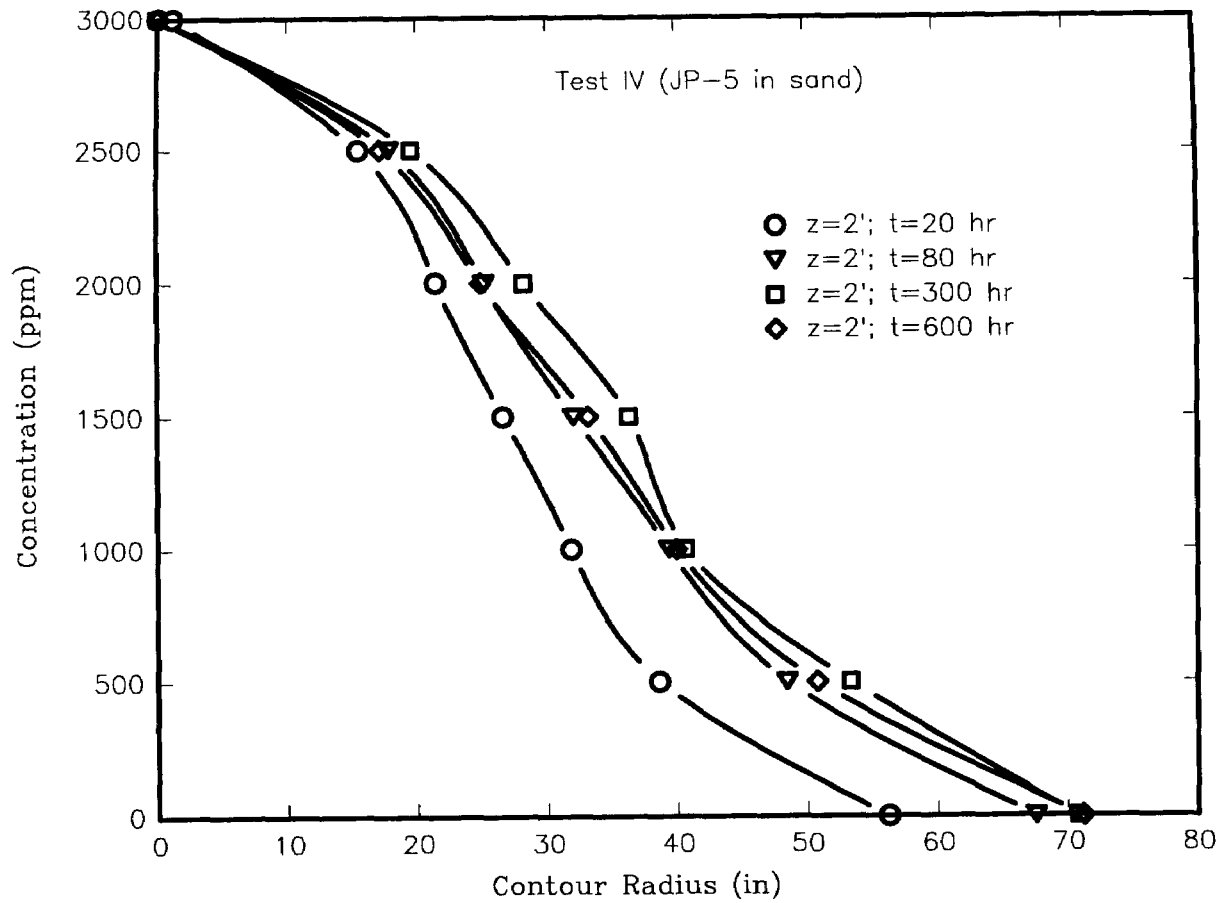


Figure 20. The JP-5 vapor concentration as a function of contour radius for Test IV at $z=2$ ft.

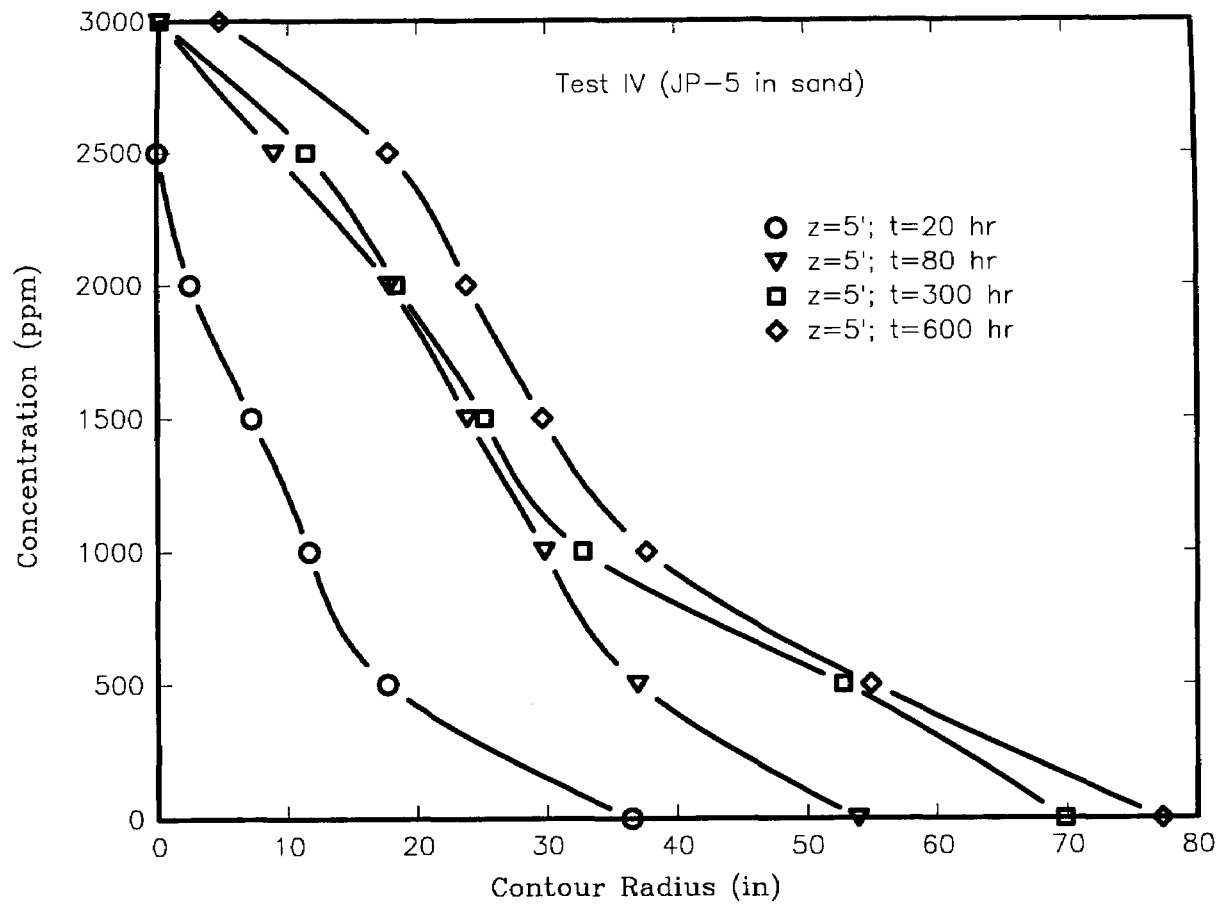


Figure 21. The JP-5 vapor concentration as a function of contour radius for Test IV at $z=5$ ft.

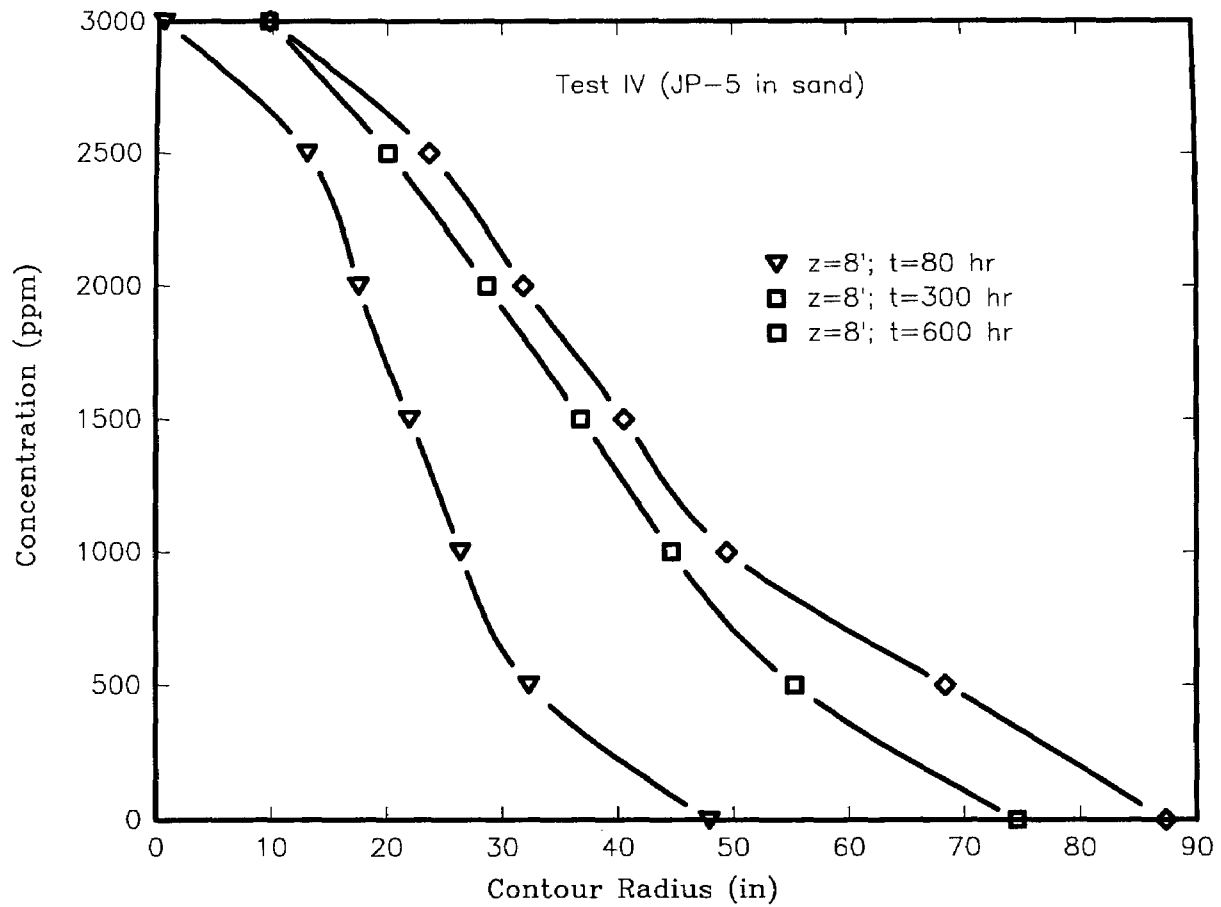


Figure 22. The JP-5 vapor concentration as a function of contour radius for Test IV at $z=8$ ft.

The concentration profile for a fully developed dispersion type of propagation should have three sections. Inside the major fuel body a pseudo-equilibrium concentration is reached and the propagation concentration gradient in the region is small. In front of the fuel, faster vapor diffusion and liquid suction lead to another relatively flat region. The middle portion of the curve, representing a transition zone of concentration from the frontier low concentration to the pseudo equilibrium high concentration, has a higher concentration gradient, which indicates a greater propagation resistance in the region.

At the 5 foot deep level, only the frontier section of the dispersion type of concentration profile was seen after 100 hours (Figure 18). After a full profile was developed after 300 hours, the propagation slowed down tremendously. Both the frontier and the middle transition zones appeared in the 300 hour concentration profile of level #3 (Figure 19). The pseudo-equilibrium region barely emerged on the 600 hour curve. More lateral spreading of JP-5 than diesel in sand was also observed from the concentration vs. contour radius plots. Comparing Figures 20-22 with Figures 17-19, it was found that JP-5 contaminated larger areas than diesel at all three levels. A dispersion type of concentration profile at level #1 was developed quickly in less than 20 hours (Figure 20). After 20 hours the horizontal propagation velocity was very low and became virtually zero after 80 hours. A significant concentration of JP-5 was found at level #2 after 20 hours and the propagation rate decreased after 80 hours (Figure 21). The front of JP-5 reached 77 inches at level #2. At the bottom level horizontal JP-5 migration continued to the end of the test (Figure 22).

IV.5 Diesel wetted soil pictures.

Diesel migration in natural soil was observed in Test III. During 700 hours of the experimental period, only sensors at the top and middle levels ($z=2$ and 5 ft.) of the first circle ($r=15$ in.) detected strong diesel vapor. The concentration changes as a function of time were presented in Figure 7. Low hydraulic permeability of soil retarded the diesel penetration. Fine particle sizes and high organic carbon content of soil produced a large adsorption capacity for the fuel. Diesel was confined in a much smaller volume in soil than in sand. The vapor envelope of the diesel wetted area in soil is also expected to be much smaller because of the high adsorption capacity of soil. High concentrations were found in the detectable area (Figure 7).

Strong adsorption of diesel on soil made the diesel wetted front clearly visible. Figures 23 and 24 are pictures taken at the end of the test which show a clearly wetted area on the surface of the test chamber. The nearly perfect round area with a surface diameter of 30 inches indicated that a fairly homogeneous spreading of diesel occurred in the soil media. When soil was first dug out from the chamber after testing, the wetted area below the surface was not seen as clearly as that on the surface because of the existing soil moisture. After leaving the soil under the sun for a few minutes, moisture evaporated faster than diesel and the diesel-wetted boundary became clear. Figures 25-27 are pictures taken after a portion of the soil was excavated, showing the vertical cross sections of diesel wetted area. A full view of the vertically wetted area can be seen in Figure 26. The "egg-shaped" boundary showed no fingering and the diesel only migrated to 75 inches in 700 hours (Figure 27). The largest horizontal diameter of the wetted area occurred at the depth of 35 inches, with a value of 58 inches. The measured location of the diesel wetting front at the end of the experiment

is listed in Table 4.

Table 4. The measured location of diesel wetting front at the end of Test III

Vertical distance z (in.)	0	6	12	24	35	48	75
Horizontal radius r (in.)	15	21	21	22	29	23.5	0



Figure 23. Soil surface picture taken at the end of Test III

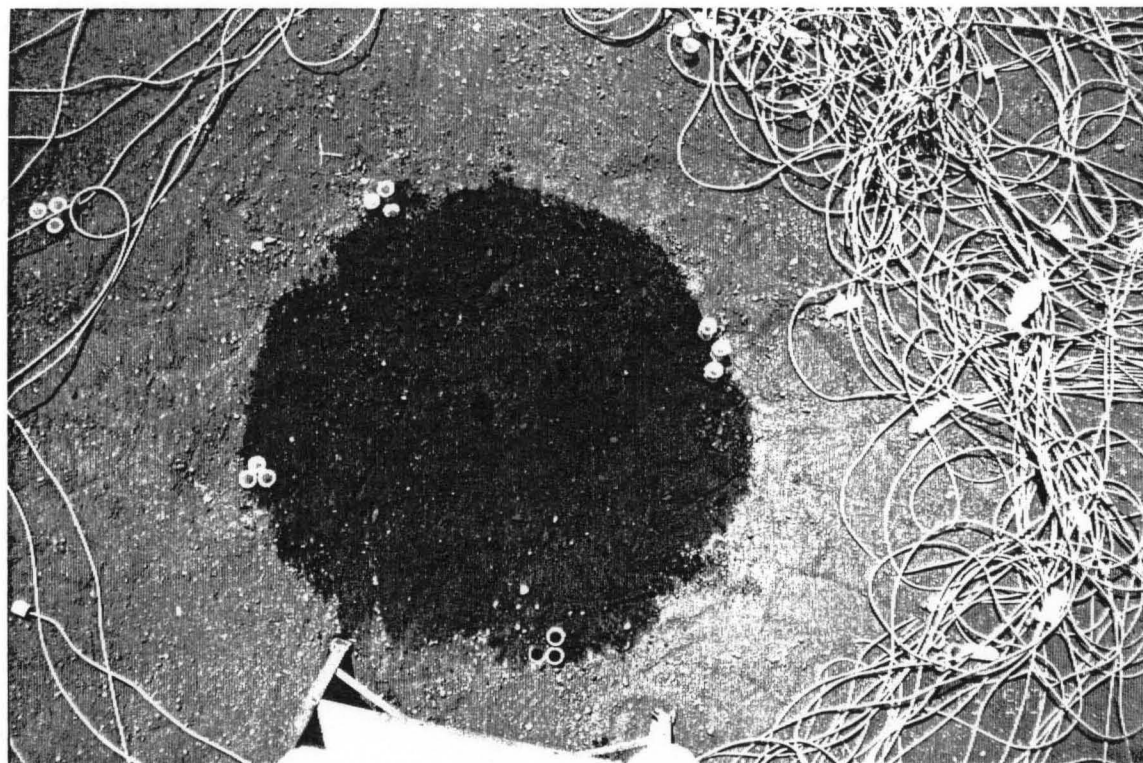


Figure 24. Diesel wetted soil surface at the end of Test III

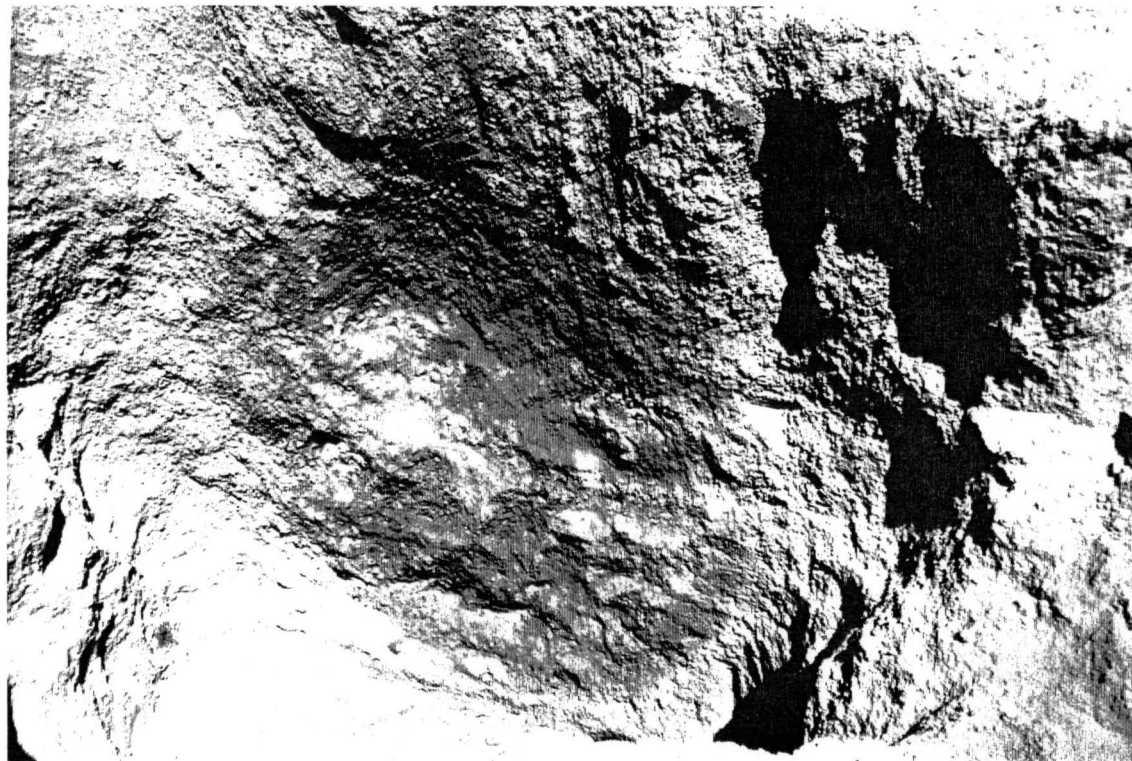


Figure 26. Vertical view of diesel wetted soil at the end of Test III (b)

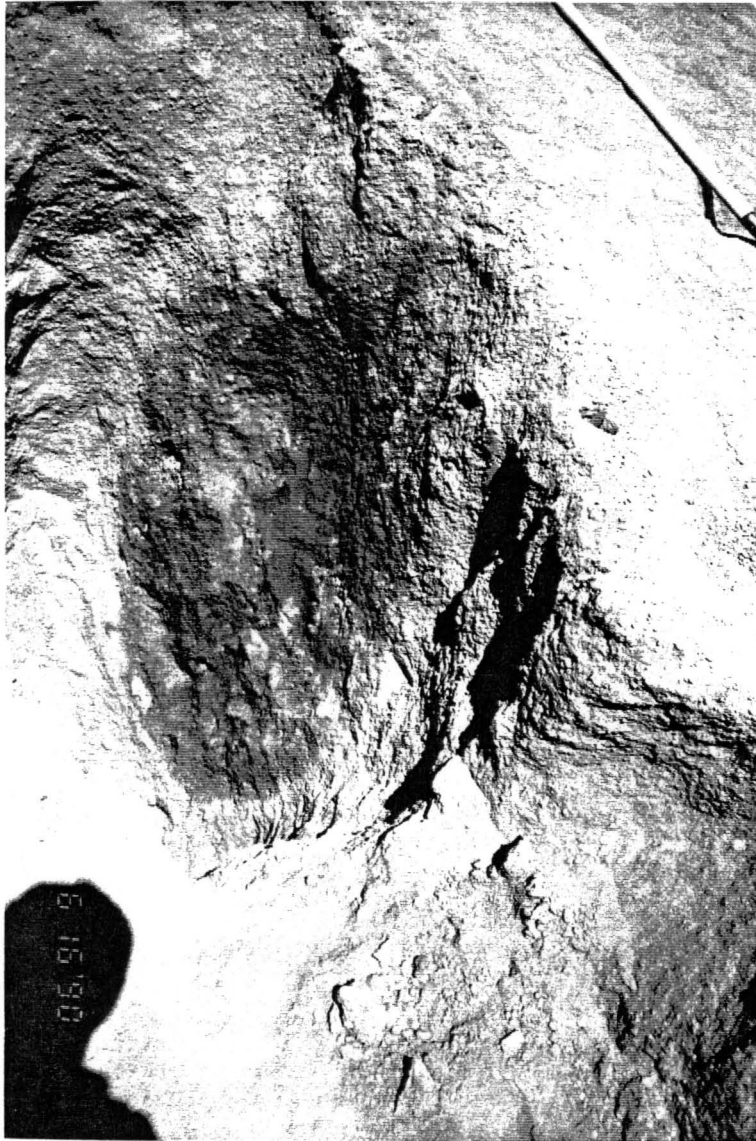


Figure 27. Vertical view of diesel wetted soil at the end of Test III (c)



Figure 25. Vertical view of diesel wetted soil at the end of Test III (a)

V. MATHEMATICAL SIMULATION

V.1 Governing Equation

The continuum approach has been used in studying transport phenomena in porous media from a microscopic level for many years (Bear and Bachmat, 1967; Nikolaevski et al., 1970; Bachmat, 1972; Hassanizadeh and Gray, 1979a, b, 1980; Marle, 1982; Bowen, 1984; Carbonell and Whitaker, 1984; Bachmat and Bear, 1986, Prat, 1989;). To avoid describing the complex geometry of each phase in a practical porous medium domain from a true microscopic level, the continuum approach treats each phase as a fictitious continuum which fills up the entire domain. Competitions and interactions between phases are thus described by a set of overlapping continua. Such treatment allows state properties of each phase at any spatial point in a porous medium domain to be represented by a meaningful average value over a so-called representative elementary volume (REV). The fundamental requirement for a porous medium to be treated by the continuum approach is the existence of the REV in which the average quantities are independent of the size of the volume and are continuous over time and space.

According to Bachmat and Bear (1986), if a porous medium domain can be treated as *continuum*, the averaging rules outlined by them can be applied to the general microscopic mass balance equation:

$$\frac{\partial \rho_{\alpha}}{\partial t} + \nabla \cdot (\rho_{\alpha} \mathbf{v}_{\alpha} + \mathbf{J}^{m_{\alpha}} U_{\alpha}) - \rho_{\alpha} \Gamma^{m_{\alpha}} = 0 \quad (1)$$

where ρ_α = the mass density of α phase. $[M/L^3]$;

v_α = the volume weighted velocity of α phase $[L/T]$;

$J^{m_\alpha U_\alpha} = \rho_\alpha (v^{m_\alpha} - v_\alpha)$ = the diffusive mass flux with respect to the velocity v_α $[M/L^2T]$;

Γ^{m_α} = the net production rate of α phase $[1/T]$.

The intrinsic phase average over a REV of Equation (1) gives the general macroscopic mass balance of α -phase over the REV:

$$\frac{\partial}{\partial t} (\theta_\alpha \bar{\rho}_\alpha) = -\nabla \cdot \theta_\alpha (\bar{\rho}_\alpha \bar{v}_\alpha + \bar{\rho}'_\alpha \bar{v}'_\alpha + \bar{J}^{m_\alpha U_\alpha}) + \theta_\alpha \bar{\rho}_\alpha \bar{\Gamma}^{m_\alpha} - \frac{1}{U_{0\alpha}} \int_{A_{\alpha\beta}} [\rho_\alpha (v_\alpha - u) + J^{m_\alpha U_\alpha}] \cdot n_\alpha dA \quad (2)$$

where $\theta_\alpha = \frac{U_{0\alpha}}{U_0}$ = the volume fraction of α phase inside the REV $[L^3/L^3]$;

U_0 = the volume of the REV $[L^3]$;

$U_{0\alpha}$ = the volume of α phase inside the REV $[L^3]$;

$\bar{\rho}_\alpha = \frac{1}{U_{0\alpha}} \int \rho_\alpha dU_\alpha$ = the intrinsic average density of α phase $[M/L^3]$;

\bar{v}_α = the volume weighted intrinsic average velocity of α phase $[L/T]$;

$\rho'_\alpha = \rho_\alpha - \bar{\rho}_\alpha$ = the deviation of ρ_α at a point within the REV from its intrinsic value;

$\bar{J}^{m_\alpha U_\alpha}$ = the intrinsic average of the diffusive mass flux;

$A_{\alpha\beta}$ = the interfacial area between α phase and β phase;

u = the velocity of the interface movement;

n_α = the unit normal vector at $\alpha\beta$ interface pointing outward of $U_{0\alpha}$.

The left-hand-side (LHS) of Equation (2) represents the intrinsic average mass accumulation. The first part of the right-hand-side (RHS) of the equation counts for

the mass change attributed to the fluxes inside the body of α phase. These fluxes include advective flux $\bar{\rho}_\alpha \bar{v}_\alpha$, dispersive flux $\rho_\alpha \dot{v}_\alpha$, and diffusive flux $\bar{J}^{m_\alpha U_\alpha}$. The second term on the RHS of the equation is the net production term which reflects mass change due to pumping, recharging, etc. The contribution of the actions occurring at the $\alpha\beta$ interface sums the interfacial dispersive flux $\rho_\alpha (v_\alpha - u)$ and diffusive flux $J^{m_\alpha U_\alpha}$ which is expressed as the last term of the equation.

For a single component α -phase fluid $v^{m_\alpha} = v_\alpha$, therefore $\bar{J}^{m_\alpha U_\alpha} = 0$. If no mass transfer between phases and no net production are assumed, the surface integral and production terms of RHS of Equation (2) vanish. Equation (2) becomes:

$$\frac{\partial}{\partial t}(\theta_\alpha \bar{\rho}_\alpha) = -\nabla \cdot \theta_\alpha (\bar{\rho}_\alpha \bar{v}_\alpha + \overline{\rho_\alpha \dot{v}_\alpha}) \quad (3)$$

If the dispersive flux can be neglected compared with advective flux, Equation (3) further becomes:

$$\frac{\partial}{\partial t}(\theta_\alpha \bar{\rho}_\alpha) = -\nabla \cdot \theta_\alpha (\bar{\rho}_\alpha \bar{v}_\alpha) \quad (4)$$

$\theta_\alpha \bar{v}_\alpha$ can be related to the hydraulic pressure of the α phase through Darcy's Law:

$$\theta_\alpha \bar{v}_\alpha = -K_\alpha \nabla \Phi_\alpha \quad (5)$$

where K_α is the hydraulic conductivity of the porous medium, and

$$\Phi_\alpha = \frac{P_\alpha}{\rho g} + z' = \phi_\alpha + z' \quad (6)$$

is the hydraulic pressure of the α phase. P_α is the hydrodynamic pressure of the α -phase and z' the elevation with respect to an arbitrary energy datum. In a space with z axis directing downward and the elevation datum chosen at the location of $z=0$, equation (6) becomes:

$$\Phi_\alpha = \frac{P_\alpha}{\rho g} - z = \varphi_\alpha - z \quad (7)$$

Substitution of Equation (5) and (7) into Equation (4) results in:

$$\frac{\partial}{\partial t}(\theta_\alpha - \bar{\rho}_\alpha) = \nabla(\bar{\rho}_\alpha K_\alpha \nabla \varphi_\alpha) - \frac{\partial}{\partial z}(\bar{\rho}_\alpha K_\alpha) \quad (8)$$

Let n be the porosity of the porous media and S_α the saturation of the α phase and we then have

$$\theta_\alpha = n S_\alpha \quad (9)$$

Assuming that the soil matrix is nondeformable and the liquid incompressible, equation (8) became:

$$n \frac{\partial S_\alpha}{\partial t} = \nabla(K_\alpha \nabla \varphi_\alpha) - \frac{\partial K_\alpha}{\partial z} \quad (10)$$

During infiltration, the drainage process usually does not occur; therefore, monotonic relationships of $\varphi_\alpha \sim S_\alpha$ and $K_\alpha \sim S_\alpha$ can be applied.

$$\text{Let } K_\alpha \nabla \varphi_\alpha = K_\alpha \frac{d\varphi_\alpha}{dS_\alpha} \nabla S_\alpha \text{ and } \frac{\partial K_\alpha}{\partial z} = \frac{dK_\alpha}{dS_\alpha} \frac{\partial S_\alpha}{\partial z} .$$

The governing equation becomes:

$$n \frac{\partial S_\alpha}{\partial t} = \nabla \left(K_\alpha \frac{d\varphi_\alpha}{dS_\alpha} \nabla S_\alpha \right) - \frac{dK_\alpha}{dS_\alpha} \frac{\partial S_\alpha}{\partial z} \quad (11)$$

K_α is related to intrinsic permeability k and relative permeability $k_{r\alpha}$ through equation:

$$K_\alpha = \frac{k \bar{\rho}_\alpha g}{\mu} k_{r\alpha} \quad (12)$$

If the porous medium is isotropic and the process isothermal, equation (11) is further simplified:

$$\frac{\partial S_\alpha}{\partial t} = \frac{k \bar{\rho}_\alpha g}{n\mu} \left[\nabla \left(k_{r\alpha} \frac{d\varphi_\alpha}{dS_\alpha} \nabla S_\alpha \right) - \frac{dk_{r\alpha}}{dS_\alpha} \frac{\partial S_\alpha}{\partial z} \right] \quad (13)$$

Under the assumption of axial symmetry, the expansion of Equation (13) in cylindrical coordinates gives:

$$\begin{aligned} \frac{\partial S_\alpha}{\partial t} = \frac{k \bar{\rho}_\alpha g}{n\mu} & \left[\frac{\partial}{\partial r} \left(k_{r\alpha} \frac{d\varphi_\alpha}{dS_\alpha} \frac{\partial S_\alpha}{\partial r} \right) + \frac{k_{r\alpha}}{r} \frac{d\varphi_\alpha}{dS_\alpha} \frac{\partial S_\alpha}{\partial r} + \right. \\ & \left. + \frac{\partial}{\partial z} \left(k_{r\alpha} \frac{d\varphi_\alpha}{dS_\alpha} \frac{\partial S_\alpha}{\partial z} \right) - \frac{dk_{r\alpha}}{dS_\alpha} \frac{\partial S_\alpha}{\partial z} \right] \quad (14) \end{aligned}$$

Let $B = \frac{k \bar{\rho}_\alpha g}{n\mu}$ and $\Pi = k_{r\alpha} \frac{d\varphi_\alpha}{dS_\alpha}$:

$$\frac{\partial S_\alpha}{\partial t} = B \left[\frac{\partial}{\partial r} \left(\Pi \frac{\partial S_\alpha}{\partial r} \right) + \frac{\Pi}{r} \frac{\partial S_\alpha}{\partial r} + \frac{\partial}{\partial z} \left(\Pi \frac{\partial S_\alpha}{\partial z} \right) - \frac{d\Pi}{dS_\alpha} \frac{\partial S_\alpha}{\partial z} \right] \quad (15)$$

V.2 Initial and Boundary Conditions

Under the assumption of axial symmetry, only half of the test chamber needs to be studied (Figure 28). All boundaries can be treated as impermeable including the center line boundary ($r=0$).

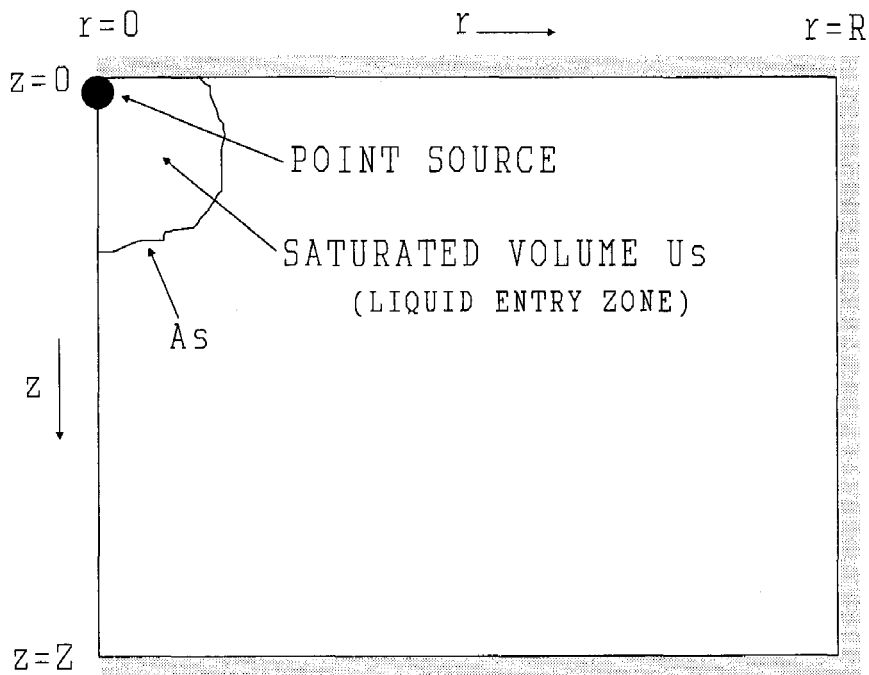


Figure 28

V.2a Initial conditions:

The experiments were conducted by introducing fuels into clean soils. Therefore, a constant saturation initially exists everywhere inside the concerned volume (Equation (16)). In our case, the constant initial saturation is zero.

$$S_{\alpha} \Big|_{r=0}(r,z) = S_{\alpha}^0 \quad 0 \leq r \leq R; \quad 0 \leq z \leq Z \quad (16)$$

V.2b Boundary conditions:

If evapotranspiration and adsorption are negligible, the zero flux boundary condition (Equation (17)) exists at all the boundaries except near the infiltration source.

$$-K_{\alpha} \nabla \Phi_{\alpha}(r,z) = 0 \quad \begin{array}{l} (r=0 \text{ and } r=R; \quad z_s \leq z \leq Z \\ z=0 \text{ and } z=Z; \quad r_s \leq r \leq Z) \end{array} \quad (17)$$

In cylindrical coordinates, Equation (17) can be written as:

$$\frac{\partial S_{\alpha}}{\partial r} = 0 \quad r=0 \text{ and } r=R; \quad z_s \leq z \leq Z \quad (18)$$

$$\frac{d\phi_{\alpha}}{dS_{\alpha}} \frac{\partial S_{\alpha}}{\partial z} = 1 \quad z=0 \text{ and } z=Z; \quad r_s \leq r \leq R \quad (19)$$

When liquid is discharged into porous media from a point source, a high saturation zone is usually formed around the source (Figure 28). We call the highly saturated zone the *liquid entry zone*. It is assumed that the soil inside the liquid entry zone is fully saturated with liquid. The size and shape of the entry zone depend not only on the characteristics of both liquid and soil but also on the liquid discharging rate. The higher the discharging rate, the larger the entry zone. The entry zone also

changes with time. At the beginning fast absorption created by the high liquid potential gradient keeps the entry zone small. As the infiltration proceeds, the absorption rate decreases and the liquid entry zone swells and eventually reaches an equilibrium when the infiltration rate equals the discharge rate.

Let U_s and A_s denote the volume and area of the liquid entry zone. A constant saturation of α phase exists everywhere inside U_s :

$$S_\alpha(r,z) = S_{\alpha_s} \quad (r,z) \in U_s \quad (20)$$

Equation (20) becomes a complete boundary condition for the governing equation only when U_s and A_s are known.

If the size of the liquid entry zone is larger than the minimum limit of the REV, a macroscopic mass balance can be applied. The mass balance of α phase over U_s gives:

$$\frac{\partial m_\alpha|_{U_s}}{\partial t} + \iint_{A_s} (\bar{\rho}_\alpha \bar{v}_\alpha)|_{A_s} \cdot \mathbf{n} dA_s = F_{\alpha m} \quad (21)$$

where $m_\alpha|_{U_s} = \bar{\rho}_\alpha S_{\alpha_s} n U_s$ is the mass of α phase inside U_s ;

$F_{\alpha m} = F_\alpha \bar{\rho}_\alpha$ is the mass discharging rate of α phase from the point source;

\mathbf{n} is the unit vector normal to A_s and directing outward U_s .

F_α is the volumetric discharging rate of α phase.

When applying Darcy's Law and dividing Equation (21) by the averaged density, the following equation can be obtained:

$$S_{\alpha_s} n \frac{\partial U_s}{\partial t} - \iint_{A_s} \frac{k \bar{\rho}_\alpha g}{\mu} k_{r\alpha} \left(\frac{d\phi_\alpha}{dS_\alpha} \nabla S_\alpha - \nabla z \right) \cdot \mathbf{n} dA = F_\alpha \quad (22)$$

Equations (20) and (22) form a complete boundary condition for the governing equation along the liquid entry zone.

In order to solve Equation (22), the shape of the liquid entry zone must be determined first. An irregular shape of the liquid entry zone is expected according to the nonlinearity of the mass balance equation over the entry zone. Physically the shape depends on many factors including liquid discharge rate, the characteristics of both the liquid and porous medium, and all the driving forces of the liquid movement.

In the case of a high liquid discharge rate, a free liquid "pond" may form on top of the soil medium, and the boundary condition (Equation (22)) should be modified to include the ponding effect. When the porous medium domain is heterogeneous, the prediction of the liquid entry zone shape becomes even more difficult.

If the discharge rate is not very high and the porous medium domain can be treated as homogeneous, the capillary suction tends to force the liquid entry zone to be spherical or hemispherical depending on the location of the discharge point. The gravitational force meanwhile pulls liquid downward into a column shape. The overall effects result in a swelling egg-shaped saturated zone (Figure 29).

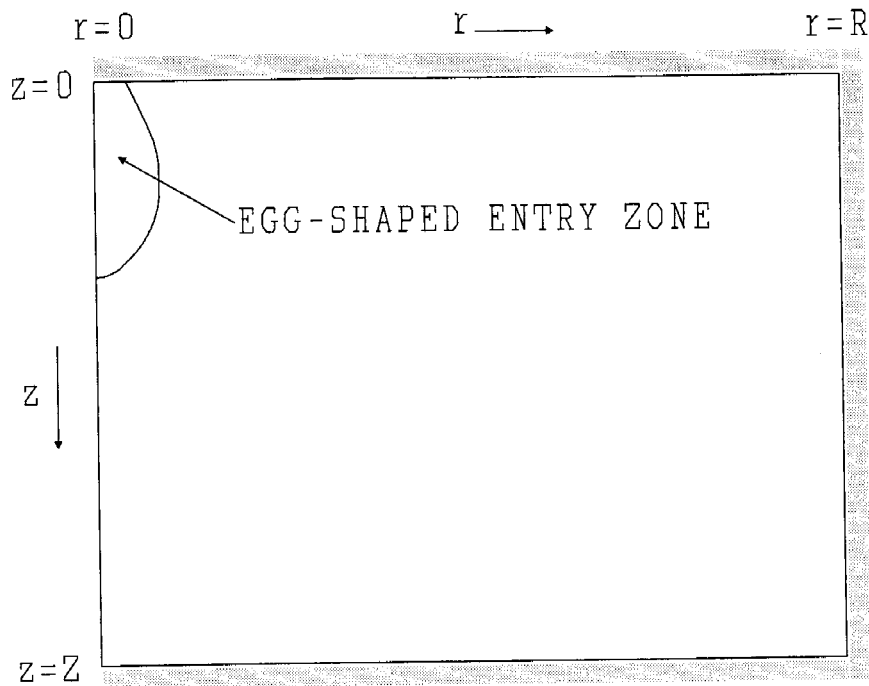


Figure 29

Simplifications are needed to solve Equation (22). A common way is to assume the growing shape of the liquid entry zone and then solve the integral equation together with the governing equation.

A. Disk-like liquid entry zone

The first model for simulating transient liquid infiltration concerning a changing size of liquid entry zone is credited to Brandt et al.(1971). In the model the liquid entry zone was treated as a zero thickness round disk on the top of the soil (Figure 30).

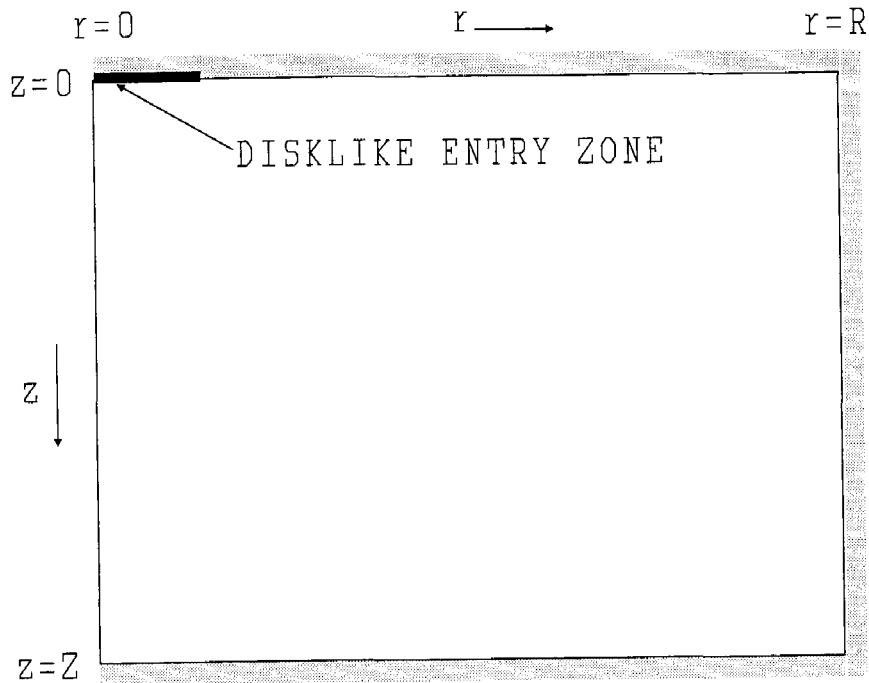


Figure 30

The mass accumulation term in Equation (22) vanishes due to the zero thickness assumption. Equation (22) is then reduced to

$$-2\pi \int_0^{R_s} \frac{k_{r\alpha} \bar{\rho}_\alpha}{\mu} \left(\frac{d\phi_\alpha}{dS_\alpha} \nabla S_\alpha - 1 \right) r dr = F_\alpha \quad (23)$$

where R_s is the radius of the entry disk.

B. Column-like liquid entry zone

Although the disk-like entry zone simplifies Equation (22) in a very effective

way, it can only be applied to the case in which the longitudinal permeability of the soil medium is much larger than its transverse permeability and the liquid discharge rate is relatively high. When the discharge rate is small and soils are isotropic, the formation of such a disk-like zone is very unlikely. A column-like entry zone is more likely because of the gravitational effect.

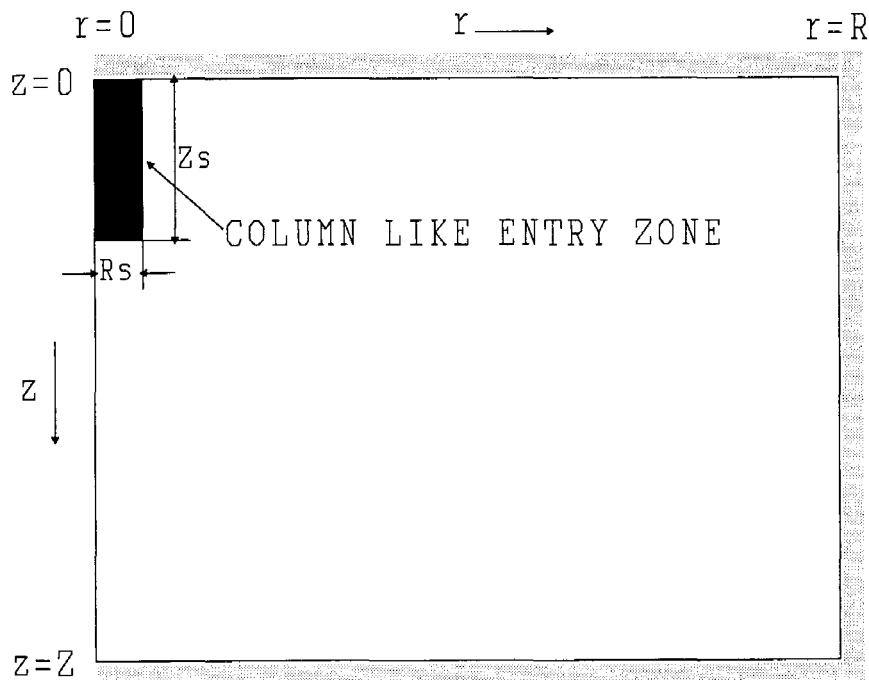


Figure 31

Assuming the liquid entry zone as a growing column with a *constant* radius R_s (Figure 31), the area of the liquid entry zone A_s from which the liquid enters the unsaturated soil equals the summation of two areas perpendicular to the z and r

directions, respectively. The top area of the column is treated as impermeable.

$$A_s = A_{s1} + A_{s2} \quad (24)$$

The volume of the liquid entry zone is easily obtained.

$$U_s = \pi R_s^2 Z_s \quad (25)$$

Equation (22) becomes (26) for a column-like entry zone.

$$S_{\alpha s} n \frac{\partial(\pi R_s^2 Z_s)}{\partial t} - \frac{k_{\rho\alpha}}{\mu} \pi R_s [2 \int_0^{z_s} k_{r\alpha} \frac{d\phi_{\alpha}}{dS_{\alpha}} \frac{\partial S_{\alpha}}{\partial r} \Big|_{r=R_s} dz + (k_{r\alpha} \frac{d\phi_{\alpha}}{dS_{\alpha}} \frac{\partial S_{\alpha}}{\partial z} \Big|_{z=z_s} - k_{r\alpha})_{ave} R_s] = F_{\alpha} \quad (26)$$

In Equation (26) the subscript *ave* means the average value over A_{s2} .

C. Spherical liquid entry zone

As it is pointed out earlier, the liquid entry zone tends to be spherical (or hemispherical if the discharge point is at the top of the soil) at the early stage of infiltration due to strong capillary suction (Figure 32).

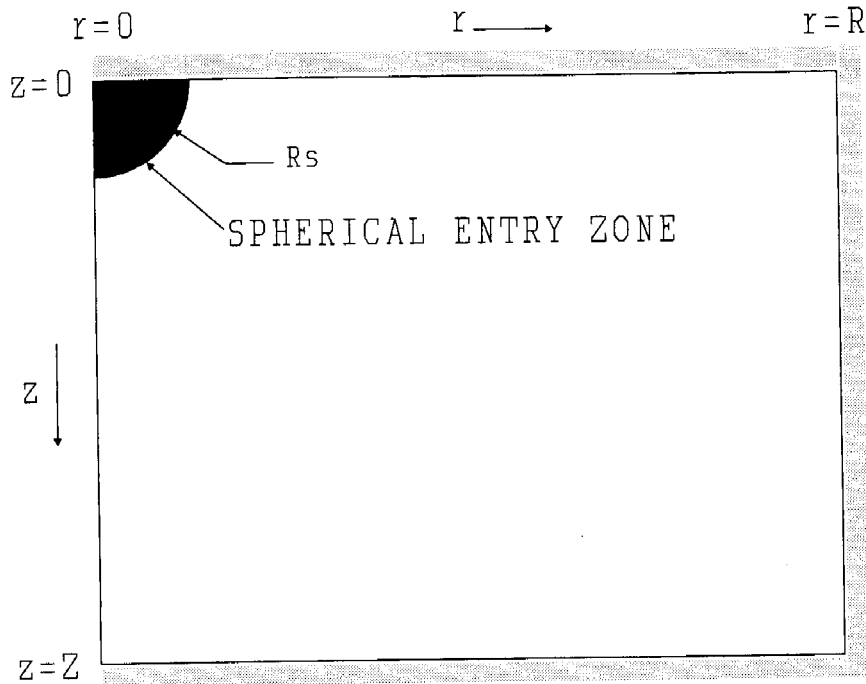


Figure 32

If a swelling hemisphere is assumed as the liquid entry zone, the mass balance equation (Equation (22)) becomes

$$S_{\alpha_s} n \frac{\partial^3 \pi R_s}{\partial t} - \iint_{A_s} \frac{\bar{k} \bar{\rho}_\alpha}{\mu} k_{r\alpha} \left(\frac{d\varphi}{dS_\alpha} \nabla S_\alpha - \nabla z \right) \cdot n dA = F_\alpha \quad (27)$$

Equations (23), (26) and (27) can be used together with Equation (20) as the boundary conditions along the liquid entry zone.

V.3 Parameters

In order to solve the governing equation (Equation (15)) to obtain the transient liquid saturation distribution profile, corresponding relationships between capillary pressure vs. saturation and relative permeability vs. saturation must be known, along with physical properties of the liquid and the soil medium such as density, viscosity, porosity, etc. Field data as well as empirical models have been used to represent the non-linear functional dependence of capillary pressure and relative permeability on liquid saturation. Many models predicting the capillary pressure vs. saturation and relative permeability vs. saturation relationships have been developed. But *selecting a more accurate model* is indeed a meaningless statement due to the uncertainties admitted by all the models. Nonetheless, it has been found that even simple approximate methods can generally lead to the same level of accuracy as using field data in terms of predictions of the saturation over the entire field (Dagan and Bresler, 1983).

It is not the intention of this study to develop a model for capillary pressure or relative permeability, or to provide a thorough review of all the existing models. Here we only briefly describe a few popular models.

V.3a Capillary pressure

If α -phase is the wetting phase, the hydraulic head ϕ_α of α -phase is related to the capillary pressure through equation (28)

$$\phi_\alpha = \frac{P_\alpha}{\rho_\alpha g} = \frac{1}{\rho_\alpha g} (P_{nw} - P_c) \quad (28)$$

There are many models developed to predict the capillary pressure and saturation relationship by hydrologists and by petro-hydrologists (Brooks and Corey, 1964; Corey, 1977; Haverkamp et al., 1977; van Genuchten, 1980; McKee et al., 1983; Bumb 1987; Parker et al., 1987). Among them, models by Brooks and Corey, and by van Genuchten are most often cited.

Brooks and Corey's Model: (Brooks and Corey, 1964)

After extensive study of the experimental data obtained from number of soils, Brooks and Corey (1964) suggested:

$$S_e = \frac{S - S_r}{S_m - S_r} = \left(\frac{P_b}{P_c} \right)^\lambda$$

where S_e - effective saturation;

S_r - irreducible saturation;

S_m - maximum attainable saturation;

P_b - bubbling pressure;

P_c - capillary pressure;

λ - the pore-size distribution index.

Rawls et al. (1982) tabulated thousands of soil data points collected from all over the United States and fit them to Brooks and Corey's model using USDA's Soil Conservation Service classification. The results are listed in the Table 2 of Bumb et al.'s paper (1988).

van Genuchten's Model: (van Genuchten, 1980)

In his attempt to develop a model predicting the hydraulic conductivity of unsaturated soils, van Genuchten introduced the following formula for hydraulic pressure head:

$$S_e = \left[\frac{1}{1 + (\alpha \phi_\alpha)^n} \right]^m \quad (29)$$

where α , n , and $m=1-1/n$ are curve fitting parameters. Detailed discussion on α , n and m can be found in van Genuchten's original paper (van Genuchten, 1980) as well as by Parker et al. (Parker et al., 1987).

V.3b *Relative permeability*

Many models relating the relative permeability and saturation have been developed. Some are purely empirical and others more theoretically based. In general, however, a relative permeability relation to saturation is developed through a power function of various forms.

Capillary model:(Purcell, 1949; Burdine, 1953)

Considering a porous medium as a bundle of capillary tubes with various diameters distributed randomly and applying Darcy's law and Poiseuille's law, relative permeability vs. saturation relationship was developed as follows:

$$k_{rw} = (S_e)^{1 + \frac{2(1+b)}{\lambda}}$$

where b is the material constant and λ the so-called lithology factor.

Wyllie's model (Frick, 1962):

In Frick's *Petroleum Production Handbook*, Wyllie suggested that for well sorted unconsolidated sand:

$$k_{rn} = (1 - S_w^*)^3 \quad ; \quad k_{rw} = (S_w^*)^3$$

and for poorly sorted unconsolidated sand:

$$k_{rn} = (1 - S_w^*)^2 [1 - (S_w^*)^{1.5}] \quad ; \quad k_{rw} = (S_w^*)^{3.5}$$

Sigmund and McCaffery (1979):

$$k_{rw} = k_{rw}^o \frac{S_e^\epsilon + 0.01 S_e}{1.01}$$

$$k_{rn} = k_{rn}^o \frac{(1 - S_e)^\epsilon + 0.01(1 - S_e)}{1.01}$$

where k_{rw} is the wetting phase relative permeability at immobile saturation and k_{rn} is the non-wetting phase relative permeability at irreducible saturation.

Hirasaki (1975):

$$k_{rw} = k_{rw}^o (S_e)^n \quad ; \quad k_{rn} = k_{rn}^o (1 - S_e)^n$$

Brooks and Corey (1964):

Combining the integral form of Burdine's relative permeability equation and their own drainage capillary pressure-saturation relationship, Brooks and Coery obtained following equation for relative permeability:

$$k_{rw} = (S_e)^{\frac{2+3\lambda}{\lambda}} = (S_e)^{3+\frac{2}{\lambda}} \quad (30)$$

Parker's Model (1987):

$$k_{rw} = S_e^{\frac{1}{2}} [1 - (1 - S_e^{\frac{1}{m}})^m]^2$$

Most of the models listed above are obtained from observations during the drainage process. However, hysteresis is not strong for wetting phase relative permeability and the above listed wetting phase relative permeability equations can, therefore, be applied in our study. For general modeling purposes Equation (31) has a good recognition by researchers and a simple form for easy adoption.

$$k_{rw} = (S_e)^3 \quad (31)$$

V.4 Finite Difference Equation

Due to the highly non-linear nature of the governing equation, an analytical solution is impossible without simplifying assumptions which distort the fundamental nature of the problem. Numerical methods must, therefore, be used. Both the finite difference method (FDM) and finite element method (FEM) have been widely used in solving for transient unsaturated liquid flow in porous media.

FEM is favored over FDM only by its ease of interpolating data and fitting odd boundaries (McKee and Bumb, 1988). The tradeoff is its longer computation time and larger storage requirements. Higher-order FEM may be well applied to smooth functions with satisfactory interpolating accuracy over a reduced number of discrete points. However, unsaturated flow often leads to a sharp saturation front which requires small elements to be used and in turns makes the computation prohibitively costly (Abou-Kassem and Aziz, 1982; McKee and Bumb, 1988). When dealing with transient problems, storage requirement by FEM can be an order of magnitude larger than for FDM. When sharp fronts are present, FEM is more likely to be numerically unstable than FDM. Nevertheless, the advantages and disadvantages of FEM vs. FDM in solving transient unsaturated liquid flow problems are almost equally divided. In this study, we selected FDM to solve the nonlinear hyperbolic partial differential equation governing the liquid flow in porous media.

We start from the governing equation (15). For convenience the phase denoting subscript α is eliminated from the saturation S and all other parameters during the derivation.

Finite difference governing equation:

Central difference approximation is used for the partial derivatives:

$$\frac{\partial S}{\partial r} = \frac{1}{2\Delta r} (S|_{r+\Delta r,z} - S|_{r-\Delta r,z}) = \frac{1}{2h} (S_{i+1,j} - S_{i-1,j}) \quad (32)$$

$$\frac{\partial S}{\partial z} = \frac{1}{2\Delta z} (S|_{r,z+\Delta z} - S|_{r,z-\Delta z}) = \frac{1}{2h} (S_{i,j+1} - S_{i,j-1}) \quad (33)$$

$$\begin{aligned} \frac{\partial}{\partial r} \left(\Pi \frac{\partial S}{\partial r} \right) &= \frac{1}{\Delta r} \left[\left(\Pi \frac{\partial S}{\partial r} \right) \Big|_{r+\frac{1}{2}\Delta r,z} - \left(\Pi \frac{\partial S}{\partial r} \right) \Big|_{r-\frac{1}{2}\Delta r,z} \right] \\ &= \frac{1}{\Delta r} \left[\Pi \Big|_{r+\frac{1}{2}\Delta r,z} \frac{1}{\Delta r} (S|_{r+\Delta r,z} - S|_{r,z}) - \Pi \Big|_{r-\frac{1}{2}\Delta r,z} \frac{1}{\Delta r} (S|_{r,z} - S|_{r-\Delta r,z}) \right] \\ &= \frac{1}{(2\Delta r)^2} \left[(\Pi \Big|_{r+\Delta r,z} + \Pi \Big|_{r,z}) (S|_{r+\Delta r,z} - S|_{r,z}) - (\Pi \Big|_{r,z} + \Pi \Big|_{r-\Delta r,z}) (S|_{r,z} - S|_{r-\Delta r,z}) \right] \\ &= \frac{1}{2h^2} \left[(\Pi_{i+1,j} + \Pi_{i,j}) (S_{i+1,j} - S_{i,j}) - (\Pi_{i,j} + \Pi_{i-1,j}) (S_{i,j} - S_{i-1,j}) \right] \end{aligned} \quad (34)$$

$$\frac{\partial}{\partial z} \left(\Pi \frac{\partial S}{\partial z} \right) = \frac{1}{2h^2} \left[(\Pi_{i,j+1} + \Pi_{i,j}) (S_{i,j+1} - S_{i,j}) - (\Pi_{i,j} + \Pi_{i,j-1}) (S_{i,j} - S_{i,j-1}) \right] \quad (35)$$

$$\frac{\Pi}{r} \frac{\partial S}{\partial r} = \frac{\Pi_{i,j}}{2h^2 i} (S_{i+1,j} - S_{i-1,j}) \quad (36)$$

$$\frac{dk_r}{dS} \frac{\partial S}{\partial z} = \frac{1}{2h} \frac{dk_r}{dS} \Big|_{i,j} (S_{i,j+1} - S_{i,j-1}) \quad (37)$$

$$\frac{\partial S}{\partial t} = \frac{1}{\Delta t} (S_{r,z}^{t+\Delta t} - S_{r,z}^t) = \frac{1}{\tau} (S_{ij}^{k+1} - S_{ij}^k) \quad (38)$$

where $i=1,2,3,\dots,M-1$, $j=1,2,3,\dots,N-1$, and $k=0,1,2,3,\dots,K$ are the indices of the discretized spatial variables r , z and τ . The discrete distances in the r and z directions were chosen to be the same and designated as h . τ is the discrete time step.

The governing equation (15) can be represented in linear algebra fashion by introducing the saturation vector,

$$\underline{S}_j = [S_{1,1} \quad S_{1,2} \quad S_{1,3} \dots S_{1,N} \quad S_{2,1} \quad S_{2,2} \dots S_{2,N} \quad S_{3,1} \dots S_{M,N}]^T .$$

The resulting equation, if solved using an explicit technique, would be conditionally stable and prohibitively expensive to solve. Straightforward implicit solution is also impractical due to the nature of the resulting matrix. Although the simple band-structured $MN \times MN$ matrix has only five non-zero diagonals, two of the non-zero diagonals are located far from the main diagonals, which makes the solution extremely difficult.

V.5 Alternating Direction Implicit (ADI) Method

The Alternating Direction Implicit (ADI) method is the most successful method to solve a two dimensional parabolic problem. First introduced by Peaceman and Rachford in the late 1950s (Peaceman and Rachford, 1955), the ADI method treats one direction implicitly at the first stage and then the other implicitly at the next stage. The overall algorithm provides a second-order accurate and unconditionally stable solution for the problem.

The finite difference expressions of our governing equation for the two ADI stages are as follows:

First stage:

$$\begin{aligned} \frac{S_{ij}^{k+\frac{1}{2}} - S_{ij}^k}{\frac{\tau}{2}} &= \frac{B}{2h^2} \{ [(\Pi_{i+1,j} + \Pi_{ij})(S_{i+1,j} - S_{ij}) - (\Pi_{ij} + \Pi_{i-1,j})(S_{ij} - S_{i-1,j}) + \frac{\Pi_{ij}}{i}(S_{i+1,j} - S_{i-1,j})]^{k+\frac{1}{2}} \\ &+ [(\Pi_{ij+1} + \Pi_{ij})(S_{ij+1} - S_{ij}) - (\Pi_{ij} + \Pi_{ij-1})(S_{ij} - S_{ij-1}) + h \frac{dk_r}{dS} \Big|_{ij} (S_{i+1,j} - S_{i-1,j})]^{k+1} \} \end{aligned} \quad (39)$$

Second stage:

$$\begin{aligned} \frac{S_{ij}^{k+\frac{1}{2}} - S_{ij}^k}{\frac{\tau}{2}} &= \frac{B}{2h^2} \{ [(\Pi_{i+1,j} + \Pi_{ij})(S_{i+1,j} - S_{ij}) - (\Pi_{ij} + \Pi_{i-1,j})(S_{ij} - S_{i-1,j}) + \frac{\Pi_{ij}}{i}(S_{i+1,j} - S_{i-1,j})]^{k+\frac{1}{2}} \\ &+ [(\Pi_{ij+1} + \Pi_{ij})(S_{ij+1} - S_{ij}) - (\Pi_{ij} + \Pi_{ij-1})(S_{ij} - S_{ij-1}) + h \frac{dk_r}{dS} \Big|_{ij} (S_{i+1,j} - S_{i-1,j})]^{k+1} \} \end{aligned} \quad (40)$$

V.6 Finite difference initial conditions:

$$S_{ij}^o = S^o \quad i=0,1,2,\dots,M; \quad j=0,1,2,\dots,N \quad (41)$$

V.7 Finite difference boundary conditions:

For the impermeable boundaries:

$$\frac{1}{2h}(-3S_{0j}^{k+\frac{1}{2}} + 4S_{1j}^{k+\frac{1}{2}} - S_{2j}^{k+\frac{1}{2}}) = 0 \quad j=j_s, j_s+1, \dots, N \quad (42)$$

$$\frac{1}{2h}(-3S_{Mj}^{k+\frac{1}{2}} + 4S_{M-1,j}^{k+\frac{1}{2}} - S_{M-2,j}^{k+\frac{1}{2}}) = 0 \quad j=j_s, j_s+1, \dots, N \quad (43)$$

$$\left(\frac{d\phi}{dS}\right)_{i,0}^{k+\frac{1}{2}} \cdot \frac{1}{2h}(-3S_{i,0}^{k+\frac{1}{2}} + 4S_{i,1}^{k+\frac{1}{2}} - S_{i,2}^{k+\frac{1}{2}}) = 1 \quad i=i_s, i_s+1, \dots, M \quad (44)$$

$$\left(\frac{d\phi}{dS}\right)_{i,N}^{k+\frac{1}{2}} \cdot \frac{1}{2h}(-3S_{i,N}^{k+\frac{1}{2}} + 4S_{i,N-1}^{k+\frac{1}{2}} - S_{i,N-2}^{k+\frac{1}{2}}) = 1 \quad i=i_s, i_s+1, \dots, M \quad (45)$$

For the liquid entry zone:

$$S_{ij}^{k+\frac{1}{2}} = S_s \quad i=0,1,2,\dots,i_s; \quad j=0,1,2,\dots,j_s \quad (46)$$

Equation (22) can be used to calculate i_s and j_s , which involves again the solution to a nonlinear partial differential equation itself. To simplify the problem an arbitrary shape of the liquid entry zone is made. Although three different shapes were introduced in the previous section, only the disk-like entry zone has actually been used in the simulation of infiltration by previous researchers. As mentioned previously, the disk-like entry zone assumption has the potential of overestimating the infiltration rate

by neglecting the accumulation of liquid inside the entry zone. To overcome such a problem we introduce a new way of treating the liquid entry zone. We assumed that the liquid entry zone grows by differentiated elements in the sequence shown in Figure 33.

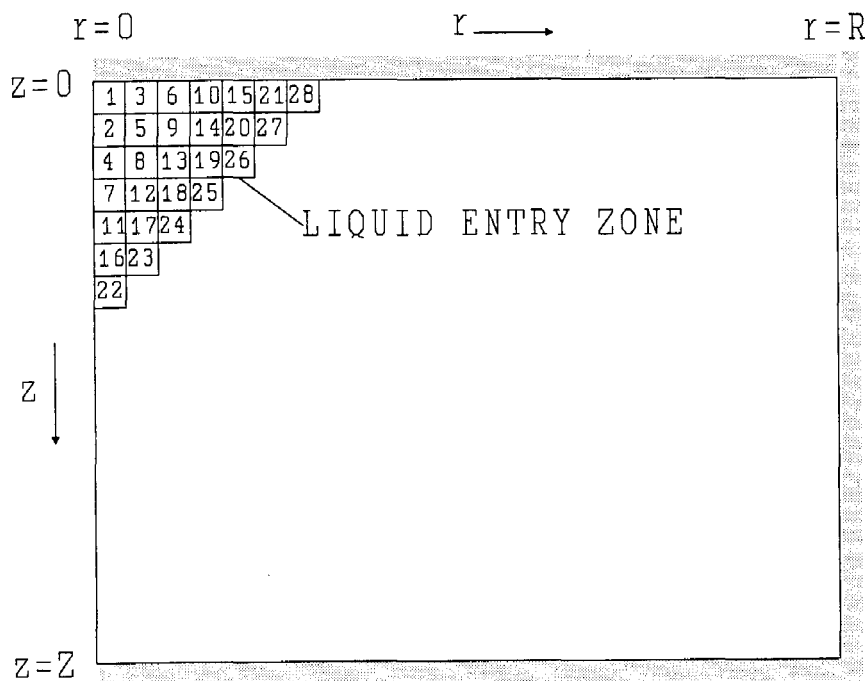


Figure 33

Rewriting Equation (22) into (47) gives:

$$S_s \frac{\partial U_s}{\partial t} - B \iint_{A_s} (\Pi \nabla S - k_r \nabla z) \cdot n dA = \frac{F}{n} \quad (47)$$

Applying the finite difference scheme to Equation (47) produces:

$$\frac{\partial U_s}{\partial t} = \frac{U_s^{k+\frac{1}{2}} - U_s^k}{\frac{\tau}{2}} \quad (48)$$

$$\iint_{A_s} (\Pi \nabla S + k_r \nabla z) \cdot n dA = \iint_{A_r} \Pi \frac{\partial S}{\partial r} dA + \iint_{A_z} (\Pi \frac{\partial S}{\partial z} - k_r) dA \quad (49)$$

$$\iint_{A_r} \Pi \frac{\partial S}{\partial r} = \sum_i^{i_s} \Pi_{ij}^{k+\frac{1}{2}} \frac{S_{i+1,j}^{k+\frac{1}{2}} - S_{i-1,j}^{k+\frac{1}{2}}}{2h} \cdot 2\pi h^2 = \sum_i^{i_s} \Pi_{ij}^{k+\frac{1}{2}} (\pi h) (S_{i+1,j}^{k+\frac{1}{2}} - S_{i-1,j}^{k+\frac{1}{2}}) \quad (50)$$

$$\iint_{A_z} (\Pi \frac{\partial S}{\partial z} - k_r) dA = \sum_j^{j_s} (\Pi_{ij}^{k+\frac{1}{2}} \frac{S_{i,j+1}^{k+\frac{1}{2}} - S_{i,j-1}^{k+\frac{1}{2}}}{2h} - k_{rij}^{k+\frac{1}{2}}) \cdot \pi (2i-1) h^2 \quad (51)$$

Equation (47) must be solved together with the governing equation and the condition equations for the i_s and j_s . The nonlinear equations require an iteration technique to be used.

Let ℓ denote the number of the differentiated entry zone element. We start from $i_s=1$ and $j_s=1$ with $\ell=1$ and solve the governing equation and the condition equations. Once $S_{ij}^{k+\frac{1}{2}}$ is known, the following inequality is checked:

$$S_s \frac{U_s^{k+\frac{1}{2}} - U_s^k}{\frac{\tau}{2}} - B \left[\left(\Pi_{1,1}^{k+\frac{1}{2}} \frac{S_{1,2}^{k+\frac{1}{2}} - S_{1,0}^{k+\frac{1}{2}}}{2h} + k_{r,1,1}^{k+\frac{1}{2}} \right) \pi h^2 + \Pi_{1,1}^{k+\frac{1}{2}} (\pi h) (S_{2,1}^{k+\frac{1}{2}} - S_{0,1}^{k+\frac{1}{2}}) \right] < \frac{F^{k+\frac{1}{2}}}{n} \quad (52)$$

for $\ell=1$

and

$$S_s \frac{U_s^{k+\frac{1}{2}} - U_s^k}{\tau} - B \sum_{j=1}^l \sum_{i=1}^{l-1} [(\Pi_{ij}^{k+\frac{1}{2}} \frac{S_{i,j+1}^{k+\frac{1}{2}} - S_{i,j-1}^{k+\frac{1}{2}}}{2h} - k_{rij}^{k+\frac{1}{2}}) \cdot \pi (2i-1)h^2 + \Pi_{ij}^{k+\frac{1}{2}} (\pi ih)(S_{i+1,j}^{k+\frac{1}{2}} - S_{i-1,j}^{k+\frac{1}{2}})] < \frac{F^{k+\frac{1}{2}}}{n} \quad \text{for } l \geq 2 \quad (53)$$

The procedure then is to increase l by 1 and solve the governing equation again with the new condition equations continuing until the inequality fails.

V.8 Picard Iteration Method

At a given time step the finite difference governing equations and the boundary conditions form a nonlinear equation system which can be solved by using the Picard iteration method.

Rewriting the nonlinear equation system in algebraic form for Stage I gives:

$$\underline{\underline{P}}_j(\underline{S}_j^{k+\frac{1}{2}}) \cdot \underline{S}_j^{k+\frac{1}{2}} = \underline{D}_j(\underline{S}_j^k) \quad j=1,2,3,\dots,N \quad (54)$$

and for Stage II:

$$\underline{\underline{P}}_i(\underline{S}_i^{k+1}) \cdot \underline{S}_i^{k+1} = \underline{D}_i(\underline{S}_i^{k+\frac{1}{2}}) \quad i=1,2,3,\dots,M \quad (55)$$

where \underline{S} is the saturation vectors defined as:

$$\underline{S}_j = [S_{1j} \quad S_{2j} \quad S_{3j} \dots S_{Mj}]^T \quad \text{for Stage I, and}$$

$$\underline{S}_i = [S_{i,1} \quad S_{i,2} \quad S_{i,3} \dots S_{i,N}]^T \quad \text{for Stage II;}$$

$\underline{\underline{P}}$ is the coefficient matrix whose elements are function of \underline{S} ;

\underline{D} is the constant vector which is a function of \underline{S} at earlier time step.

For Equation (54) of Stage I, the Picard iteration method (also called the substitution method) begins with an initial guess $(\underline{S}_j^{k+\frac{1}{2}})_o = \underline{S}_j^k$ and solves the system of linear equations:

$$\underline{\underline{P}}_j(\underline{S}_j^{k+\frac{1}{2}})_o \cdot (\underline{S}_j^{k+\frac{1}{2}})_n = \underline{D}_j(\underline{S}_j^k) \quad (56)$$

to obtain the new solution $(\underline{S}_j^{k+\frac{1}{2}})_n$. Substitute $(\underline{S}_j^{k+\frac{1}{2}})_o$ with $(\underline{S}_j^{k+\frac{1}{2}})_n$ in Equation (56) and solve the next new solution. Continue the iteration until a "true" solution is obtained when following convergence criterion is satisfied:

$$\underline{R}_j^{k+\frac{1}{2}} = (\underline{S}_j^{k+\frac{1}{2}})_n - (\underline{S}_j^{k+\frac{1}{2}})_o \leq \underline{\varepsilon} \quad (57)$$

where $\underline{\varepsilon}$ is the tolerance vector.

Similarly, Equation (55) of Stage II can be solved with the Picard iteration scheme.

The ADI treatment makes the coefficient matrix, \underline{P} , a tridiagonal matrix (The elements of the matrix are listed in Appendix B) which can be easily solved with methods such as a specialized Gaussian elimination.

V.9 Mass Transfer in the Gas Phase

V.9a Gas Diffusion Equation in Porous Media

Following Bachmat and Bear (1988), the intrinsic average of the mass balance of i species in α phase over the REM is as follows:

$$\frac{\partial}{\partial t}(\theta_{\alpha} \bar{\rho}_{\alpha i}) = -\nabla \cdot \theta_{\alpha} (\bar{\rho}_{\alpha i} \bar{\mathbf{v}}_{\alpha} + \bar{\rho}_{\alpha i} \bar{\mathbf{y}}_{\alpha} + \bar{\mathbf{J}}^{m_{\alpha i} U_{\alpha}}) + \theta_{\alpha} \bar{\rho}_{\alpha} \Gamma^{m_{\alpha i}} - \frac{1}{U_{0\alpha}} \int_{A_{\alpha\beta}} [\rho_{\alpha i} (\bar{\mathbf{v}}_{\alpha} - \mathbf{u}) + \mathbf{J}^{m_{\alpha i} U_{\alpha}}] \cdot \mathbf{n}_{\alpha} dA \quad (58)$$

where $\bar{\rho}_{\alpha i} = \frac{1}{U_{0\alpha}} \int_{U_{\alpha}} \rho_{\alpha i} dU_{\alpha}$ = the intrinsic average density of species i in α phase [M/L³];

$\bar{\mathbf{J}}^{m_{\alpha i} U_{\alpha}}$ = the intrinsic average of the diffusive mass flux of i species

in α phase;

$\Gamma^{m_{\alpha i}}$ = the net production rate of i species [1/T].

Equation (58) states that the mass accumulation of i species in the α phase is equal to the summation of many terms including the transport due to advection, dispersion and diffusion, the net production and the interfacial mass transfer between α and β phases. For the migration of petroleum fuels in soil, the net production is mainly due to loss by the biodegradation process. Under normal conditions biodegradation is a very slow process. Baehr (1987) simulated the migration of gasoline fuel in natural soils and concluded that the loss of gasoline contaminants due to biodegradation over a 100 year period was only 4%. Neglecting the biodegradation process is, therefore, an appropriate assumption in our case.

The mass transfer resistance of volatile organic chemicals at the air-water or

air-soil interface has been found small, and rapid air-water equilibrium been assumed in many simulations of organic contaminant transport in soils (Abriola and Pinder, 1985b; Lindstrom and Piver, 1986; Baehr and Corapcioglu, 1987; Gierke et al., 1990).

If biodegradation and interfacial mass transfer are neglected, Equation (58) reduces to:

$$\frac{\partial}{\partial t}(\theta_{\alpha} \bar{\rho}_{\alpha i}) = -\nabla \cdot \theta_{\alpha} (\bar{\rho}_{\alpha i} \bar{v}_{\alpha} + \bar{\rho}_{\alpha i} \bar{v}_{\alpha} + \bar{J}^{m_{\alpha i} U_{\alpha}}) \quad (59)$$

In the case of slow liquid discharge into soils, the formation of a dynamic pressure gradient in the gas phase due to the liquid discharge is very unlikely. Under isothermal conditions, the only possible advection of the gas phase is gravitational. The density difference of volatile organic chemicals from air has been found to cause the advective transport of the chemicals in the gas phase in porous media (Falta et al., 1989; Sleep and Sykes, 1989; Mendoza and Frind, 1990a). After the sensitivity study over the gas density, Mendoza and Frind (1990b) found that the diffusion process became dominant for TCE (Trichloroethylene) vapor migration in soils when the relative density defined by Equation (60) is less than 1.15. Compared with TCE both diesel and JP-5 fuels have much lower vapor pressures and the densities of the volatile species are closer to that of air than TCE. The relative densities of diesel and JP-5 vapors are unlikely to exceed 1.15. Therefore, the advective transport of diesel and JP-5 vapors in soils can be neglected.

$$\rho_{rv} = \frac{\rho_c}{\rho_a} = \frac{X_c M_c + (1 - X_c) M_a}{M_a} \quad (60)$$

where ρ_{rv} = the relative density [ML³/ML³];

ρ_c = the density of the chemical vapor [M/L³];

ρ_a = the density of air [M/L³];

X_c = the mole fraction of chemical in the gas phase [mole/mole];

M_c = the molecular weight of the chemical [M/mole];

M_a = the molecular weight of air [M/mole].

The first and second terms of the RHS of Equation (59) vanish if the gas phase is assumed to be stagnant and Equation (59) becomes:

$$\frac{\partial}{\partial t}(\theta_\alpha \bar{\rho}_{\alpha i}) = -\nabla \cdot \theta_\alpha (\bar{J}^{m_{\alpha i} U_\alpha}) \quad (61)$$

The diffusive flux, at the microscopic level, is expressed by Fick's Law:

$$\bar{J}^{m_{\alpha i} U_\alpha} = \rho_{\alpha i} (\mathbf{v}^{m_{\alpha i}} - \mathbf{v}_\alpha) = -D_{\alpha i} \nabla \rho_{\alpha i} \quad (62)$$

If the diffusivity is independent of the concentration of i species, the intrinsic volumetric averaging of Equation (59) over the α phase inside the REV gives:

$$\bar{J}^{m_{\alpha i} U_\alpha} = -D_{\alpha i}^* \nabla \bar{\rho}_{\alpha i} = -D_{\alpha i}^* (\nabla \bar{\rho}_{\alpha i} + \frac{1}{U_{\alpha A_\alpha}} \int \rho_{\alpha i} \mathbf{n} dA) \quad (63)$$

where $D_{\alpha i}^*$ = the diffusivity tensor of i species in α phase and is a function of the saturation of the α phase.

By substitution of Equation (63) into Equation (61), the mass balance equation becomes:

$$\frac{\partial}{\partial t}(\theta_\alpha \bar{\rho}_{\alpha i}) = -\nabla \cdot \theta_\alpha \bar{J}^{m_{\alpha i} U_\alpha} = \nabla \cdot \theta_\alpha D_{\alpha i}^* (\nabla \bar{\rho}_{\alpha i} + \frac{1}{U_{\alpha A_\alpha}} \int \rho_{\alpha i} \mathbf{n} dA) \quad (64)$$

If no adsorption/desorption is assumed, Equation (64) is simplified to:

$$\frac{\partial}{\partial t}(\theta_{\alpha} \bar{\rho}_{\alpha i}) = \nabla \cdot \theta_{\alpha} \mathbf{D}_{\alpha i}^* (\nabla \bar{\rho}_{\alpha i}) \quad (65)$$

Expansion of Equation (65) gives:

$$\frac{\bar{\rho}_{\alpha i}}{\theta_{\alpha}} \frac{\partial \theta_{\alpha}}{\partial t} + \frac{\partial \bar{\rho}_{\alpha i}}{\partial t} = \nabla \cdot (\mathbf{D}_{\alpha i}^* \nabla \bar{\rho}_{\alpha i}) + \frac{\mathbf{D}_{\alpha i}^*}{\theta_{\alpha}} (\nabla \bar{\rho}_{\alpha i}) (\nabla \theta_{\alpha}) \quad (66)$$

The first term of LHS of Equation (66) represents the accumulation of i species caused by the change of α saturation and the second term of RHS shows the effect of α phase saturation on the diffusion of i species.

When we assume that the partition of i species in air and in liquid reaches equilibrium at a certain saturation, say θ'_i (irreducible saturation), the contribution of fuel saturation on its vapor transport can then be neglected. Equation (66) is then reduced to the gas diffusion equation in porous media:

$$\frac{\partial \bar{\rho}_{\alpha i}}{\partial t} = \nabla \cdot \mathbf{D}_{\alpha i}^* (\nabla \bar{\rho}_{\alpha i}) \quad (67)$$

Substituting $\bar{\rho}_{\alpha i}$ with the normalized concentration of i, $C_i = \frac{\bar{\rho}_{\alpha i}}{\rho_{\alpha i}^o}$, where $\rho_{\alpha i}^o$ is the saturated concentration of i species in air, produces:

$$\frac{\partial C_i}{\partial t} = \nabla \cdot \mathbf{D}_{\alpha i}^* (\nabla C_i) \quad (68)$$

In cylindrical coordinates with axially symmetrical distribution, Equation (68) is written as:

$$\frac{\partial C_i}{\partial t} = \frac{\partial}{\partial r} (D_{\alpha i}^* \frac{\partial C_i}{\partial r}) + \frac{D_{\alpha i}^*}{r} \frac{\partial C_i}{\partial r} + \frac{\partial}{\partial z} (D_{\alpha i}^* \frac{\partial C_i}{\partial z}) \quad (69)$$

Equation (69) is identical to Equation (15) when $B=1$; $\Pi=D_{\alpha i}^*$; $S_{\alpha}=C_i$; and $\frac{dk_{r\alpha}}{dS_{\alpha}}=0$. Therefore, the numerical algorithm used in solving Equation (15) can also be used here.

V.9b Initial and Boundary Conditions

A. Initial conditions

The soil medium is initially clean and the initial conditions for the gas diffusion equation are simple:

$$C_i|_{t=0}(r,z) = C_i^0 = 0 \quad 0 \leq r \leq R; \quad 0 \leq z \leq Z \quad (70)$$

B. Boundary conditions

If no fuel vapor escapes from the chamber through the top cover and the impermeable wall and bottom liners zero flux boundary conditions can be applied as follows:

$$\begin{aligned} \frac{\partial C_i}{\partial r} = 0 & \quad r=0, \quad Z_c \leq z \leq Z \\ \frac{\partial C_i}{\partial r} = 0 & \quad r=R, \quad 0 \leq z \leq Z \end{aligned} \quad (71)$$

$$\begin{aligned} \frac{\partial C_i}{\partial z} = 0 & \quad z=0, \quad R_c \leq r \leq R \\ \frac{\partial C_i}{\partial z} = 0 & \quad z=Z, \quad 0 \leq r \leq R \end{aligned} \quad (72)$$

When we assume the existence of vapor-liquid equilibrium at certain liquid saturation near the wetting front, the boundary condition there is of the first-type with a constant saturated vapor concentration (Equation (73)). Due to the propagation of the wetting front the boundary is actually moving and the process is to be treated as a moving boundary problem. Fortunately the location of this moving boundary is not significantly affected by the gas diffusion process based on the assumption that mass transfer in the gas phase has negligible effect on the liquid movement. Unlike a normal moving boundary problem where the location of the boundary is determined by the solution of the differential equations, the boundary here is known prior to solving the diffusion equation.

$$C_i = C_i^s \quad z = Z_c, \quad r = R_c \quad (73)$$

Simultaneous gas diffusion and liquid infiltration require that the governing equations for both processes be solved together. However, the independence of liquid infiltration from the gas diffusion allows the liquid propagation profile to be obtained before the gas diffusion solved. The diffusion equation can, therefore, be solved anytime after the liquid infiltration profile is known.

V.9c *Diffusion Coefficient in Porous Media*

Molecules travel longer distances in a porous medium than in a bulk gas phase because of the tortuosity of the medium. Diffusion coefficients in porous media D_{ai}^* are therefore different from the molecular diffusivities used to describe diffusion processes in bulk gases. As reviewed by Weeks et al. (1982), Nielson et al. (1984),

and Bruell and Hoag (1986), several models concerning gas diffusion in porous media have introduced the concept of the effective diffusion coefficient, expressed as:

$$D_{ai}^* = D_{ai} \theta_\alpha \tau_\alpha \quad (74)$$

where D_{ai} is the molecular diffusion coefficient,
 τ_α is the tortuosity of the porous media.

Among many existing correlations predicting the tortuosity of the air-filled porous media (Roy and Griffin, 1987), Millington and Quirk's model (Millington, 1959; Millington and Quirk, 1961) is the most often cited (Shearer et al., 1973; Farmer et al., 1980; Sallam et al., 1984; Bruell and Hoag, 1986; Baehr, 1987; Sleep and Sykes, 1989; Shoemaker et al., 1990; Gierke et al., 1990; Jury et al., 1990). The model relates the tortuosity to the volumetric fraction of air and the porosity of the media via Equation (75):

$$\tau_\alpha = \frac{\theta_\alpha^3}{n^2} \quad (75)$$

The molecular diffusion coefficients of nonpolar organics in air can be calculated from the Wilke-Lee modification of the Hirschfelder-Bird-Spotz method:

$$D_{ai} = \frac{[4.336 - (0.0345 + M_A^{-1})^{0.5}] T^{1.5} (0.0345 + M_A^{-1})^{0.5}}{P(0.118 V_A^{0.33} + 0.371)^2 f(0.1025 T T_b^{-0.5})} \quad (76)$$

where M_A is the molecular weight [M/mol],
 T is the temperature [°K],
 P is the atmospheric pressure [M/L²/T²],

V_A is the molar volume [L^3/mol],

T_b is the boiling temperature [$^{\circ}K$],

f is the collision function.

The collision function f can be obtained from Treybal (1980).

V.10 Numerical Algorithm

The following numerical algorithm is developed to construct the Fortran code to solve the numerical model described in the previous sections:

1. Let $k=0$, $\ell=0$, and initialize $\underline{S}_j^k = S_0$;
2. Let $j=0$;
3. Let $(\underline{S}_j^{k+\frac{1}{2}})_o = \underline{S}_j^k$. Construct the coefficient matrix of Stage I of the ADI procedure, $\underline{P}(\underline{S}_j^{k+\frac{1}{2}})_o$, and solve Equation (56) for $\underline{S}_j^{k+\frac{1}{2}}$ with Picard iteration scheme;
4. Let $j=j+1$, go to Step 3 until $j=N$;
5. Check equalities (52) and (53). If the equalities are satisfied, let $\ell = \ell + 1$ and go to Step 2. Otherwise, continue;
6. Find the wetting front nodes ($z=Zc$ and $r=Rc$) where the vapor concentration is assumed as Equation (68). Solve the vapor diffusion problem for time step $k + \frac{1}{2}$ with the scheme similar to that used in solving the saturation profile.
7. Let $i=0$;
8. Let $(\underline{S}_i^{k+1})_o = \underline{S}_i^{k+\frac{1}{2}}$. Construct the coefficient matrix of Stage II of the ADI procedure, $\underline{P}(\underline{S}_i^{k+1})_o$, and solve \underline{S}_i^{k+1} with the Picard iteration scheme;
9. Let $i=i+1$, go to Step 3 until $i=M$;
10. Check equalities (52) and (53). If the equalities are satisfied, let $\ell = \ell + 1$ and go to Step 7. Otherwise, continue;
11. Find the wetting front nodes ($z=Zc$ and $r=Rc$) and solve the vapor diffusion problem for time step $k+1$;
12. Let $k=k+1$ and go to Step 2 until the final time is reached.

V.11 Parameter Estimation and The Complex Method of Box

The difficulty of predicting volatile hydrocarbon transportation in a porous medium not only arises from the mathematical complexity of the process but also from the great uncertainty of the physical parameters involved. As many as eight parameters may be required (McKee and Bumb, 1988) for soil characterization alone. Direct measurements of the parameters are often either expensive or experimentally difficult. Field measurement of the liquid saturation distribution reveals no direct information on the characteristics of the capillary pressure, nor does it provide the hydraulic conductivity and saturation relationships. Parameter estimation based on optimization techniques, however, may assist in fitting back those relationships from the measurements, which is often referred to as "inverse problem".

The complex method of Box (Box, 1965) is a sequential search technique effective in solving the optimization problem of nonlinear multivariable functions with inequality constraints. In our study, the complex method is applied in searching the maximum of the following objective function:

$$F(p_1, p_2, \dots, p_N) = \frac{1}{n} \sqrt{\sum_{i=1}^n (C_i^{sim}(p_1, p_2, \dots, p_N) - C_i^{obs})^2} \quad (77)$$

subject to

$$p_k^{\min} \leq p_k \leq p_k^{\max} \quad k=1, 2, \dots, N \quad (78)$$

where n is the number of observation points;

C_i^{obs} is the observed concentration at point i ;

$C_i^{sim}(p_1, p_2, \dots, p_N)$ is the simulated vapor concentration at point i ;

$p = [p_1, p_2, p_3, \dots, p_N]^T$ is the parameters to be estimated;

p_i^{\min} and p_i^{\max} are the boundaries of the parameter constraints.

Following the complex method, the procedure to minimize the objective function $F(p)$ is compiled as follows:

1. Construct an initial complex of $K \geq N + 1$ points randomly distributed within the given boundaries:

$$p_{ij} = p_i^{\min} + r_{ij}(p_i^{\max} - p_i^{\min}) \quad i=1,2,\dots,N \text{ and } j=1,2,\dots,K \quad (79)$$

where r_{ij} are random numbers between 0 and 1.

2. Evaluate the objective function at each point. The point having the lowest function value is rejected and replaced with a new point. The new point is selected at a location on the line from the rejected point to the centroid of the remaining points but at the other side of the centroid. The distance between the new point and the centroid is equal to α ($\alpha \geq 1$) times the distance between the rejected point and the centroid:

$$p_{ij}^{new} = \alpha (p_i^{cen} - p_{ij}^{old}) + p_i^{cen} \quad i=1,2,\dots,N \quad (80)$$

where the centroid of the remaining points is defined as:

$$p_i^{cen} = \frac{1}{k-1} \left[\sum_{j=1}^k p_{ij} - p_{ij}^{old} \right] \quad i=1,2,\dots,N \quad (81)$$

3. Check the new point against the constraints. If any constraint is violated, the point is moved a small distance δ inside the violated limit:

$$p_{ij}^{new} = p_i^{max} - \delta (p_i^{max} - p_i^{min}) \quad (82)$$

if p_{ij} is larger than p_i^{max} , or

$$p_{ij}^{new} = p_i^{min} + \delta (p_i^{max} - p_i^{min}) \quad (83)$$

if p_{ij} is smaller than p_i^{min} .

4. If the new point still generates the lowest function value, move it half way in towards the centroid:

$$p_{ij}^{(new)} = \frac{1}{2}(p_{ij}^{new} + p_i^{cen}) \quad (84)$$

5. Repeat the search until the objective function reaches the maximum within a tolerance ϵ or the number of iteration exceeds a given limit.

VI. RESULTS AND DISCUSSION

Fortran codes using the numerical algorithm described earlier were developed to solve the coupled liquid infiltration and vapor diffusion problems. Codes to estimate the parameters using the complex method of Box were also developed. The results obtained from the numerical simulation are described and discussed in the following sections. The codes were first tested using literature data for methodology and programming verification. Using the hypothetical data, generated with a given set of parameters, as observed data, the parameter optimization codes were applied to estimate the parameters within certain ranges. Experimental data from Test II and Test III were used to estimate the experimental parameters. The vapor concentration distribution and liquid front migration were then simulated using the estimated parameters and the results compared to the experimental observations.

VI.1 Model Verification

Before testing the model against literature or experimental data, convergence and stability of the numerical solution were first studied by using different temporal and spatial increments with different parameters such as liquid discharge rate, hydraulic property, porosity, liquid viscosity, etc. The simulations showed general capability of converging and fairly stable operation at relatively small temporal and spatial increments when the liquid discharge rate is within a normal range. When the liquid discharge rate becomes very low, the mass balance around the liquid entry zone may fail if the spatial increment is not also set very small. The codes failed to converge when very low permeability was used and became unstable for the case of

very high permeability.

A literature search found no experimental measurement of simultaneous liquid infiltration and vapor transportation with initial and boundary conditions generally similar to those of importance here. Three dimensional organic liquid infiltration data are also unavailable. Most experimental studies of liquid infiltration were conducted with water by soil physicists and geohydrologists.

To test the model against literature data, experimental measurements described by Clothier and Scotter (1982) were selected. The liquid wetting front was measured in a 200 mm by 200 mm by 300 mm sand box infiltrated with water at a volumetric flux of $0.9 \times 10^{-4} \text{ m}^3/\text{h}$ from the upper corner of the box. A cavity of approximate 4 mm in radius filled with water was thus formed following the infiltration and maintained during the experiment. Based on the experimental data and the parameters recommended by Healy and Warrick (1988), simulation of water infiltration was conducted to describe the saturation distribution at times of 0.17, 1.00, 2.75, and 6.00 hours. The parameters used in the simulation are summarized in Table 5.

During the simulation, a cubic function (Equation 31) was used for relative permeability versus water saturation relationship. The simulation results were plotted as saturation distribution contour maps in Figures 34 to 37.

Since Clothier and Scotter's observation only provides the time-stamped location of the liquid wetting front, comparison of the simulated results to their data requires the determination of the wetting front from the simulated liquid saturation profile. Defining the wetting front from a three dimensional saturation profile is, however, arguable and rather arbitrary (Clothier and Scotter, 1982; Healy and Warrick, 1988; Lafolie et al., 1989a). Clothier and Scotter used a saturation value of 0.15 to

Table 5. Simulation Parameters for Clothier and Scotter's data

Parameters	Value
Liquid application rate (m ³ /sec)	1.0×10 ⁻⁷
Liquid density (kg/m ³)	1000.0
Liquid viscosity (kg/m/sec)	1.0×10 ⁻³
Initial saturation	0.06
Irreducible saturation	0.05
Maximum attainable saturation	0.95
Porosity	0.47
Intrinsic permeability (m ²)	1.1336×10 ⁻¹¹
α factor of van Genuchten's formula (1/m)	2.80
n factor of van Genuchten's formula	3.55
Numerical spatial increment dh (m)	0.01
Numerical time increment dt (sec)	120
Total nodal points in r direction	20
Total nodal points in z direction	30
Simulation time (hrs)	0.17, 1.00, 2.75, 6.00

define the wetting front based on the argument that this value is where a pronounced color change was observed in another experiment (Bruce and Klute, 1956). The saturation contour lines of $S=0.15$ at the four observation times predicted by our model were plotted in Figure 38 together with the experimental results as well as the results by others (Ben-Asher et al., 1986; Healy and Warrick, 1988).

Figure 38 shows an excellent agreement of the current model prediction and the experimental measurement at the times equal to 1.00, 2.75, and 6.00 hours. The predictions by others were poor and failed to demonstrate the gravitational effects at these time steps. At 0.17 hour, our model predicted a more advanced wetting front than the measurement. The error might be caused by using a relatively larger spatial increment during the simulation, recalling that the experiment was conducted with a cavity of only about 4 mm in radius which is smaller than the size of our basic cell. In our model the liquid entry zone takes at least one cell which may produce a higher

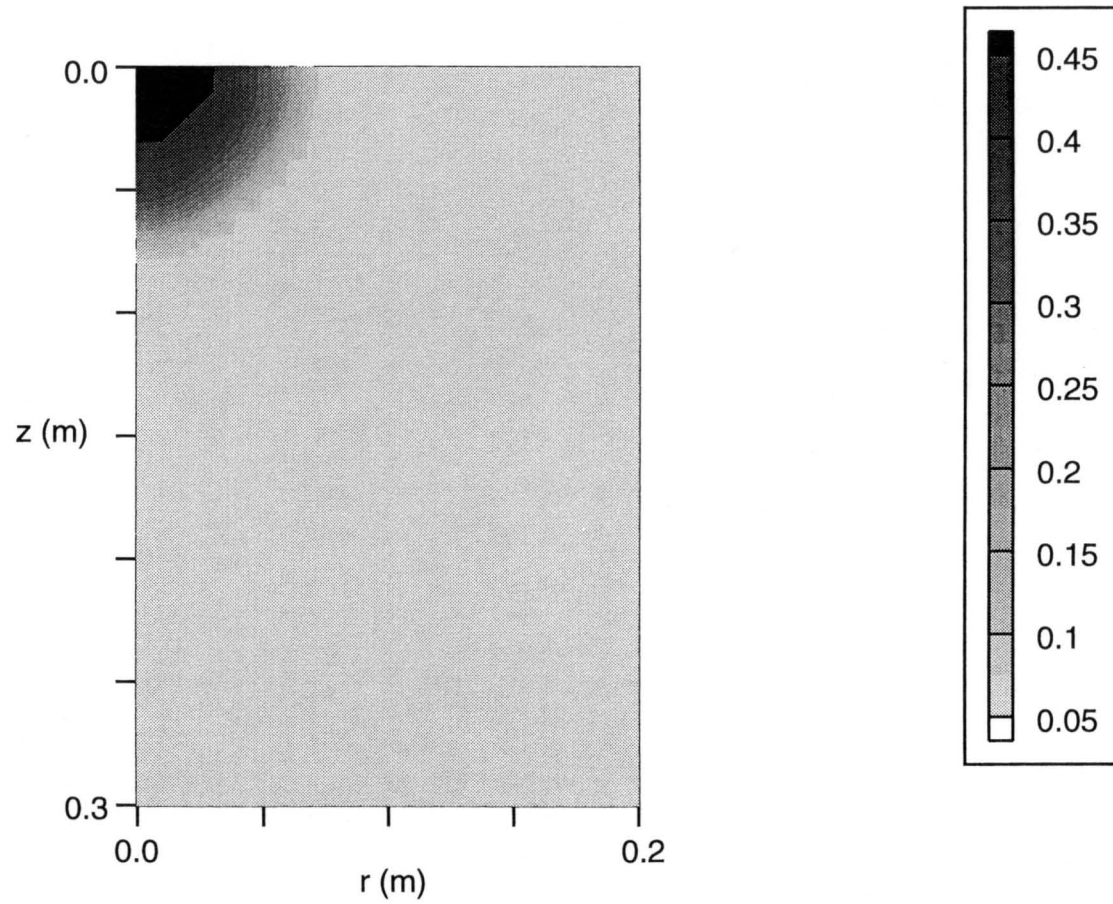


Figure 34. Predicted water content distribution at $t=0.17$ hr.

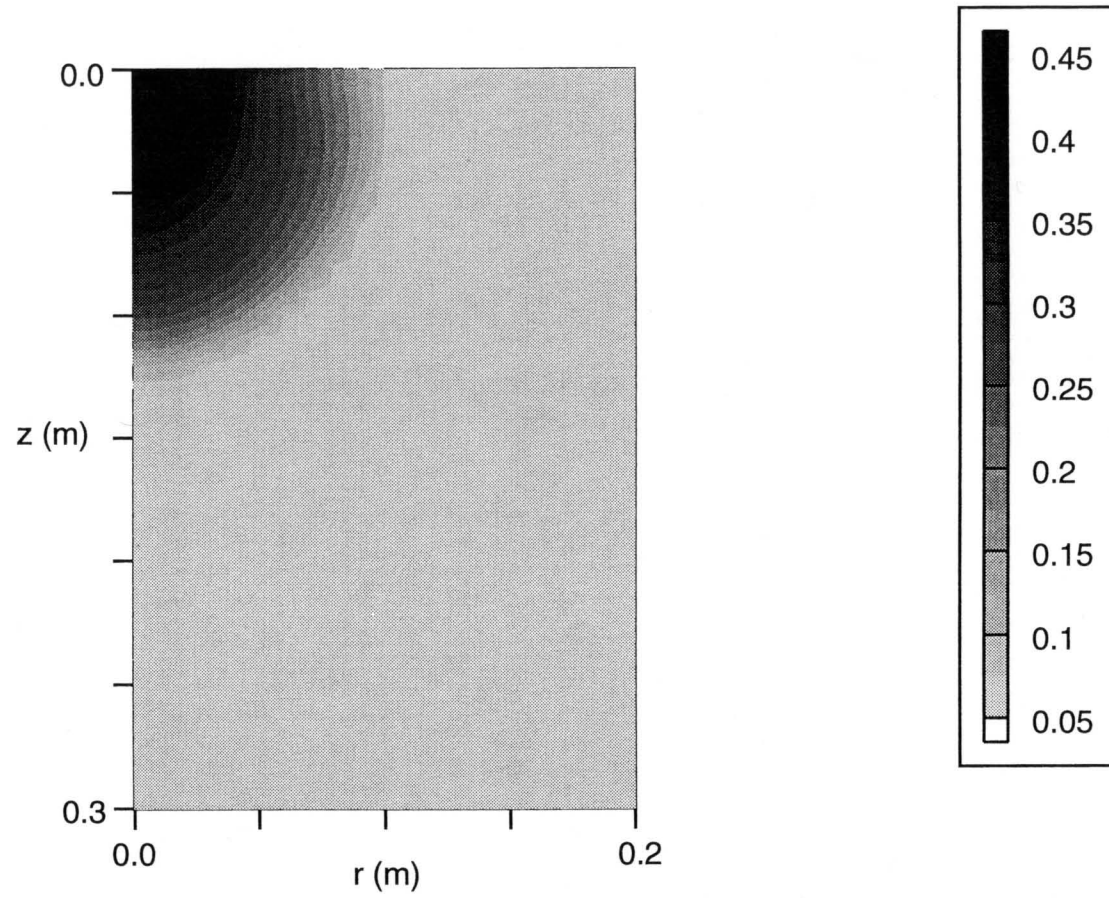


Figure 35. Predicted water content distribution at $t=1.00$ hr.

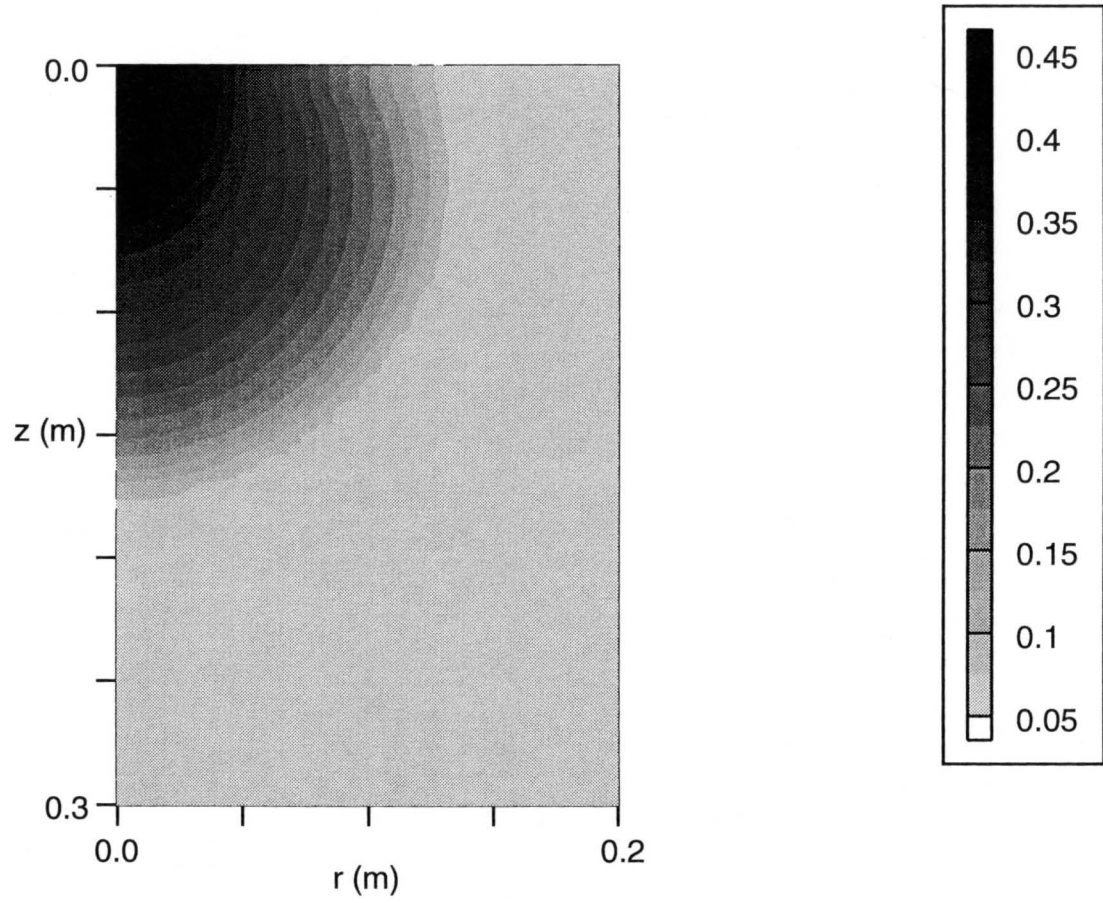


Figure 36. Predicted water content distribution at $t=2.75$ hr.

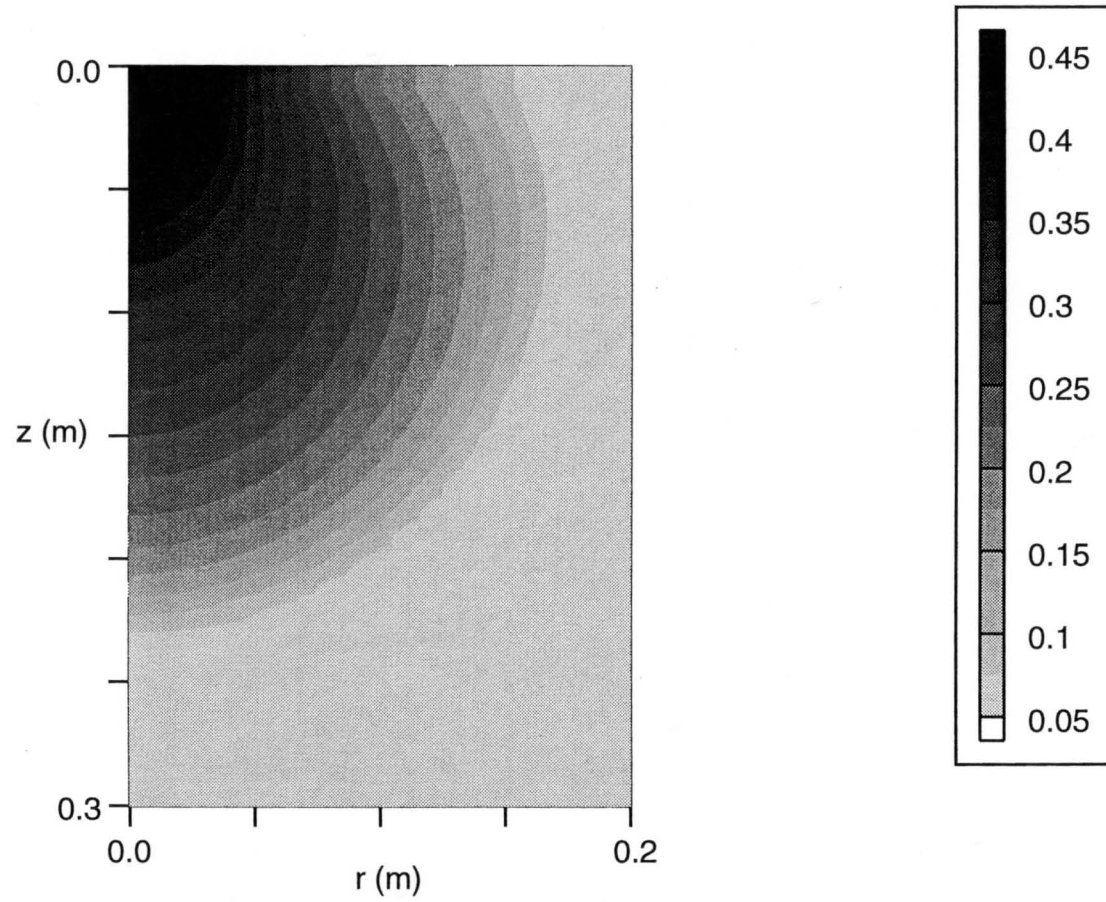


Figure 37. Predicted water content distribution at $t=6.00$ hr.

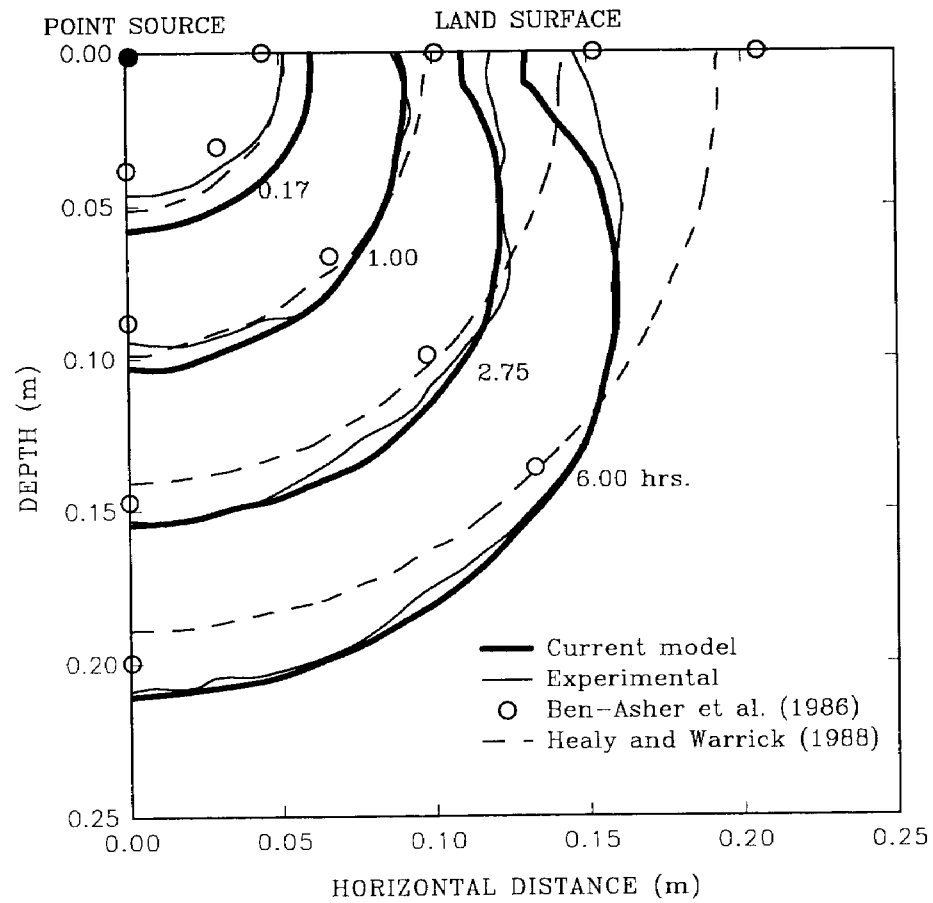


Figure 38. Comparison of predicted water wetting fronts to the experimental observations and the predictions by others

than actual simulated infiltration rate at an early stage.

In our simulation, the soil medium is assumed to be homogeneous and the longitudinal and transverse permeabilities to have the same values. No matter how carefully the sand was packed during the experiment, higher longitudinal permeability is always expected, which could result in a faster horizontal spreading than that in a perfect homogeneous medium. This might be the reason for the difference between our prediction and the measurement near the land surface.

Other than the errors near the land surface and at the early stage of infiltration, the simulation demonstrates that our model is capable of predicting liquid infiltration from a point source with accuracy. The comparison to the experimental data also validates our treatment of the boundary condition along the liquid entry zone. The prediction shows the gravitational and the capillary movements of liquid described by the current model to be accurate.

VI.2 Parameters Estimated With the Complex Method

Among the parameters involved in the current model, some are easily defined from material properties, while others are more interactive. For the parameters whose values depend only on the properties of either the porous material or the liquid, laboratory measurement is usually inexpensive and produces satisfactory results. In this study the measurements made on the total porosity of the top soil and sand media, and the density and viscosity of diesel and JP-5 fuels are considered as reliable and directly used in the simulation.

The interactive parameters, such as the α and n factor of van Genuchten's equation (Equation 29) and the λ of Equation 30 defining the functional relationships

of capillary pressure and relative permeability versus saturation, as well as the virtual diffusivity of organic vapor in porous media, are more difficult and expensive to measure. The literature review revealed no reliable estimates for these parameters for a similar materials measured or for similar hydrodynamic conditions; therefore, we decided to use the parameter estimation technique to identify them based on the experimentally observed vapor concentration profile. Accordingly we selected the following five parameters to be estimated with the Complex method: the α and n factors of Equation 29, the λ factor of Equation 30, the virtual vapor diffusivity in porous media, D , and the intrinsic permeability, k .

As discussed earlier, the capillary pressure dependence on liquid saturation has been studied extensively and both the tabular field experimental data and empirical closed form relations intended to represent them have been used in the mathematical prediction of unsaturated liquid flow in soil. The selection of van Genuchten's equation in this study is arbitrary, made with no intention to minimize the value of other models, such as the one by Brooks and Corey (1964). The parameters α and n of van Genuchten's equation are the "curve fitting" parameters which vary over a relatively wide range depending on the soil type (Table 6).

Table 6. Estimated Values of α And n For Selected Soils
(van Genuchten, 1980)

Soil name	α (m^{-1})	n
Hygiene sandstone	0.79	10.4
Touchet Silt Loam	0.50	7.09
Silt Loam	0.423	2.06
Guelph Loam (drying)	1.15	2.03
Guelph Loam (wetting)	2.00	2.76
Beit Netofa Clay	0.152	1.17

The relative permeability versus the saturation relationship is another uncertain property interactively characterized by both the porous medium and the liquid flowing through it. Many functional relationships have been previously proposed. The cubic function (Equation 31) cannot be generalized to many different systems. The function proposed by Brooks and Corey (Equation 30) was used in our simulations of the experiments with the parameter λ being identified by the parameter estimation technique.

The magnitude of the gas diffusivity in a porous medium is less than in air due to the tortuous pathway through which the gas molecules must travel. Estimating gas diffusivity in porous media has been a challenging topic for many researchers from both fields of soil mechanics and chemical catalysis. Different measurements have been conducted and models developed (Penman, 1940; Marshall, 1959; Millington, 1959; Jackson, 1964; Grismer et al., 1986; Grismer, 1988; Bruckler et al., 1989; etc.). The selection of a suitable model to describe the diffusivities of diesel and JP-5 fuels in the soil media of this study can lead to a long debate about the credibility of those models. Parameter estimation applied to gas diffusivity in soil not only avoids such debates but also indirectly incorporates the retardation effect into the simulation which was neglected during the model development.

The wide range in observed values of the saturated hydraulic conductivity of soil media is well recognized and admitted by all hydrologists (Table 7). Theoretically, the saturated hydraulic conductivity is related to the intrinsic permeability through Equation 12 and the intrinsic permeability solely depends on the porous medium. The intrinsic permeability of a soil can, therefore, be determined from the measurement of the saturated hydraulic conductivity. Previous research,

however, has found that the intrinsic permeability of a soil measured with water can be different from that measured with organic chemicals (Brown and Anderson, 1980). Intrinsic permeability k was also selected to be identified through parameter estimation and the results to be compared with the ones calculated from the hydraulic conductivity measurements.

Table 7. Typical Values of Hydraulic Conductivity and Permeability
(From Bear, 1972, pp.136)

	-2	-1	0	1	2	3	4	5	6	7	8	9	10	11
Permeability	Pervious			Semipervious						Impervious				
Aquifer	Good				Poor					None				
Soils	Clean Gravel		Clean sand, or sand and gravel			Very fine sand, silt, loess, loam, solonetz								
					Peat		Stratified clay			Unweathered clay				
Rocks					Oil rocks			Sandstone		Good limestone, dolomite		Breccia, granite		
$-\log_{10}K(\text{cm/s})$	3	4	5	6	7	8	9	10	11	12	13	14	15	16
$\log_{10}k(\text{md})$	8	7	6	5	4	3	2	1	0	-1	-2	-3	-4	-5

VI.3 Objective Function

The inverse problem of fluid flow and transport in porous media is often ill-posed because of the nonuniqueness and instability of the identified parameters (Yeh, 1986). It has been found that when the identified parameters are constant rather than distributed, there are generally more observations than unknowns and the inverse problem is thus generally unique (Chavent, 1974). The instability of the inverse solution appears when small errors in the observations tend to cause significant errors in the identified parameters. Proper construction of an objective function is vital to reduce the ill-posedness caused by the instability of the inverse solution.

In the previous section, we have defined the objective function as the sum of the squares of the difference between the observed and the model-predicted vapor concentrations. To study the stability of the inverse problem with this objective function, numerical experiments were conducted with a set of hypothetical data generated with a given set of parameters. The objective function was then calculated and plotted against each parameter while keeping the others at their "true" values (Figures 39-41). It was found that the first derivative of the objective function discontinued at certain points which caused the search to be unstable. Further investigation indicated that the instability was mainly caused by the model assumption that the vapor concentration is equal to a constant equilibrium value when the liquid saturation reaches a specific level. At the points where the first derivative of the objective function became unstable, one or more model-predicted vapor concentrations were actually calculated according to the assumption other than the diffusion equation.

Although the Box method does not require the continuity of the first derivative of the objective function, we have found that the search became extremely slow and sometime even collapsed when the abrupt changes in the objective function were frequently encountered. To eliminate the instability caused by the model assumption, the model predicted vapor concentration values were screened when calculating the objective function and those determined by the equilibrium assumption were discarded. The objective function thus only accounts for the observations and model predictions whose vapor concentration values are determined by the diffusion equation. Our further numerical experiments showed that such treatment produced a smoother objective function whose first derivatives to the searched parameters were continuous (Figures 42-44) and, therefore, greatly improved the convergence of the search.

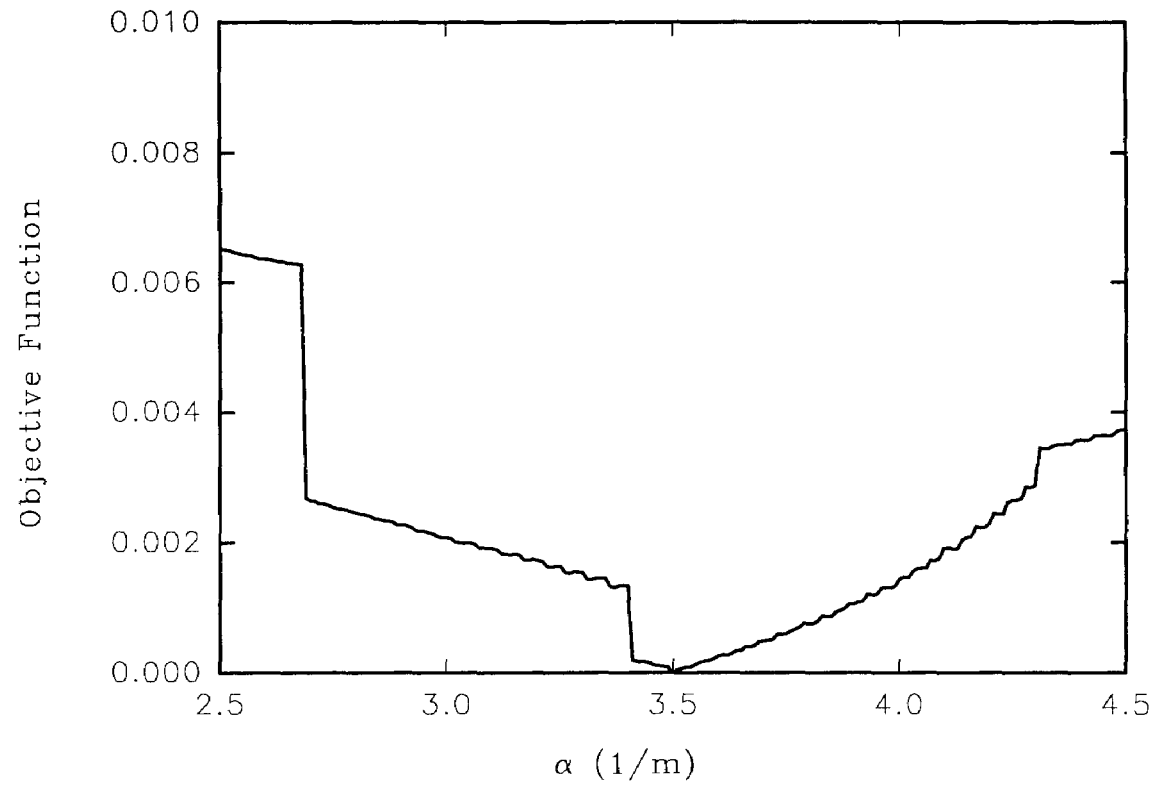


Figure 39. The objective function constructed with unscreened vapor concentration observations changes with α factor

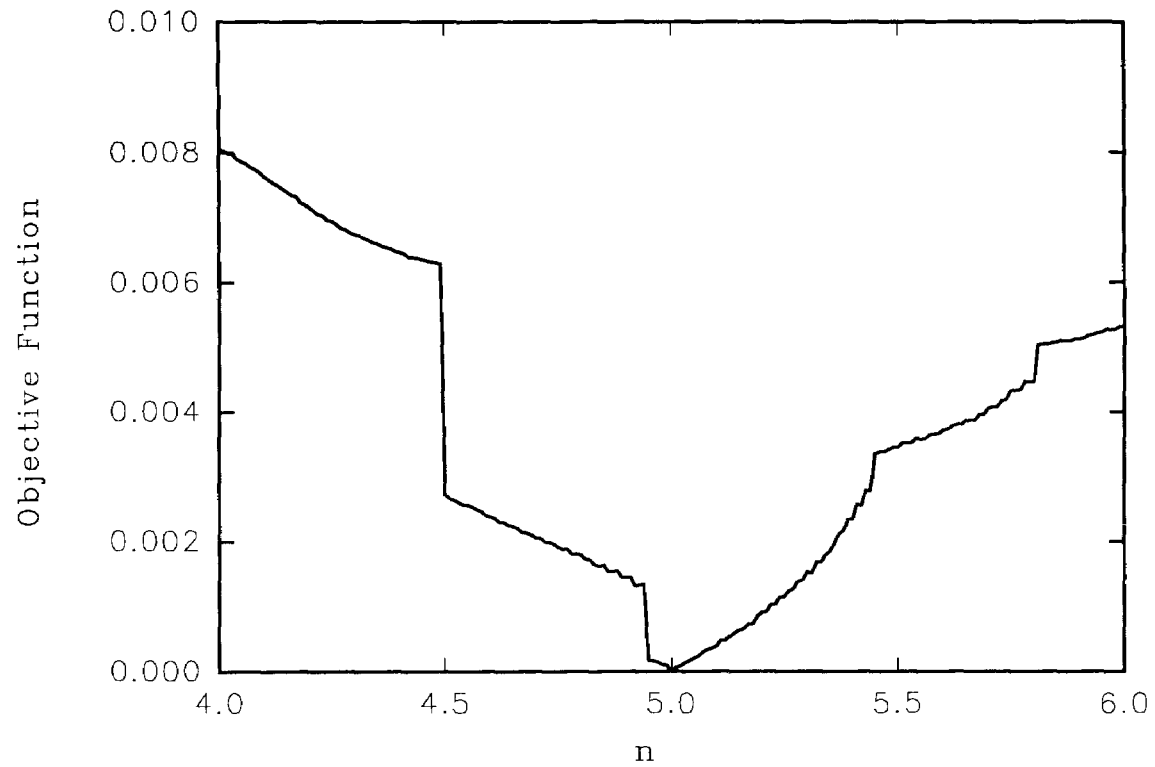


Figure 40. The objective function constructed with unscreened vapor concentration observations changes with n factor

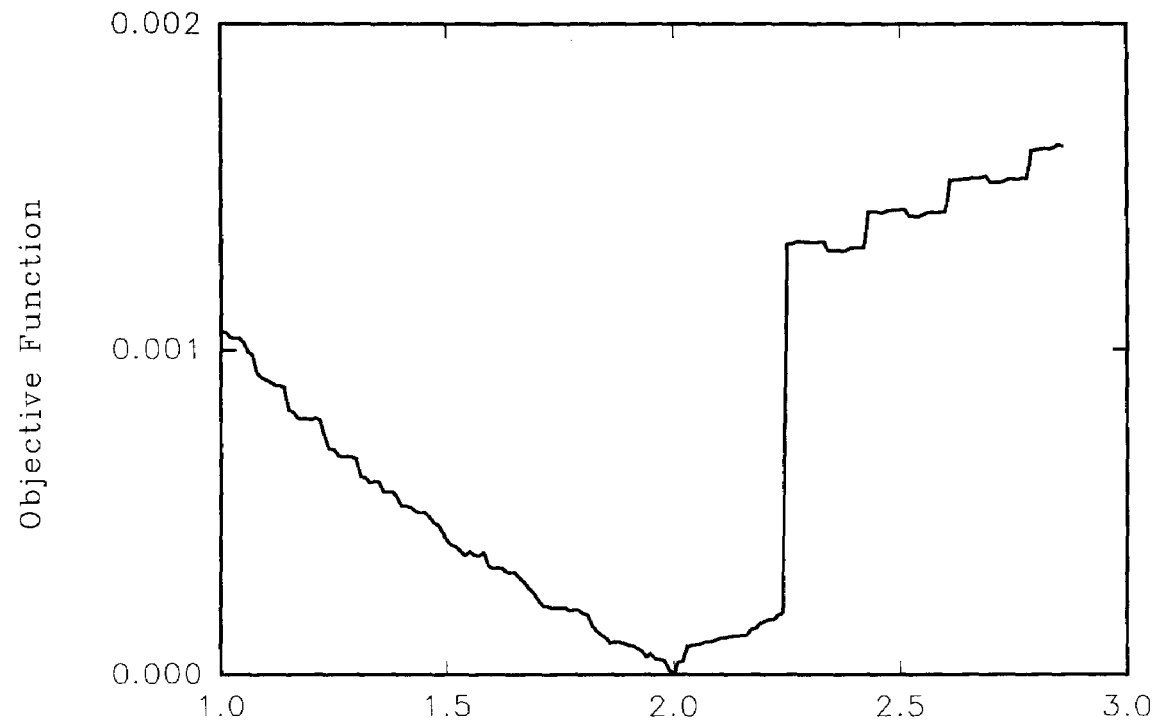


Figure 41. The objective function constructed with unscreened vapor concentration observations changes with factor

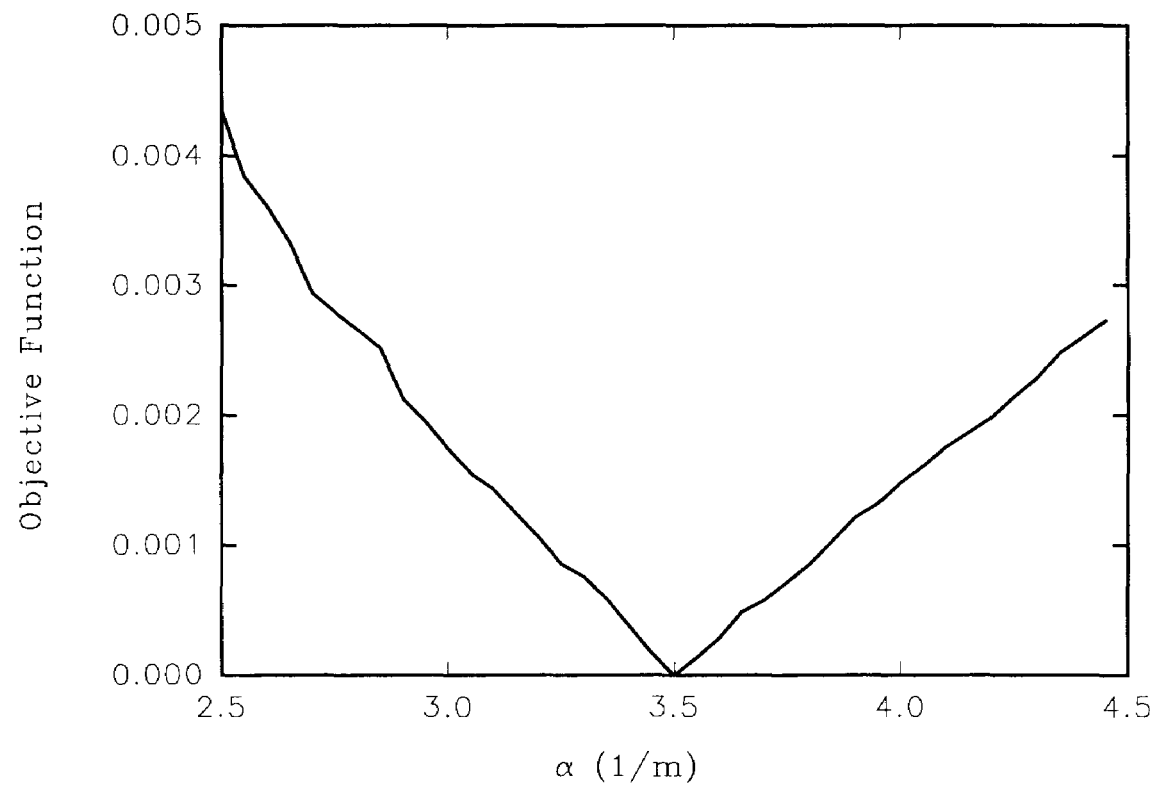


Figure 42. The objective function constructed with screened vapor concentration observations changes with α factor

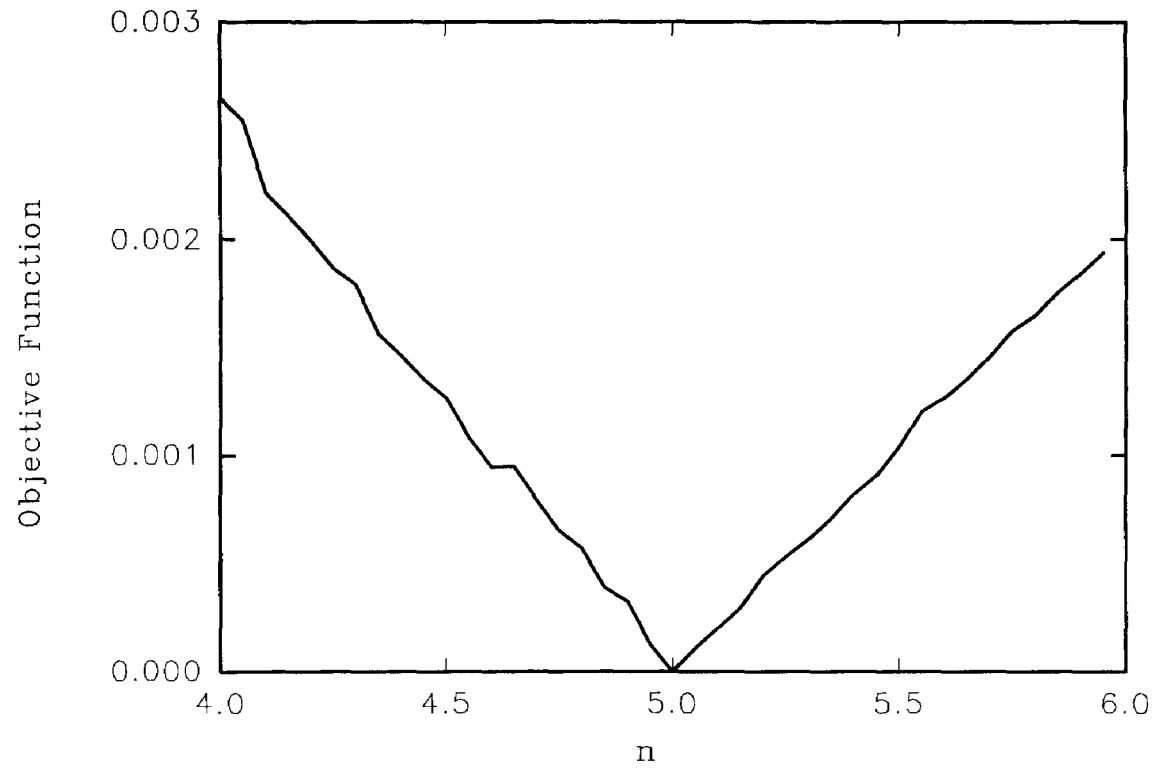


Figure 43. The objective function constructed with screened vapor concentration observations changes with n factor

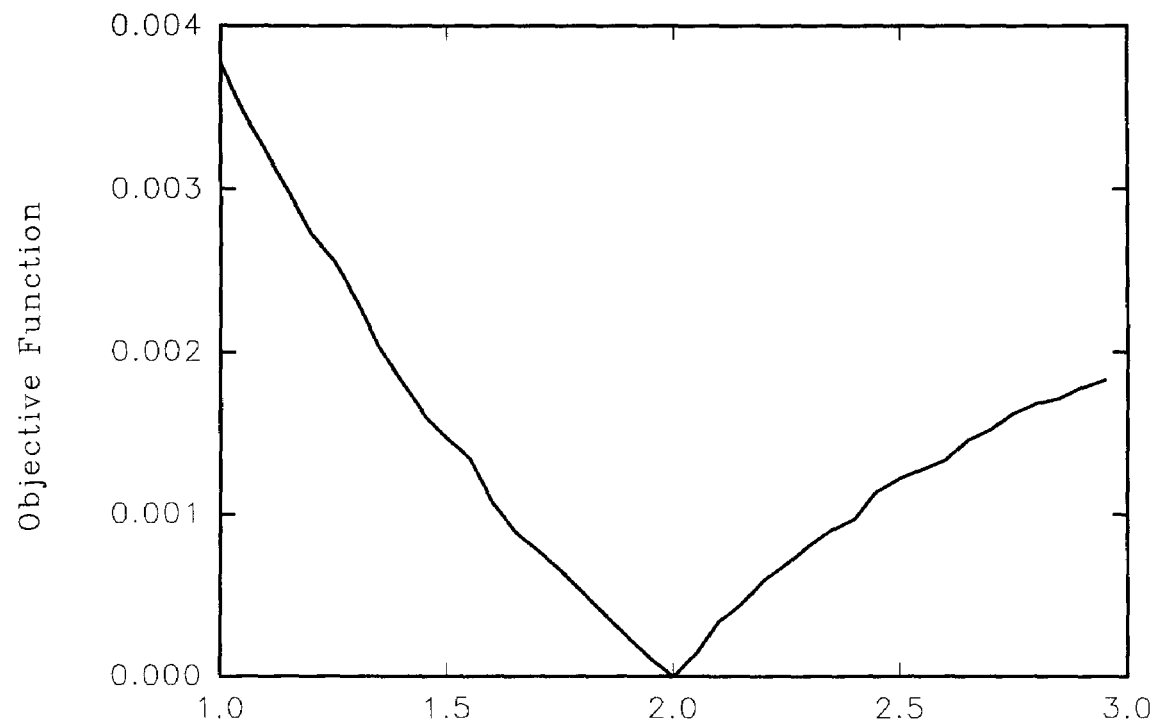


Figure 44. The objective function constructed with screened vapor concentration observations changes with factor

VI.4 Parameter Estimation Using Hypothetical Data

To verify the applicability of the complex method of Box in the current model in optimizing the parameters discussed earlier, a set of hypothetical data were first generated using the liquid infiltration and vapor diffusion model with the known set of parameters listed in Table 8. Vapor concentration profiles were generated at the times of 0.5, 1.0 and 2.0 hours. Thirty five (35) spatial nodes were selected and the vapor concentration at these nodes at the three time intervals (Table 9) were used as the "observation" values for the objective function of the parameter estimation model.

Table 8. Simulation parameters used to generate the hypothetical data

Parameters	Value
Liquid application rate (m ³ /sec)	2.0×10 ⁻⁷
Liquid density (kg/m ³)	1000.0
Liquid viscosity (kg/m/sec)	1.0×10 ⁻³
Initial saturation	0.06
Irreducible saturation	0.05
Maximum attainable saturation	0.95
Normalized equilibrium vapor concentration	0.90
Porosity	0.38
Intrinsic permeability (m ²)	2.947×10 ⁻¹¹
α factor of van Genuchten's formula (1/m)	3.50
n factor of van Genuchten's formula	5.00
λ factor of Equation 30	2.00
Numerical spatial increment dh (m)	0.03
Numerical time increment dt (sec)	90
Total nodal points in r direction	8
Total nodal points in z direction	12
Simulation time (hrs)	0.5, 2.0, 4.0

Table 9. Hypothetical "observation" data

r (m)	z (m)	Hypothetical vapor concentration			Perturbed vapor concentration		
		t=0.5	t=2.0	t=4.0	t=0.5	t=2.0	t=4.0
0.00	0.00	0.90000	0.90000	0.90000	0.87526	0.90000	0.87289
	0.06	0.90000	0.90000	0.90000	0.86866	0.87277	0.90000
	0.12	0.41768	0.90000	0.90000	0.43506	0.87230	0.85601
	0.18	0.04637	0.90000	0.90000	0.04804	0.89296	0.90000
	0.24	0.00300	0.24917	0.90000	0.00300	0.24307	0.90000
	0.30	0.00013	0.05965	0.38749	0.00013	0.05957	0.37717
	0.36	0.00003	0.03433	0.29169	0.00003	0.03450	0.30228
0.06	0.00	0.90000	0.90000	0.90000	0.90000	0.87248	0.90000
	0.06	0.90000	0.90000	0.90000	0.90000	0.90000	0.90000
	0.12	0.26708	0.90000	0.90000	0.26141	0.88274	0.86005
	0.18	0.02754	0.61577	0.90000	0.02683	0.60508	0.85841
	0.24	0.00186	0.19065	0.68353	0.00186	0.18354	0.70785
	0.30	0.00009	0.04975	0.33370	0.00009	0.05114	0.33110
	0.36	0.00002	0.02925	0.26137	0.00002	0.02891	0.26914
0.12	0.00	0.27863	0.90000	0.90000	0.28269	0.88303	0.89701
	0.06	0.18902	0.90000	0.90000	0.18740	0.90000	0.88807
	0.12	0.04655	0.63056	0.90000	0.04628	0.64186	0.87288
	0.18	0.00572	0.28507	0.72571	0.00544	0.27161	0.74437
	0.24	0.00042	0.09880	0.43091	0.00044	0.09551	0.41215
	0.30	0.00002	0.02912	0.23965	0.00002	0.03023	0.22837
	0.36	0.00000	0.01783	0.19755	0.00000	0.01726	0.20295
0.18	0.00	0.01699	0.28676	0.72332	0.01656	0.28949	0.75088
	0.06	0.01392	0.29359	0.72675	0.01335	0.28348	0.71008
	0.12	0.00415	0.22722	0.67575	0.00402	0.22732	0.68852
	0.18	0.00058	0.11543	0.47504	0.00056	0.11701	0.49514
	0.24	0.00005	0.04427	0.29068	0.00005	0.04350	0.30335
	0.30	0.00000	0.01441	0.17435	0.00000	0.01393	0.17032
	0.36	0.00000	0.00918	0.14817	0.00000	0.00915	0.14086
0.24	0.00	0.00000	0.17290	0.61838	0.00000	0.17046	0.62721
	0.06	0.00000	0.16977	0.61185	0.00000	0.16977	0.63692
	0.12	0.00003	0.13141	0.54042	0.00003	0.12930	0.51693
	0.18	0.00002	0.07182	0.39670	0.00002	0.07487	0.41618
	0.24	0.00000	0.02939	0.24984	0.00000	0.03020	0.25054
	0.30	0.00000	0.01010	0.15432	0.00000	0.01033	0.15022
	0.36	0.00000	0.00658	0.13259	0.00000	0.00648	0.13285

The parameter estimation technique was used to estimate the parameters describing the physical properties of the soil, the liquid and the vapor for the hypothetical data set. The number of parameters to be estimated, N , is 5 in our study, as discussed earlier. The number of vertices in the complex, K , is arbitrary as long as it is set larger than or equal to $N+1$. However it has been found that with $K=N+1$ the search is very likely to collapse into a subspace where it tends to flatten itself against the first constraint encountered and thus stop when a corner is reached (Box, 1965). Subspace collapse was also occasionally observed in this study even with K set to be 7 or 8. Increasing the number of vertices of the complex will reduce the chance of subspace collapse; however, the trade-off is the increased computational cost because of the increasing number of iterations needed to converge. In our study we selected $K=2\times N$ after a number of trials with different K 's. We adopted the reflection factor $\alpha=1.3$ recommended by Box.

Another problem experienced during the parameter search is local optima. Although the complex method is more robust than many other methods in the way that it provides higher probability of jumping across a local optimum, it is not perfect and can also land on a local optimum depending on the characteristic of the objective function. Unfortunately, none of the current optimization methods can avoid local optima. A larger number of vertices in the complex may increase the chance of jumping over a local optimum but also increases computation time.

To assure the optimization to be global or near global, we ran the optimization program at least eight times for each problem with differently selected random starting locations, controlled by a random number generator index R (Table 10). Results from all runs were examined no matter if the search had satisfied the converging criteria,

Table 10. Input Values for The Parameter Estimation Model
Simulating the Hypothetical Data

Input Items	Values
Number of parameters N	5
Number of vertices of the complex K	10
Reflection factor α	1.3
Number of "observation" point	108
Constraints:	
Intrinsic permeability (m^2)	2.3×10^{-14} - 2.3×10^{-12}
van Genuchten α factor (1/m)	2.4 - 4.6
van Genuchten n factor	3.9 - 6.1
λ of Equation 30	1.4 - 3.5
Vapor diffusivity (m^2/s)	1.0×10^{-8} - 1.0×10^{-5}
Random number generator	5

or it had reached a local optimum, or it had collapsed into a subspace. The one which produces the minimum objective function value was selected and a "global" optimization was assumed.

It must be noted that the use of the random number generator index is purely arbitrary, because the computer used in this study generates a series of sequential "pseudo-random" numbers as most computers do. Different R's seed the computer to provide different random numbers. If a computer generated truly random numbers, there would be no need for the index R.

The parameter search using the hypothetical data within the constraints listed in Table 10 was conducted and the one with R=5 was selected as the search results. A total of 254 iterations were made during the search and the objective function converged from the initial worst value of 1.76×10^{-2} to the final minimum of 7.0×10^{-5} (Figure 45).

The parameter values of each vertex are plotted in Figure 46 to 50. It can be seen from these figures that for all parameters the initial wide range of distribution was

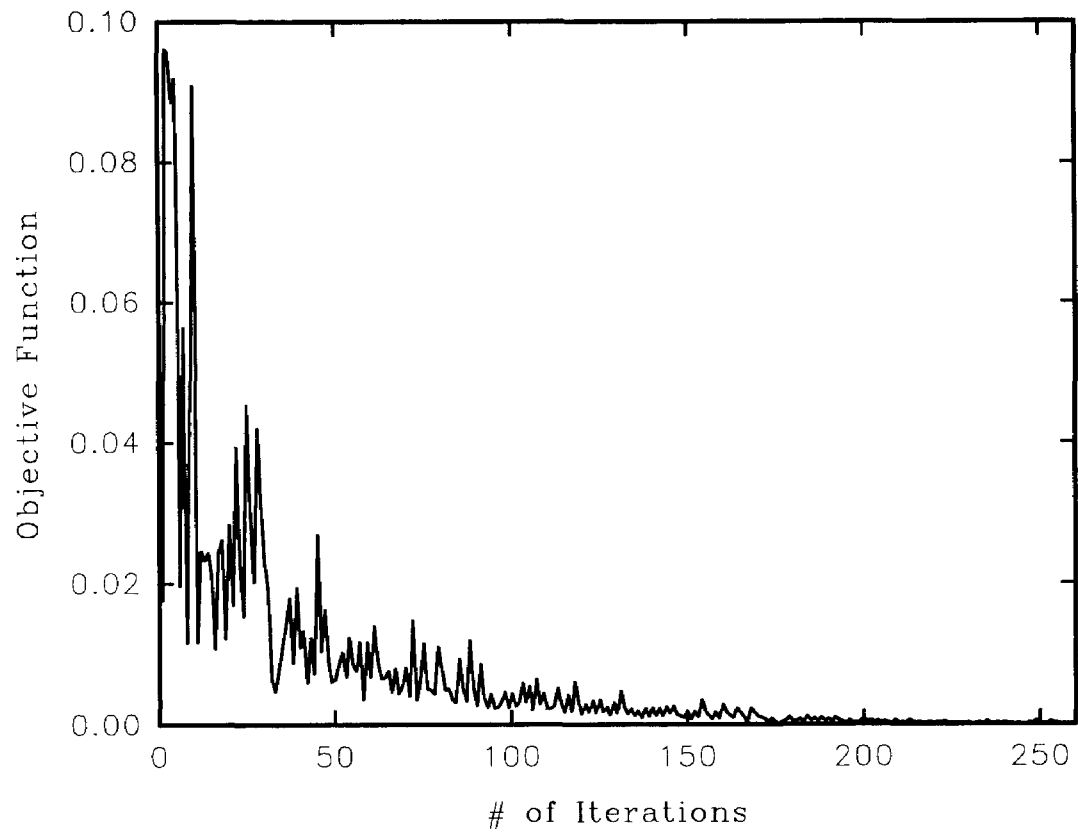


Figure 45. The convergence of the objective function

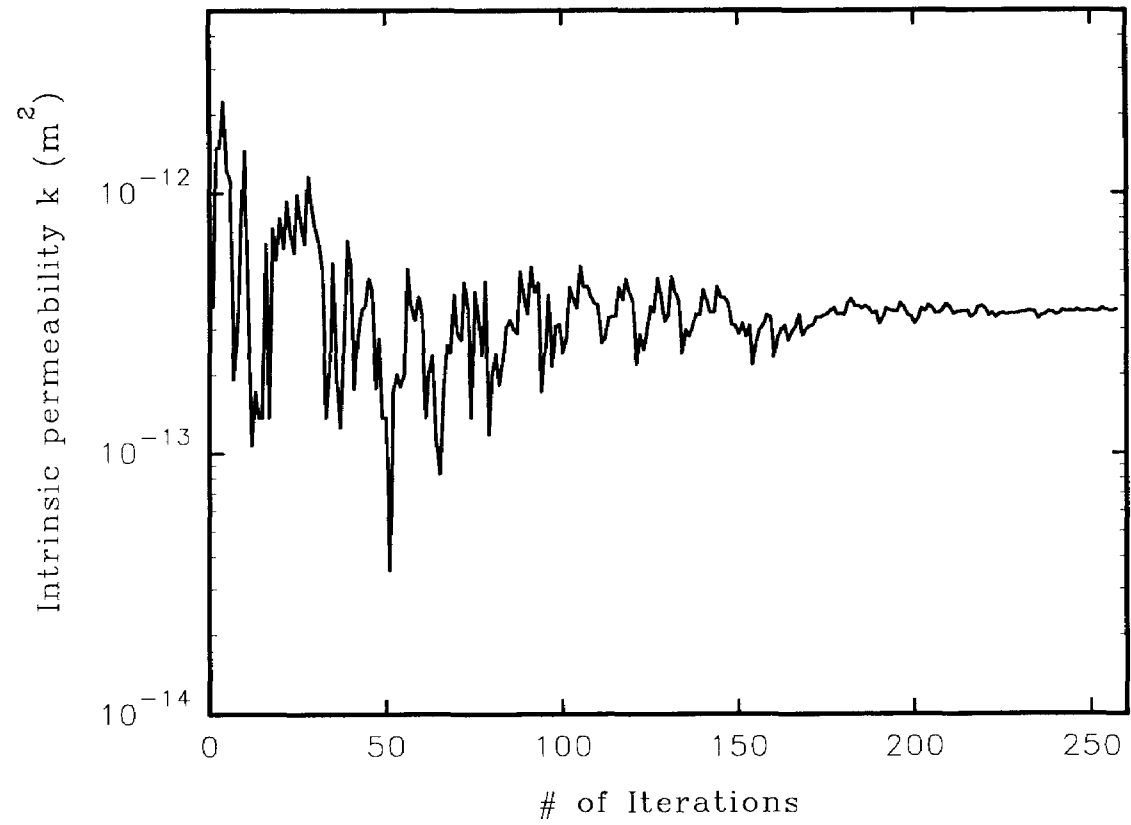


Figure 46. Intrinsic permeability values searched by the parameter estimation technique

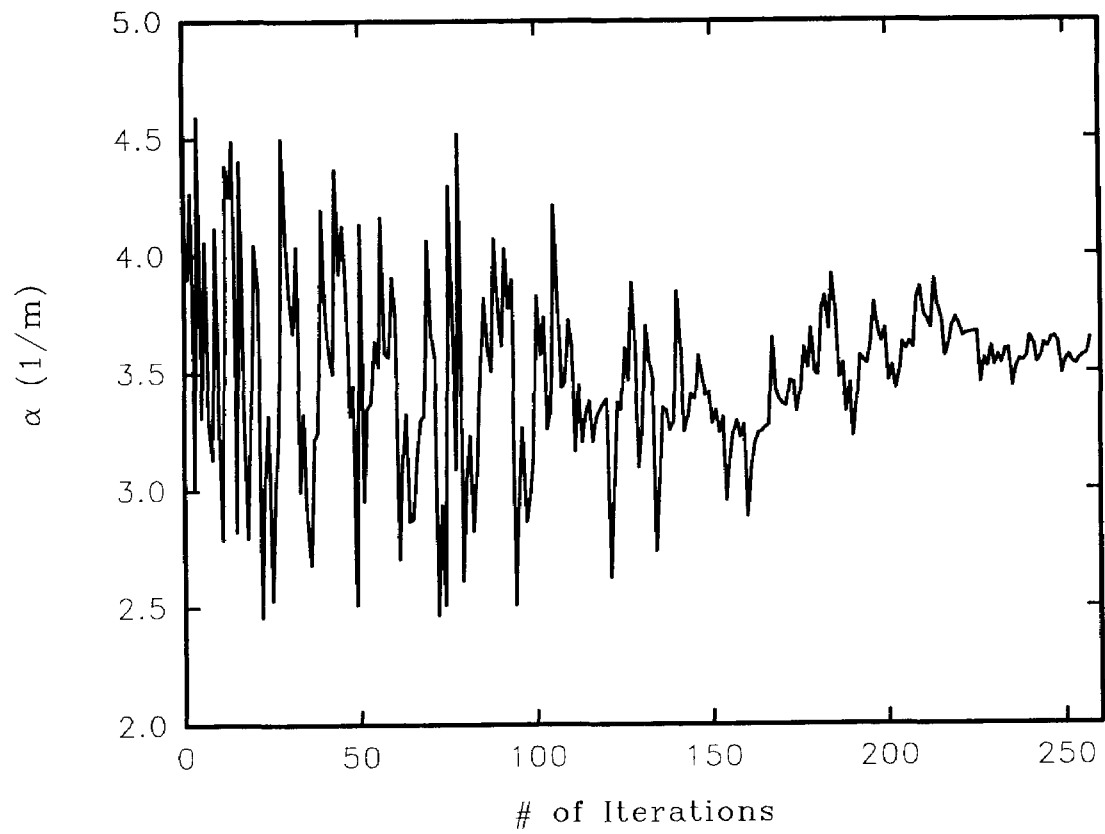


Figure 47. van Genuchten's α values searched by the parameter estimation technique

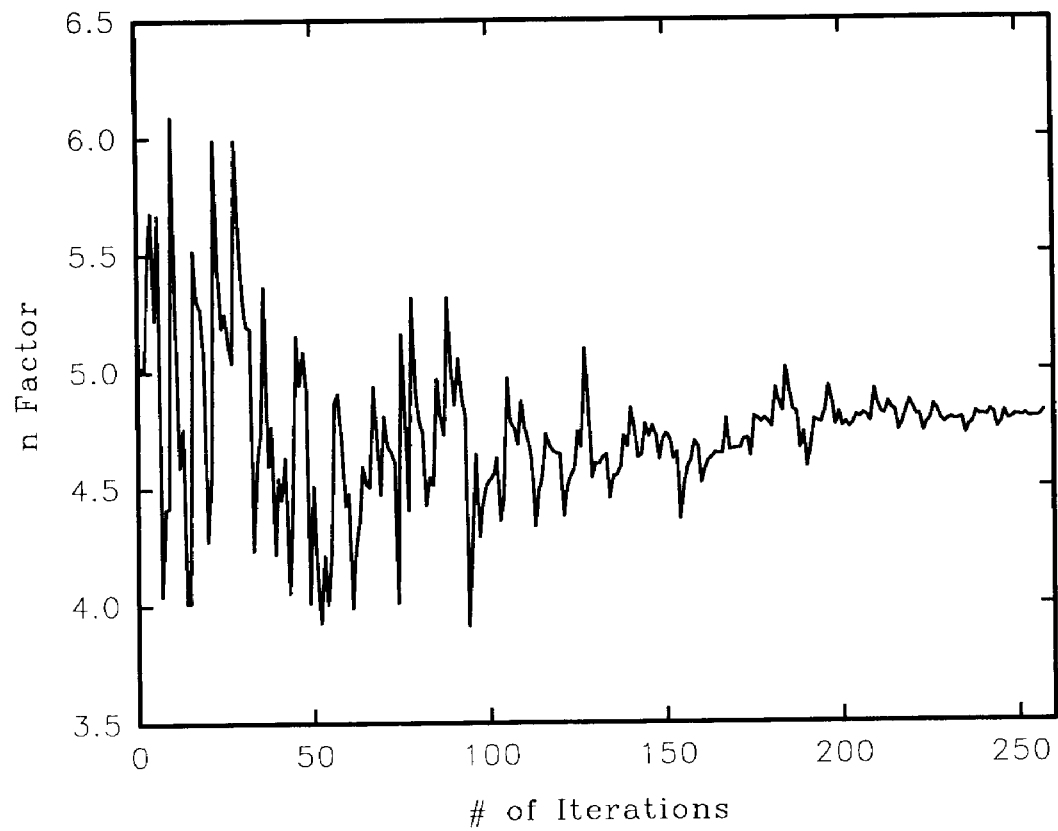


Figure 48. van Genuchten's n values searched by the parameter estimation technique

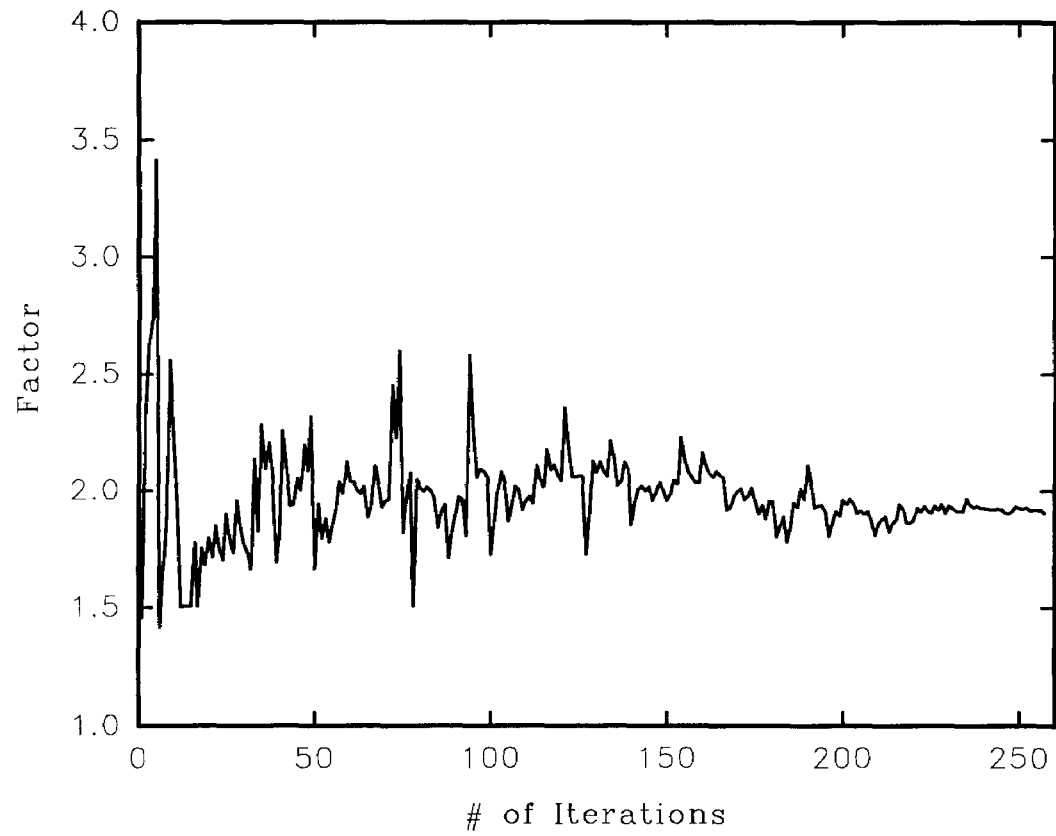


Figure 49. factor values searched by the parameter estimation technique

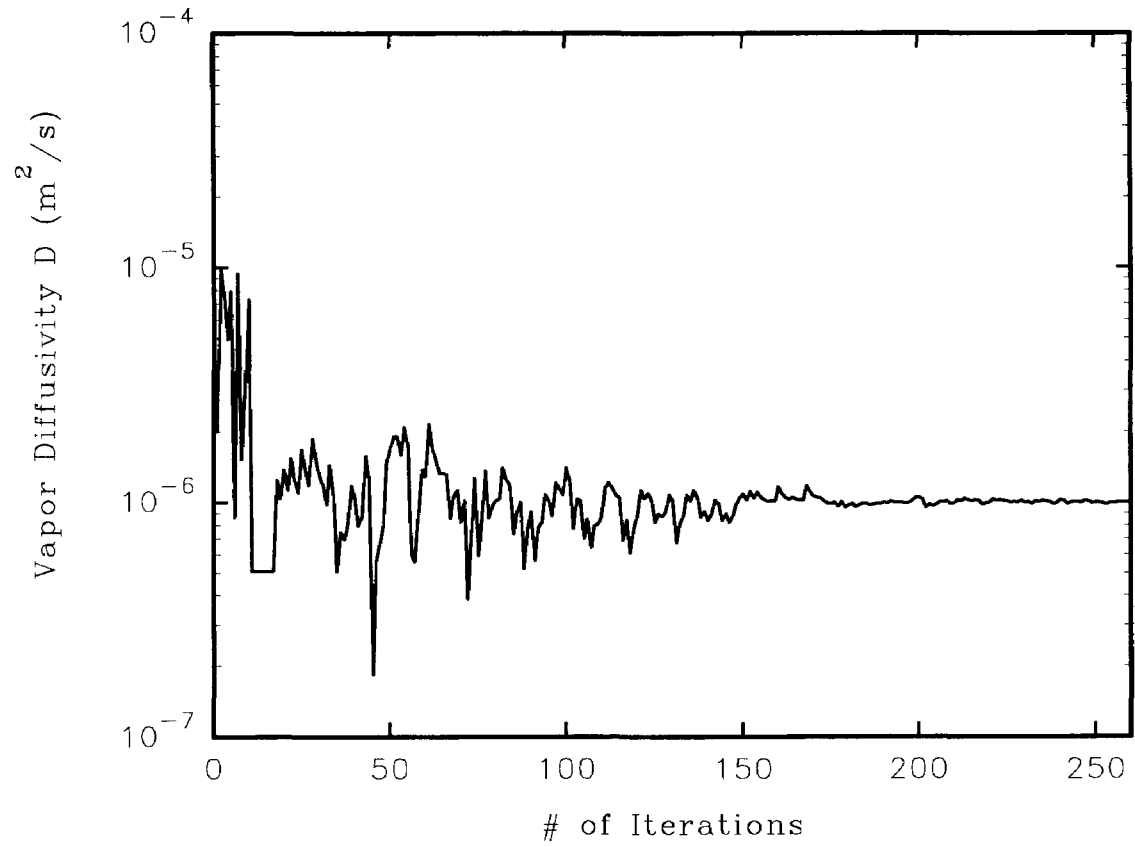


Figure 50. Vapor diffusivity values searched by the parameter estimation technique

adjusted to a stable value after a certain number of iterations. However, the number of iterations needed for such adjustment is different for different parameters. The figures show that it takes about 170 iterations to identify the intrinsic permeability and the vapor diffusivity to the stable values, but the identification of van Genuchten's factors, α and n and the λ factor of Equation 30 needs about 250 iterations. This difference indicates that the objective function has different sensitivities towards these parameters. Parameters requiring fewer iterations for identification are more sensitive to the objective function. Therefore, the intrinsic permeability and the vapor diffusivity are more sensitive to the objective function than the van Genuchten's factors and the λ factor in this study. The reason why vapor diffusivity plays a more important role than the hydraulic pressure-saturation and relative permeability-saturation relationships is because the objective function is constructed with the profile of vapor concentration rather than liquid saturation. If the liquid saturation data are used to generate the objective function, the hydraulic pressure and the relative permeability will be more important, but they are not expected to be more sensitive than the intrinsic permeability.

The estimated parameters are listed in Table 11. The estimated parameter values are all very close to the known values with the maximum estimation error of 3.68% for the α factor. The parameters were accurately identified from the hypothetical data.

To further test the parameter estimation technique, small perturbations of the hypothetical data were made, and the optimization technique was used to identify the parameters. The objective was to evaluate the structure of the model and search procedure. A $\pm 5\%$ perturbation was made on all the hypothetical data (Table 9). If

Table 11. Parameter Estimation Results for the Hypothetical Data

Parameters	Given value	Estimated value from hypothetical data	Estimated value from perturbed data
Intrinsic permeability (m ²)	2.947×10^{-13}	2.999×10^{-13}	2.848×10^{-13}
van Genuchten α factor (1/m)	3.50	3.641	3.604
van Genuchten n factor	5.00	4.816	5.112
λ of Equation 30	2.00	1.906	2.591
Vapor diffusivity (m ² /s)	1.0×10^{-6}	0.998×10^{-6}	1.018×10^{-6}

the resulting perturbed vapor concentration fell beyond the concentration bounds of 0.0 to 0.9, the data were forced to the boundary values. The parameter estimation model was applied to the perturbed data with the same input data as those used for estimation against the hypothetical data (Table 10). Eight searches were made, and the sixth search with R=6 yielded a minimum objective function value of 1.21×10^{-3} . The initial worst value of the objective function was 9.38×10^{-2} . The results of the estimated parameters are also listed in Table 11.

It can be seen that the estimated parameter values from the perturbed data set do not agree as well with the given values as those from the hypothetical data set. Except the λ factor, all other four parameters (k , α , n and D) were accurately estimated and are judged to be acceptable. Fortunately, the relative permeability is less sensitive to the objective function using vapor concentration as observed data. The proposed parameter estimation technique is, therefore, a plausible method to identify the parameters characterizing the simultaneous liquid infiltration and vapor diffusion in porous media from a point source.

VI.5 Experimental Parameter Estimation and Result Simulation

The parameter estimation technique demonstrated earlier was applied to the experimental data. Transient hydrocarbon vapor concentration data collected during experiments were first normalized in the way described later in this section and then used to estimate the five parameters discussed earlier. The estimated parameters were then used to simulate the experimental results of the liquid and vapor transport.

VI.5a Normalized Hydrocarbon Vapor Concentration

To use the experimental data in the numerical model with its idealized assumptions, the transient vapor concentration profile (Figure 5-12) must be normalized. In Figure 5-12, each curve represents the averaged vapor concentration in ppm (parts per million) at a specific monitoring circle. The axial symmetry assumption allows the use of the averaged concentration. As described during the model development, the vapor concentration should be normalized with the saturated vapor concentrations at the corresponding locations. If the liquid used in the experiment had been a single component chemical, the saturated vapor concentration would have been equal to the vapor pressure of the chemical everywhere inside the test chamber under the isothermal and isobaric conditions. When mixed hydrocarbons are used, as in our study, chromatographic separation occurs during the transport process due to the different adsorption and desorption mechanisms of various chemicals on the soil surface, which results in a composition change along the migration. Different saturated vapor concentrations at different monitoring locations were expected and indeed observed in the experiment. The different concentration levels at the later flat portion of each curve in Figure 5-12 indicates the change of the saturated

concentration. Concentration normalization must address this change.

During Test II, diesel vapor was detected by the sensors at 10 monitoring locations (Figure 5, 6). Only the sensors at locations R1L1, R1L2, R1L3 and R2L3 demonstrated fully saturated vapor concentration by the end of the test. Diesel vapor was detected at only two monitoring locations (namely, R1L1 and R1L2) and the concentrations at both locations were believed to have reached an equilibrium at the end of Test III. In Test IV, however, many sensors detected significant concentration of JP-5 by the end of the test (Figures 8-12). The number of monitoring rings where JP-5 had been observed was 15. Equilibrium concentrations were reached at 13 of the 15 locations by the end of the test. The two locations at $r=60''$, $z=5'$ and $r=75''$, $z=8'$ did not show strong signs of reaching the maximum concentration. The data at these two locations were, therefore, not used in the parameter estimation due to insufficient information on the saturated vapor concentrations there.

The saturated vapor concentration at each location was determined from the corresponding transient vapor concentration curve. The general trend of the concentration curve showed that after a period of rapid concentration increase, the vapor build-up rate declined. At some locations negative rates were observed which might be caused by the delayed adsorption/desorption process. For locations not experiencing a concentration decrease, the concentration value at the time when its rate of increase was minimum was selected as the saturated concentrations. For the curves whose concentrations reached a maximum and then declined, the maximum concentration values were used. These saturated vapor concentrations at the locations of interest are listed in Table 12. The concentration data were normalized with the saturated vapor concentrations to a maximum of 0.95. The normalized concentrations

after the time that defines the saturated vapor concentration were forced to be 0.95 to ignore the effects believed to be due to adsorption/desorption process.

Table 12. Determined Saturated Hydrocarbon Vapor Concentration

Sensor Location	Coordinates		Saturated concentration (ppm)		
	r (in)	z (in)	Test II	Test III	Test IV
R0L1	0	24			3300
R0L2	0	60			3300
R0L3	0	96			5500
R1L1	15	24	3200	8000	2700
R1L2	15	60	2300	6000	2200
R1L3	15	96	2800		3300
R2L1	30	24			1500
R2L2	30	60			1500
R2L3	30	96	470		2000
R3L1	45	24			600
R3L2	45	60			650
R3L3	45	96			1800
R4L3	60	96			1050

VI.5b Parameter Estimation for Test II and Test III

Normalized temporal concentration data at locations R1L1, R1L2, R1L3 and R2L3 of Test II and R1L1 and R1L2 of Test III (Appendix C) were used to estimate the five model parameters for the simulation of the simultaneous diesel liquid infiltration and vapor diffusion in sand and in soil. The estimated parameters and the given constraints are listed in Table 13.

Figure 51 shows the estimated diesel capillary pressure and saturation relationship in sand and top soil. The relationship of diesel capillary pressure and saturation in sand determined by Abdul (1988) is also plotted for comparison. Literature data on the relationship between diesel capillary pressure and saturation in the media similar to the top soil are not available.

Table 13. Parameter Estimation Results for Test II and Test III

Parameters	Test II (diesel in sand)		Test III (diesel in soil)	
	Estimation range	Estimation results	Estimation range	Estimation results
Number of parameters N	5		5	
Number of vertices K	10		10	
Reflection factor	1.3		1.3	
Number of observation points	264		146	
Intrinsic permeability (m ²)	5.0×10^{-13} - 5.0×10^{-12}	8.505×10^{-12}	5.0×10^{-14} - 5.0×10^{-13}	3.034×10^{-13}
van Genuchten α factor (1/m)	2.0 - 5.0	8.166	2.0 - 5.0	3.108
van Genuchten n factor	2.0 - 5.0	3.123	2.0 - 5.0	5.093
λ of Equation 30	1.0 - 5.0	4.448	1.0 - 5.0	3.100
Vapor diffusivity (m ² /s)	1.0×10^{-8} - 1.0×10^{-6}	9.178×10^{-7}	1.0×10^{-8} - 1.0×10^{-6}	8.972×10^{-8}

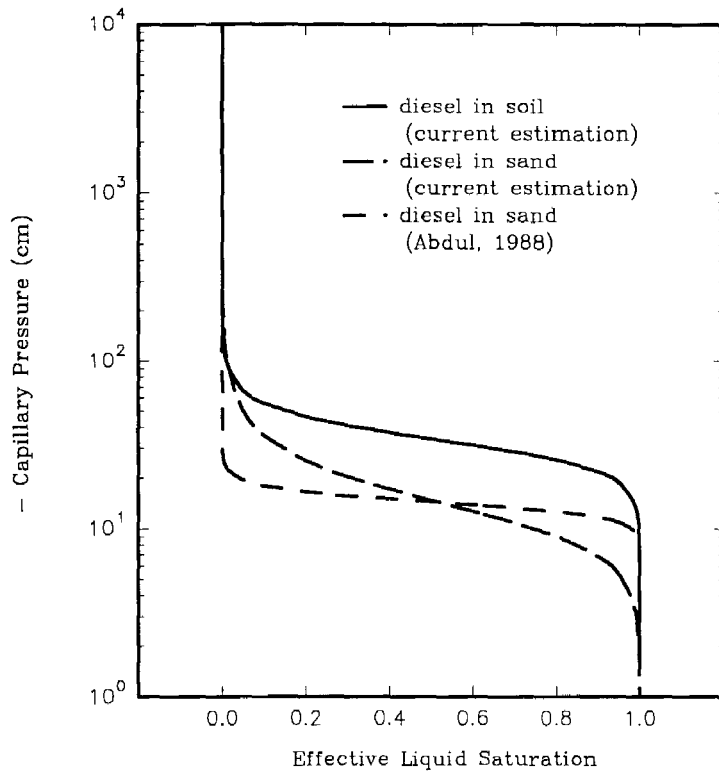


Figure 51. Estimated capillary pressure vs. saturation function for diesel in soils

The magnitude of capillary pressure depends on the wetting and non-wetting phase interface curvature at a "microscopic" point inside the void space (Bear, 1972). It is, therefore, characterized by the geometry of the void space, the nature of the solid matrix and the fluids, and, most sensitively, the degree of saturation. Compared with a sand medium, natural soil provides finer pore structure and higher interfacial tension. The capillary pressure of diesel in soil is generally higher than in sand. Our estimated diesel capillary pressure supports such a trend. The sharp change of the sand curve by Abdul compared to ours indicates that the sand that we used has a much wider range of pore size distribution compared to theirs, whose particle size ranged between 150 μm to 250 μm .

Studies on the impact of organic solvents and petroleum fuels on soil permeability have shown that the intrinsic permeability of a soil measured with concentrated organic solvents and petroleum products is generally higher than when measured with water (Brown and Anderson, 1980; Anderson and Brown, 1982, Brown et al., 1983; Bolton, 1984; Brown et al., 1984; Brown et al., 1986; Shram et al., 1986; Dagon, 1988). The differences can be as large as several orders of magnitude, especially for soils with high clay content. The essential causes are unknown and are subject to further investigation. The estimated intrinsic permeability of the top soil is $3.034 \times 10^{-13} \text{ m}^2$ which is 1.75 times of the value of $1.7346 \times 10^{-13} \text{ m}^2$ calculated from hydraulic conductivity measurement. The intrinsic permeability for the sand medium, however, was estimated to be $8.505 \times 10^{-13} \text{ m}^2$ which is very close to the value of $8.4693 \times 10^{-13} \text{ m}^2$ determined from the hydraulic conductivity.

VI.5c Numerical Simulation Results for Test III

Simulation results using the estimated parameters are shown in Figure 52 with the normalized vapor concentration observation also plotted. Table 14 lists all the input parameters for the simulation.

Table 14. Simulation Parameters for Test III (diesel in soil)

Parameters	Value
Liquid application rate (m ³ /sec)	3.68×10 ⁻⁸
Liquid density (kg/m ³)	880.0
Liquid viscosity (kg/m/sec)	5.01×10 ⁻³
Initial saturation	0.11
Irreducible saturation	0.10
Maximum attainable saturation	0.65
Normalized equilibrium vapor concentration	0.95
Porosity	0.476
Intrinsic permeability (m ²)	3.034×10 ⁻¹³
α factor of van Genuchten's formula (1/m)	3.108
n factor of van Genuchten's formula	5.093
λ factor of Equation 30	3.100
Vapor diffusivity (m ² /s)	8.972×10 ⁻⁷
Numerical spatial increment dh (m)	0.1016
Numerical time increment dt (sec)	900
Total nodal points in r direction	19
Total nodal points in z direction	30
Total simulation time (hrs)	720

Figure 52 shows a later arrival of the simulated vapor plume at location R1L1 than that observed. Inaccurate estimations on van Genuchten's factors, α and n, might have resulted in an under estimation of the early capillary controlled liquid movement. But a more convincing reason for the misfit may be blamed to the model's negligence of the chromatographic separation. As discussed in Section VI.4a, when a petroleum mixture migrates in a porous medium, chromatographic separation occurs and causes a change in the vapor composition. Such change in the vapor composition affects the

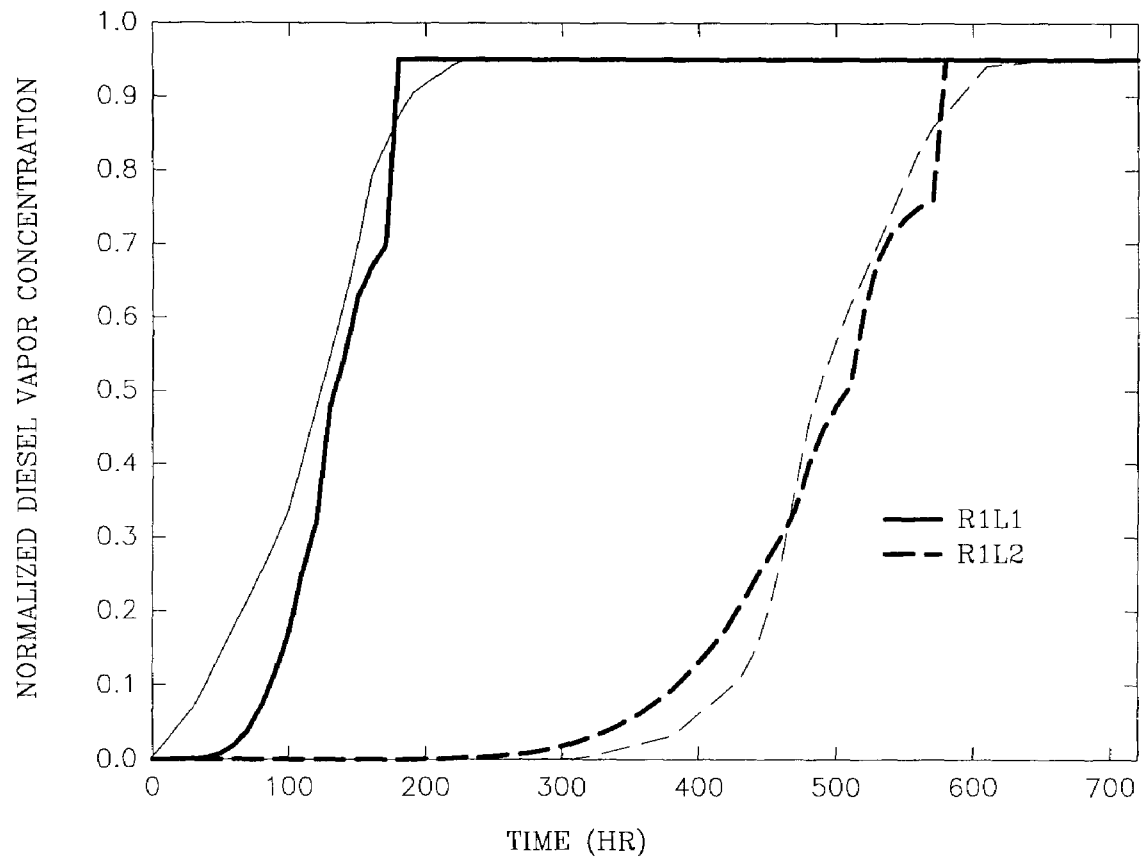


Figure 52. Normalized diesel vapor concentration profile of model predictions (thick lines) and experimental observations (thin lines) for Test III (diesel in soil)

vapor diffusivity. The constant vapor diffusivity value used in the model may have underestimated the diffusion process during the early stage of the experiment.

There is a sharp increase in the simulated concentration from 0.67 to 0.95 at the time of 155 hr. at location R1L1, which was the estimated time when the liquid front should have reached the location. The simple assumption that the vapor concentration takes the saturated value at the liquid wetting front resulted in the unsmoothed curve. A similar change was also observed on the simulations at location R1L2.

At the end of Test III, diesel wetted soil pictures were obtained (Figures 23-27) and the dimensions of the wetted areas were measured (Table 4). The pictures and the data were the only direct observations of liquid movement available from the experiment. The diesel liquid saturation distribution at $t=720$ hrs simulated by the model is shown in Figure 53. The front shape is similar to those in the pictures. Again, assuming the wetting front saturation to be 0.15, the simulated wetting front location gives a very close match to the observed one (Figure 54). The estimated intrinsic permeability which controls the liquid movement is, therefore, a reasonable value.

VI.5d. *Numerical simulation results for Test II*

Numerical simulation of Test II (diesel in sand) was conducted using the transport model. The model input data are summarized in Table 15.

Figure 55 shows the simulated diesel vapor concentration profile, as compared to the experimental results. The simulated diesel vapor front arrived location R1L1 ($r=15$ in. and $z=2$ ft.) later than the experimentally observed vapor front. Similar to

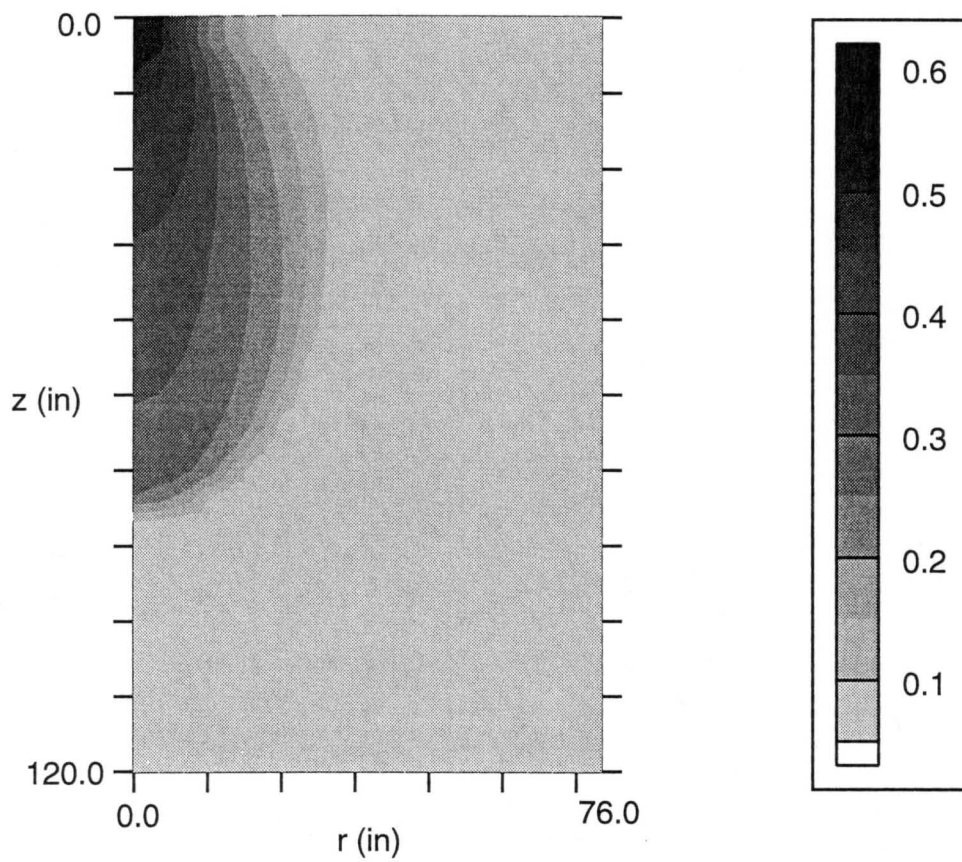


Figure 53. Predicted diesel saturation distributon at the end of Test III (t=720 hrs.)

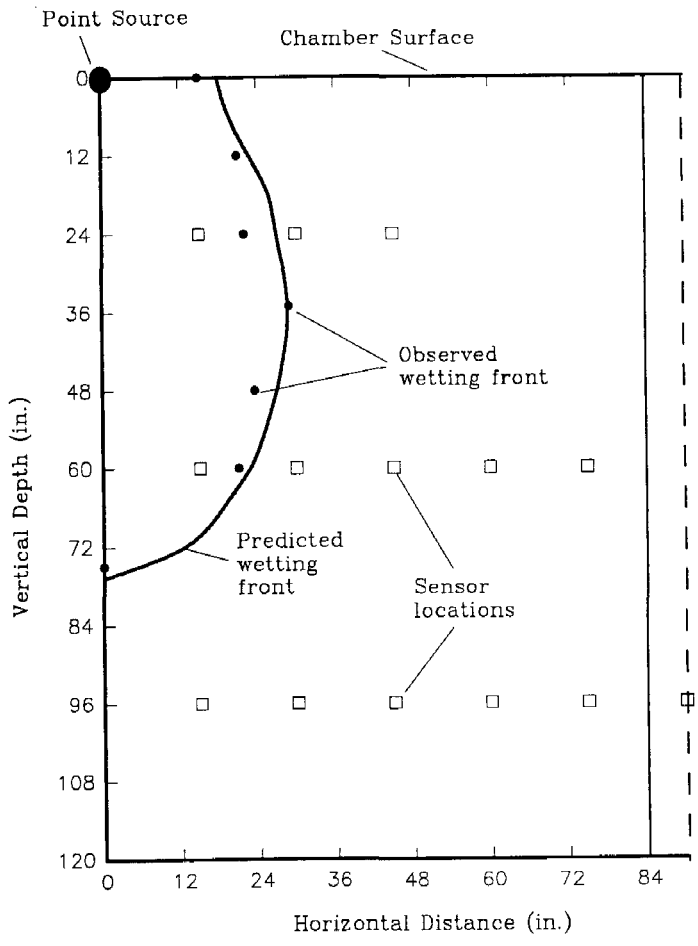


Figure 54. Predicted diesel wetting front at the end of Test III and the observed location

Table 15. Simulation Parameters for Test II (diesel in sand)

Parameters	Value
Liquid application rate (m ³ /sec)	3.456×10 ⁻⁸
Liquid density (kg/m ³)	880.0
Liquid viscosity (kg/m/sec)	5.01×10 ⁻³
Initial saturation	0.11
Irreducible saturation	0.10
Maximum attainable saturation	0.85
Normalized equilibrium vapor concentration	0.95
Porosity	0.401
Intrinsic permeability (m ²)	8.505×10 ⁻¹³
α factor of van Genuchten's formula (1/m)	8.166
n factor of van Genuchten's formula	3.123
λ factor of Equation 30	4.448
Vapor diffusivity (m ² /s)	9.1782×10 ⁻⁷
Numerical spatial increment dh (m)	0.1016
Numerical time increment dt (sec)	900
Total nodal points in r direction	19
Total nodal points in z direction	30
Total simulation time (hrs)	650

the case of diesel transport in soil discussed earlier, the diesel vapor diffusion in sand may have also been underestimated for the early stage of the experiment. At location R1L2 (r=15 in. and z=5 ft.) a relaxed vapor front was predicted compared to the experimental observation. This indicates that the vapor diffusion may have been overestimated or the liquid movement underestimated at the location.

When the infiltrating diesel liquid reaches the bottom of the test chamber, it tends to flow horizontally on top of the impermeable liner. As the liquid spreads horizontally along the bottom boundary, its vapor diffuses upward. The current model, however, simply treats the bottom boundary through a no-vertical-flux boundary condition. The horizontal flow on top of the liner is not considered by the model, nor is the upward vapor diffusion. The model simulated diesel vapor concentration at

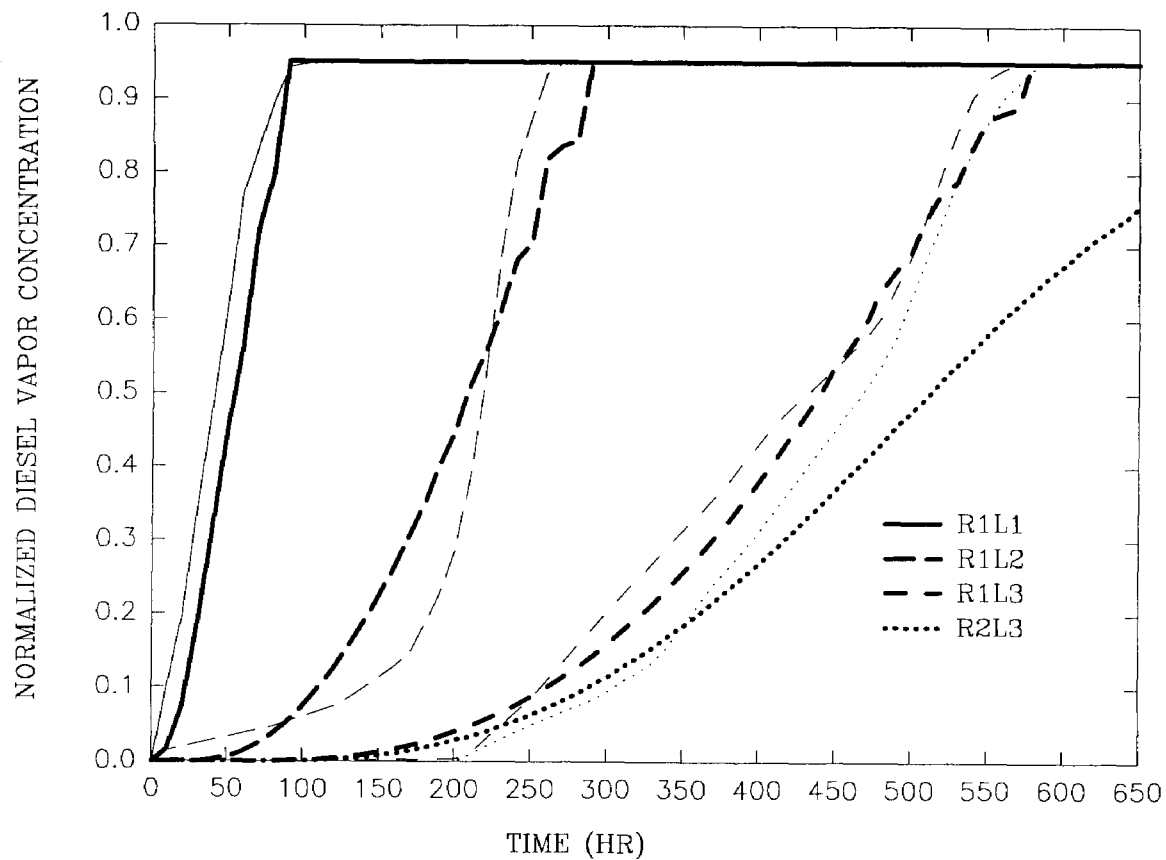


Figure 55. Normalized diesel vapor concentration profile of model predictions (thick lines) and experimental observations (thin lines) for Test II (diesel in sand)

location R2L3 ($r=30$ in. and $z=8$ ft.) is, therefore, lower than the experimental value especially during the later time of the experiment. We believe that both the horizontal diffusion from the center liquid body and the upward diffusion from the diesel spread on top of the bottom liner have contributed to the actual diesel vapor level at the location by the time close to the end of the experiment.

Figure 56 shows the model-simulated diesel saturation distribution in sand at the end of Test II. At the bottom boundary, the simulation only shows a small area of high saturation representing the liquid cumulation when the impermeable boundary is encountered. The model is not capable of predicting a horizontal flow on top of the boundary.

VI.5e Numerical simulation for Test IV

An attempt was also made to fit the model parameters to the data obtained from Test IV (JP-5 in sand). Among the eight search runs with different initial vertices controlled by the random number generator index R , the one of $R=4$ converged to a final objective function value of 0.017 after 75 iterations. It was, however, found that the objective function was improved very little (Figure 57). The unimproved objective function implied that the parameter search was not successful. Nevertheless, the obtained parameters (Table 16) were used to simulate the experiment of JP-5 transport in sand. The results poorly fit with the experimental observations (Figure 58).

Near the infiltration center (area within a horizontal radius of 15"), the model-simulated vapor front migrated much slower than the observed front, especially at locations of 5 and 8 feet below the surface.

For the monitoring locations further out, the model predicted early arrival of

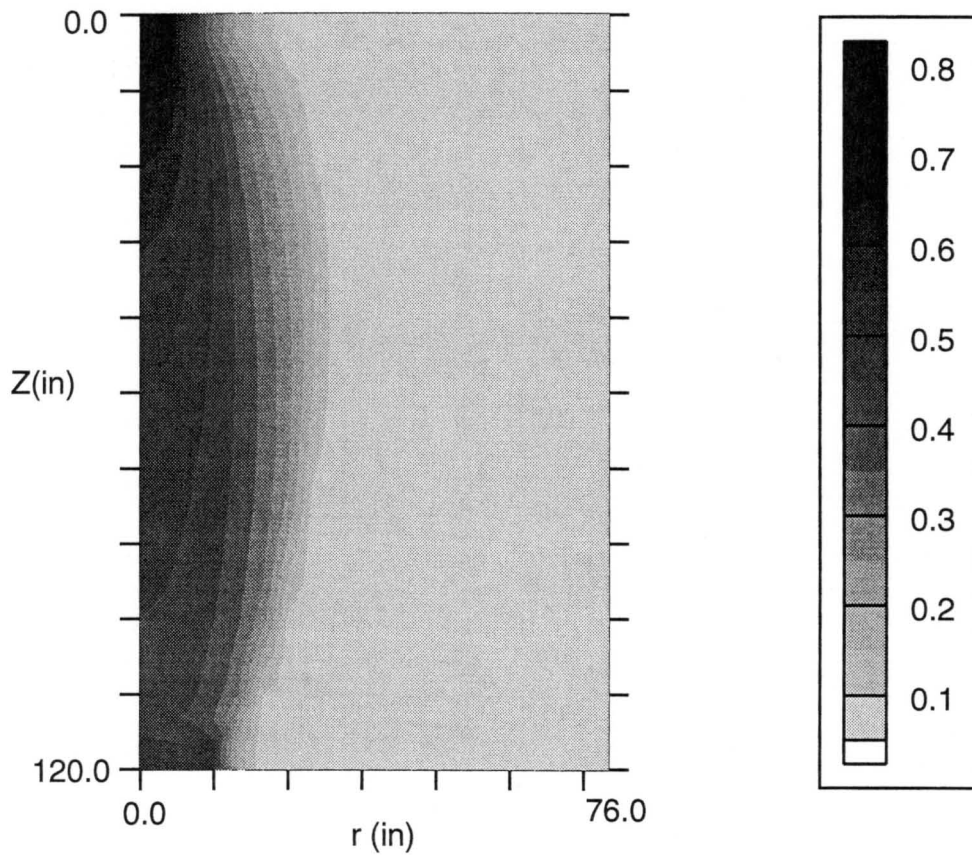


Figure 56. Predicted diesel saturation distributon at the end of Test II (t=650 hrs.)

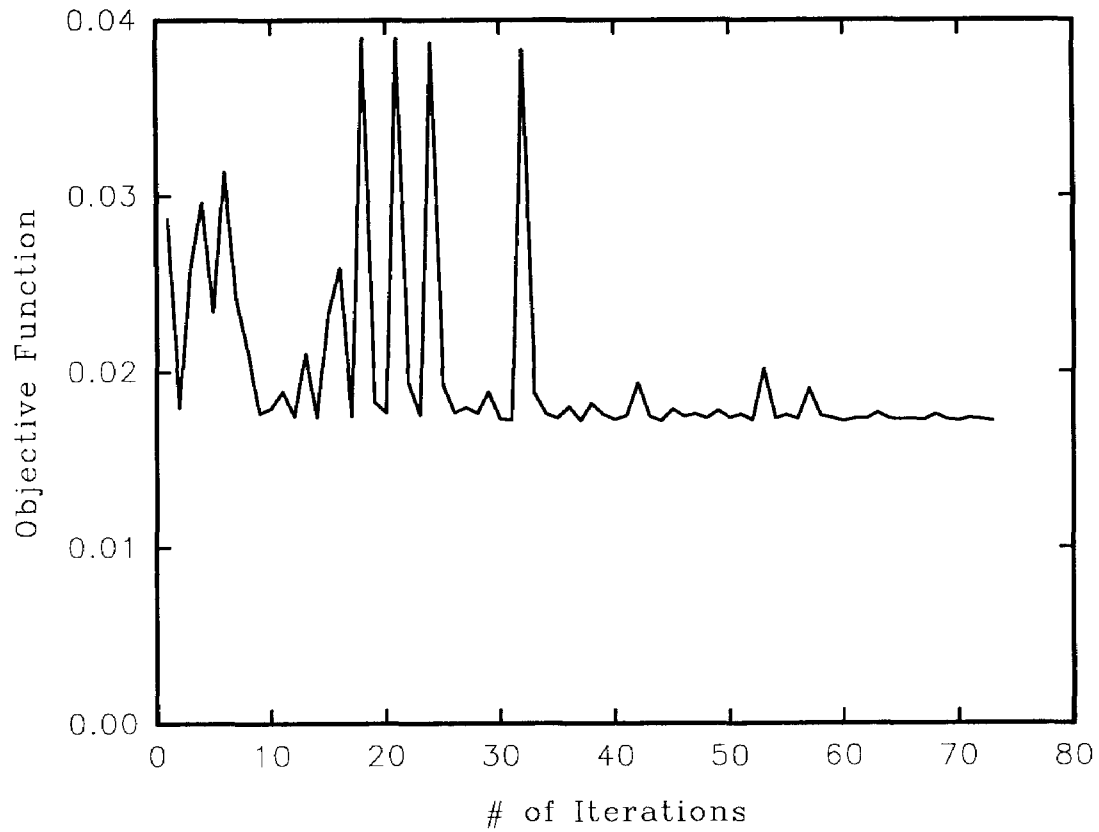


Figure 57. Parameter search resulted in little improvement in the objective function when applied to the data of Test IV (JP-5 in sand)

Table 16. Simulation Parameters for Test IV (JP-5 in sand)

Parameters	Value
Liquid application rate (m ³ /sec)	5.047×10 ⁻⁸
Liquid density (kg/m ³)	820.0
Liquid viscosity (kg/m/sec)	2.23×10 ⁻³
Initial saturation	0.06
Irreducible saturation	0.05
Maximum attainable saturation	0.85
Normalized equilibrium vapor concentration	0.95
Porosity	0.401
Intrinsic permeability (m ²)	2.2601×10 ⁻¹²
α factor of van Genuchten's formula (1/m)	1.317
n factor of van Genuchten's formula	1.814
λ factor of Equation 30	1.347
Vapor diffusivity (m ² /s)	2.0161×10 ⁻⁵
Numerical spatial increment dh (m)	0.1016
Numerical time increment dt (sec)	900
Total nodal points in r direction	19
Total nodal points in z direction	30
Total simulation time (hrs)	580

JP-5. The error is quite significant for location R4L3.

A possible cause to the mismatch is due to the high volatility of JP-5. As the fuel migrated in sand, a significant amount of its light components may evaporate from the liquid body. Loss of light components leads to the increase of the liquid infiltration resistance as a result of increased viscosity and decreased wettability. Chromatographic separation as discussed earlier can also contribute to the mismatch.

A more complicated model capable to address changes in liquid viscosity and hydrodynamic properties due to the significant evaporation loss of the light components of JP-5 during its infiltration is required to more accurately simulate the process. The model should also consider the temporal and spatial variation of vapor diffusivity caused by chromatographic separation. Additional experimental observations will be needed to validate the improved model.

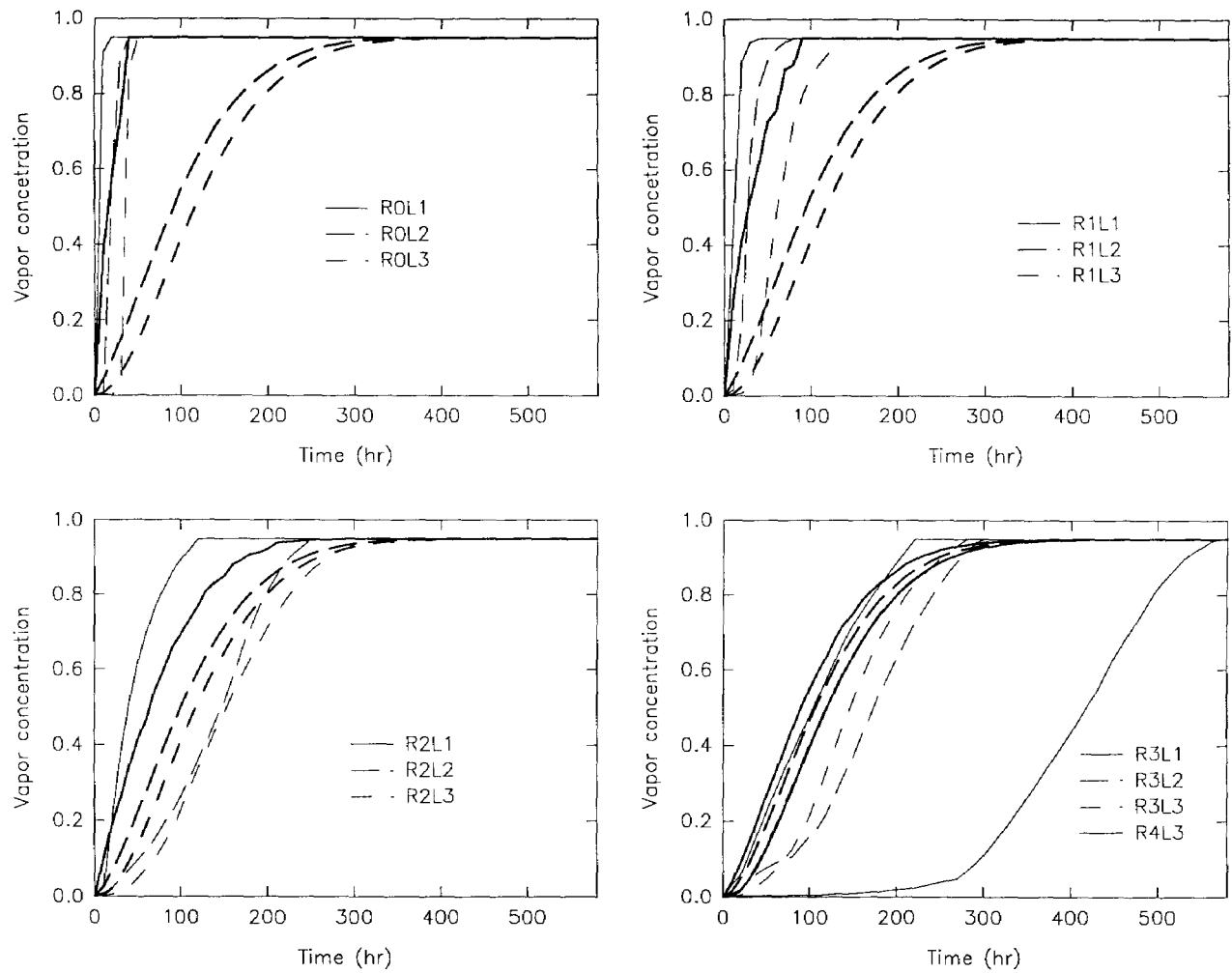


Figure 58. Normalized JP-5 vapor concentration profile of model predictions (thick lines) and experimental observations (thin lines) for Test IV (JP-5 in sand)

VII. CONCLUSIONS AND RECOMMENDATIONS FOR FUTURE WORK

VII.1 Summary and Conclusions

Three experiments investigating the transport of diesel and JP-5 fuels in porous media (sand and soil) were performed and three dimensional monitoring data of the temporal and spatial distribution of hydrocarbon vapor concentration inside the test chamber (12×14×10 ft.) were obtained. A number of observations and conclusions were obtained from the analysis of the experimental results:

1. The movement of JP-5 in sand was much faster than diesel, both vertically and laterally.
2. The faster JP-5 movement was due to both its lower viscosity and higher vapor pressure, as compared to diesel fuel. Other factors such as source strength and seasonal temperature may have also contributed.
3. The capillary-force-dominated movement was observed only in very early stages (within 10 hours) of each experiments. Gravitational movement became dominant as the experiments progressed.
4. The lateral spreading of diesel in sand was very limited, which discourages the use of vadose zone vapor monitoring as a leak detection method for diesel.
5. Enhanced lateral spreading of both diesel and JP-5 near the impermeable bottom boundary was observed for the experiments conducted with sand. Such a finding suggests that a vadose zone hydrocarbon leak monitoring system would be more effective when installed above the surface of a less permeable geographic layer under an underground storage tank.
6. Despite the careful sand loading and compaction, the hydrocarbon vapor

concentration contour maps exhibited heterogeneities in the transport of both diesel and JP-5.

7. The area averaging technique was used to estimate the vapor concentration contour radius at each monitoring level. From the plots of vapor concentration vs. contour radius, it was found that lateral propagation of the fuels became very slow and insignificant after a certain time, especially at shallow depth.
8. The spatial variance of the Time of Arrival (TOA) data indicates that a shallow monitoring well is very likely to fail to detect a leak unless it is horizontally very close to the leak source.
9. The confinement of diesel in a small volume of soil during the entire test period suggests the much greater fuel retention capacity for soil than for sand.
10. Although the overall diesel migration in soil was much slower than in sand, the initial fast capillary-force-driven movement was equivalent.

Another objective of this study was to develop a numerical model to simulate the simultaneous transport of a petroleum liquid and its vapor in unsaturated soil from a point source. Using the alternating direction implicit (ADI) finite difference method, the Richards equation governing the unsaturated liquid movement and the vapor diffusion equation were solved in cylindrical coordinates. Use of a traditional method considering the saturated liquid entry zone as a swelling surface disk of zero thickness may result in an overestimation of the infiltration rate by neglecting the liquid accumulation inside the entry zone. A new scheme treating the liquid entry zone as a conical discrete moving boundary was developed and incorporated the accumulation term into the mass balance equation of the liquid entry zone. The Picard iteration method was used to solve the resulting nonlinear equation systems.

To verify the liquid infiltration model, experimental data obtained by Clothier and Scotter (1982) were simulated using the parameters recommended by Healy and Warrick (1988). Compared to the predictions by others (Ben-Asher et al., 1986, and Healy and Warrick, 1988), the current model was more accurate, and closely matched to the experimental observations.

The complex method of Box coupled with the transport model was used to identify six selected model parameters. Least-square relationship between the observed and model-predicted vapor concentrations was used as the objective function. Using hypothetical data generated by the transport model with a given set of parameters, the parameter estimation scheme accurately identified the parameters from substantially wide intervals. Using hypothetical data with random noise ($\pm 5\%$) the search technique produced acceptable estimations for the intrinsic permeability, the coefficients of van Genuchten's formula which describes the functional relationship between of capillary pressure and saturation, the λ factor of the relative permeability vs. saturation function, and the vapor diffusivity inside the porous medium.

The model was next used to simulate the diesel vapor concentration profile obtained from Test II (diesel in sand and Test III (diesel in soil). Numerical simulation using the estimated parameters produced satisfactory results of both liquid front and vapor concentration distribution.

Parameter search and numerical simulation on Test IV (JP-5 in sand) were not successful. It is believed that the hydrodynamic property change caused by the evaporation loss of the light components of JP-5 and the vapor diffusivity variation due to chromatographic separation are significant for JP-5 and should be included in a model simulating the JP-5 transport in sand.

VII.2 Recommendations for Future Research

Future research efforts in studying VOC transport in unsaturated soil should be both experimental and theoretical efforts.

1. More information on the liquid VOC saturation distribution is needed. A tracer dye may be used to study VOC transport in sand so that the liquid front can be clearly measured at the end of the test.
2. The liquid infiltration model should be expanded to include the effects of anisotropy.
3. The liquid entry zone treatment can be improved by assuming a hemispherical geometry and developing a numerical scheme for the boundary.
4. The numerical scheme can be accelerated by allowing variable spatial increments. Near the infiltration source, finer spatial nodes should be used, and increased nodal spaces at greater distances from the source can reduce the computation time.
5. For highly volatile chemicals, the volatilization loss should be included in the liquid infiltration equation.
6. For vapor diffusion, a multi-component model can eliminate the uncertainty of the saturated vapor concentration near the liquid front.
7. The convergence of the complex method is relatively slow. Selecting narrower ranges for the parameters to be estimated will reduce the number of iterations. Reducing the number of unknown parameters will provide even greater computation time reduction.

VIII. REFERENCES

- Abadou, R., 1981, "Modélisation des transferts hydriques dans le solen irrigation localisée", Thesis, Univ. de Grenoble, France.
- Abdul, A. S., 1988, "Migration of Petroleum products through sandy hydrogeologic systems", *Ground Water Monitoring Review.*, 8(4), 73-81.
- Abriola, L. J., and G. F. Pinder, 1985a, "A multiphase approach to the modeling of porous media contamination organic compounds, 1. Equation development", *Water Resour. Res.*, 21(1), 11-18.
- Abriola, L. M., and G. F. Pinder, 1985b, "A multiphase approach to the modeling of porous media contamination by organic compounds, 2. Numerical simulation", *Water Resour. Res.* 21(1), 19-26.
- Abou-Kassem, J. H., and K. Aziz, 1982, "Grid orientation during steam displacement", *Soc. Petr. Eng. of AIME*, SPE Paper 10497.
- Acher, A. J., P. Bodevie, and B. Yaron, 1989, "Soil pollution by petroleum products, I. Multiphase migration of kerosene components in soil columns", *J. Contam. Hydrol.*, 4, 333-31.
- American Petroleum Institute (API), 1972, "The migration of petroleum products in soil and ground water, Principles and countermeasures", technical report, 35 pp., Amer. Petrol. Inst., Washington D.C.
- Amoiozegar, A., A. W. Warnick, and W. H. Fuller, 1986, "Movement of selected organic liquids into dry soils", *Hazardous Waste and Hazardous Materials*, 3(1), 29-41.
- Anderson, D., and K. W. Brown, 1981, "Organic leachate effects on to permeability of clay liners", in D. W. Schultz (Ed.), *Land Disposal: Hazardous Wastes*, Proc. 7th Ann. Res. Symp., Philadelphia, Pennsylvania, 16-18 March 1981, Mun. Environ. Res. Lab, ORD, U.S. EPA, Cincinnati, Ohio.
- Angelakis, N. A., 1977, "Time dependent soil water distribution in a two-dimensional profile of clay loam soil under circular trickle source", M.S. thesis, University of California, Davis, California.
- Bachmat, Y., and J. Bear, 1986, "Macroscopic modelling of transport phenomena in porous media. 1: the continuum approach", *Transport in Porous Media*, 1, 213-240.
- Baehr, A. L., 1987, "Selective transport of hydrocarbons in the unsaturated zone due to aqueous and vapor phase partitioning", *Water Resour. Res.*, 23(10), 1926-1938.
- Baehr, A. L., and M. Y. Corapcioglu, 1987, "A compositional multiphase model for groundwater contamination by petroleum products, 2. Numerical solution",

- Water Resour. Res., 23(1), 201-213.
- Bar Yosef, B., and M. R. Sheikholeslami, 1976, "Distribution of water and ions in soils irrigated and fertilized from a trickle source", Soil Sci. Soc. Amer. J., 409, 575-582.
- Barbee, G. C., and K. W. Brown, 1986, "Movement of xylene theory unsaturated soils following simulated spills", Waste, Air, and Soil Pollution, 29, 321-331.
- Bastien, F., P. Muntzer, and L. Zilliox, 1977, "Pollution by petroleum products: Transfer of hydrocarbons in water and migration of the contaminants in the aquifer", Prot. Eaux. Souterr. Captees Aliment. Hum. Commun. Colloq. Natls.,2, 1-9.
- Bear, J., 1972, Dynamics of Fluids in Porous Media, American Elsevier, New York.
- Bear, J. and Y. Bachmat, 1967, "A generalized theory on hydrodynamic dispersion in porous media", I.A.H.S. Symmp. Artificial Recharge and Management of Aquifers, Haifa, Israel, P. N. 72, 1967, pp. 7-16.
- Bear, J., and Y. Bachmat, 1986, "Macroscopic modelling of transport phenomena in porous media. 2: applications to mass, momentum and energy transport", Transport in Porous Media, 1, 241-296.
- Ben-Asher, J., Ch. Charach, and A. Zemel, 1986, "Infiltration and water extraction from trickle irrigation source. The effective hemisphere model", Soil Sci. Soc. Amer. J., 50, 882-887.
- Bowen, R. M., 1984, "Porous media model formulations by the theory of mixtures", in J. Bear and Y. Corapcioglu (eds.), Proc. 1982 NATO - Advanced Study Instituted on the Fundamentals of Transport Phenomena in Porous Media, Martinus Nijhoff, pp. 63-119.
- Box, M. J., 1965, "A new method of constrained optimization and a comparison with other methods", Computer J., 8, 42-52.
- Bolton, M. W., 1984, "Movement of Trichloroethylene Solution Through Soils", M.S. Thesis, University of Arizona, Tucson, Arizona. 55 pp.
- Brandt, A., E. Bresler, N. Diner, I. Ben-Asher, J. Heller and D. Goldberg, 1971, "Infiltration from a trickle source. I. mathematical models", Soil Sci. Soc. Amer. Proc., 35, 675-682.
- Bresler, E., and R. J. Hanks, 1969, "Numerical method of estimating simultaneous flow of water and salt in unsaturated soil", Soil Sci. Soc. Amer. Proc., 33, 827-832.
- Bresler, E., J. Heller, N. Diner, I. Ben-Aszher, A. Brandt, and D. Goldberg, 1971, "Infiltration from a trickle source. II. Experimental data and theoretical predictions", Soil Sci. Soc. Amer. Proc., 35, 683-689.

- Brooks, R. H., and A. T. Corey, 1964, "Hydraulic properties of porous media", Hydrol. Pap. 3. Colorado State University, Fort Collins.
- Brown, K. W., and D. Anderson, 1980, "Effect of organic chemicals or clay liner permeability", In D.W. Schultz (Ed.) Disposal of hazardous wastes, Proc. 6th Ann. Res. Symp., Chicago, Illinois, 1-20 March, 1980, Mun. Environ. Res. Lab, ORD, U.S. EPA, Cincinnati, Ohio.
- Brown, K. W., and J. C. Thomas, 1984, "Conductivity of three commercially available clays to petroleum products and organic solvents", Hazardous Waste and Hazardous Materials, 1, 545-553.
- Brown, K. W., J. C., Thomas, and J. W. Green, 1984, "Permeability of compacted soils to solvents mixtures and petroleum products", In Land disposal of hazardous waste, Proc. of 10th Ann. Res. Symp., Ft. Mitchell, Kentucky, April 3-5, 1984. Mun. Environ. Res. Lab., ORD, U.S. EPA, Cincinnati, Ohio.
- Brown, K. W., J. C. Thomas, and H. W. Green, 1986, "Field cell verification of the effects of concentrated organic solvents on the conductivity of compacted soils", Hazardous Waste and Hazardous Materials, 3(1), 1-19.
- Bruckler, L., B. C. Ball, and P. Renault, 1989, "Laboratory estimation of gas diffusion coefficient and effective porosity in soils", Soil Science, 147, 1-10.
- Bruell, C. J., and G. E. Hoag, 1986, "The diffusion of gasoline-range hydrocarbon vapors in porous media, experimental methodologies", in Proceedings of the National Water Well Association/American Petroleum Institute Conference on Petroleum Hydrocarbons and Organic Chemicals Groundwater, Nov. 12-14, 1986, Houston, Texas.
- Bumb, A., 1987, Unsteady-state Flow of Methane and Water in Coalbeds, Ph.D. dissertation, Dept. of Chemical Engineering, University of Wyoming, Laramie, Wyoming.
- Bumb, A. C., C. R. McKee and R. B. Evans, 1988, "Design of Lysimeter leak detector networks for surface impoundments and landfills", Ground Water Monitoring Review, 8(2), 102-114.
- Burdine, N. T., 1953, "Relative permeability calculation from pore-size distribution data", Petr. Trans., Am. Inst. Mining Metall. Eng., 198, 71-77.
- Carbonell, R. C. and S. Whitaker, 1984, "Heat and mass transfer in porous media", in J. Bear and Y. Corapcioglu (eds.), Proc. 1982 NATO - Advanced Study Instituted on the Fundamentals of Transport Phenomena in Porous Media, Martinus Nijhoff, pp. 121-1989.
- Chavent, G., 1974, "Identification of functional parameters in partial differential equations", in Identification of Parameters in Distributed Systems, edited by Goodson, R.E. and M. Polis, pp.31-48, American Society of Mechanical Engineers, New York, 1974.

- Childs, E. C., 1967, "Soil moisture theory", *Adv. Hydrosoci.*, 4, 73-117.
- Clothier, B. E., and D. K. Scotter, 1982, "Constant-flux infiltration from a hemispherical cavity", *Soil Sci. Soc. Amer. J.*, 46, 696-700.
- Corey, A., 1977, "Mechanics of Heterogeneous Fluids in Porous Media", Water Resources Publications, Fort Collins, Colorado.
- Corapcioglu, M. Y., and A. L. Baehr, 1987, "A compositional multiphase model for groundwater contamination by petroleum products, 1. Theoretical consideration", *Water Resour. Res.*, 23(1), 191-200.
- Dagan, G., and E. Bresler, 1983, "Unsaturated Flow in Spatially Variable Fields, 1. Derivation of Models of Infiltration and Redistribution", *Water Resources Research*, 19, 413-420.
- deWiest, R. J. M., 1969, *Flow through porous media*, Academic Press, New York.
- Dragun, J., 1988, *The soil chemistry of hazardous materials*. Hazardous Materials Control Research Institute, pp.47.
- Dullien, F. A. L., 1979, *Porous media, Fluid Transport and Pore Structure*, Acad. Press, New York.
- Eklund, A. G., and B. Eklund, 1988, "External petroleum leak and release detection monitoring systems for use with underground storage tanks", in *Leak Detection Methods for Underground Storage Tanks*, Speaker Papers, U.S.E.P.A., CERI-88-64.
- Falta, R. W., I. Javandel, K. Pruess, and P. A. Witherspoon, 1989, "Density-driven flow of gas in the unsaturated zone due to the evaporation of volatile organic compounds", *Water Resources Research*, 25, 2159-2109.
- Farmer, W. J., M. S. Young, J. Letey and W. F. Spencer, 1980, "Hexa-chlorobenzene: its vapor pressure and vapor phase diffusion in soil", *Soil Sci. Soc. Am. J.*, 44, 676-680.
- Faust, C. R., 1985, "Transport of immiscible fluids within and below the unsaturated zone: A numerical model", *Water Resour. Res.*, 21(4), 587-596.
- Fletcher Armstrong, C., and T. V. Wilson, 1983, "Computer model for moisture distribution in stratified soil under a trickle source", *Trans. ASAE*, 26, 1704-1709.
- Foreman, D. E., and D. E. Danial, 1984, "Effects of hydraulic gradient and method of testing on the hydraulic conductivity of compacted clay to water, methanol, and heptane", in *Land Disposal of Hazardous Waste, Proc. 10th Ann. Res. Symp.*, Ft. Nitchell, Kentucky, 3-5 April 1984, Mun. Environ. Res. Lab, ORD, U.S. EPA, Cincinnati, Ohio.

- Frankenberger, W. T., Jr., and F. R. Troech, 1982, "Bacterial utilization of simple alcohols and their influence on saturated hydraulic conductivity", *Soil, Sci. Soc. Amer. J.*, 46, 535-538.
- Frick, T., Ed., *Petroleum Production Handbook*, Vol. 2, Society of Petroleum Engineers of AIME, Dallas, Texas, pp. 25.
- Fried, J. J., P. Muntzer, and L. Zilliox, 1979, "Ground-water pollution by transfer of oil hydrocarbons", *Groundwater*, 17(6), 584-594.
- Gierke, J. S., N. J. Hutzler and J. C. Crittenden, 1990, "Modeling the movement of volatile organic chemicals in columns of unsaturated soil", *Water Resources Research*, 26, 1529-1547.
- Goldberg, D., B. Gormat, and Y. Bar, 1971, "The distribution of roots, water and minerals as a result of trickle irrigation", *J. Amer. Soc. Horticult. Sci.*, 96(5), 645-648.
- Grismer, M. E., D. B. McWhorter, and A. Klute, 1986, "Determination of diffusivity and hydraulic conductivity in soils at low water contents from non-destructive transient flow observations", *Soil Science*, 141, 10-19.
- Grismer, M. E., 1988, "Vapor transport during solution displacement in soils", *Soil Science*, 146, 215-220.
- Guthrie, V. B., 1967, "Petroleum products", in *Petroleum Processing Handbook*, W. F. Bland and R. L. Davidson (ed.), McGraw-Hill, Inc., New York, pp.11-31, 33, 37.
- Hachum, A. Y., J. F. Alfaro, and L. S. Willardson, 1976, "Water movement in soil from trickle source", *J. Img. Drain Div., Proc. ASCE*, 102(IR2), 179-192.
- Hassanizadeh, M., and W. G. Gray, 1979a, "General Conservation Equations for Multi-phase Systems: 1. Averaging Procedure", *Advances in Water Resources*, 2(9), 131-44.
- Hassanizadeh, M., and W. G. Gray, 1979b, "General Conservation Equations for Multi-phase Systems: 2. Mass, Momenta, Energy, and Entropy Equations", *Advances in Water Resources*, 2(12), 191-203.
- Hassanizadeh, M. and W. G. Gray, 1980, "General conservation equations for multiphase systems, 3. Constitutive theory for porous media flow", *Advances in Water Resources*, 3, 25-40.
- Haverkamp, R., M. Vauclin, J. Tovina, P. Wierenga, and G. Vachaud, 1977, "A Comparison of Numerical Simulation Models For One-dimensional Infiltration", *Soil Sci. Soc. Amer. Proc.* 41, 285-294.
- Healey, R. W., and A. W. Warrick, 1988, "A generalized solution infiltration from a

- surface point source", *Soil Sci. Soc. Amer. J.*, 52, 1245-1251.
- Hirasaki, G. J., 1975, "Sensitivity coefficients for history matching oil displacement processes", *Society of Petroleum Engineers Journal*, (2), 39-49.
- Hochmuth, D. P., 1981, "Two-phase flow of immiscible fluids in groundwater systems", M.S. thesis, Colo. State Uni., Fort Collins.
- Hochmuth, D. P., and D. K. Sunada, 1985, "Ground-water model of two phase immiscible flow in coarse material", *Ground Water*, 23(5), 617-626.
- Hoffmann, B., 1971, "Dispersion of soluble hydrocarbons in ground water stream", in *Advances Water Pollution Research Proceedings of the 5th International Conference 1970*, Pergamon, New York.
- Kim, J. H., and M. K. Stenstrom, 1994a. "An Integrated Groundwater Model Using Multicomponent Multiphase Theory 1. Theoretical Development", submitted to *Water Resources Research*.
- Kim, J. H., and M. K. Stenstrom, 1994b. "An Integrated Groundwater Model Using Multicomponent Multiphase Theory 2. Numerical Analysis and Model Applications", submitted to *Water Resources Research*.
- Jackson, R. D., 1964, "Water vapor diffusion in relatively dry soil: 1. Theoretical considerations and sorption experiments", *Soil Sci. Soc. Am. Proc.*, 28, 172-176.
- Jaynes, D. B., 1990, "Temperature variations effects on field measure infiltration", *Soil Sci. Soc. Amer. J.*, 54, 305-312.
- Jury, W. A., D. Russo, G. Steile, and H. Elabd, 1990, "Evaluation of volatilization by organic chemicals residing below the soil surface", *Water Resources Research*, 26, 13-20.
- Kalaydjian, F., 1987, "A Macroscopic Description of Multiphase Flow in Porous Media Involving Spacetime Evolution of Fluid/Fluid Interface", *Transport in Porous Media*, 2, 537-552.
- Kaluarachchi, J. J., and J. C. Parker, 1989, "A efficient finite element method for modeling multiphase flow", *Water Resour. Res.*, 25, 43-54.
- Kaluarachchi, J. J., and J. C. Parker, 1990, "Modeling multicomponents organic chemical transport in three-fluid phase porous media", *J. Contam. Hydro.*, 5, 349-374.
- Kuppusamy, T., J. Sheng, J. C. Parker, and R. J. Lenhard, 1987, "Finite elements analysis of multiphase immiscible flow through soils", *Water Resour. Res.*, 23, 625-632.
- Lafolie, F., R. Guennelon, and M. Th. van Genuchten, 1989a, "Analysis of water flow

- under trickle irrigation: I. theory and numerical solution", *Soil Sci. Soc. Am. J.*, 53, 1310-1318.
- Lafolie, F., R. Guennelon, and M. Th. van Genuchten, 1989b, "Analysis of water flow under trickle irrigation: II. experimental evaluation", *Soil Sci. Soc. Am. J.*, 53, 1318-1323.
- Laughlin, R. D., and J. E. Davies, 1961, "Some aspects of capillary absorption in Fibrous textile wicking", *Textile Research J.*, 31, 904-910.
- Lenhard, R. J., J. H. Dane, J. C. Parker, and J. J. Kaluarachchi, 1988, "Measurement and simulation of one dimensional transient three-phase flow for monostonic liquid drainage", *Water Resour. Res.*, 24(6), 853-863.
- Levin, I., P. C. van Rooyen, and F. C. van Rooyen, 1979, "The effect of discharge rate and intermittent water application by point-source irrigation on the soil moisture distribution pattern", *Soil Sci. Soc. Am. J.*, 43, 8-16.
- Lindstrom, F. T., and W. T. Piver, 1986, "Vertical-horizontal transport and fate of low water solubility chemicals in unsaturated soils", *J. Hydrol.*, 86, 93-131.
- Mackey, D. M., P. V. Roberts, and J. A. Cherry, 1985, "Transport of organic contaminants in groundwater", *Environ. Sci. Technol.*, 19(5), 384-392.
- Marle, C. M., 1982, "On macroscopic equations governing multiphase flow with diffusion and chemical reactions in porous media", *Int. J. Eng. Sci.*, 20, 643-662.
- Marshall, T. J., 1959, "The diffusion of gases through porous media", *J. Soil Sci.*, 10, 79-82.
- Muskat, M., and M. W. Meres, 1936, *Physics*, 7, 346.
- Muskat, M., H. G. Wyckoff, M. W. Botset, and M. W. Meres, 1937, *Trans. AIME*, 123, 69.
- McKee, C., and A. Bumb, 1984, "The Importance of Unsaturated Flow Parameters in Designing a Monitoring System for a Hazardous Waste Site", *Proc. National Conf. on Hazardous Waste and Environmental Emergencies*, Houston, Texas, March 1984, 50-58.
- McKee, C. R., and A. C. Bumb, 1988, "A three-dimensional analysis model to aid in selecting monitoring locations in the vadose zone", *Ground Water Monitoring Review*, 8(1), 124-136.
- Mendoza, C. A., and E. O. Frind, 1990a, "Advective-dispersive transport of dense organic vapors in the unsaturated zone, 1. model development", *Water Resources Research*, 26, 379-387.
- Mendoza, C. A., and E. O. Frind, 1990a, "Advective-dispersive transport of dense

organic vapors in the unsaturated zone, 2. sensitivity analysis", *Water Resources Research*, 26, 388-398.

Millington, R. J., 1959, "Gas diffusion in porous media", *Science*, 130, 100-102.

Millington, R. J. and J. P. Quirk, 1961, "Permeability of porous solids", *Trans. Faraday Soc.*, 57, 1200-1207.

Mostaghimi, S., and J. K. Mitchell, 1983, "Pulse trickling effect on soil moisture distribution", *Water Resour. Bull.*, 19, 605-612.

Mull, R., 1971, "Migration of oil products in the subsoil with regard to ground water pollution by oil", in *Advances in Water Pollution Research Proceedings of the 5th International Conference 1970*, Pergamon, New York.

Nelson, L. and J. Dablow, 1986, "Case study: storage tanks-vapor detection monitoring", *Hazardous Materials & Waste Management Magazine*, July-August, 31-33.

Nielson, D. R., J. W. Biggar, and J. M. Davidson, 1962, "Experimentation consideration of diffusion analysis in unsaturated flow problems", *Soil Sci. Soc. Amer. Proc.*, 26, 107-111.

Nielson, K. K., V. C. Rogers, and G. W. Gee, 1984, "Diffusion of radon through soils", *Soil Sci. Soc. Am. J.*, 1(48), 482-487.

Nikolaevski, V. N., K. S. Basniev, A. T. Gorbunov, and G. A. Zotov, 1970, *Mechanics of Saturated Porous Media*, NEDRA, Moscow.

Parker, J. C., R. J. Lenhard, and T. Kuppasany, 1987, "A parameter model for constitutive properties governing multiphase flow in porous media", *Water Resour. Res.*, 23(4), 618-624.

Parker, J. C., and R. J. Lenhard, 1987, "A model for hysteretic constitutive relations governing multiphase flow", *Water Resour. Res.*, 23(12), 2187-2206.

Peaceman, D. W., and H. H. Rachford, 1955, "The numerical solution of parabolic and elliptic differential equations", *J. Soc. Indust. Appl. Math.*, 3, 28-41.

Peaceman, D. W., 1977, *Fundamentals of numerical reservoir simulation developments in petroleum science*, Vol 6., Elsevier, Amstered.

Penman, H. L., 1940, "Gas and vapor movements in the soil. I. The diffusion of vapours through porous solids", *J. Agric. Sci. (Camb.)*, 30, 473-62.

Philip, J. R., 1968, "Steady infiltration from buried point sources and spherical cavities", *Water Resour. Res.* 4, 1039-1047.

Philip, J. R., 1969, "Theory of infiltration", *Adv. Hydrosci.*, 5, 216-296.

- Philip, J. R., 1970, *Ann. Rev. Fluid Mech.*, 2, 1977.
- Philip, J. R., 1971, "General theorem on steady infiltration from surface sources", *Soil Sci. Soc. Amer. Proc.*, 35, 867-871.
- Philip, J. R., 1973, "On solving the unsaturated flow equation: 1. The flux-concentration relation", *Soil, Sci.*, 116, 328-335.
- Pinder, G. F., and L. M. Abriola, 1986, "On the simulation of nonaqueous phase organic compounds in the subsurface", *Water Resour. Res.*, 22(9), 109S-119S.
- Prat, M., 1989, "On the Boundary Conditions at the Macroscopic Level", *Transport in Porous Media*, 4, 259-280.
- Purcell, W. R., "Capillary pressures - their measurement using mercury and the calculation of permeability therefrom", *Trans. AIME*, 186, 39.
- Quintard, M., and S. Whitaker, "Two-Phase Flow in Heterogeneous Porous Media: The Method of Large-Scale Averaging", *Transport in Porous Media*, 3, 357-413.
- Raats, P. A. C., 1970, "Steady infiltration from line sources and furrows", *Soil Sci. Soc. Amer. Proc.*, 34, 709-714.
- Raats, P. A. C., 1971, "Steady infiltration from point sources, cavities and basins", *Soil Sci. Soc. Amer. Proc.*, 35, 689-694.
- Raats, P. A. C., 1972, "Steady infiltration from sources at arbitrary depth", *Soil Sci. Soc. Amer. Proc.*, 36, 399-401.
- Ragab, R., J. Feyen, and D. Hillel, 1984, "Simulating infiltration in sand from a trickle line source using the matric flux potential concept", *Soil Science*, 137, 120-127.
- Rawls, W. J., D. L. Brakensiek, and K. E. Saxton, 1982, "Estimation of soil water properties", *Trans. Amer. Soc. Agr. Engr.*, 25, 1316-1320, 1328.
- Roth, R. L., 1974, "Soil moisture distribution and wetting pattern from a point source", pp. 246-251. in *Proc. Int. Drip. Irrig. Congr. 2nd*, San Diego, CA 7-14 July, University of California, Riverside.
- Roy, W. R., and R. A. Griffin, 1987, "Vapor-phase movement of organic solvents in the unsaturated zone", *Open File Rep.*, 16, 37pp. *Environ. Inst. of Waste Manage. Studies*, Univ. of Alabama, Tuscaloosa, June, 1987.
- Sallam, A., W. A. Jury and J. Letey, 1984, "Measurement of gas diffusion coefficient under relatively low air-filled porosity", *Soil Sci. Soc. Am. J.*, 48, 3-6.
- Scheinfeld, R. A., J. B. Robertson and T. G. Schwendeman, 1986, "Underground storage tank monitoring: observation well based systems", *Ground Water*

Monitoring Review, 6, 49-55.

- Schiegg, H. O., 1977, Methode zur Abschätzung der Ausbreitung von Erdolderivaten in im't Wasser until luft Erfüllten Boden, Mitt. Versuchsanst. Wasserbau Eidgeniss. Tech. Hochsch. Zurich, 22.
- Schramm, M., A. W. Warnick, and W. H. Fuller 1986, "Permeability of soils to four organic solvents and water", Hazardous Waste and Hazardous Materials, 3(11).
- Schwille, F., 1967, "Petroleum contamination of subsoil. A hydrological problem", in Joint Problems of Oil and Water Industries, Institute of Petroleum, London, 1967.
- Schwille, F., 1981, "Groundwater pollution in porous media by fluids immiscible with water", Sci. total Environ., 21, 173-185.
- Schwille, F., 1984, "Migration of organic fluids immiscible with water in the unsaturated zone", in Pollutants in porous media, Ecol. Stud. Vol. 47, pp 27-48, Springer-Verdag, New York.
- Schwille, F., 1988, Dense Chlorinated Solvents in Porous and Fractured Media. Model Experiments, translated by J. F. Pankow, Lewis Publishers, Inc. Chelsea Michigan.
- Shearer, R. C., J. Letey, W. J. Farmer and A. Klute, 1973, "Lindane diffusion in soil", Soil Sci. Soc. Am. Proc., 37, 189-193.
- Shram, M. A., A. W. Warrick, and W. H. Fuller, 1986, "Permeability of Soils to Four Organic Solvents and Water", Hazardous Waste & Hazardous Materials, 3(1),
- Shoemaker, C. A., T. B. Culver, L. W. Lion, and M. G. Peterson, 1990, "Analytical methods of the impact of two-phase sorption on subsurface transport of volatile chemicals", Water Resources Research, 26, 745-758.
- Sigmund, P. M., and F. G. McCaffery, 1979, "An improved unsteady-state procedure for determining the relative permeability characteristics of heterogeneous porous media", Society of Petroleum Engineers Journal, (2), 15-28.
- Sleep, B. E. and J. F. Sykes, 1989, "Modeling the transport of volatile organics in variably structured media", Water Resources Research, 25, 81-92.
- Taghavi, S. A., M. A. Manro, and D. E. Rolsen, 1984, "Infiltration from trickle irrigation source", J. Irrig. Drain. Div. ASCE, 110, 331-341.
- Treybal, R. E., 1980, Mass Transfer Operations, 784pp, McGraw-Hill, New York.
- Tscheschke, P. D. et al., 1974, "Trickle irrigation soil water potential as influenced by management of highly saline water", Soil Sci., 117(4), 226-231.
- van Genuchten, M. Th., 1980, "A Closed-form Equation for Predicting the Hydraulic

- Conductivity of Unsaturated Soils", *Soil Sci. Soc. Am. J.*, 44, 892-898.
- van der Ploeg, R. R., and P. Benecke, 1974, " Unsteady unsaturated, n-dimensional moisture flow in soil: a computer simulation program", *Soil Sci. Soc. Am. Proc.*, 38, 881-885.
- Warrick, A. W., J. W. Biggard and D. R. Nielsen, 1971, "Simultaneous solute and water transfer for an unsaturated soil", *Water Resour. Res.*, 7, 1216-1225.
- Warrick, A. W., 1974, "Time dependent linearized infiltration, I. Point Sources", *Soil Sci. Soc. Amer. Proc.*, 38, 383-386.
- Weeks, E. P., D. E. Earp and G. M. Thompson, 1982, "Use of atmospheric fluorocarbons F-11 and F-12 to determine the diffusion parameters of the unsaturated zone in the southern high plains of Texas", *Water Resources Research*, 18, 1365-1378.
- Wilke, C. R., and C. Y. Lee, 1955, "Estimation of diffusion coefficients for gases and vapors", *Ind. Eng. Chem.* 47, 1253-1257.
- Wooding, R. A., 1968, "Steady infiltration from a shallow circular pond", *Water Resour. Res.*, 4, 259-273.
- Wooding, R. A., and H. J. Morel Seytoux, 1976, *Annu. Rev. Fluid Mech.*, 8, m233.
- Yeh, W. W-G., 1986, "Review of Parameter Identification Procedures in Groundwater Hydrology: The Inverse Problem", *Water Resources Research*, 22, 95-108.
- Young, W. S., 1986, "Vapor Diffusions in Soil", in *Proceedings of the Conference on Southwestern Ground Water Issues*, Tempe, Arizona, October 20-22, 1986. 426-439.

for $i=is+2, is+3, \dots, M-2$

where:

$$R_{ij}^k = \left[\left(\Pi_{ij-1} + \Pi_{ij} + h \frac{dk_r}{dS} \Big|_{ij} \right) S_{ij-1} - \left(\Pi_{ij-1} + 2\Pi_{ij} + \Pi_{ij+1} \right) S_{ij} + \left(\Pi_{ij} + \Pi_{ij+1} - h \frac{dk_r}{dS} \Big|_{ij} \right) S_{ij+1} \right]^k$$

For the is boundary, when $is = 0$:

$$B_{1j}^{k+\frac{1}{2}} = \left[\frac{1}{3} \Pi_{0j} - 2\Pi_{1j} - \Pi_{2j} - \frac{4h^2}{B\tau} \right]^{k+\frac{1}{2}}$$

$$C_{1j}^{k+\frac{1}{2}} = \left[-\frac{1}{3} \Pi_{0j} + 2\Pi_{1j} + \Pi_{2j} \right]^{k+\frac{1}{2}}$$

$$D_{1j}^{k+\frac{1}{2}} = - \left[R_{1j} + \frac{4h^2}{B\tau} S_{1j} \right]^k$$

$$S_{0j}^{k+\frac{1}{2}} = \left[\frac{4}{3} S_{1j} - \frac{1}{3} S_{2j} \right]^{k+\frac{1}{2}}$$

and when $is \neq 0$:

$$B_{is+1j}^{k+\frac{1}{2}} = \left[- \left(\Pi_{isj} + 2\Pi_{is+1j} + \Pi_{is+2j} + \frac{4h^2}{B\tau} \right) \right]^{k+\frac{1}{2}}$$

$$C_{is+1j}^{k+\frac{1}{2}} = \left[\left(1 + \frac{1}{i} \right) \Pi_{is+1j} + \Pi_{is+2j} \right]^{k+\frac{1}{2}}$$

$$D_{is+1j}^{k+\frac{1}{2}} = - \left[R_{is+1j} + \frac{4h^2}{B\tau} S_{is+1j} \right]^k - \left[\Pi_{isj} + \left(1 - \frac{1}{i} \right) \Pi_{is+1j} \right]^{k+\frac{1}{2}} S_s$$

For the M boundary:

$$A_{M-1j}^{k+\frac{1}{2}} = \left[\Pi_{M-2j} + \left(\frac{2}{3} - \frac{4}{3(M-1)} \right) \Pi_{M-1j} - \frac{1}{3} \Pi_{Mj} \right]^{k+\frac{1}{2}}$$

$$B_{M-1j}^{k+\frac{1}{2}} = -[\Pi_{M-2j}^+ (\frac{2}{3} - \frac{4}{3(M-1)} \Pi_{M-2j}^- - \frac{1}{3} \Pi_{Mj}^+ + \frac{4h^2}{B\tau})]^{k+\frac{1}{2}}$$

$$D_{M-1j}^{k+\frac{1}{2}} = -[R_{M-1j}^+ + \frac{4h^2}{B\tau} S_{M-1j}]^k$$

$$S_{Mj}^{k+\frac{1}{2}} = [-\frac{1}{3} S_{M-2j} + \frac{4}{3} S_{M-1j}]^{k+\frac{1}{2}}$$

For the js boundary, when js=0:

$$B_{i,1}^{k+1} = \left[\frac{1}{3} \Pi_{i,0} - \frac{5}{3} \Pi_{i,1} - \Pi_{i,2} + h \frac{dk_r}{dS} \Big|_{i,1} - \frac{4h^2}{B\tau} \right]^{k+1}$$

$$C_{i,1}^{k+1} = \left[-\frac{1}{3} \Pi_{i,0} + \frac{2}{3} \Pi_{i,1} + \Pi_{i,2} - \frac{4}{3} h \frac{dk_r}{dS} \Big|_{i,1} \right]^{k+1}$$

$$D_{i,1}^{k+1} = \left[\frac{1}{3} (\Pi_{i,0} + \Pi_{i,1} + h \frac{dk_r}{dS} \Big|_{i,1}) \frac{2h}{\frac{d\varphi}{dS} \Big|_{i,0}} \right]^{k+1} - \left[Z_{i,1} + \frac{4h^2}{B\tau} S_{i,1} \right]^{k+\frac{1}{2}}$$

$$S_{i,0}^{k+1} = \left[\frac{4}{3} S_{i,1} - \frac{1}{3} S_{i,2} - \frac{2h}{3 \frac{d\varphi}{dS} \Big|_{i,0}} \right]^{k+1}$$

when js \neq 0:

$$B_{i,js+1}^{k+1} = - \left[\Pi_{i,js} + 2\Pi_{i,js+1} + \Pi_{i,js+2} + \frac{4h^2}{B\tau} \right]^{k+1}$$

$$C_{i,js+1}^{k+1} = \left[\Pi_{i,js+1} + \Pi_{i,js+2} - h \frac{dk_r}{dS} \Big|_{i,js+1} \right]^{k+1}$$

$$D_{i,js+1}^{k+1} = - \left[\left[Z_{i,js+1} + \frac{4h^2}{B\tau} S_{i,js+1} \right]^{k+\frac{1}{2}} + \left[\Pi_{i,js} + \Pi_{i,js+1} + h \frac{dk_r}{dS} \Big|_{i,js+1} \right]^{k+1} S_s \right]$$

For the N boundary:

$$A_{i,N-1}^{k+1} = \left[\Pi_{i,N-2} + \frac{2}{3} \Pi_{i,N-1} - \frac{1}{3} \Pi_{i,N} + \frac{4}{3} h \frac{dk_r}{dS} \Big|_{i,N-1} \right]^{k+1}$$

$$B_{i,N-1}^{k+1} = - \left[\Pi_{i,N-2} + \frac{2}{3} \Pi_{i,N-1} - \frac{1}{3} \Pi_{i,N} + \frac{4h^2}{B\tau} + \frac{4}{3} h \frac{dk_r}{dS} \Big|_{i,N-1} \right]^{k+1}$$

$$D_{i,N-1}^{k+1} = - \left[Z_{i,N-1} + \frac{4h^2}{B\tau} S_{i,N-1} \right]^{k+\frac{1}{2}} + \left[\frac{1}{3} (\Pi_{i,N-1} + \Pi_{i,N} - h \frac{dk_r}{dS} \Big|_{i,N-1}) \frac{2h}{\frac{d\phi}{dS} \Big|_{i,N}} \right]^{k+1}$$

$$S_{i,N}^{k+1} = \left[-\frac{1}{3} S_{i,N-2} + \frac{4}{3} S_{i,N-1} - \frac{2h}{3 \frac{d\phi}{dS} \Big|_{i,N}} \right]^{k+1}$$

APPENDIX B

Vapor Concentration Contour Maps

T2L1H50

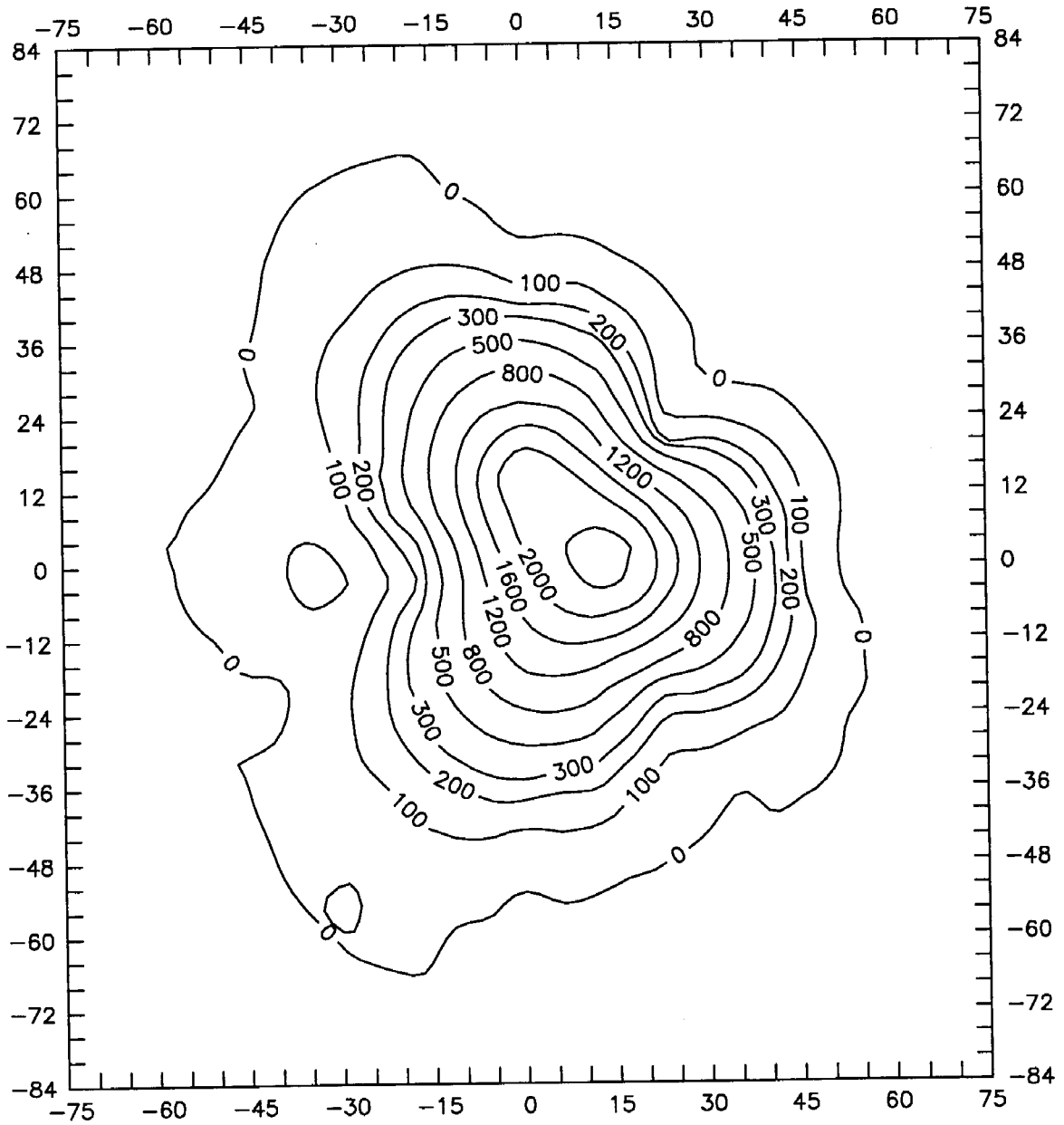


Figure B.1. Vapor concentration contour map
(Test II, Level 1, 50 hrs)

T2L1H100

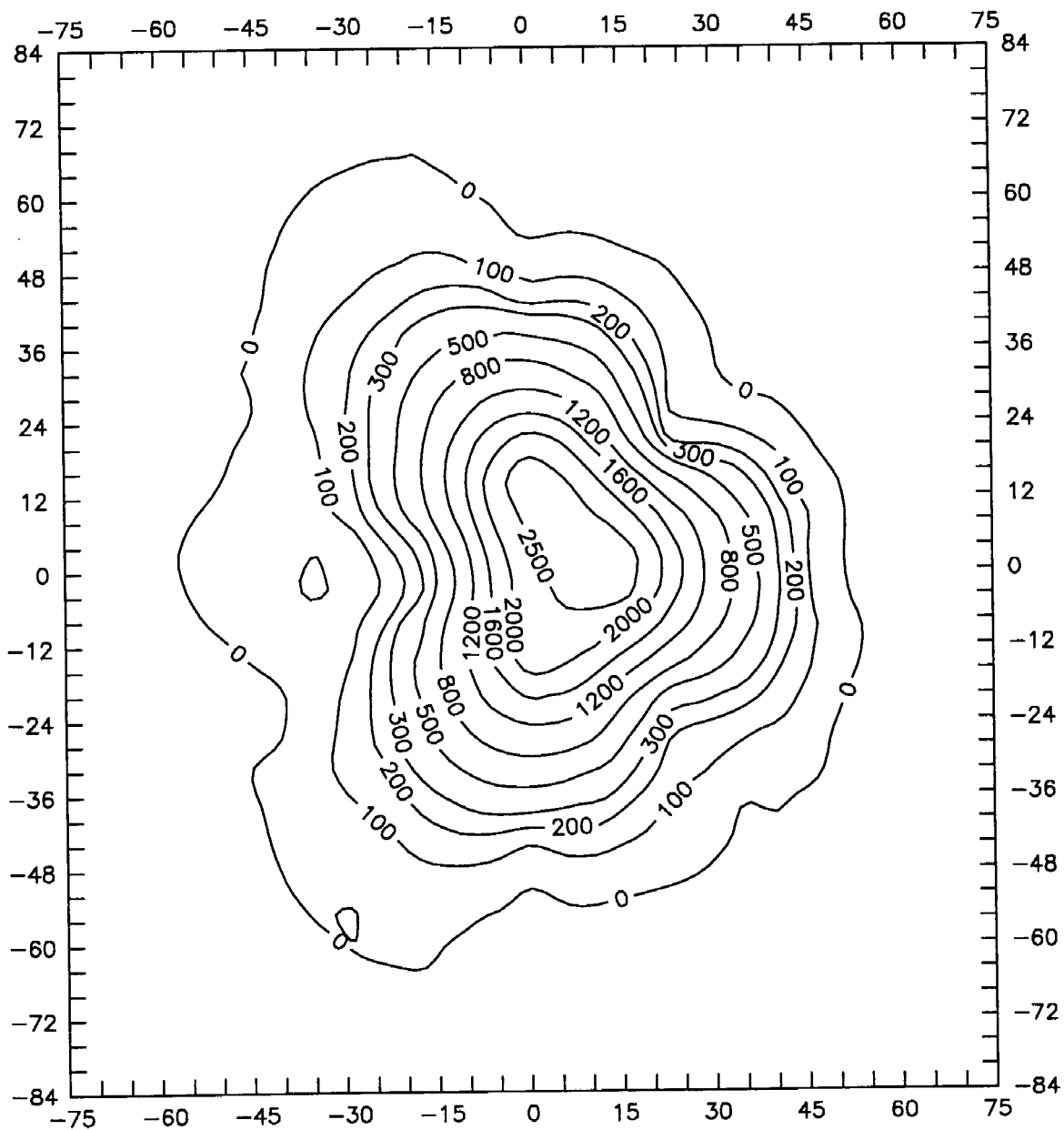


Figure B.2. Vapor concentration contour map
(Test II, Level 1, 100 hrs)

T2L1H300

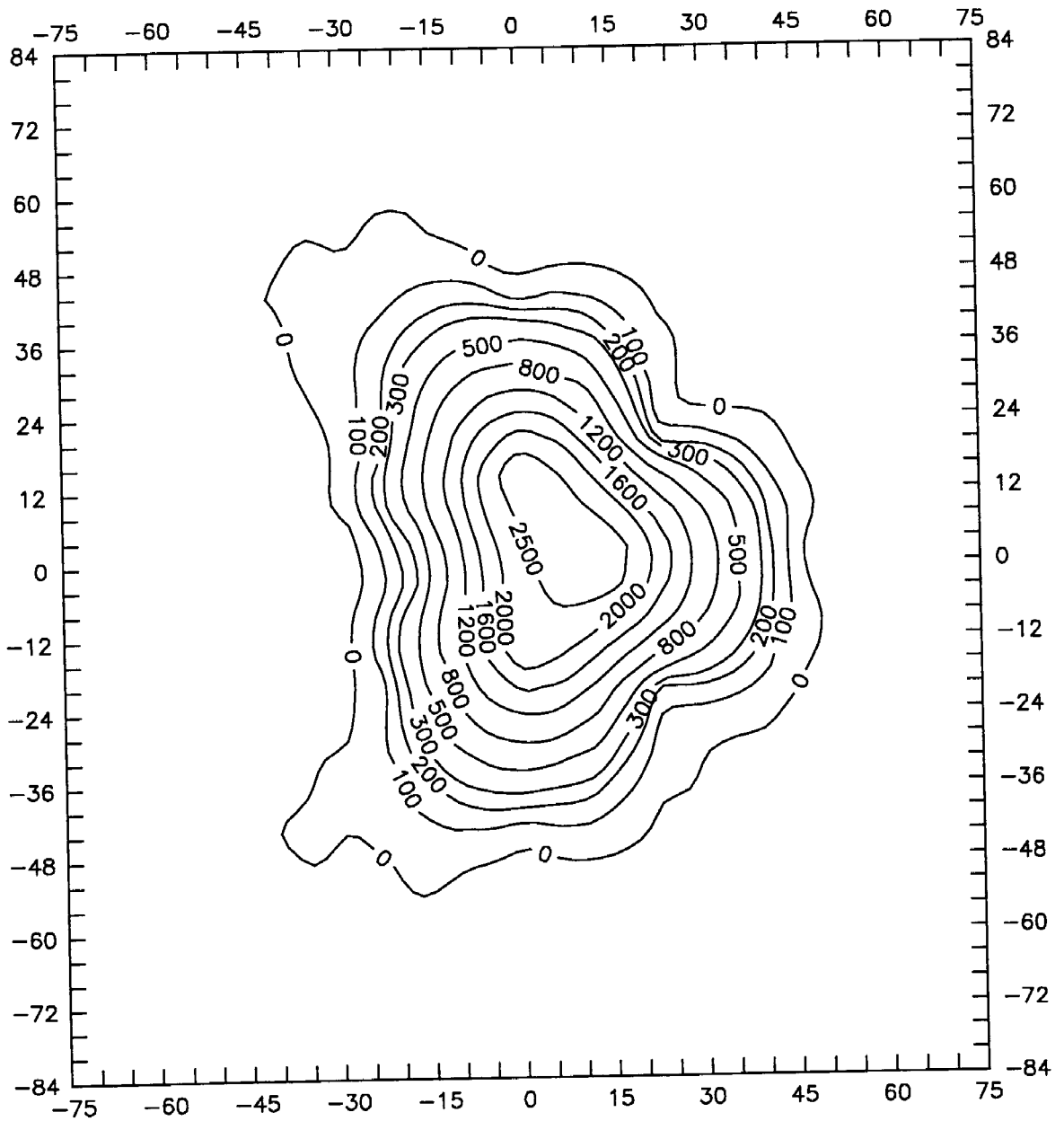


Figure B.3. Vapor concentration contour map
(Test II, Level 1, 300 hrs)

T2L1H600

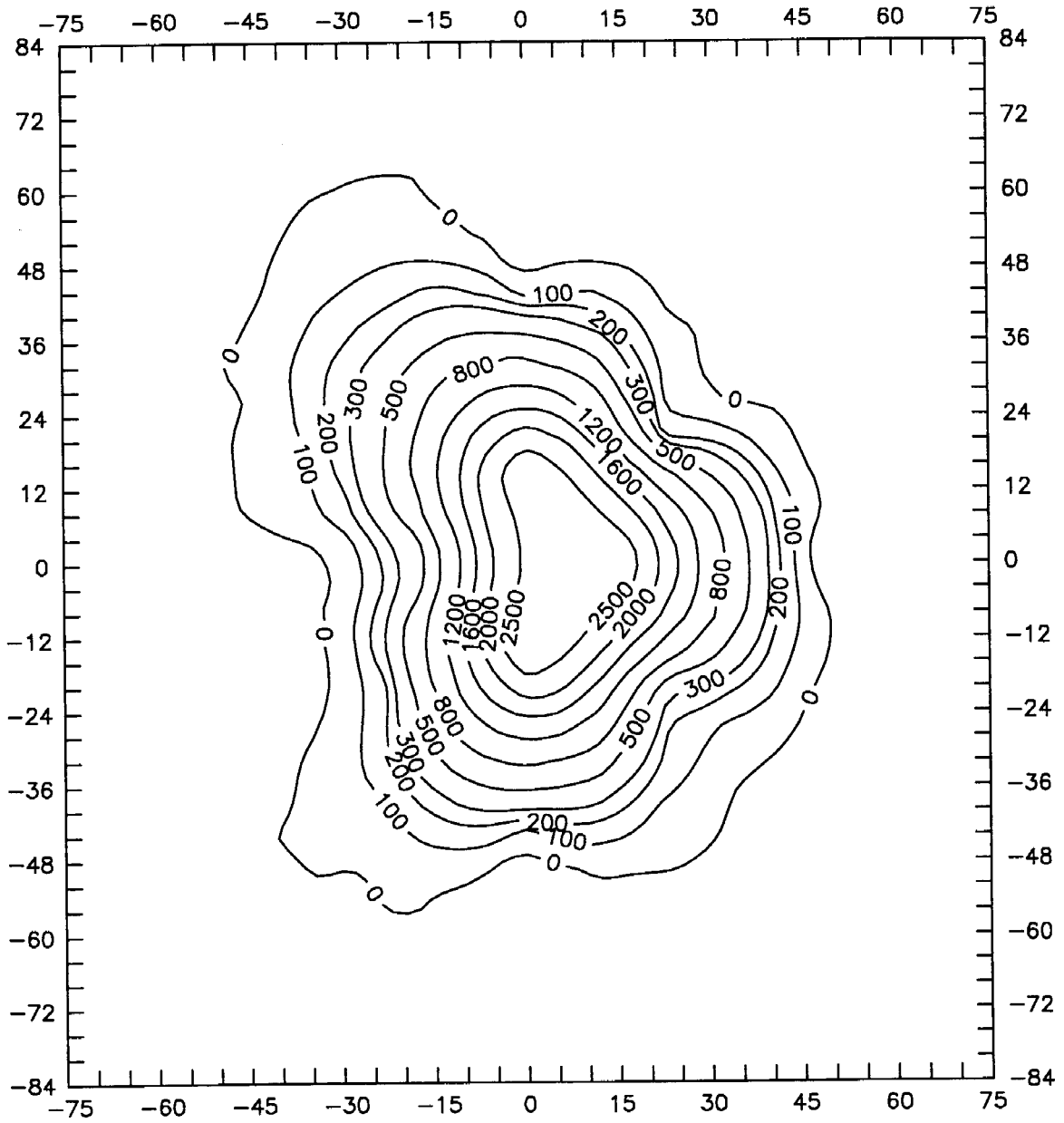


Figure B.4. Vapor concentration contour map
(Test II, Level 1, 600 hrs)

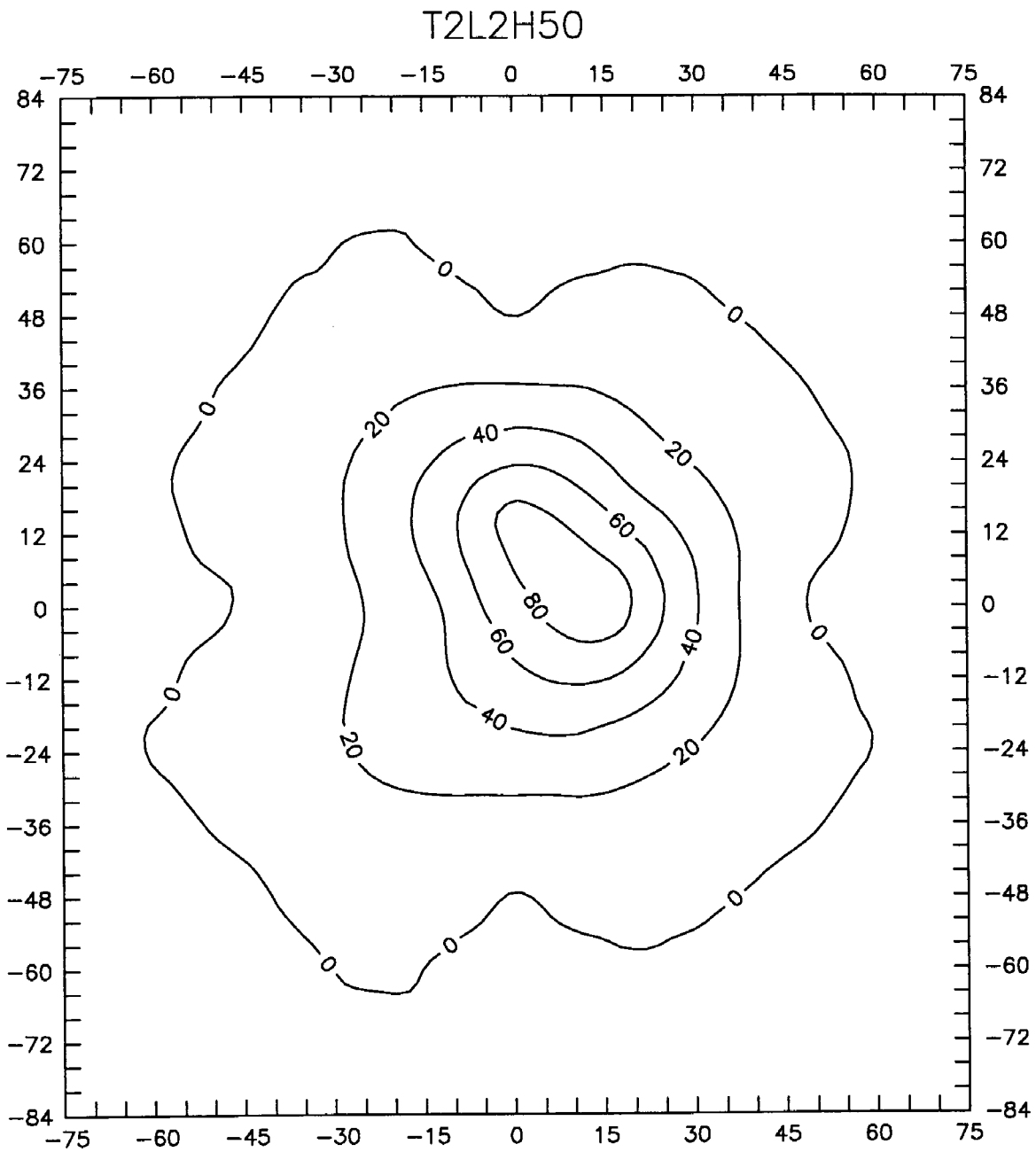


Figure B.5. Vapor concentration contour map
(Test II, Level 2, 50 hrs)

T2L2H100

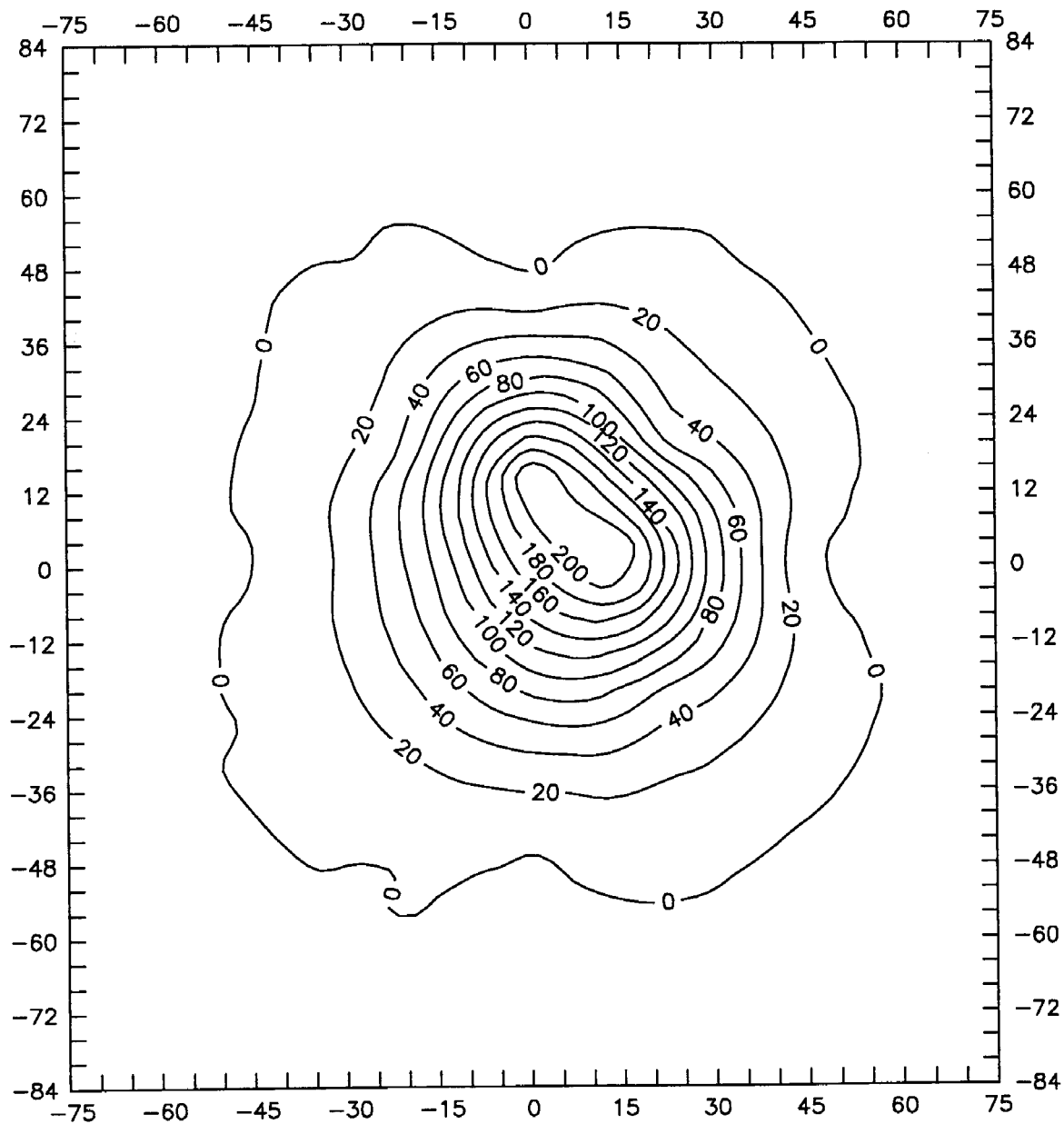


Figure B.6. Vapor concentration contour map
(Test II, Level 2, 100 hrs)

T2L2H300

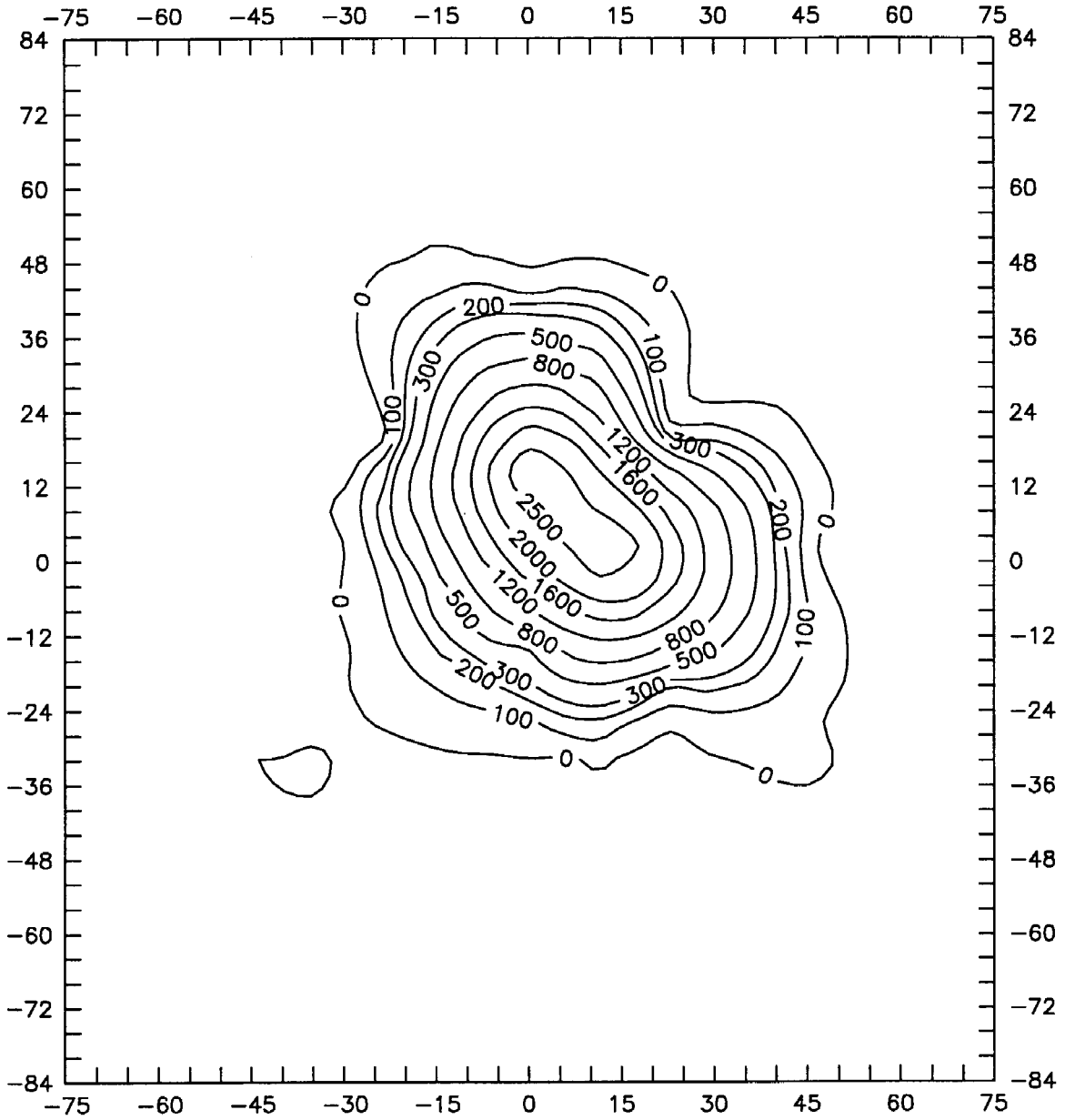


Figure B.7. Vapor concentration contour map
(Test II, Level 2, 300 hrs)

T2L2H600

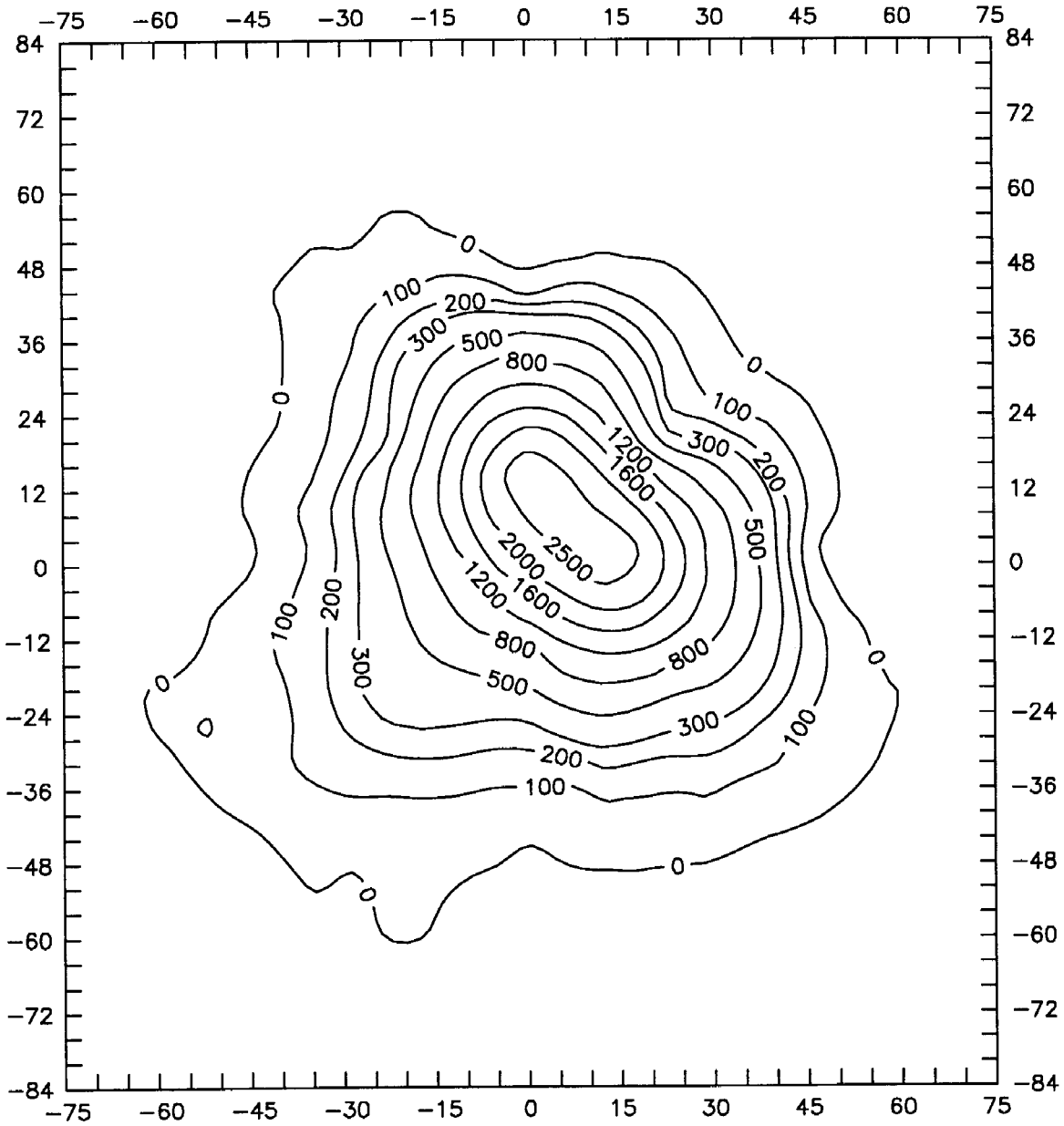


Figure B.8. Vapor concentration contour map
(Test II, Level 2, 600 hrs)

T2L3H300

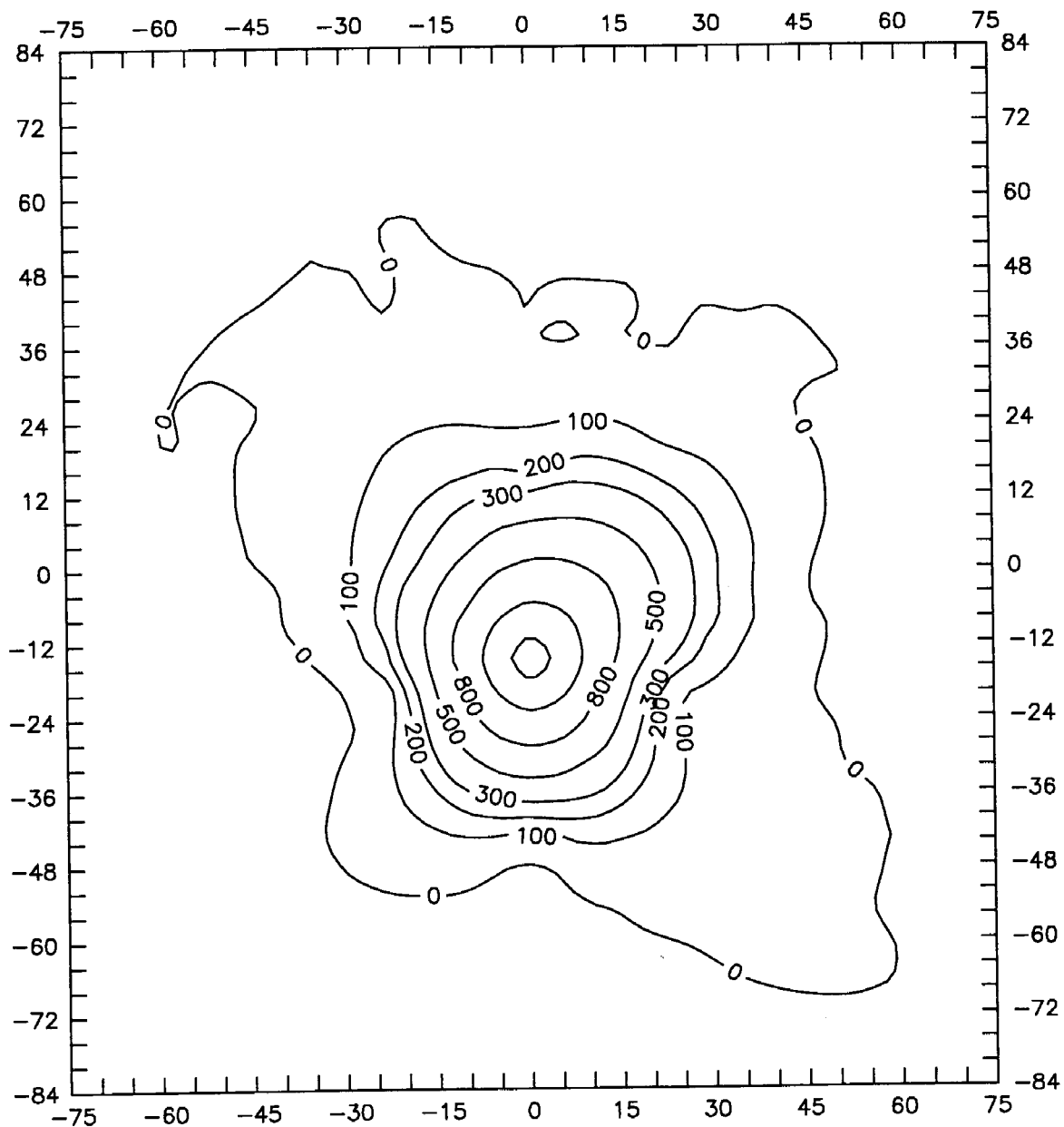


Figure B.9. Vapor concentration contour map
(Test II, Level 3, 300 hrs)

T2L3H600

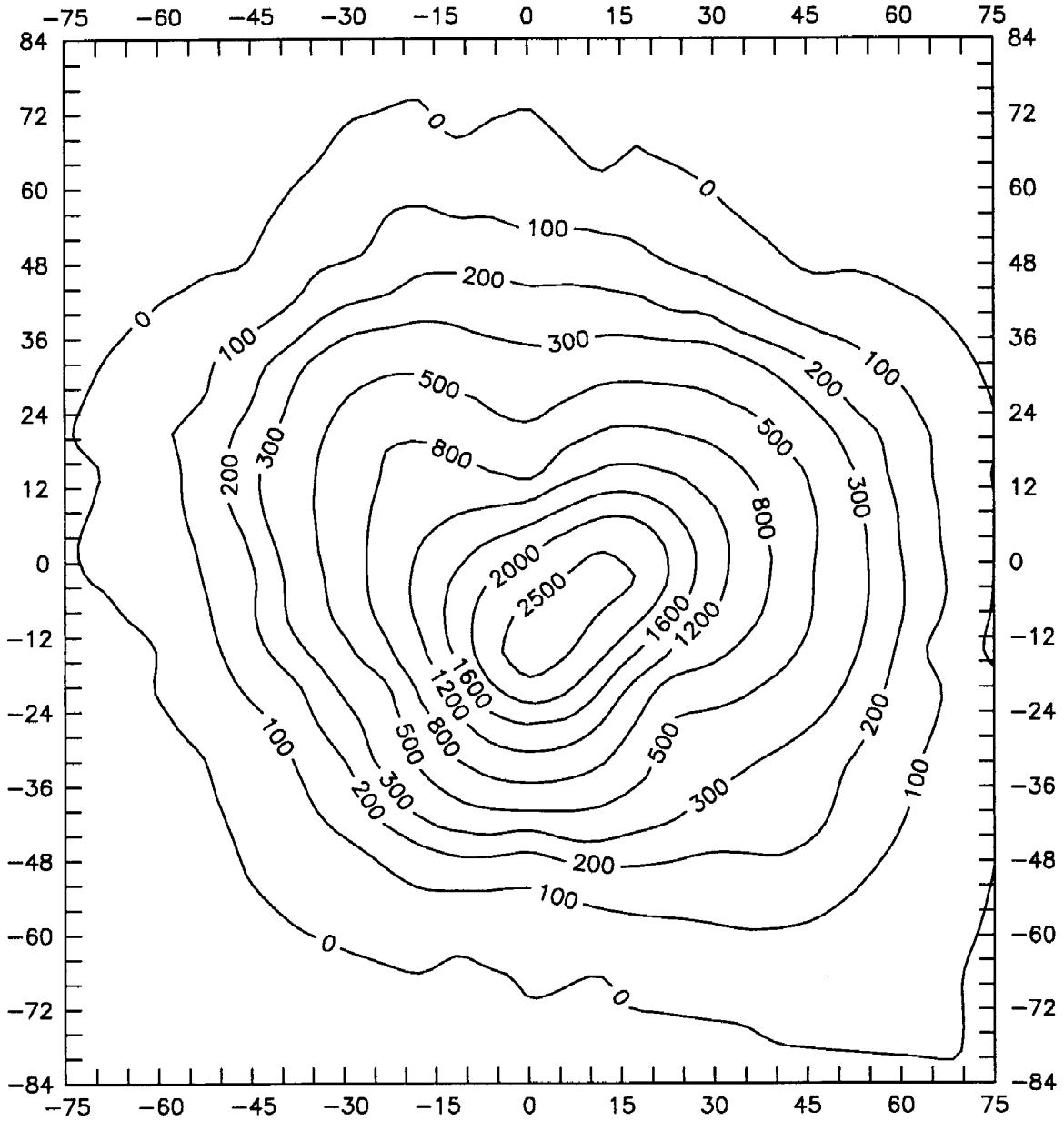


Figure B.10. Vapor concentration contour map
(Test II, Level 3, 600 hrs)

T4L1H2O

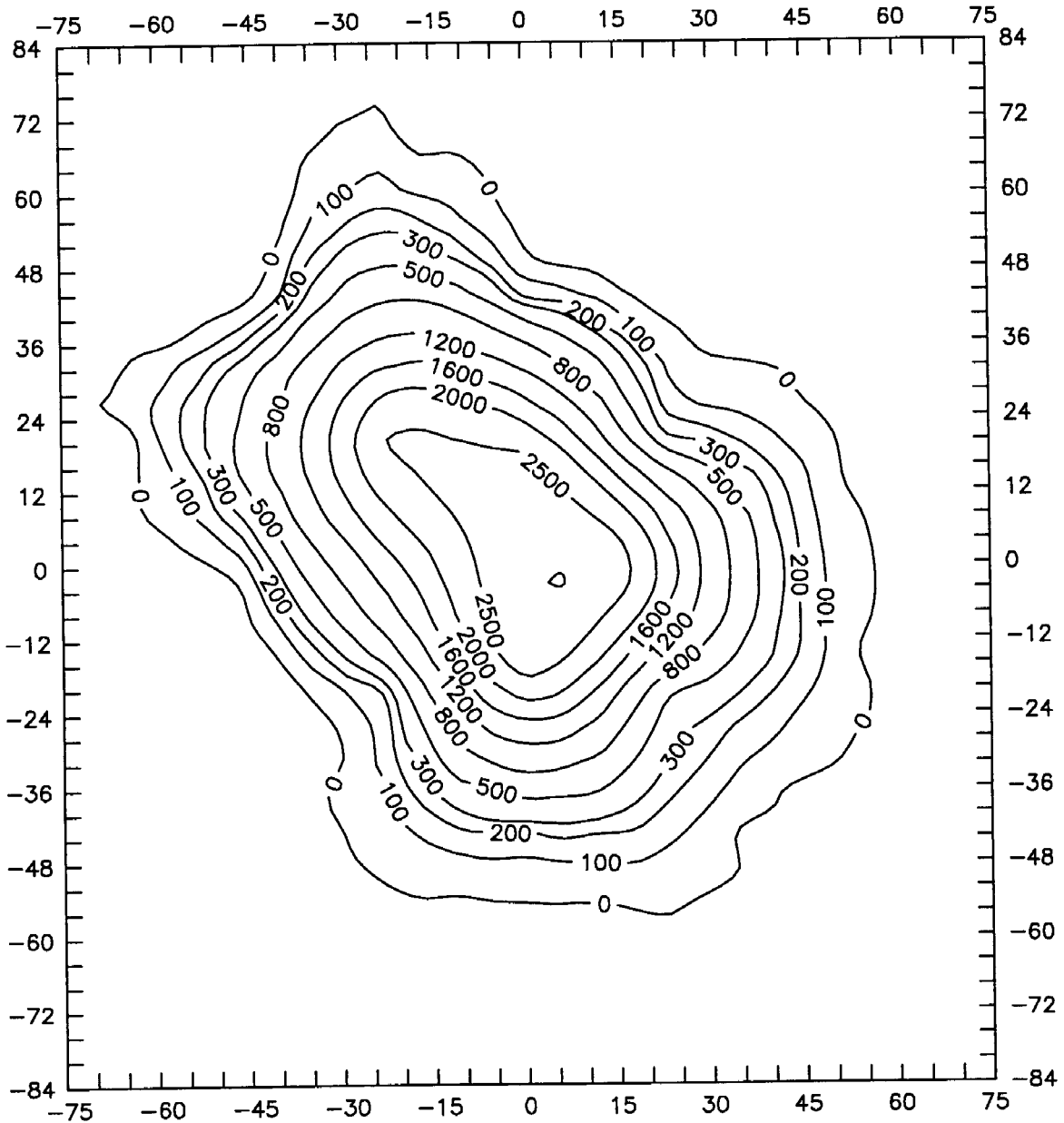


Figure B.11. Vapor concentration contour map
(Test IV, Level 1, 20 hrs)

T4L1H80

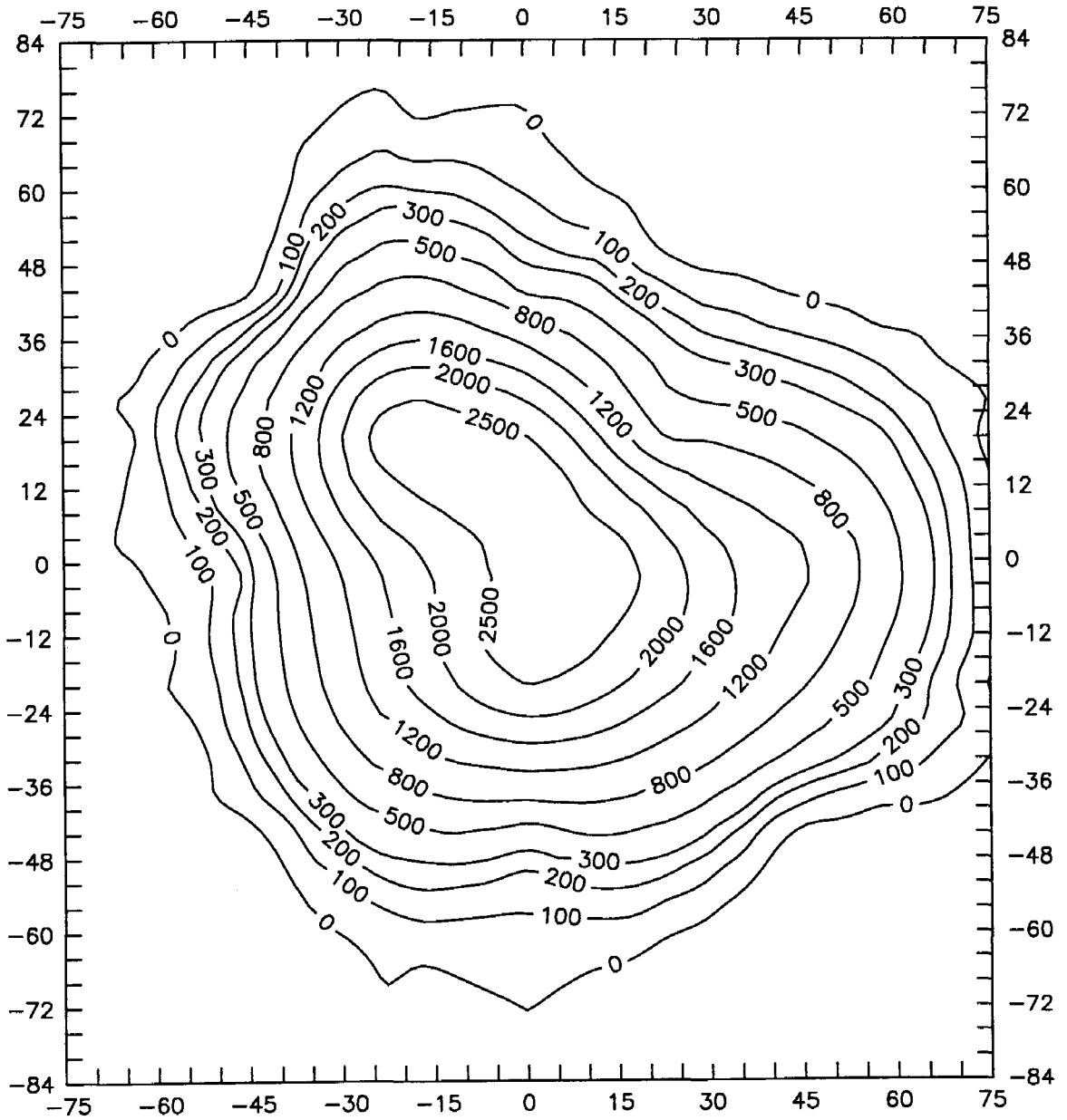


Figure B.12. Vapor concentration contour map
(Test IV, Level 1, 80 hrs)

T4L1H300

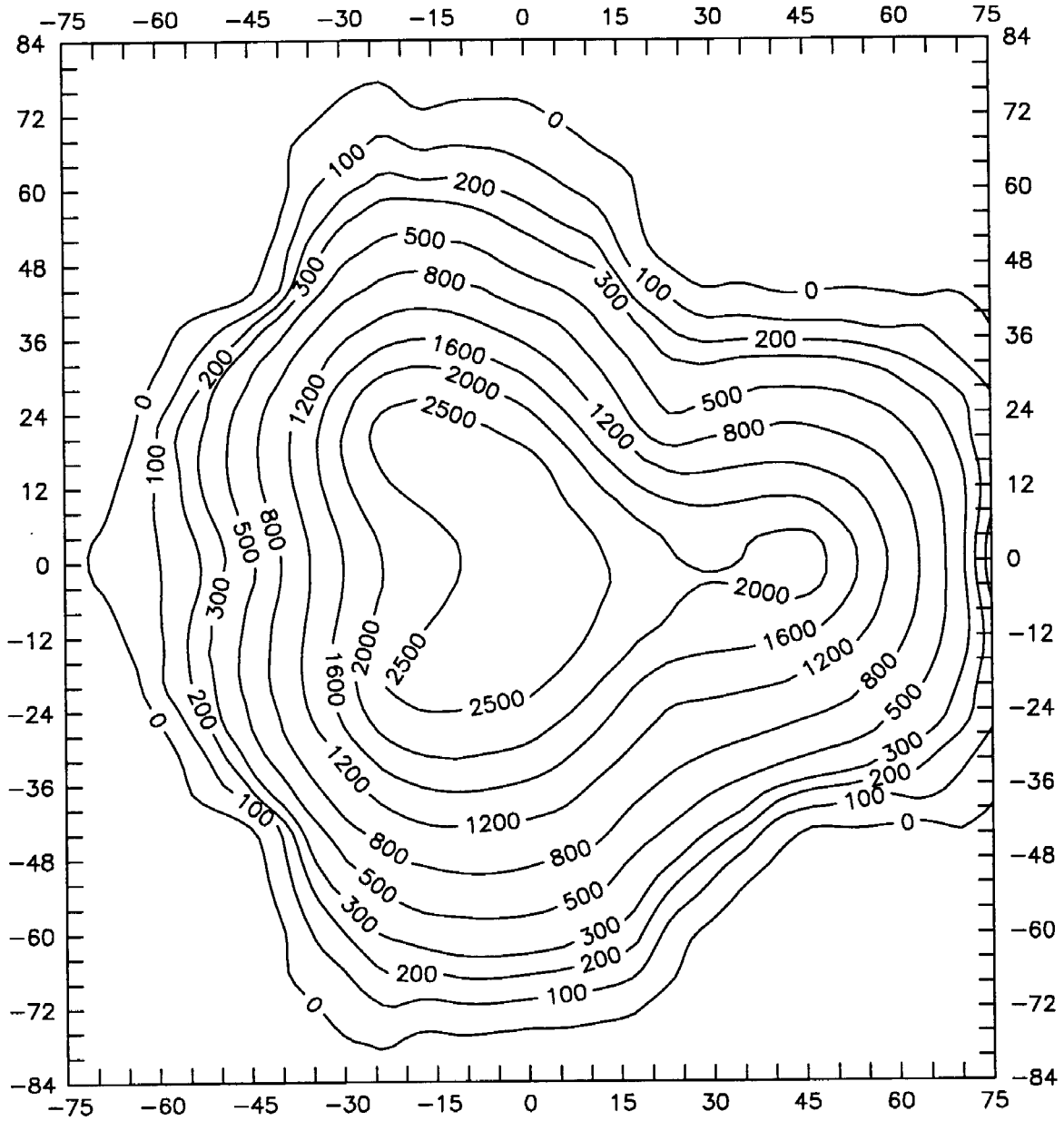


Figure B.13. Vapor concentration contour map
(Test IV, Level 1, 300 hrs)

T4L1H600

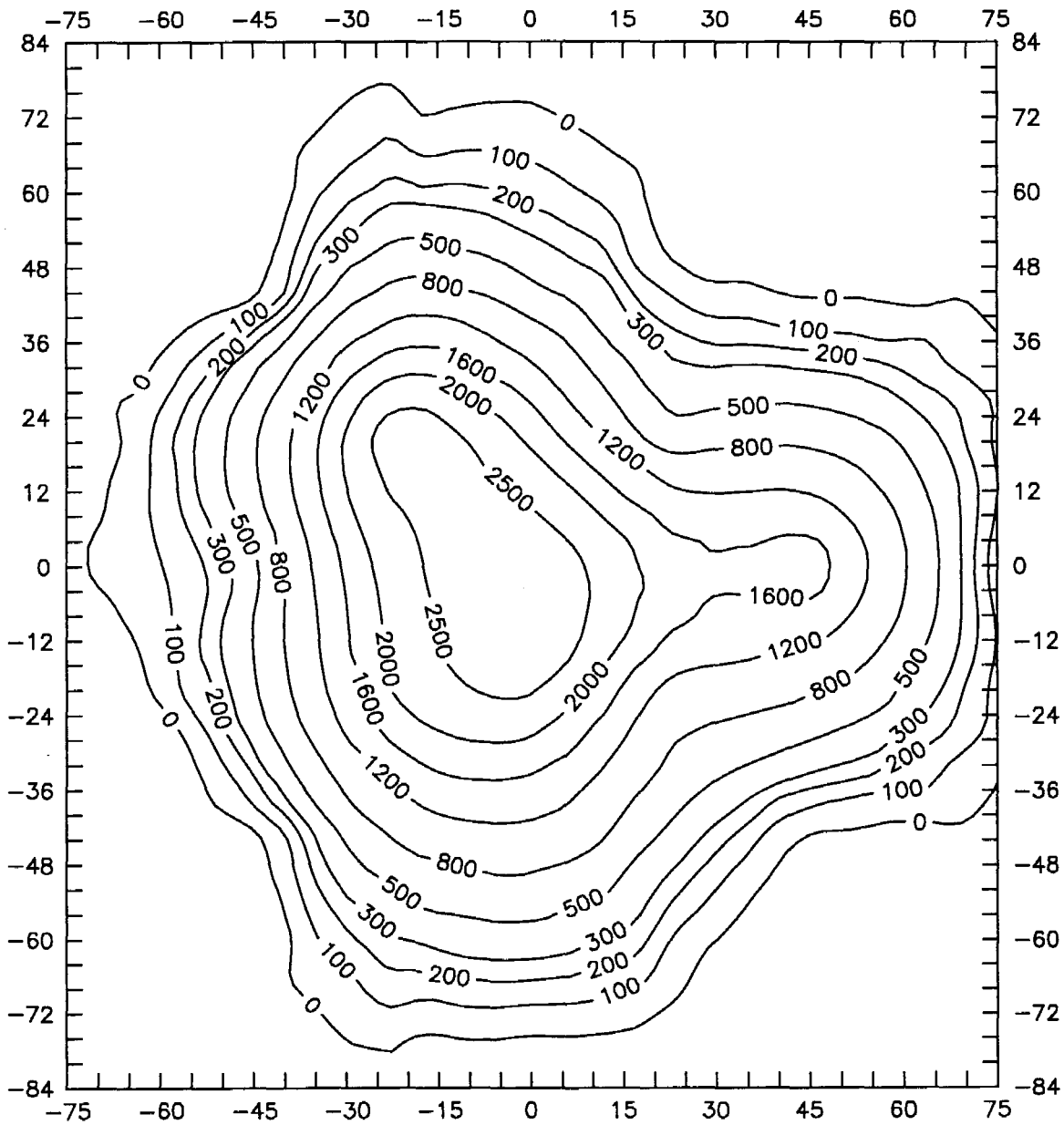


Figure B.14. Vapor concentration contour map
(Test IV, Level 1, 600 hrs)

T4L2H20

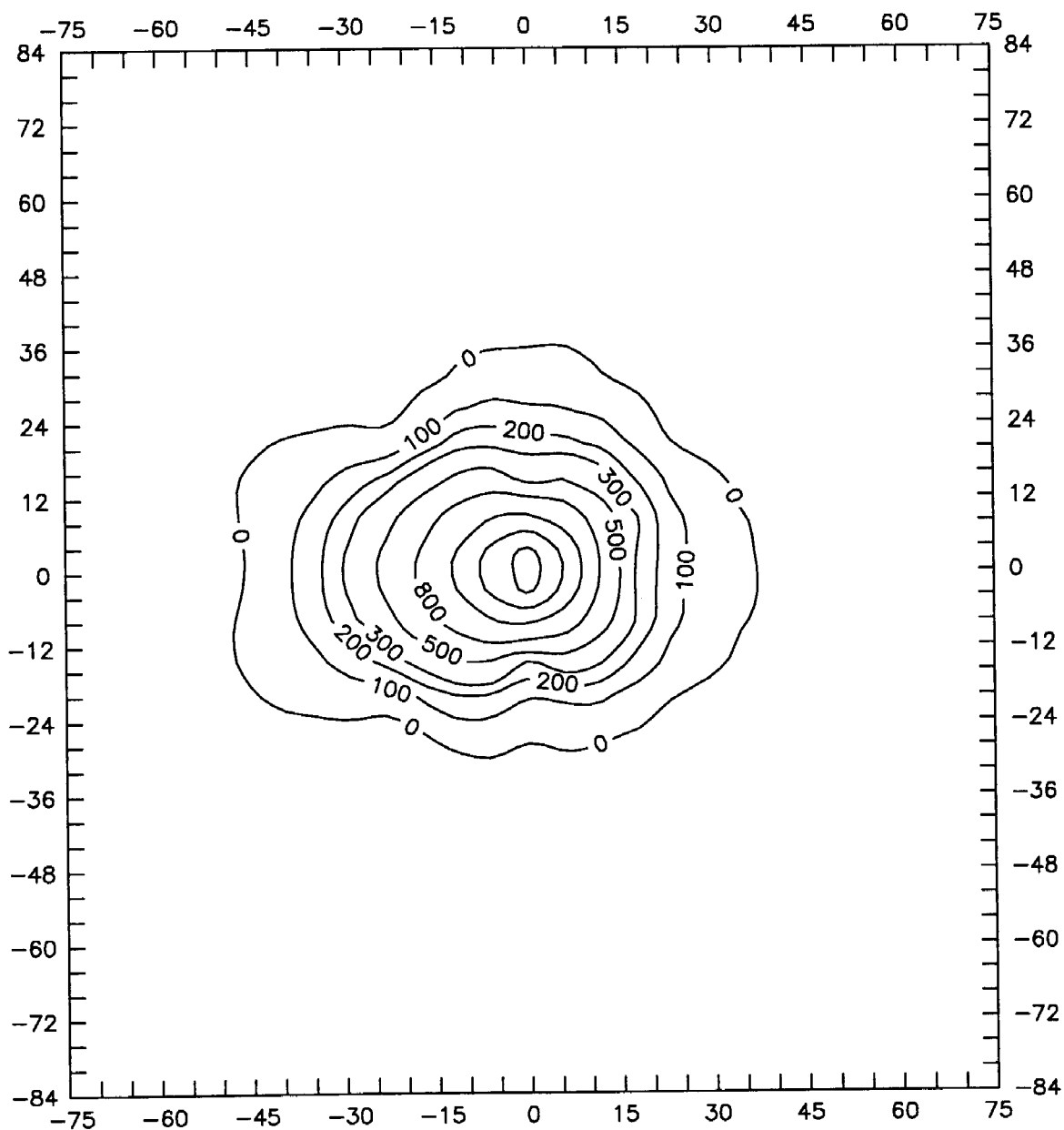


Figure B.15. Vapor concentration contour map
(Test IV, Level 2, 20 hrs)

T4L2H80

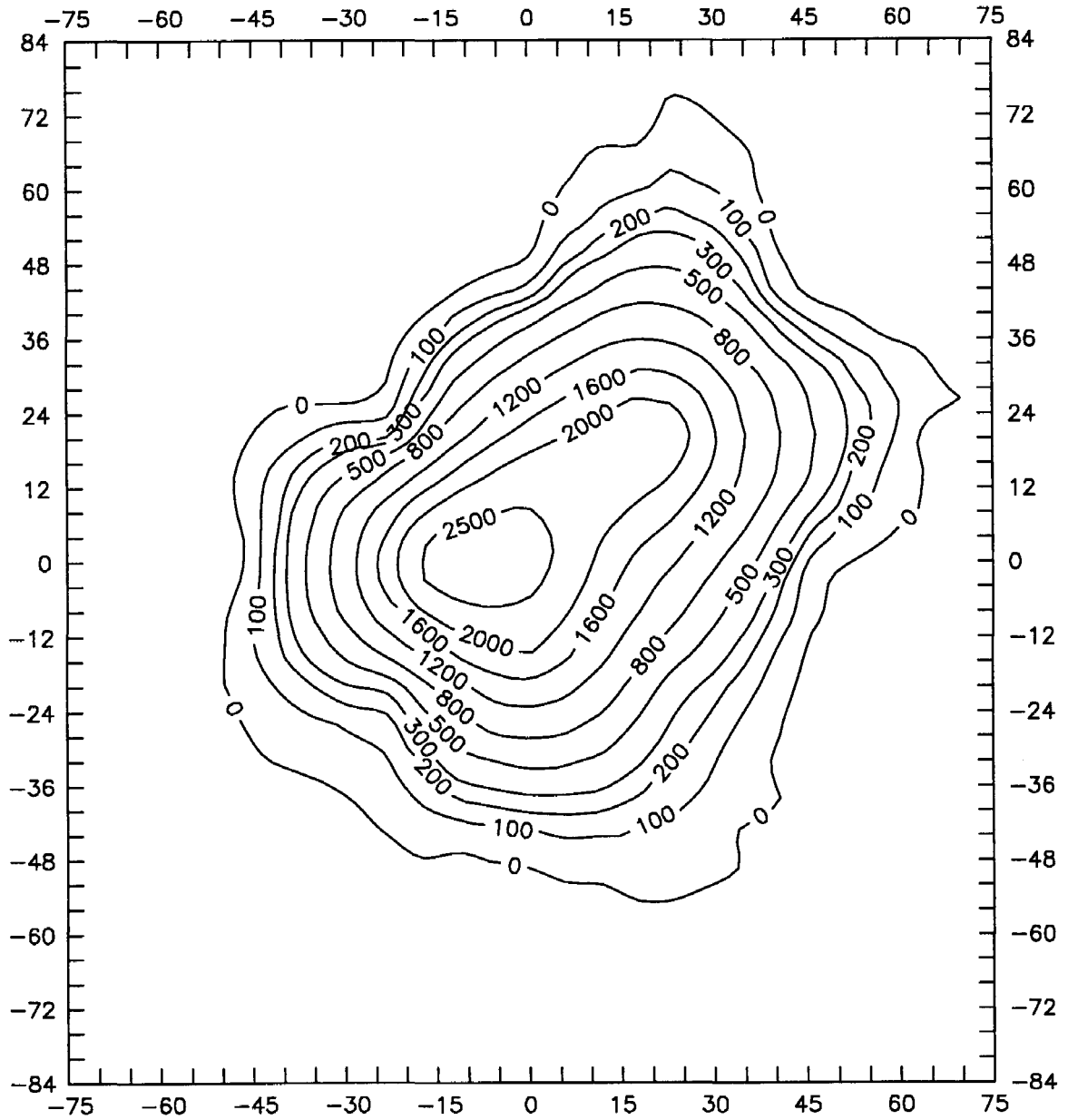


Figure B.16. Vapor concentration contour map
(Test IV, Level 2, 80 hrs)

T4L2H300

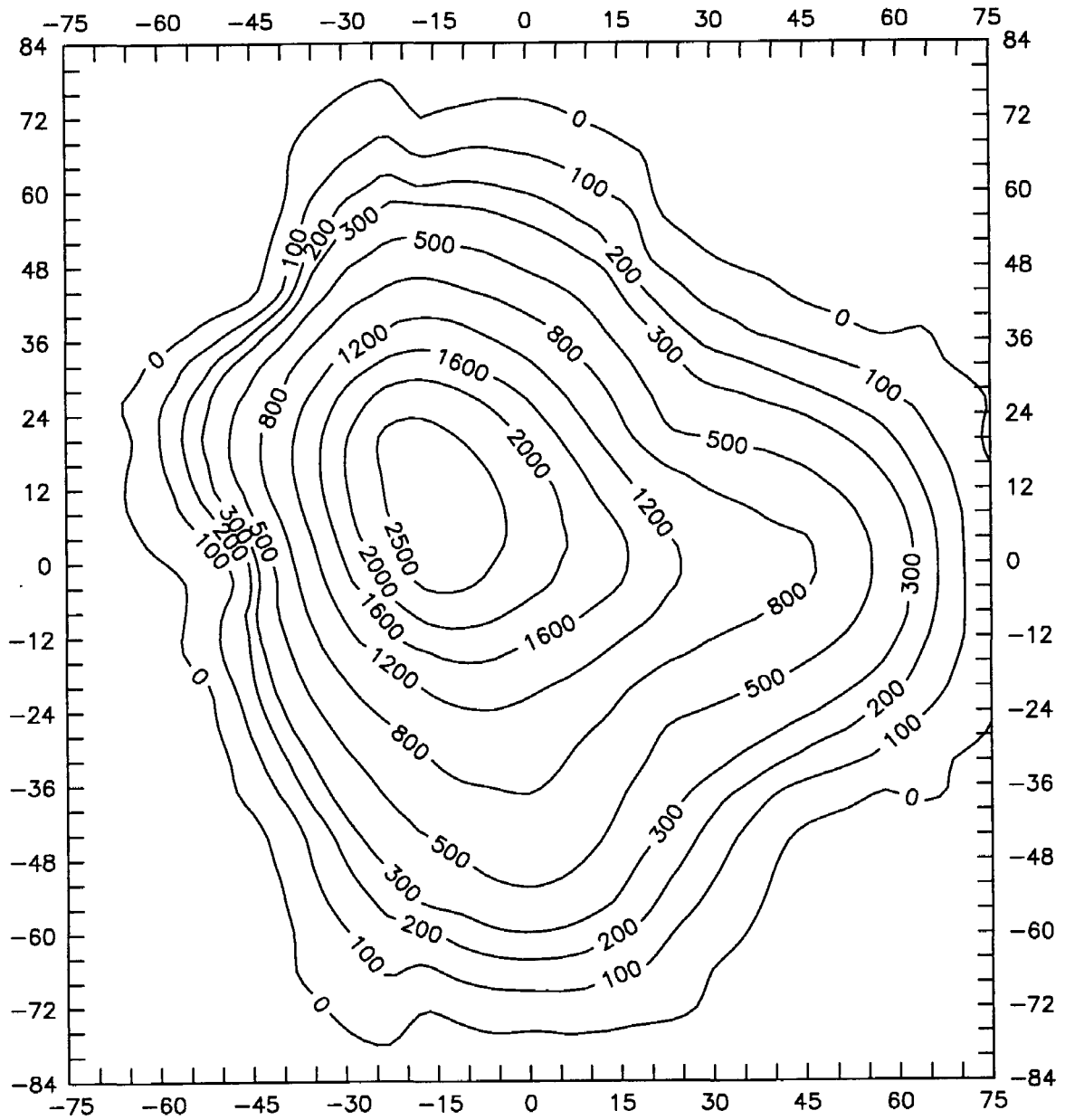


Figure B.17. Vapor concentration contour map
(Test IV, Level 2, 300 hrs)

T4L2H600

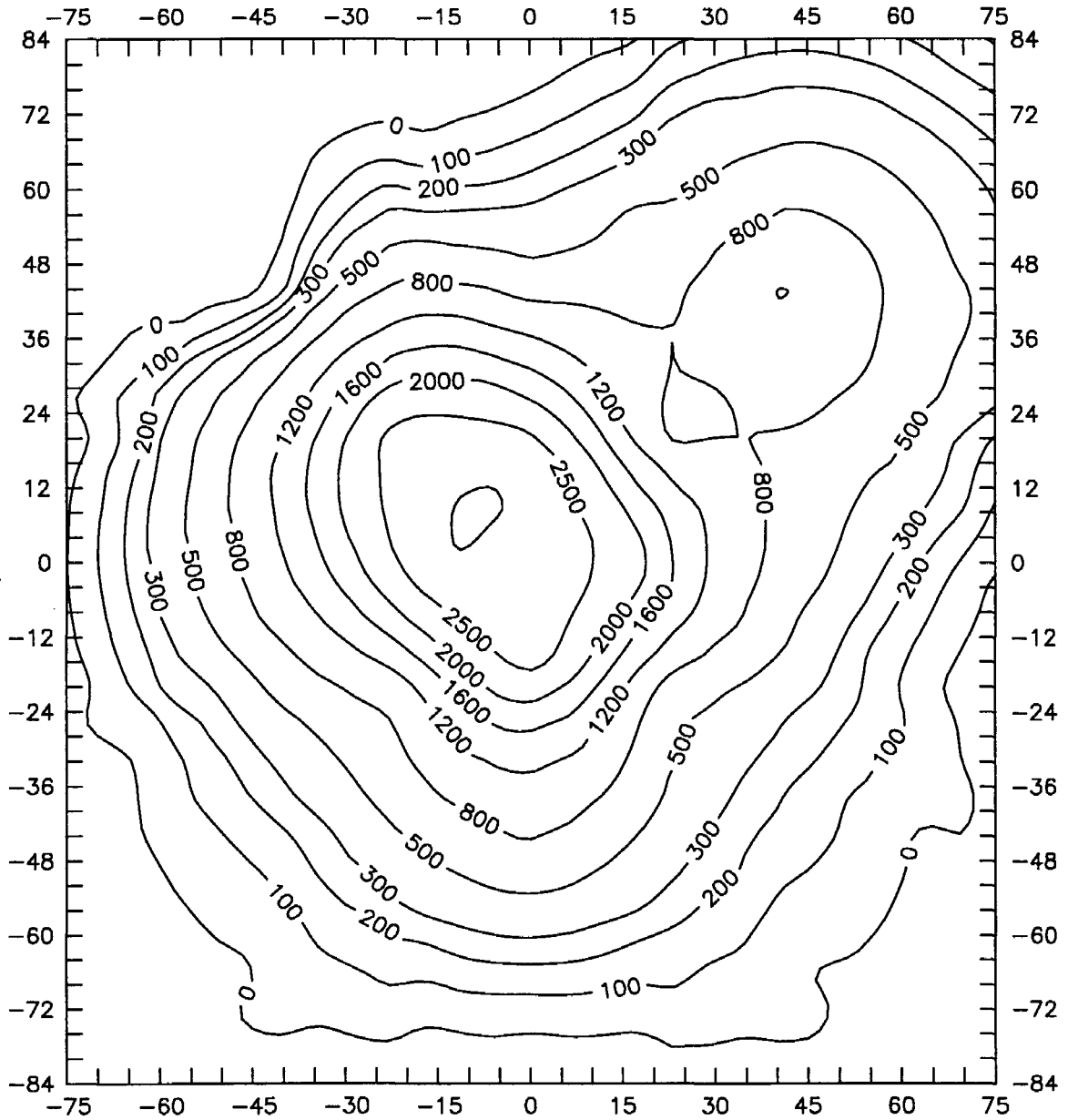


Figure B.18. Vapor concentration contour map
(Test IV, Level 2, 600 hrs)

T4L3H80

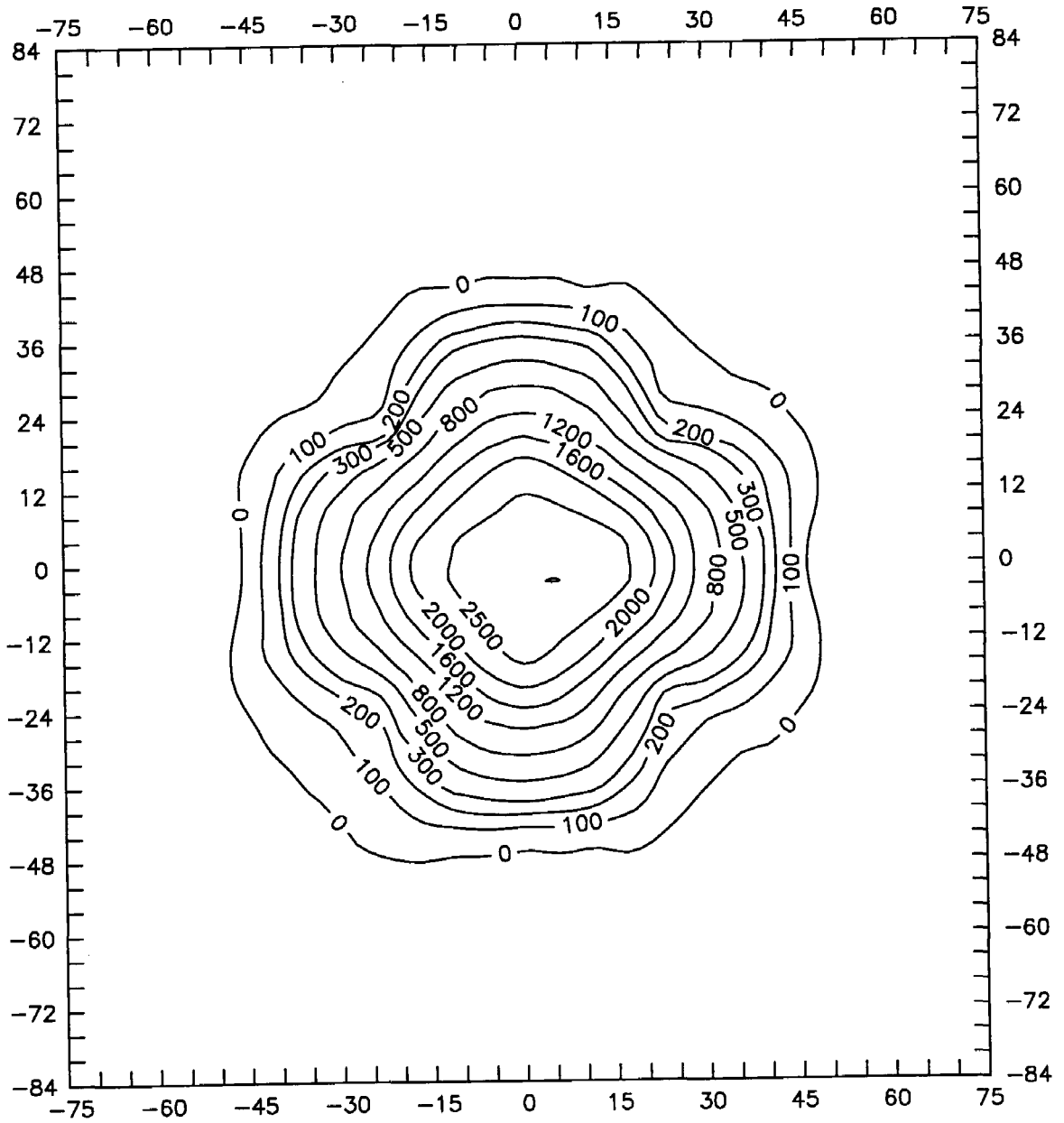


Figure B.19. Vapor concentration contour map
(Test IV, Level 3, 80 hrs)

T4L3H300

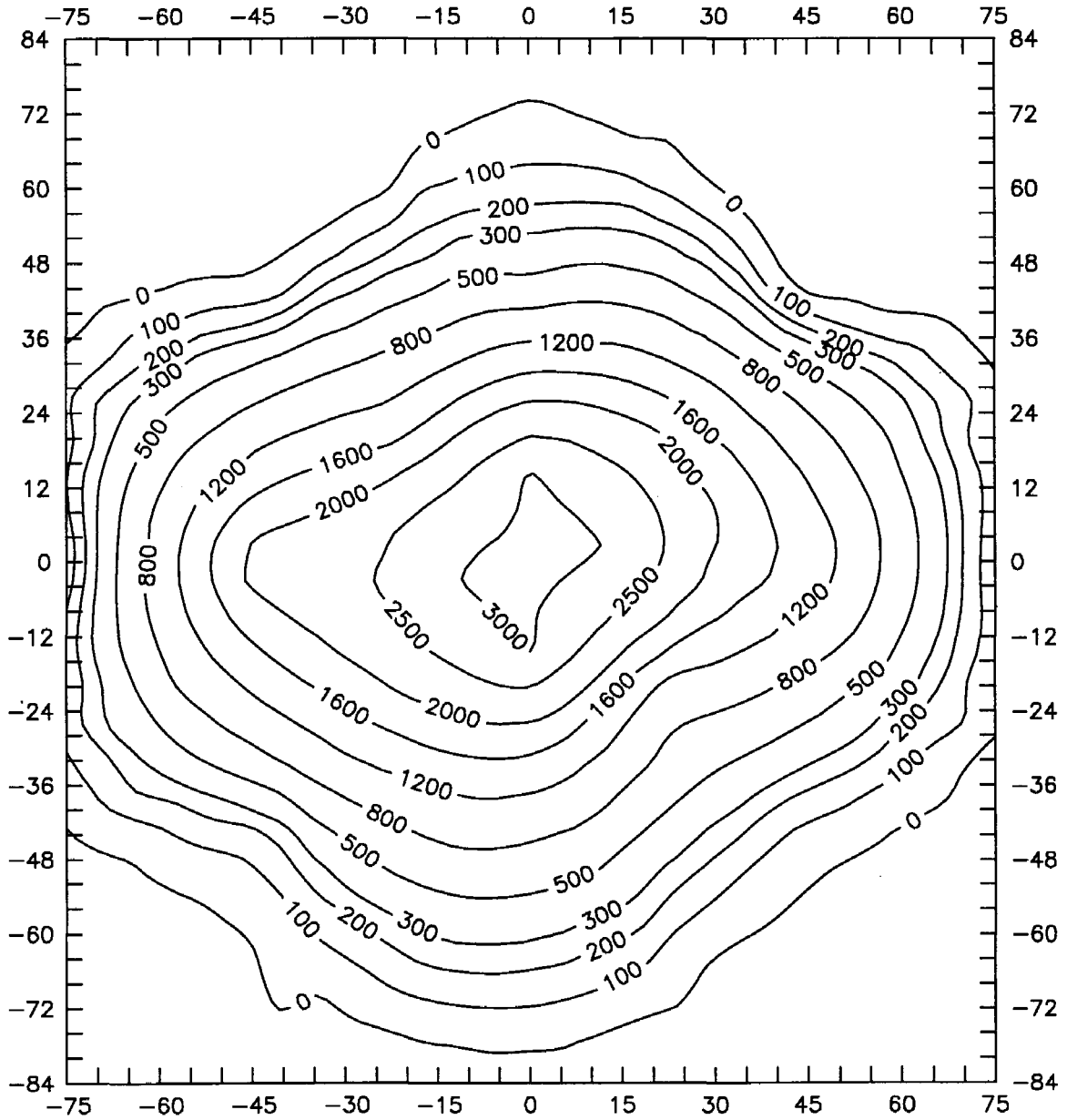


Figure B.20. Vapor concentration contour map
(Test IV, Level 3, 300 hrs)

T4L3H600

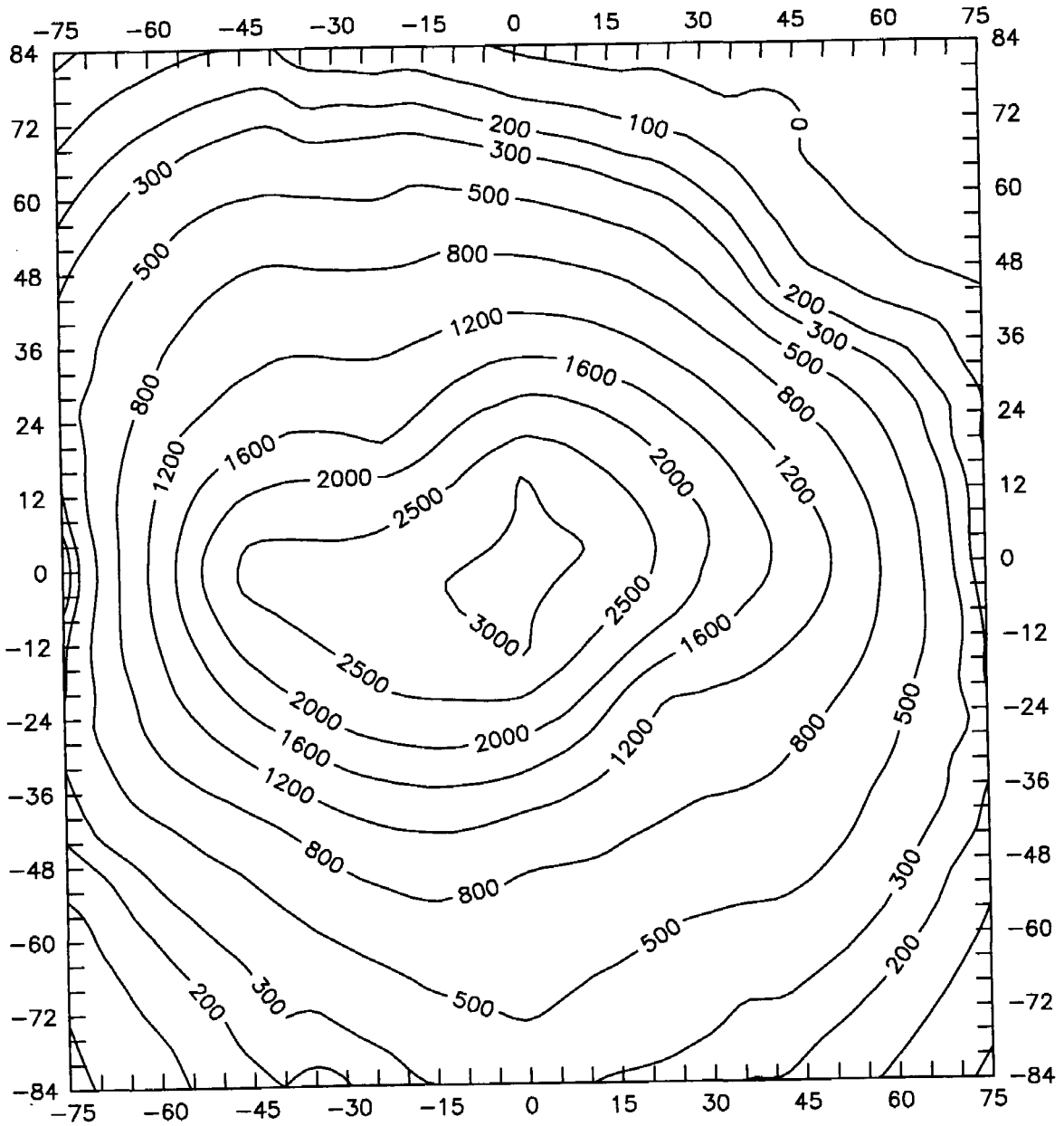


Figure B.21. Vapor concentration contour map
(Test IV, Level 3, 600 hrs)

APPENDIX C

Experimentally Observed Vapor Concentration Data

Table C1. Diesel vapor concentration for Test II and Test III
(in ppm of n-butane + i-pentane)

Time (hr)	Test II				Test III	
	R1L1	R1L2	R1L3	R2L3	R1L1	R2L2
0	0	0	0	0	0	0
10	325	33	0	0	215	6
20	631	46	1	0	395	8
30	1103	59	2	0	575	10
40	1563	70	3	0	872	12
50	2015	80	4	0	1195	14
60	2510	90	5	0	1508	14
70	2718	100	6	0	1814	10
80	2920	113	6	1	2123	6
90	3075	130	6	1	2471	2
100	3090	146	6	0	2848	0
110	3104	163	6	0	3448	0
120	3119	180	6	0	4036	0
130	3134	207	6	0	4614	0
140	3148	242	6	0	5236	0
150	3143	276	7	0	5903	0
160	3120	311	7	0	6671	0
170	3097	351	8	0	7026	0
180	3074	449	9	0	7364	0
190	3050	546	9	0	7626	0
200	3049	691	10	0	7731	0
210	3075	932	32	5	7836	0
220	3100	1259	86	10	7942	0
230	3126	1664	139	15	8010	0
240	3152	1970	193	20	8029	0
250	3177	2118	247	25	8049	0
260	3193	2262	317	29	8069	0
270	3208	2298	388	33	8089	1
280	3223	2334	458	37	8109	3
290	3237	2369	528	41	8146	5
300	3252	2405	595	47	8191	7
310	3269	2434	661	53	8236	9
320	3287	2463	727	60	8281	27
330	3304	2491	792	66	8327	55
340	3322	2519	858	76	8372	83
350	3340	2552	923	91	8404	112
360	3367	2588	987	105	8432	140

(Continued next page)

(Table C1.-Continued)

Time (hr)	Test II				Test III	
	R1L1	R1L2	R1L3	R2L3	R1L1	R2L2
370	3418	2624	1052	118	8460	168
380	3468	2660	1120	130	8488	196
390	3519	2696	1198	142	8504	292
400	3568	2729	1275	155	8483	391
410	3613	2761	1352	169	8463	489
420	3658	2794	1409	182	8442	588
430	3703	2827	1465	196	8422	686
440	3748	2861	1522	210	8401	902
450	3791	2899	1581	223	8371	1239
460	3834	2936	1640	237	8339	1697
470	3877	2974	1698	251	8306	2322
480	3938	3012	1778	266	8273	2893
490	4020	3062	1900	285	8241	3287
500	4102	3128	2021	312	8208	3592
510	4184	3193	2187	339	8214	3893
520	4241	3259	2362	364	8249	4158
530	4282	3324	2518	390	8283	4423
540	4323	3408	2660	411	8318	4688
550	4365	3498	2741	431	8353	4947
560	4351	3587	2776	446	8409	5205
570	4316	3677	2812	456	8471	5420
580	4282	3778	2843	466	8533	5553
590	4247	3882	2840	476	8595	5686
600	4203	3985	2837	482	8640	5819
610	4152	4124	2834	488	8653	5948
620	4101	4302	2831	494	8667	6005
630	4050	4469	2847	499	8680	6061
640	4039	4592	2864	504	8694	6117
650	4029	4715	2881	508	8735	6173
660					8793	6230
670					8851	6288
680					8909	6346
690					8978	6403
700					9084	6457
710					9190	6496
720					9198	6534

Table C2a. JP-5 vapor concentration for Test IV
(in ppm of n-butane + i-pentane)

Time (hr)	R0L1	R0L2	R0L3	R1L1	R1I2	R1L3
0	0	0	0	0	0	0
10	3163	2	0	1249	38	7
20	3231	1705	8	2526	438	24
30	3101	3104	208	2670	1499	104
40	2980	3282	5032	2748	1911	474
50	2863	3171	5464	2779	2058	1095
60	2787	3056	5541	2791	2132	1682
70	2720	2938	5447	2792	2173	2094
80	2667	2817	5353	2773	2204	2517
90	2619	2695	5263	2742	2204	2776
100	2571	2588	5178	2711	2204	2950
110	2561	2502	5097	2696	2202	3067
120	2566	2415	5033	2683	2197	3152
130	2575	2352	4970	2670	2191	3230
140	2606	2299	4939	2657	2186	3296
150	2637	2246	4928	2642	2181	3363
160	2668	2203	4918	2626	2176	3413
170	2689	2184	4907	2610	2171	3462
180	2709	2166	4896	2594	2166	3511
190	2730	2148	4914	2578	2161	3556
200	2749	2132	4938	2563	2156	3598
210	2769	2126	4962	2558	2155	3640
220	2788	2120	4985	2552	2154	3681
230	2808	2114	5008	2547	2154	3730
240	2830	2109	5027	2542	2153	3781
250	2855	2117	5046	2537	2153	3833
260	2879	2126	5065	2527	2154	3884
270	2903	2134	5085	2515	2163	3941
280	2926	2143	5112	2503	2172	3999
290	2949	2158	5142	2490	2181	4057
300	2972	2180	5173	2478	2190	4115
310	2994	2201	5203	2468	2200	4176
320	3011	2223	5226	2459	2218	4238
330	3028	2243	5242	2450	2235	4300
340	3045	2254	5257	2441	2252	4360

(Continued next page)

(Table C2a.-Continued)

Time (hr)	R0L1	R0L2	R0L3	R1L1	R1I2	R1L3
350	3065	2266	5272	2432	2269	4414
360	3097	2277	5288	2426	2291	4467
370	3129	2292	5303	2420	2322	4520
380	3161	2315	5329	2413	2353	4573
390	3199	2338	5367	2407	2384	4626
400	3242	2361	5406	2401	2415	4678
410	3286	2384	5445	2397	2448	4733
420	3321	2407	5483	2402	2480	4797
430	3346	2428	5523	2407	2513	4861
440	3371	2448	5566	2412	2545	4926
450	3390	2468	5608	2418	2582	4988
460	3402	2489	5651	2423	2634	5045
470	3413	2509	5693	2427	2686	5101
480	3424	2528	5736	2431	2739	5157
490	3446	2548	5766	2436	2791	5213
500	3474	2568	5788	2440	2856	5263
510	3501	2591	5809	2450	2922	5314
520	3528	2623	5831	2460	2989	5364
530	3555	2655	5852	2469	3056	5408
540	3582	2687	5883	2479	3123	5442
550	3609	2712	5918	2479	3190	5477
560	3636	2702	5953	2479	3258	5506
570	3678	2692	5989	2479	3325	5528
580	3728	2682	6025	2480	3396	5550

Table C2b. JP-5 vapor concentration for Test IV (ppm)
(in ppm of n-butane + i-pentane)

Time (hr)	R2L1	R2L2	R2L3	R3L1	R3L2	R3I3	R4L3
0	0	0	0	0	0	0	0
10	36	16	5	19	5	1	3
20	320	37	12	37	15	13	3
30	591	75	30	71	32	29	3
40	808	114	55	106	44	54	4
50	974	153	104	142	53	91	4
60	1104	192	157	177	61	131	4
70	1210	245	215	210	67	185	4
80	1284	300	285	241	73	240	4
90	1358	358	367	272	91	318	5
100	1412	417	475	303	109	407	5
110	1454	487	592	335	127	517	6
120	1496	567	702	366	151	635	7
130	1509	646	811	397	186	754	8
140	1521	730	918	428	220	873	9
150	1529	814	1022	457	255	991	10
160	1529	914	1122	478	292	1098	12
170	1529	1025	1222	500	330	1197	15
180	1528	1122	1318	522	368	1297	17
190	1524	1209	1413	543	400	1374	19
200	1521	1282	1499	562	433	1445	21
210	1518	1341	1578	581	465	1515	24
220	1516	1400	1653	600	496	1572	28
230	1515	1440	1713	617	521	1618	33
240	1514	1468	1773	615	545	1664	38
250	1513	1496	1820	614	570	1702	43
260	1506	1518	1858	613	591	1736	49
270	1497	1518	1895	610	609	1770	54
280	1488	1518	1923	607	626	1799	74
290	1478	1518	1943	604	644	1821	96
300	1469	1514	1964	600	653	1843	121
310	1459	1510	1984	597	656	1865	152
320	1449	1505	1999	596	659	1876	184
330	1438	1498	2009	594	662	1887	217
340	1428	1491	2019	593	665	1897	253

(Continued next page)

(Table C2b.-Continued)

Time (hr)	R2L1	R2L2	R2L3	R3L1	R3L2	R3I3	R4L3
350	1418	1484	2028	592	668	1908	289
360	1407	1478	2038	591	667	1917	325
370	1396	1474	2042	587	665	1926	363
380	1386	1469	2046	583	664	1934	402
390	1375	1465	2050	578	663	1943	441
400	1364	1462	2054	574	662	1952	481
410	1355	1460	2058	569	662	1961	523
420	1346	1458	2061	566	661	1970	564
430	1337	1456	2064	563	661	1980	607
440	1329	1454	2067	560	660	1989	656
450	1320	1451	2070	557	659	1996	705
460	1316	1449	2075	554	657	2003	746
470	1311	1446	2080	551	655	2010	786
480	1306	1444	2085	550	654	2017	826
490	1301	1443	2090	548	652	2024	866
500	1295	1442	2094	546	650	2030	907
510	1287	1441	2095	544	649	2037	938
520	1279	1440	2096	545	650	2044	965
530	1271	1436	2098	548	651	2051	992
540	1261	1431	2099	552	651	2059	1010
550	1249	1425	2098	555	652	2068	1027
560	1237	1420	2098	560	653	2076	1043
570	1228	1419	2097	569	659	2085	1054
580	1228	1421	2096	578	664	2093	1065

APPENDIX D

LAVS-1 MOS Hydrocarbon Vapor Sensor Sensitivity

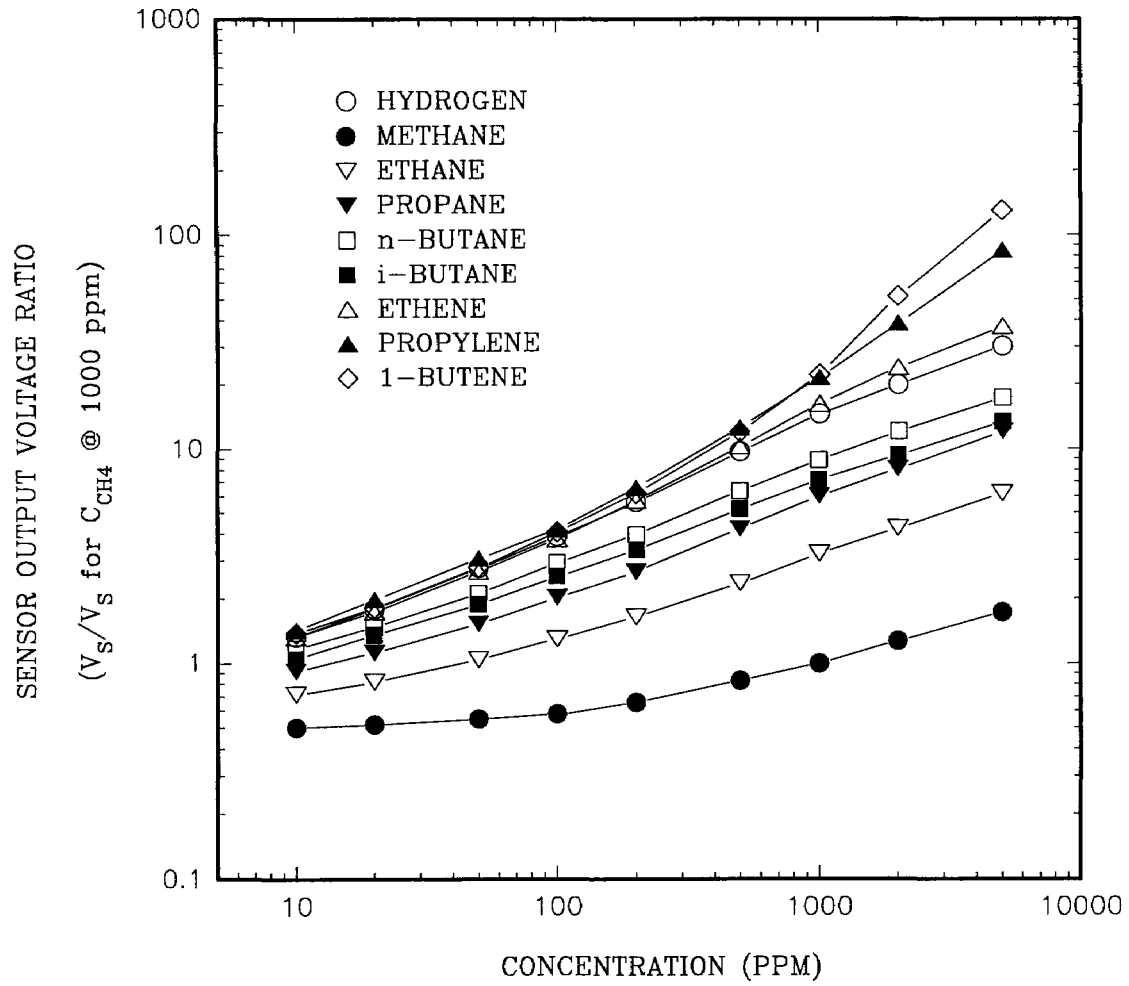


FIGURE D1. LAVS-1 SENSOR SENSITIVITY TO VARIOUS HYDROCARBONS

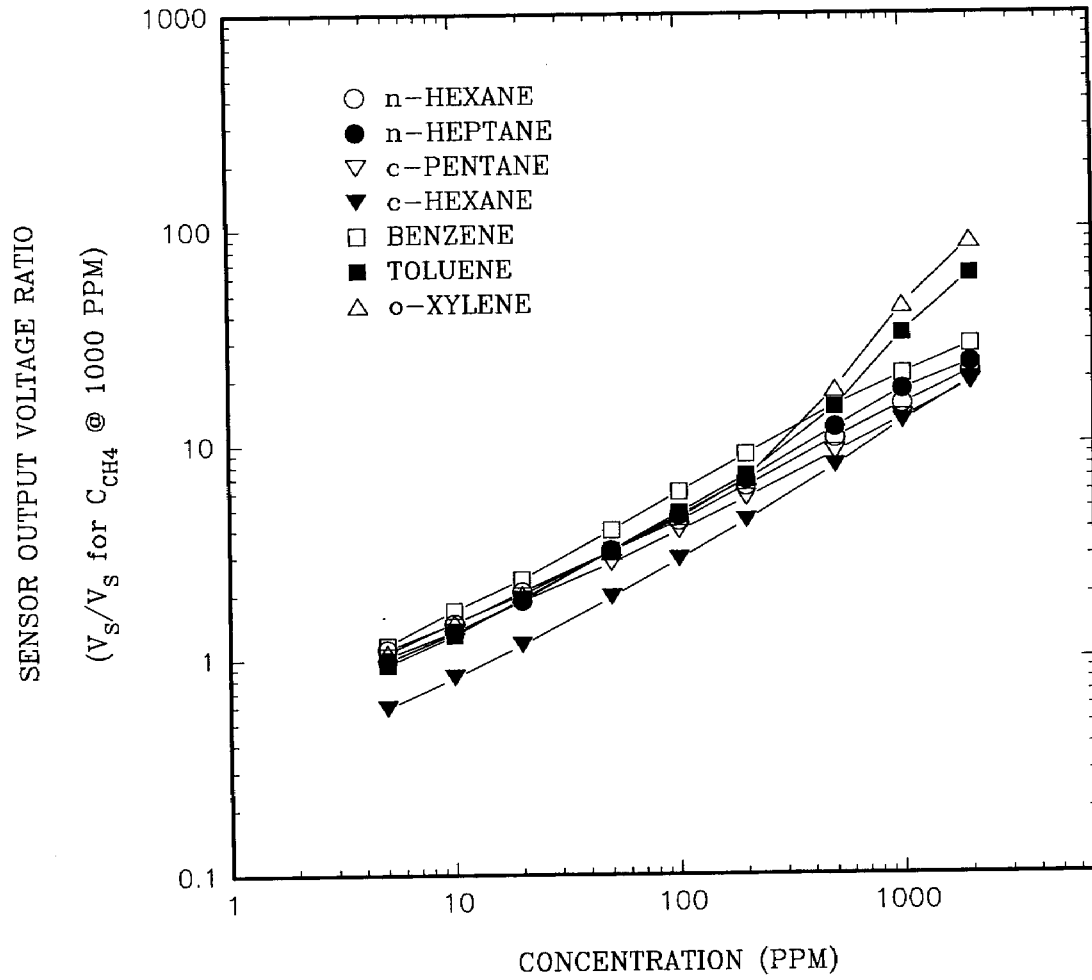


FIGURE D2. LAVS-1 SENSOR SENSITIVITY TO VARIOUS HYDROCARBONS

APPENDIX F

Program Source Code (written in FORTRAN)


```

C=====
C
C This program is designed to simulate the simultaneous transport of
C organic liquid and its vapor in a porous medium after infiltrated
C from a point source with parameter estimation capability. The main
C program starts from the parameter search routine: the complex
C algorithm of Box. Depending on the input value of the parameter
C search control number nsearch, the program will either conduct the
C search or just simulate the transport with a set of input parameters.
C
C Main program for complex algorithm of Box
C
  program mbox2
  implicit double precision (a-h,o-z)
  integer gamma
  character prf1*12,prf2*12,prf3*12
  dimension x(10,5),r(10,5),f(10),g(5),h(5),xc(5),
1tobs(100),ijobs(50,2),cobs(100,50),cest(100,50)
  n=5
  m=5
  k=10
  no=66
  open(unit=55,file='filename.inp',status='old')
  read(55,*)prf1,prf2,prf3,nrand
  close(55)
  call parainput(nsearch,n,m,k,itmax,ic,alpha,beta,gamma,delta,
1x,ntobs,nobs,tobs,ijobs,cobs,g,h,prf1)
  if(nsearch.eq.0)then
  call infdiff(k,m,i,x,ntobs,tobs,nobs,ijobs,cest,prf2,
+itfunc,nsearch)
  stop
  endif
  open(unit=no,file=prf3,status='unknown')
  write(no,50) n,m,k,itmax,ic,alpha,beta,gamma,delta
  write(no,'(5x,1hg,5x,6(:e12.5))')(g(ii),ii=1,n)
  write(no,'(5x,1hh,5x,6(:e12.5),/)'')(h(ii),ii=1,n)
  write(no,60)(jj,jj=1,5)
  close(no)
  call consx(n,m,k,itmax,ntobs,nobs,alpha,beta,gamma,delta,
1x,r,f,it,iev2,g,h,xc,cobs,cest,ijobs,tobs,prf2,prf3,no,
2nrnd,nsearch)
C
  open(unit=no,file=prf3,status='old')
  if(it.gt.itmax)then
  write(no,'(/)')
  write(no,*)'too bad, iteration exceeds the limit.'
  elseif(it.eq.-1)then
  write(no,'(/)')
  write(no,*)'oops, you hit a dead corner.'
  write(no,*)'search cannot go any further.'
  elseif(it.eq.-2)then
  write(no,*)'Picar iteration failed to converge.'
  elseif(it.eq.-3)then
  write(no,*)'liquid entry zone mass balance failed.'
  endif
  if(iev2.eq.0)goto 70
  write(no,'(/)')
  if(it.lt.0)then
  write(no,*)'failed function and x value:'
  else

```

```

        write(no,*)'final function and x value:'
    endif
    write(no,500)iev2,f(iev2),(x(iev2,j),j=1,n)
50    format(2x,4hn = ,i2,3x,4hm = ,i2,3x,4hk = ,i2,2x,8hitmax = ,
        i14,2x,5hic = ,i2,/,2x,8halpha = ,f5.2,5x,7hbeta = ,f10.5,3x,
        28hgamma = ,i2,3x,8hdelta = ,f6.5,/)
60    format(1x,1hi,4x,1hf,4x,5(5x,1hx,i1,5x))
70    close(no)
500    format(i2,f9.5,6(:e12.5))
        stop
        end
c=====
c
c This subroutine calculates the mass balance of the LEZ
c subroutine balanceloz(diffmass,fr,fz,iez)
c implicit double precision (a-h,o-z)
c common /param/ poros,bconst,dh,dt,constb,scmax
c common /satparam/ satmax,satirr,satrange,flowrate
c
c dimension scold(0:150,0:150),sat(0:150,0:150),
+         conc(0:150,0:150)
c common /saturation/ scold,sat,conc
c dimension ns(0:20),iez(0:1,0:220)
c common /entry/ lez,ms,ns
c parameter(pi=3.1415926)
c Calculate the new LEZ volume
c cum=0.
c do 10 l=1,lez
c     i=iez(0,l)
c     j=iez(1,l)
c     re=dfloat(i)
c     cum=cum+(2.*re-1.)*pi*dh*dh*poros*(satcellfunc(i,j,sat)-
+         satcellfunc(i,j,scold))
10 continue
c cum=cum/dt
c Calculate the flux across the vertical boundary of the LEZ
c fluxrs=0.
c do 30 is=ms,1,-1
c     k=ns(is+1)+1
c     if(is.eq.ms)k=1
c     do 30 js=k,ns(is)
c Assign some intermediate variables
c     pif1=pifunction(effsatfunc(sat(is,js)))
c     pif2=pifunction(effsatfunc(sat(is,js-1)))
c     fluxrs=fluxrs+pi*dfloat(is)*dh/2.*(pif1+pif2)*
+         (sat(is,js-1)+sat(is,js)-
+         sat(is+1,js-1)-sat(is+1,js))
30 continue
c Calculate the flux across the horizontal boundary of the LEZ
c fluxzs=0.
c do 60 is=1,ms
c     js=ns(is)
c     effs1=effsatfunc(sat(is,js))
c     effs2=effsatfunc(sat(is-1,js))
c     pif1=pifunction(effs1)
c     pif2=pifunction(effs2)
c     rkr1=relpermfunc(effs1)
c     rkr2=relpermfunc(effs2)
c     fluxzs=fluxzs+(1./4./dh*(pif1+pif2)*(sat(is-1,js)+
+         sat(is,js)-sat(is-1,js+1)-sat(is,js+1)))+

```

```

+          0.5*(rkr1+rkr2))*pi*(2.*dfloat(is)-1.)*dh*dh
60 continue
   fr=fluxrs*bconst
   fz=fluxzs*bconst
   diffmass=bconst*(fluxrs+fluxzs)+cum-flowrate
   return
   end
C=====
C
C This subroutine calculates the coefficients at boundaries
  subroutine boundcoeff(aa,bb,cc,dd,ss0,ks,ijs,n,d)
  implicit double precision (a-h,o-z)
  common /param/ poros,bconst,dh,dt,constb,scmax
  common /diffpara/ concmax,diff,kdiff
  common /satparam/ satmax,satirr,satrange,flowrate
C
  dimension aa(0:150),bb(0:150),cc(0:150),dd(0:150),
+          ss0(0:150),dphi(2),d(0:1)
C
  dphi(1)=0.
  dphi(2)=0.
  scmax=concmax
  if(kdiff.eq.1)then
    scmax=satmax
    dphi(1)=dh/dphidsfunc(effsatfunc(ss0(0)))
    dphi(2)=dh/dphidsfunc(effsatfunc(ss0(n)))
  endif
  goto (100,200) ks
100 continue
  if (ijs.ne.0) then
    bb(ijs+1)=bb(ijs+1)
    cc(ijs+1)=cc(ijs+1)
    dd(ijs+1)=d(0)-aa(ijs+1)*scmax
  else
    bb(ijs+1)=bb(ijs+1)+4./3.*aa(ijs+1)
    cc(ijs+1)=cc(ijs+1)-1./3.*aa(ijs+1)
    dd(ijs+1)=d(0)
  endif
  aa(n-1)=aa(n-1)-1./3.*cc(n-1)
  bb(n-1)=bb(n-1)+4./3.*cc(n-1)
  dd(n-1)=d(1)
  return
200 continue
  if (ijs .ne. 0) then
    bb(ijs+1)=bb(ijs+1)
    cc(ijs+1)=cc(ijs+1)
    dd(ijs+1)=d(0)-aa(ijs+1)*scmax
  else
    bb(ijs+1)=bb(ijs+1)+4./3.*aa(ijs+1)
    cc(ijs+1)=cc(ijs+1)-1./3.*aa(ijs+1)
    dd(ijs+1)=d(0)+1./3.*aa(ijs+1)*2.*dphi(1)
C
  dd(ijs+1)=d(0)
  endif
  aa(n-1)=aa(n-1)-1./3.*cc(n-1)
  bb(n-1)=bb(n-1)+4./3.*cc(n-1)
  dd(n-1)=d(1)+1./3.*cc(n-1)*2.*dphi(2)
C
  dd(n-1)=d(1)
  return
  end
C=====

```

```

c
c this subroutine calculates the saturations on the impermeable
c boundaries
  subroutine boundsc(ks,n1,n2)
    implicit double precision (a-h,o-z)
c
  dimension scold(0:150,0:150),sat(0:150,0:150),
+          conc(0:150,0:150)
  common /saturation/ scold,sat,conc
c
  goto (100,200) ks
100 continue
  do 30 i=0,n1
    sat(i,0)=sat(i,1)
    conc(i,0)=conc(i,1)
    sat(i,n2)=sat(i,n2-1)
  30 conc(i,n2)=conc(i,n2-1)
  return
200 continue
  do 40 i=0,n1
    conc(0,i)=conc(1,i)
    sat(0,i)=sat(1,i)
    conc(n2,i)=conc(n2-1,i)
  40 sat(n2,i)=sat(n2-1,i)
  return
  end
=====
c
c This subroutine calculates the centroid of the complex
  subroutine centr(n,m,k,iev1,i,xc,x,k1)
    implicit double precision (a-h,o-z)
c
  dimension x(k,m),xc(n)
c
  do 20 j=1,n
    xc(j)=0.0
    do 10 il=1,k1
10    xc(j)=xc(j)+x(il,j)
    rk=k1
20    xc(j)=(xc(j)-x(iev1,j))/(rk-1.0)
  return
  end
=====
c
c This subroutine check the new vertex against the constraints and
c makes the necessary adjustment when needed
  subroutine check(n,m,k,x,g,h,i,kode,xc,delta,k1)
    implicit double precision (a-h,o-z)
    dimension x(k,m),g(m),h(m),xc(n)
  10 kt=0
c check against the explicit constraints
  do 50 j=1,n
    if(x(i,j)-g(j))20,20,30
  20 x(i,j)=g(j)+delta*(h(j)-g(j))
    go to 50
  30 if(h(j)-x(i,j))40,40,50
  40 x(i,j)=h(j)-delta*(h(j)-g(j))
  50 continue
    if(kode)110,110,60
c check against the implicit constraints

```

```

60 nn=n+1
   do 100 j=nn,m
   if(x(i,j)-g(j))80,70,70
70 if(h(j)-x(i,j))80,100,100
80 ievl=i
   kt=1
   call centr(n,m,k,ievl,i,xc,x,k1)
   do 90 jj=1,n
     x(i,jj)=(x(i,jj)+xc(jj))/2
90 continue
100 continue
   if(kt)110,110,10
110 return
   end
=====
c
c This subroutine calculates the coefficients, AR, BR and CR for
c the 1st stage or AZ, BZ and CZ for the 2nd stage. The coefficients
c are stored in aa, bb, and cc arrays
   subroutine coeffroutine(ss0,ijs,n,ks,aa,bb,cc)
   implicit double precision (a-h,o-z)
   common /param/ poros,bconst,dh,dt,constb,scmax
c
   dimension ss0(0:150),pf(0:150),dkrds(0:150),aa(0:150),
+         bb(0:150),cc(0:150)
c
c Calculate the PI function and derivative of relative permeability
   do 30 i=ijs,n
     sateff=effsatfunc(ss0(i))
     dkrds(i)=dkrdsfunc(sateff)
     pf(i)=pifunction(sateff)
30 continue
c
   goto (100, 200) ks
100 continue
   do 110 i=ijs+1,n-1
     aa(i)=pf(i-1)+(1.-1./dfloat(i))*pf(i)
     bb(i)=- (pf(i+1)+2.*pf(i)+pf(i-1)+constb)
     cc(i)=pf(i+1)+(1.+1./dfloat(i))*pf(i)
110 continue
   return
200 continue
   do 210 i=ijs+1,n-1
     aa(i)=pf(i)+pf(i-1)+dh*dkrds(i)
     bb(i)=- (pf(i+1)+2.*pf(i)+pf(i-1)+constb)
     cc(i)=pf(i+1)+pf(i)-dh*dkrds(i)
210 continue
   return
   end
=====
c
c This subroutine is the main body of the complex algorithm
   subroutine consx(n,m,k,itmax,ntobs,nobs,alpha,beta,gamma,
+delta,x,r,f,it,iev2,g,h,xc,cobs,cest,ijobs,tobs,prf2,prf3,
+no,nrand,nsearch)
   implicit double precision (a-h,o-z)
   real rrand
   integer gamma
   character prf2*12,prf3*12
   dimension x(k,m),r(k,n),f(k),g(m),h(m),xc(n),

```

```

+cobs(100,50),cest(100,50),ijobs(50,2),tobs(100)
  it=1
  kount=1
  kode=0
  if(m.gt.n)kode=1
  do 30 ii=1,k
  do 30 jj=1,n
  ndum=-(nrand+(ii-1)*n+jj-1)
  r(ii,jj)=rrand(ndum)
30  continue
c calculate complex points and check against constraints
do 65 ii=1,k
do 50 j=1,n
50  x(ii,j)=g(j)+r(ii,j)*(h(j)-g(j))
  i=ii
  k1=ii
  call check(n,m,k,x,g,h,i,kode,xc,delta,k1)
65  continue
  k1=k
  open(unit=no,file=prf3,status='old')
  write(no,*)'initial complex function and x value:'
  close(no)
  do 70 i=1,k
  call func(n,m,k,x,f,i,ntobs,tobs,nobs,ijobs,cobs,
+cest,prf2,itfunc)
  open(unit=no,file=prf3,status='old')
  write(no,500)i,f(i),(x(i,j),j=1,n)
  close(no)
  if(itfunc.lt.0)then
  it=itfunc-1
  goto 240
  endif
70  continue
  open(unit=no,file=prf3,status='old')
  write(no,*)'adjusted function and x value:'
  close(no)
c find point with the lowest function value
80  iev1=1
  do 100 icm=2,k
  if(f(iev1)-f(icm))100,100,90
90  iev1=icm
100 continue
  fmin=f(iev1)
c find the point with the highest function value
  iev2=1
  do 120 icm=2,k
  if(f(iev2)-f(icm))110,110,120
110 iev2=icm
120 continue
  fmax=f(iev2)
c check convergence criteria
  if(fmax-fmin.le.beta)goto 240
c replace point with the lowest function value
  call centr(n,m,k,iev1,i,xc,x,k1)
  do 160 jj=1,n
160  x(iev1,jj)=(1.0+alpha)*xc(jj)-alpha*x(iev1,jj)
170  i=iev1
  call check(n,m,k,x,g,h,i,kode,xc,delta,k1)
  call func(n,m,k,x,f,i,ntobs,tobs,nobs,ijobs,cobs,
+cest,prf2,itfunc)

```

```

        open(unit=no,file=prf3,status='old')
        write(no,500)iev1,f(iev1),(x(iev1,j),j=1,n)
        close(no)
        if(itfunc.lt.0)then
            it=itfunc-1
            goto 240
        endif
c replace new point if it repeats as lowest function value
        iev3=1
        do 190 icm=2,k
            if(f(iev3)-f(icm))190,190,180
180     iev3=icm
190     continue
        if(iev3.eq.iev1)then
            if(dabs(f(iev1)-fmin).le.(.1*beta))then
                kount=kount+1
                if(kount.eq.10)then
                    it=-1
                    goto 240
                endif
            else
                kount=1
            endif
            fmin=f(iev1)
            do 210 jj=1,n
210     x(iev1,jj)=(x(iev1,jj)+xc(jj))/2.0
                it=it+1
                go to 170
            endif
            it=it+1
            if(it-itmax)80,80,240
240     continue
            if(it.lt.0)iev2=i
500     format(i2,f9.5,6(:e12.5))
        return
        end
c=====
c
c Define functions
c The derivative of relative permeability function
        double precision function dkrdsfunc(sateff)
        implicit double precision (a-h,o-z)
        common /satparam/ satmax,satirr,satrange,flowrate
        common /diffpara/ concmax,diff,kdiff
        common /dphdtparam/ alpha,am,an,sem,plamda
        dkrdsfunc=0.
        if(kdiff.eq.1)dkrdsfunc=(3.+2./plamda)/satrange*
+           sateff**(2.+2./plamda)
        return
        end
c=====
c
c The derivative of hydrolic pressure function using
c van Genuchten's formula
        double precision function dphidsfunc(sateff)
        implicit double precision (a-h,o-z)
        common /satparam/ satmax,satirr,satrange,flowrate
        common /diffpara/ concmax,diff,kdiff
        common /dphdtparam/ alpha,am,an,sem,plamda
        dphidsfunc=0.

```

```

    if(kdiff.eq.1)then
      if(sateff.ge.sem)then
        dphidsfunc=(sem**(-1./am)-1.)**(1./an-1.)*
+          sem**(-1./am-1.)/alpha/an/am/satrange
      else
        dphidsfunc=(sateff**(-1./am)-1.)**(1./an-1.)*
+          sateff**(-1./am-1.)/alpha/an/am/satrange
      endif
    endif
  return
end

C=====
C
c The effective saturation function
double precision function effsatfunc(sat)
implicit double precision (a-h,o-z)
common /satparam/ satmax,satirr,satrange,flowrate
common /diffpara/ concmax,diff,kdiff
if(kdiff.eq.1) effsatfunc=(sat-satirr)/satrange
return
end

C=====
C
c Calculate the geometry of liquid entry zone (LEZ)
subroutine entrygeom(l)
implicit double precision (a-h,o-z)
dimension nodd(0:20),ns(0:20)
common /entry/ lez,ms,ns
c Initialize the odd which stores the cell index of the surface row
c of the LEZ
do 10 i=1,20
  nodd(i)=0
  do 10 j=1, i
    10 nodd(i)=nodd(i)+j
c Find ms, the most right side cell of the LEZ
do 20 i=1,l+1
  if (l.lt.nodd(i)) then
    ms=i-1
    goto 30
  endif
20 continue
c Find ms storing the vertical lengths of nodes of the LEZ
30 k=l-nodd(ms)
  ns(0)=ms
  do 40 i=1,ms
    40 ns(i)=ms-i+1
    if (k.gt.0) then
      do 50 j=0,k
        50 ns(j)=ns(j)+1
      endif
    return
  end
C=====
C
c Calculate the coordinates of liquid entry cell nodes
subroutine entrynodes(iez)
implicit double precision (a-h,o-z)
dimension iez(0:1,0:220)
i=0
do 10 k=1,20

```



```

        do 10 j=1,k
            i=i+1
            iez(0,i)=j
10    iez(1,i)=k-j+1
        return
    end
C=====
C
C This subroutine calculates the objective function of the search
  subroutine func(n,m,k,x,f,i,ntobs,tobs,nobs,ijobs,cobs,
+cest,prf2,itfunc,nsearch)
  implicit double precision (a-h,o-z)
  character prf2*12
  common /diffpara/concmax,diff,kdiff
  dimension x(k,m),f(k),cest(100,50),cobs(100,50),tobs(100),
+ijobs(50,2)
C
  call infdiff(k,m,i,x,ntobs,tobs,nobs,ijobs,cest,prf2,
+itfunc,nsearch)
  f(i)=0.
  nn=0
  do 20 kk=1,ntobs
  do 20 ii=1,nobs
      if(cobs(kk,ii).gt.0.0001)then
          if((cobs(kk,ii).lt.concmax).and.(cest(kk,ii).lt.concmax))then
              f(i)=f(i)+(cest(kk,ii)-cobs(kk,ii))*2
              nn=nn+1
          endif
      endif
20  continue
  f(i)=-dsqrt(f(i))/nn
  return
  end
C=====
C
C This subroutine calculates the simulated concentration at
c an observation point
  subroutine funcconc(conc,iobs,jobs,cij)
  implicit double precision (a-h,o-z)
  dimension ri(0:6),jz(3),conc(0:150,0:150)
  ri(0)=0.
  ri(1)=3.75
  ri(2)=7.5
  ri(3)=11.25
  ri(4)=15.
  ri(5)=18.75
  ri(6)=22.5
  jz(1)=6
  jz(2)=15
  jz(3)=24
  i=int(ri(iobs))
  f=1.-(ri(iobs)-int(ri(iobs)))
  j=jz(jobs)
  cij=conc(i,j)*f+conc(i+1,j)*(1.-f)
  return
  end
C=====
C
C This subroutine is the main body of the transport simulation model
  subroutine infdiff(kx,mx,ip,paraest,ntobs,tobs,nobs,ijobs,

```

```

+cest,prf2,itinf,nsearch)
  implicit double precision (a-h,o-z)
  dimension paraest(kx,mx),cest(100,50),tobs(100),
+ijobs(50,2)
-----
c Declare parameters
c
c perm:      intrinsic permeability [L^2]
c poros:    porosity [L^3/L^3]
c plamda:   soil index number for kr vs. s (Corey's equation)
c alpha:    factor for van Genuchten's equation
c an, am:   factors for van Genuchten's equation
c flowrate: liquid discharge rate [L^3/T]
c dh:       increment in space [L]
c dt:       time increment [T]
c diff:     gas diffusion coefficient [L^2]
-----
c Output/input file name
  character fname1*12,fname2*12,prf2*12
-----
c Declare the arrays:
c
c scold -- saturations at time kt*dt;
c sat & conc -- saturation/concentration at time (kt+1)*dt;
c cappi -- capillary pressure of the primary direction at kt*dh;
c ns -- depths of the LEZ at locations: is = 1...ms;
c sctmp -- starting saturation/concentration for the picar iteration,
c         of the nodes of primary and its adjacent chains
c         are stored;
c ssiter-- resulting saturation of the picar iteration
-----
c Total nodes in r and z directions, mm and nn; and their larger one,
c mn
  dimension scold(0:150,0:150),sat(0:150,0:150),conc(0:150,0:150),
+         ns(0:20),sctmp(0:150,3),ssiter(0:150),iez(0:1,0:220),
+         sleztmp(0:21,0:21),printtime(10)
  common /saturation/ scold,sat,conc
  common /mmnn/ mm,nn
  common /diffpara/concmax,diff,kdiff
  common /entry/lez,ms,ns
  common /param/ poros,bconst,dh,dt,constb,scmax
  common /scparam/ sat0,sc0,satconc
  common /dphdtparam/alpha,am,an,sem,plamda
  common /satparam/satmax,satirr,satrange,flowrate
  common /printcom/printtime,iprinttotal,irpf,izpf
-----
c Initialize the common parameters
  call readparam(prf2,fname1,fname2,perm,dens,viscos,ksatonly)
c Create the output files
  nfn1=7
  nfn2=8
  open(unit=nfn1,file=fname1,status='unknown')
  open(unit=nfn2,file=fname2,status='unknown')
c New vertex
  if(nsearch.eq.0)goto 5
  perm=paraest(ip,1)
  alpha=paraest(ip,2)
  an=paraest(ip,3)
  am=1.-1./an
  sem=(an/(2.*an-1.))*((an-1.)/an)

```

```

        plamda=paraest(ip,4)
        diff=paraest(ip,5)
5      continue
c Print parameters
      call printparameter(nfn1,perm,dens,viscos)
      perm=perm*9.8*dens/viscos
c Calculate the entrynode coordinates
      call entrynodes(iez)
c Initialize print control index: ipp=0 to print saturation
c and 1 to print concentration, iprint controls the time to print
      itinf=0
      kkk=1
      iprint=1
c
c Initialize the saturation and concentration arrays
      do 10 i=0,mm
        do 10 j=0,nn
          sat(i,j)=sat0
          scold(i,j)=sat0
          conc(i,j)=0.
        10 continue
c
c Initial time index, number of LEZ cells, and Jrz index. Jrz
c index is the index for the secondary direction of the ADI and
c it starts from zero.
      kt=0
      lez=1
      kdiff=1
      slezbound=satmax
      slez1=satmax
      slez2=sat0
      call entrygeom(lez)
      call initentryzone(slezbound,sleztmp)
c
      30 continue
      itmass=0
      if(kdiff.eq.1)then
        kt=kt+1
        t=dfloat(kt)*dt/2./3600.
c
c Determine the stage of ADI based on the value of kt. In stage I when
c kt is an odd number, ADI solves the equations in r direction and
c stage II with even kt calculates in z direction.
      ks=kt/2-(kt-1)/2+1
      bconst=perm/poros
      sc0=sat0
      scmax=satmax
      do 33 i=0,mm
        do 33 j=0,nn
33      scold(i,j)=sat(i,j)
      elseif(kdiff.eq.0)then
        bconst=1.
        scmax=concmx
        sc0=0.
        do 34 i=0,mm
          do 34 j=0,nn
34      scold(i,j)=conc(i,j)
      endif
      constb=4.*dh*dh/bconst/dt
c

```

```

35 jrz=0
   itmass=itmass+1
   if(itmass.gt.50)then
       itinf=-2
       goto 500
   endif
40 jrz=jrz+1
c
c Assign value for array sctmp(0:n,3). sctmp(i,1:3) stores the old
c saturations at the primary node chain (jrz) and its adjacent chains
c (jrz-1 and jrz+1)
   if(ks.eq.1)then
       ks2=2
       n=mm
       n2=nn
       do 45 i=0,n
           sctmp(i,1)=scold(i,jrz-1)
           sctmp(i,2)=scold(i,jrz)
45      sctmp(i,3)=scold(i,jrz+1)
           if(kdiff.eq.1)then
               if(jrz.le.ns(0)+1)then
                   do 50 i=0,ms
                       sctmp(i,1)=sleztmp(i,jrz-1)
                       sctmp(i,2)=sleztmp(i,jrz)
50          sctmp(i,3)=sleztmp(i,jrz+1)
                   endif
               endif
           elseif(ks.eq.2)then
               ks2=1
               n=nn
               n2=mm
               do 55 i=0,n
                   sctmp(i,1)=scold(jrz-1,i)
                   sctmp(i,2)=scold(jrz,i)
55          sctmp(i,3)=scold(jrz+1,i)
                   if(kdiff.eq.1)then
                       if(jrz.le.ms+1)then
                           do 60 i=0,ns(0)
                               sctmp(i,1)=sleztmp(jrz-1,i)
                               sctmp(i,2)=sleztmp(jrz,i)
60          sctmp(i,3)=sleztmp(jrz+1,i)
                           endif
                       endif
                   endif
               endif
           endif
       endif
c
c Determine the ijs
   ijs=0
   do 70 i=0,n
       if(sctmp(i,2).ge.scmx) ijs=i
70  continue
   if(kdiff.eq.1)then
       do while(sctmp(ijs+1,2).eq.slezbound)
           ijs=ijs+1
       end do
   endif
c
call picariter(sctmp,n,ks,ijs,ssiter,itpicar)
if(itpicar.gt.50)then
    itinf=-1
    goto 500

```

```

endif
if(ks.eq.1)then
  if(kdiff.eq.1)then
    do 80 i=ijs,n
      80   sat(i,jrz)=ssiter(i)
    elseif(kdiff.eq.0)then
      do 85 i=ijs,n
      85   conc(i,jrz)=ssiter(i)
    endif
  elseif(ks.eq.2)then
    if(kdiff.eq.1)then
      do 90 i=ijs,n
      90   sat(jrz,i)=ssiter(i)
    elseif(kdiff.eq.0)then
      do 95 i=ijs,n
      95   conc(jrz,i)=ssiter(i)
    endif
  endif
endif
if(jrz.lt.n2-1) goto 40
c Calculate the saturations on the impermeable boundaries
call boundsc(ks,n,n2)
c Check the mass balance inside the LEZ
if(kdiff.eq.1)then
  call balancelez(diffmasat,fr,fz,iez)
  call satleznod(slezbound,slez1,slez2,diffmasat)
  if(dabs(slezbound).lt.0.00001)then
    slezbound=satmax
    slez1=satmax
    slez2=sat0
    goto 97
  elseif(slezbound.lt.0.)then
    lez=lez+1
    slezbound=satmax
    slez1=satmax
    slez2=sat0
    call entrygeom(lez)
    call initentryzone(slezbound,sleztmp)
    goto 35
  else
    call initentryzone(slezbound,sleztmp)
    goto 35
  endif
endif
c Print the saturation/concentration
97 continue
if(ksatonly.eq.1)kdiff=0
if(t.gt.printtime(iprint))then
  if((ks.eq.1).and.(kdiff.eq.0))then
    call printsatconc(nfn1,nfn2,irpf,izpf,ks,
+      diffmasat,t,iteration)
    iprint=iprint+1
  endif
endif
c Copy new saturations, sat, to the old ones, scold
if(kdiff.eq.0)then
  if(t.gt.tobs(kkk))then
    do 98 i=1,nobs
      ii=ijobs(i,1)
      jj=ijobs(i,2)
      call funcconc(conc,ii,jj,conc1)
    enddo
  endif
endif

```

```

          cest(kkk,i)=concl
c          cest(kkk,i)=sat(ii,jj)
c          cest(kkk,i)=conc(ii,jj)
    98      continue
          kkk=kkk+1
          endif
          do 100 i=0,mm
            do 100 j=0,nn
    100      scold(i,j)=sat(i,j)
            call initentryzone(slezbound,sleztmp)
            kdifff=1
            elseif(kdifff.eq.1)then
              do 110 i=0,mm
                do 110 j=0,nn
                  if(sat(i,j).ge.satconc)conc(i,j)=concmax
    110      scold(i,j)=conc(i,j)
                  kdifff=0
                endif
            endif
c Increment kt and go to the next ADI stage
          if(kkk.le.ntobs)goto 30
    999 format(100(:F8.5))
    500 continue
          close(nfn1)
          close(nfn2)
          return
          end
=====
c
c Initilize the LEZ and LEZ bound saturation
  subroutine initentryzone(slezbound,slez)
    implicit double precision (a-h,o-z)
    dimension scold(0:150,0:150),sat(0:150,0:150),
+           conc(0:150,0:150),
+           nodd(0:20),ns(0:20),slez(0:21,0:21)
    common /saturation/ scold,sat,conc
    common /entry/ lez,ms,ns
    common /satparam/ satmax,satirr,satrange,flowrate
    do 5 i=0,21
      do 5 j=0,21
    5 slez(i,j)=scold(i,j)
      do 10 i=0,ms
        do 10 j=0,ns(i)-1
          slez(i,j)=satmax
    10 sat(i,j)=satmax
        do 15 j=0,ns(ms)
          slez(ms,j)=slezbound
    15 sat(ms,j)=slezbound
          if(ms.gt.1)then
            do 20 i=ms-1,1,-1
              do 20 j=ns(i+1),ns(i)
                slez(i,j)=slezbound
    20 sat(i,j)=slezbound
              endif
            slez(0,ns(0))=slezbound
            sat(0,ns(0))=slezbound
          return
          end
=====
c
c This subroutine reads all the input data for parameter search

```

```

subroutine parainput(nsearch,n,m,k,itmax,ic,alpha,beta,gamma,
ldelta,lx,ntobs,nobs,tobs,ijobs,cobs,g,h,prf1)
implicit double precision (a-h,o-z)
character prf1*12
dimension x(k,m),tobs(100),ijobs(50,2),cobs(100,50),
lg(m),h(m)
integer gamma
open(unit=55,file=prf1,status='old')
read(55,*)nsearch
if(nsearch.eq.0)then
close(55)
return
endif
read(55,*)itmax,ic,alpha,beta,gamma,delta
read(55,*)(x(1,jj),jj=1,m)
read(55,*)(g(jj),h(jj),jj=1,m)
read(55,*)ntobs
read(55,*)(tobs(i),i=1,ntobs)
read(55,*)nobs
read(55,*)(ijobs(i,1),ijobs(i,2),i=1,nobs)
read(55,*)((cobs(i,j),j=1,nobs),i=1,ntobs)
close(55)
do 10 i=1,ntobs
do 10 j=1,nobs
if(cobs(i,j).lt.0.0)cobs(i,j)=0.0
if(cobs(i,j).gt.0.95)cobs(i,j)=0.95
10 continue
return
end

c=====
c
c Picard iteration subroutine
subroutine picariter(sctmp,n,ks,ijs,ss1,iteration)
implicit double precision (a-h,o-z)
common /param/ poros,bconst,dh,dt,constb,scmax
common /scparam/ sat0,sc0,satconc
common /diffpara/ concmax,diff,kdiff
c
dimension sctmp(0:150,3),ss0(0:150),ss1(0:150),
+ pifunc(0:150),rzst(0:150),aa(0:150),bb(0:150),
+ cc(0:150),dd(0:150),dkrds(0:150),d(0:1)
data alloweps /1.d-005/
c Calculate Rst or Zst depending on the current stage designated
c by ks
call rzstroutine(sctmp,ijs,n,ks,rzst)
do 10 i=0,n
ss0(i)=sctmp(i,2)
ss1(i)=ss0(i)
dd(i)=-rzst(i)-sctmp(i,2)*constb
10 continue
d(0)=dd(ijs+1)
d(1)=dd(n-1)
iteration=0
20 iteration=iteration+1
if(iteration.gt.50)goto 70
c Calculate the coefficients, AR, BR and CR, or AZ, BZ, and CZ
call coeffroutine(ss0,ijs,n,ks,aa,bb,cc)
c Calculate the coefficients of boundary nodes
c
call boundcoeff(aa,bb,cc,dd,ss0,ks,ijs,n,d)

```

```

c Solve the tridiagonal systems of equations
  call tridiagonal(aa,bb,cc,dd,ijs+1,n-1,ss1)
c Caculate the boundary saturations
  if(ijs.eq.0)then
    ssl(ijs)=(4.*ssl(ijs+1)-ssl(ijs+2))/3.
    if((kdifff.eq.1).and.(ks.eq.2))then
      ssl(ijs)=ssl(ijs)-2.*dh/
+      dphidsfunc(effsatfunc(ssl(ijs+1)))
    endif
  endif
  ssl(n)=(4.*ssl(n-1)-ssl(n-2))/3.
  if((kdifff.eq.1).and.(ks.eq.2))then
    ssl(n)=ssl(n)+2.*dh/
+    dphidsfunc(effsatfunc(ssl(n-1)))
  endif
  do 49 i=ijs,n
    if(ssl(i).gt.scmax)ssl(i)=scmax
    if(ssl(i).lt.sc0)ssl(i)=sc0
  49 continue
c Check the error
  eps=0.
  do 50 i=ijs+1,n-1
  50 eps=eps+dabs(ssl(i)-ss0(i))*2.
  eps=dsqrt(eps)
  if(eps.le.alloweps)goto 70
  do 60 i=ijs,n
  60 ss0(i)=ssl(i)
  goto 20
  70 close(9)
  return
  end

=====
c
c The PI function
  double precision function pifunction(sateff)
  implicit double precision (a-h,o-z)
  common /diffpara/ concmax,diff,kdifff
  if(kdifff.eq.0)then
    pifunction=diff
  elseif(kdifff.eq.1)then
    pifunction=relpermfunc(sateff)*dphidsfunc(sateff)
  endif
  return
  end

=====
c
c Print parameters in the file
  subroutine printparameter(nfn1,perm,dens,viscos)
  implicit double precision (a-h,o-z)
  common /param/ poros,bconst,dh,dt,constb,scmax
  common /scparam/ sat0,sc0,satconc
  common /satparam/ satmax,satirr,satrange,flowrate
  common /diffpara/ concmax,diff,kdifff
  dimension printtime(10)
  common /printcom/printtime,iprinttotal,irpf,izpf
  common /dphdsparam/ alpha,am,an,sem,plamda

c
  write(nfn1,*) 'parameters:'
  write(nfn1,100)'permeability=',perm
  write(nfn1,100)' density=',dens

```



```

        write(nfn1,100)'    viscosity=',viscos
        write(nfn1,100)'    porosity=',poros
        write(nfn1,100)'    flowrate=',flowrate
        write(nfn1,100)'    dt=',dt
        write(nfn1,100)'    dh=',dh
        write(nfn1,100)'    plamda=',plamda
        write(nfn1,100)'    alpha=',alpha
        write(nfn1,100)'    an=',an
        write(nfn1,*) 'print factors:'
        write(nfn1,300)'    irpf=',irpf
        write(nfn1,300)'    izpf=',izpf
        write(nfn1,100)'    max sat=',satmax
        write(nfn1,100)'    min sat=',satirr
        write(nfn1,100)'max conc sat=',satconc
        write(nfn1,100)'max vap conc=',concmax
        write(nfn1,100)' initial sat=',sat0
        write(nfn1,100)'initial conc=',sc0
        write(nfn1,100)' vapor diff=',diff
c
100 format(A,G12.5)
300 format(A,I2)
    return
    end
c=====
c
c Print the saturation data in a file
    subroutine printsatconc(nfn1,nfn2,irpf,izpf,ks,dm,t,it)
    implicit double precision (a-h,o-z)
    common /mmnn/ mm,nn
c
    dimension scold(0:150,0:150),sat(0:150,0:150),
+           conc(0:150,0:150)
    common /saturation/ scold,sat,conc
    common /diffpara/ concmax,diff,kdiff
    write(nfn1,*)ks,t,dm,it
    write(nfn2,*)ks,t
    do 20 j=0,nn,izpf
        write(nfn1,30) (sat(i,j),i=0,mm,irpf)
20 write(nfn2,30) (conc(i,j),i=0,mm,irpf)
30 format(151(:F7.5))
    return
    end
c=====
c
c This subroutine reads all the input parameters used by the
c transport model
    subroutine readparam(prf2,fname1,fname2,perm,dens,
+           viscos,ksatonly)
    implicit double precision (a-h,o-z)
    character prf2*12,fname1*12,fname2*12,tmpstr*10
    dimension printtime(10)
    common /param/ poros,bconst,dh,dt,constb,scmax
    common /satparam/ satmax,satirr,satrange,flowrate
    common /scparam/ sat0,sc0,satconc
    common /printcom/printtime,iprinttotal,irpf,izpf
    common /mmnn/ mm,nn
    common /diffpara/ concmax,diff,kdiff
    common /dphdsparam/ alpha,am,an,sem,plamda
c-----
    open(unit=4,file=prf2,status='old')

```

```

read(4,*)fname1,fname2
read(4,*)tmpstr,(printtime(i),i=1,10)
read(4,*)tmpstr,iprinttotal
read(4,*)tmpstr,irpf
read(4,*)tmpstr,izpf
read(4,*)tmpstr,ksatonly
read(4,*)tmpstr,perm
read(4,*)tmpstr,dens
read(4,*)tmpstr,viscos
read(4,*)tmpstr,poros
read(4,*)tmpstr,plamda
read(4,*)tmpstr,alpha
read(4,*)tmpstr,an
read(4,*)tmpstr,flowrate
read(4,*)tmpstr,satmax
read(4,*)tmpstr,satirr
read(4,*)tmpstr,sat0
read(4,*)tmpstr,satconc
read(4,*)tmpstr,dh
read(4,*)tmpstr,dt
read(4,*)tmpstr,mm
read(4,*)tmpstr,nn
read(4,*)tmpstr,diff
read(4,*)tmpstr,concmax
close(4)
satrange=satmax-satirr
am=1.-1./an
sem=(an/(2.*an-1.))**((an-1.)/an)
return
end
c=====
c
c The relative permeability function
double precision function relperfunc(sateff)
implicit double precision (a-h,o-z)
common /diffpara/ concmax,diff,kdiff
common /dphdtparam/ alpha,am,an,sem,plamda
if(kdiff.eq.1)relperfunc=sateff**(3.+2./plamda)
return
end
c=====
c
c The random number generator. The function returns a uniform
c random deviate between 0.0 and 1.0. Set idum to any negative value
c to initialize or reinitialize the sequence
function rrand(idum)
dimension r(97)
parameter (m1=259200,ia1=7141,ic1=54773,rm1=1./m1)
parameter (m2=134456,ia2=8121,ic2=28411,rm2=1./m2)
parameter (m3=243000,ia3=4561,ic3=51349)
data iff /0/
if(idum.lt.0.or.iff.eq.0)then
  iff=1
  ix1=mod(ic1-idum,m1)
  ix1=mod(ia1*ix1+ic1,m1)
  ix2=mod(ix1,m2)
  ix1=mod(ia1*ix1+ic1,m1)
  ix3=mod(ix1,m3)
  do 11 j=1,97
    ix1=mod(ia1*ix1+ic1,m1)

```

```

        ix2=mod(ia2*ix2+ic2,m2)
        r(j)=(float(ix1)+float(ix2)*rm2)*rm1
1      continue
        idum=1
      endif
      ix1=mod(ia1*ix1+ic1,m1)
      ix2=mod(ia2*ix2+ic2,m2)
      ix3=mod(ia3*ix3+ic3,m3)
      j=1+(97*ix3)/m3
      if(j.gt.97.or.j.lt.1)pause
      rrand=r(j)
      r(j)=(float(ix1)+float(ix2)*rm2)*rm1
      return
    end

C=====
C
C This subroutine calculates Rst or Zst and stores them in RZST
  subroutine rzstroutine(sctmp,ijs,n,ks,rzst)
  implicit double precision (a-h,o-z)
  common /param/ poros,bconst,dh,dt,constb,scmax
C
  dimension sctmp(0:150,3),rzst(0:150),pf(3)
  dimension dkrds(0:150)
  do 20 i=ijs+1,n-1
    do 10 j=1,3
      sateff=effsatfunc(sctmp(i,j))
      if(j.eq.2)dkrds(i)=dkrdsfunc(sateff)
      pf(j)=pifunction(sateff)
10    continue
    rzst(i)=(pf(3)+pf(2))*(sctmp(i,3)-sctmp(i,2))-(pf(2)+pf(1))*
+      (sctmp(i,2)-sctmp(i,1))
    if(ks.eq.1)then
      rzst(i)=rzst(i)-dh*dkrds(i)*(sctmp(i,3)-sctmp(i,1))
    else
      rzst(i)=rzst(i)+pf(2)*(sctmp(i,3)-sctmp(i,1))/dfloat(i)
    endif
20  continue
    return
  end

C=====
C The cell saturation function
  double precision function satcellfunc(i,j,x)
  implicit double precision (a-h,o-z)
  dimension x(0:150,0:150)
  satcellfunc=.25*(x(i,j)+x(i-1,j)+x(i,j-1)+x(i-1,j-1))
  return
  end

C=====
C This subroutine calculates the saturation of the entry cell node
  subroutine satleznode(s,s1,s2,dm)
  implicit double precision (a-h,o-z)
  common /satparam/ satmax,satirr,satrangle,flowrate
C
  errm=1.d-8
  adm=abs(dm)
  if(adm.le.errm)then
    s=0.
  else
    if(dm.lt.0.)then
      if((satmax-s).lt.0.01)then

```

```

        s=-1.
    else
        s2=s
        s=0.5*(s1+s2)
    endif
else
    s1=s
    s=0.5*(s1+s2)
endif
endif
return
end
=====
c
c This subroutine solves the tridiagonal systems of equations
c by Gauss elimination
c   subroutine tridiagonal(a,b,c,d,i0,n,x)
c   implicit double precision (a-h,o-z)
c
c   dimension a(0:150),b(0:150),c(0:150),d(0:150),x(0:150)
c   dimension beta(0:150),y(0:150)
c
c Forward elimination
beta(i0)=c(i0)/b(i0)
do 10 i=i0+1,n
    beta(i)=c(i)/(b(i)-a(i)*beta(i-1))
10 continue
y(i0)=d(i0)/b(i0)
do 20 i=i0+1,n
    y(i)=(d(i)-a(i)*y(i-1))/(b(i)-a(i)*beta(i-1))
20 continue
c
c Back substitution
x(n)=y(n)
do 30 i=n-1,i0,-1
    x(i)=y(i)-beta(i)*x(i+1)
30 continue
return
end
=====

```